Technische Universität München
TUM School of Engineering and Design

Early warning of rock slope failures – real-time monitoring, process analysis and failure time forecasting

Johannes Michael Leinauer

Vollständiger Abdruck der von der TUM School of Engineering and Design der Technischen Universität München zur Erlangung eines

Doktors der Naturwissenschaften (Dr. rer. nat.)

genehmigten Dissertation.

Vorsitz: Prof. Dr. Kurosch Thuro

Prüfende der Dissertation:

1. Prof. Dr. Michael Krautblatter
2. Prof. Dr. Andreas Lang
3. Prof. Dr. Giovanni B. Crosta

Die Dissertation wurde am 11.04.2024 bei der Technischen Universität München eingereicht und durch die TUM School of Engineering and Design am 22.11.2024 angenommen.

Declaration of authorship

I, Johannes Leinauer, declare that the thesis entitled "Early warning of rock slope failures – real-time monitoring, process analysis and failure time forecasting" and the work presented in this thesis are both my own, and have been generated by me as a result of my own original research. I confirm that:

- where I have quoted from the work of others, the source is always given
- where any parts of this thesis have been previously submitted for a degree at the Technical University of Munich or any other institution, this has been clearly stated
- I have acknowledged all main sources of help
- all published own work (authorship) or co-authored published work, regarding paper and conference proceedings originating of this thesis, are given in the following.

This dissertation has been written in accordance to the standards for cumulative dissertations at the Technical University of Munich namely the "Promotionsordnung der Technischen Universität München" of August, 23rd 2021 and the "Richtlinie für publikationsbasierte Promotionen - TUM School of Engineering and Design".

The following articles and conference proceedings originate from this dissertation (publications that are part of this thesis are highlighted in blue):

Accepted publications (full research paper, peer-reviewed):

Leinauer, J., Jacobs, B., Krautblatter, M. (2020): Anticipating an imminent large rock slope failure at the Hochvogel (Allgäu Alps). Geomechanics and Tunnelling 13, No. 6, pp. 597-603.
doi.org/10.1002/geot.202000027

Etzelmüller, B., Czekirda, J., Magnin, F., Duvillard, P.-A., Ravanel, L., Malet, E., Aspaas, A., Kristensen, L., Skrede, I., Majala, G. D., Jacobs, B., **Leinauer, J.**, Hauck, C., Hilbich, C., Böhme, M., Hermanns, R., Eriksen, H. Ø., Lauknes, T. R., Krautblatter, M., and Westermann, S. (2022): Permafrost in monitored unstable rock slopes in Norway – new insights from temperature and surface velocity measurements, geophysical surveying, and ground temperature modelling, Earth Surf. Dynam., 10, 97–129.
https://doi.org/10.5194/esurf-10-97-2022

Leinauer, J., Weber, S., Cicoira, A., Beutel, J., and Krautblatter, M. (2023): An approach for prospective forecasting of rock slope failure time. Commun Earth Environ 4, 253. doi.org/10.1038/s43247-023-00909-z

Barbosa, N., **Leinauer, J.**, Jubanski, J., Dietze, M., Münzer, U., Siegert, F., and Krautblatter, M. (2024): Massive sediment pulses triggered by a multi-stage 130 000 m³ alpine cliff fall (Hochvogel, DE–AT), Earth Surf. Dynam., 12, 249–269. https://doi.org/10.5194/esurf-12-249-2024

Full research paper in review (preprint):

Leinauer, J., Dietze, M., Knapp, S., Scandroglio, R., Jokel, M., and Krautblatter, M. (2024): How water, temperature and seismicity control the preparation of massive rock slope failure (Hochvogel, DE/AT), EGUsphere [preprint, submitted to Earth Surf. Dynam.]. https://doi.org/10.5194/egusphere-2024-231

Accepted publications (conference paper, peer-reviewed):

Leinauer, J., Jacobs, B., Krautblatter, M. (2021): High alpine geotechnical real time monitoring and early warning at a large imminent rock slope failure (Hochvogel, GER/AUT). IOP Conf. Ser.: Earth Environ. Sci. 833 012146. doi.org/10.1088/1755-1315/833/1/012146

Leinauer, J., Dietze, M., Knapp, S., Scandroglio, R., Jokel, M., and Krautblatter, M. (2024): Real-time and multi-method monitoring of the imminent Hochvogel rock slope failure (DE/AT), Interpraevent 2024, Conference Proceedings.

Conference contributions (orals and posters, selection):

Leinauer, J., Friedrich, B., Jacobs, B., Krautblatter, M. (2018): Process dynamics and early warning strategies for a preparing high-magnitude rock slope failure at the Hochvogel (Allgäu Alps). Central European Conference on Geomorphology and Quaternary Sciences 2018, Giessen, poster.

Leinauer, J., Friedrich, B., Jacobs, B., Krautblatter, M. (2019): Prozessdynamik und Frühwarn-Strategien für ein sich vorbereitendes Felssturz-Großereignis am Hochvogel (Allgäuer Alpen). Fachsektionstage Geotechnik, Forum für junge Ingenieurgeologen, Würzburg, 29.-30.10.2019, oral.

Leinauer, J., Friedrich, B., Jacobs, B., Krautblatter, M. (2019): Process dynamics and early warning strategies for a preparing high-magnitude rock slope failure at the Hochvogel (Allgäu Alps). European Geosciences Union General Assembly 2019, Vienna, Austria 07.04.-12.04.2019, oral.

Leinauer, J., Jacobs, B., Krautblatter, M. (2020): Antizipation eines bevorstehenden Felssturzes am Hochvogel (Allgäuer Alpen), 69. Geomechanik Kolloquium 2020/ Johann Golser Kolloquium, Salzburg, 08.10.2020, oral.

Leinauer, J., Jacobs, B., Krautblatter, M. (2020): Process dynamics, real time monitoring and early warning at an imminent cliff fall (Hochvogel, Allgäu Alps). European Geosciences Union General Assembly 2020, Vienna, Austria 03.05.-08.05.20, oral, doi.org/10.5194/egusphere-egu2020-19073.

Leinauer, J., Meindl, M., Jacobs, B., Stammberger, V., and Krautblatter, M. (2021): Anticipating cascading risks at the imminent Hochvogel peak failure, EGU General Assembly 2021, online, 19–30 Apr 2021, EGU21-9581, vPICO, doi.org/10.5194/egusphere-egu21-9581.

Leinauer, J., Sachs, M., Krautblatter, M. (2021): The effects of heavy rain on irreversible crack opening at the large imminent rock slope failure at the Hochvogel (GER/AUT), Mid-European Geomorphology Meeting MGM, München, 06.-09.11.2021, oral.

Leinauer, J.; Jacobs, B., Krautblatter, M. (2021): High alpine geotechnical real time monitoring and early warning at a large imminent rock slope failure (Hochvogel, GER/AUT), EUROCK 2021, Torino, 21.-24.09.2021, selected oral, doi.org/10.1088/1755-1315/833/1/012146.

Leinauer, J., Weber, S., Cicoira, A., Beutel, B., and Krautblatter, M. (2022): Towards prospective failure time forecasting of slope failures, EGU General Assembly 2022, Vienna, 23–27 May 2022, EGU22-7673, oral, doi.org/10.5194/egusphere-egu22-7673.

Leinauer, J., Dietze, M., Knapp, S., Jokel, M., Barbosa, N., and Krautblatter, M. (2022): Preparation of rock slope failure towards a high-sensitivity close-to-failure system, Mid-European Geomorphology Meeting MGM, Kaprun, 25.-28.11.2022, poster.

Leinauer, J., Dietze, M., Knapp, S., Jokel, M., Barbosa, N., Scandroglio, R., and Krautblatter, M. (2023): Rock slope failure evolution towards a sensitive close-to-failure system, EGU General Assembly 2023, Vienna, Austria, 24–28 Apr 2023, EGU23-7521., oral, doi.org/10.5194/egusphere-egu23-7521.

Leinauer, J., Jacobs, B., Scandoglio, R., Dietze, M., and Krautblatter, M. (2023): The Hochvogel outdoor laboratory: diciphering the preparatory phase of rock falls, 6th Symposium of the Virtual Alpine Observatory (VAO), Grainau, 21.-23.03.2023, oral.

Leinauer, J., Weber, S., Cicoira, A., Jokel, M., Beutel, B., and Krautblatter, M. (2023): A new concept for prospective failure time forecasting, 6th World Landslide Forum, 14.-17.11.2023, Florence, oral.

Leinauer, J. (2023): Displacement data for early warning: forecasting the time of landslides, Landaware online event 2023, 01.06.2023, invited talk.

Leinauer, J., Dietze, M., Knapp, S., Scandroglio, R., and Krautblatter, M. (2024): Echtzeit-Monitoring und Quantifizierung von treibenden Faktoren am bevorstehenden Hochvogel Felssturz, XXVII. Geoalp Wintercup 2024, Bozen, 02.02.2024, oral.

Leinauer, J. (2024): Die Vorhersage von Naturgefahren im Einfluss des Klimawandels - Freiluft-Labor Hochvogel, DAV Sektion Freising, 20.03.2024, invited talk.

Summary

Massive rock slope failures are significant geomorphic processes and globally account for a majority of the most destructive landslide events with up to 100,000 deaths. Alpine communities worldwide must regularly cope with such catastrophic events and more frequently with smaller but still destructive events. Globally, thousands of deaths due to landslides are recorded annually, and economic investments in protective structures reach billions of Euros in the Alpine Space alone. In a changing climate, landslide risk is exacerbated in many places by more frequent and intense rainstorm events, permafrost degradation, and an increasing number of people being exposed. Mitigation measures, such as protective structures and land management, can be effective but their increasing cost implications might surpass the financial capacities even of wealthy countries. Early warning systems (EWS) have proven successful in past events (e.g., Brienz, CH in June 2023) holding the highest potential to compensate for climate change effects. However, the diverse nature of landslides and the limited number of events pose many challenges, leaving the following research gaps: (i) The reliability of reasonable monitoring methods in high-alpine environment is not sufficient. (ii) Understanding and anticipation of relevant process dynamics before failure are limited. (iii) Existing failure time forecasting methods have major drawbacks in prospective applications. This thesis aims to fill these research gaps and gain further understanding in the monitoring, analysis, and forecasting of rock slope failures with one research paper plus update for each sub-topic. The first two parts have been elaborated at the Hochvogel rock slope instability (Allgäu Alps, 2,592 m a.s.l.), a benchmark for imminent high-alpine rock slope failures and EWS development in the context of climate change. As the Hochvogel has not collapsed yet, the third part is based on several historical benchmark slope failures.

(i) The first part describes the development of a high-alpine geotechnical monitoring system at the Hochvogel. The system is designed to continuously observe the pre-failure deformations of >200,000 m^3 unstable rock mass and part of a complementary multi-method approach as basis for an effective and reliable EWS. It has been improved over the years and finally consists of 4 crackmeters, 2 laser distance gauges, 4 inclinometers, a rain gauge and a webcam. Data are transmitted wireless via long-range radio (LoRa) every 10 min and fed into an online data management platform that can trigger alarms. All crackmeters are successfully protected by lightning protection and wooden roofs. The summit´s inaccessible steep SW-wall is monitored with an automatic deformation camera. Displacement rates in the main decametre-deep fracture are 2–10 mm/month. The most active crack opened >85 mm between 2020 and 2023. The developed system represents a unique benchmark

for reliable high-alpine monitoring and the data are the basis for process dynamic analyses (Part 2) and will be for the final failure time forecasting (Part 3).

(ii) For a comprehensive quantification of the most relevant drivers and triggers, more than four years of high-resolution monitoring data have been exploited. Among all potential rockfall drivers, water from rain and snowmelt, internal rock fracturing and earthquakes are identified most relevant. The correlation of slope displacements with environmental data, local seismic recordings and earthquake catalogues reveals that displacements are controlled by meltwater infiltration with high correlation and a time lag of 4-9 days during the snowmelt phase. During the snow-free summer, rainfall drives the system with a time lag of 1-16 h for up to several days without a minimum activation rain sum threshold. Rock fracturing events (>21,000), detected with machine learning, are mainly linked to temperature and freeze-thaw cycles. They are predominantly surface-near and unrelated to displacement rates. A Newmark analysis of more than 5000 local earthquakes indicates a low potential for immediate triggering of a major failure, unless being already very close to failure. Seismic topographic amplification at the summit ranges from a factor of 2-11 and is spatially heterogeneous, indicating a high criticality of the slope. The applied methodological approach enables a rare comprehensive rockfall driver evaluation and indicates, where climatic changes, e.g. in extreme precipitation, may alter the promotion of massive rock slope failures.

(iii) To increase the reliability of failure time forecasts at slope scale, a prospective concept has been developed. State-of-the-art prediction models are often confused with high-frequency slope deformation data of modern monitoring systems. Prospectively, they provide ambiguous forecasts as data filtering, starting point definition and forecast uncertainty remain arbitrary. The presented prospective concept applies multiple filtering and inverse velocity percentiles to minimize subjective decisions. It is tested with 14 historic slope failures of 10^2–10^8 m³ including 46 displacement datasets from different sensors. After automatic detection of the onset of acceleration, the failure time of all events is forecasted to within -1±17 h for higher-frequency data and -1±4 d for daily data with a final mean uncertainty of 1±1 d and 7±4 d that is estimated in real-time. Non-linear forecasting can theoretically improve the accuracy, but is more complex and improvements are often marginal. Based on a statistical post-failure analysis, the linear case $\alpha = 2$ is a reasonable choice in prospective applications. The here developed prospective approach overcomes previous long-standing problems by introducing a robust and uniform concept which performs well across various types of slope failures and sensors.

This thesis presents (i) a benchmark geotechnical monitoring system in high-alpine environment by integrating an operational wireless system into an early warning concept. The analysis of the gathered high-resolution data (ii) enables a quantification and better understanding of the most relevant drivers in the preparation phase of an imminent failure. The timing of the final failure can then be predicted with a novel prospective failure time forecasting concept (iii), which performs robustly and uniform with various failure and sensor types overcoming several state-of-the art problems. Thus, this thesis contributes to a more reliable anticipation and early warning of massive rock slope failures.

Zusammenfassung

Massive Hangbewegungen im Fels sind ein bedeutender geomorphologischer Prozess und machen weltweit einen Großteil der destruktivsten Hangbewegungen mit bis zu 100.000 Todesopfern aus. Alpine Gemeinden müssen regelmäßig mit solchen katastrophalen Ereignissen und noch häufiger mit kleineren aber dennoch destruktiven Ereignissen umgehen. Jährlich kommen weltweit tausende durch Hangbewegungen ums Leben und die wirtschaftlichen Investitionen in Schutzbauten erreichen allein im Alpenraum mehrere Milliarden Euro. In Zeiten klimatischer Veränderungen wird das Risiko vielerorts durch häufigere und intensivere Regenfälle, Permafrostrückgang und eine zunehmende Anzahl an Menschen im gefährdeten Raum, verschärft. Maßnahmen zur Risikominderung wie Schutzbauten und Flächenmanagement sind effektiv, doch ihre steigenden Kosten können die finanziellen Kapazitäten selbst wohlhabender Länder überschreiten. Frühwarnsysteme können erfolgreich sein (z.B. Brienz, CH im Juni 2023) und bergen großes Potenzial, Auswirkungen des Klimawandels zu kompensieren. Die große Diversität und begrenzte Anzahl von Hangbewegungen führen jedoch zu vielen Herausforderungen, die folgende Forschungslücken offen lassen: (i) Die Zuverlässigkeit angemessener Monitoringmethoden im hochalpinen Raum ist nicht ausreichend. (ii) Prozessverständnis und Antizipation vor dem Versagen sind begrenzt. (iii) Bestehende Methoden zur Vorhersage des Absturzzeitpunkts haben bei prospektiver Anwendungen Probleme. Diese Arbeit zielt darauf ab, die Forschungslücken zu schließen. Überwachung, Analyse und Vorhersage von Felsversagen werden mit je einer Publikation plus Update pro Thema bearbeitet. Die ersten beiden Teile werden am Hochvogel (Allgäuer Alpen, 2.592 m) erarbeitet, einem Benchmark für bevorstehende hochalpine Felsstürze und die Entwicklung von Frühwarnsystemen im Kontext des Klimawandels. Der dritte Teil basiert auf gut dokumentierten vergangenen Ereignissen.

(i) Im ersten Teil wird die Entwicklung eines hochalpinen geotechnischen Monitoringsystems am Hochvogel beschrieben. Als Teil eines umfassenden Multi-Methoden-Ansatzes überwacht das System kontinuierlich Deformationen der instabilen Felsmasse (>200.000 m^3) und ermöglicht so effektive und zuverlässige Frühwarnung. Nach stetiger Verbesserung besteht das System nun aus 12 Sensoren mit Blitzschutz und Schutzdächern. Die Daten werden drahtlos alle 10 Minuten mittels LoRa übertragen und in eine Online-Plattform eingespeist, die Alarme auslösen kann. Die unzugängliche steile SW-Wand des Gipfels wird mit einer automatischen Deformationskamera überwacht. Die Deformationen im Zehnermetertiefen Hauptspalt betragen 2–10 mm/Monat. Der aktivste Spalt öffnete sich zwischen 2020 und 2023 um mehr als 85 mm. Das hier entwickelte Benchmark-System für zuverlässige

hochalpine Überwachung ist einzigartig, und dessen Daten bilden die Grundlage für Prozess-Analysen (Teil 2) und die endgültige zeitliche Vorhersage der Felssturzes (Teil 3).

(ii) Für eine umfassende Quantifizierung der vorbereitenden und auslösenden Faktoren wurden mehr als vier Jahre hochaufgelöste Monitoringdaten analysiert. Von allen potenziellen Faktoren sind am Hochvogel Regen, Schneeschmelze, interne Felsbrüche und Erdbeben am relevantesten. Die Korrelation von Deformation mit Wetterdaten, seismischen Daten und Erdbeben zeigt, dass die Deformationen im Frühling mit einer Zeitverzögerung von 4-9 d durch Schmelzwasser kontrolliert werden. Während des schneefreien Sommers kontrolliert Regen das System mit einer Zeitverzögerung von 1-16 h, oft für mehrere Tage und bereits ab kleinen Regensummen. Mit maschinellem Lernen detektierte Felsbrüche (>21.000) stehen vor allem im Zusammenhang mit Temperatur- und Frost-Tau-Zyklen. Sie sind überwiegend oberflächennah und unabhängig von Deformationsraten. Eine Newmark-Analyse von mehr als 5000 lokalen Erdbeben deutet auf ein geringes unmittelbares Auslöse-Potenzial für größere Versagen hin, außer für Blöcke nahe dem Grenzgleichgewicht. Seismische Wellen werden am Gipfel mit Faktor 2-11 heterogen topographisch verstärkt, was auf einen kritischen Zustand des Hanges hindeutet. Der hier angewandte methodische Ansatz ermöglicht eine seltene umfassende Analyse der treiben Faktoren und zeigt auf, wo klimatische Veränderungen die Vorbereitung von massiven Felsversagen beeinflussen können.

(iii) Um die Zuverlässigkeit von zeitlichen Vorhersagemethoden zu erhöhen, wurde ein prospektives Konzept entwickelt. Bestehende Vorhersagemodelle haben meist Probleme mit hochfrequenten Daten moderner Monitoringsysteme. Prospektiv liefern sie uneindeutige Vorhersagen, da Datenglättung, Definition des Startzeitpunkts für Vorhersagen und Unsicherheit der Vorhersagen unklar sind. Das entwickelte Konzept minimiert subjektive Entscheidungen durch mehrstufiges Filtern und Perzentile der inversen Geschwindigkeit. Es wurde mit 46 Datensätzen unterschiedlicher Sensoren von 14 historischen Hangversagen mit 10^2-10^8 m³ getestet. Nach der automatischen Erkennung der Beschleunigungsphase stimmen Vorhersage und Realität im Mittel bei hochfrequenten Daten auf -1±17 h und bei täglichen Daten auf -1±4 d genau überein. Die mittlere in Echtzeit ermittelte Unsicherheit beträgt 1±1 d und 7±4 d. Nichtlineare Prognosen können theoretisch die Genauigkeit verbessern, sind jedoch komplexer und die Verbesserungen sind meist marginal. Basierend auf einer statistischen Post-Event-Analyse ist die lineare Version $\alpha = 2$ optimal bei prospektiven Anwendungen. Der hier entwickelte Ansatz überwindet vorherige Probleme durch robuste und einheitliche Vorhersagen bei verschiedenen Versagenstypen und Sensoren.

Diese Dissertation (i) beschreibt die Entwicklung eines operativen geotechnischen Benchmark-Monitoringsystems mit drahtlosen Sensoren in hochalpiner Umgebung als Teil eines Frühwarnsystems. Die Analyse der hochaufgelösten Daten (ii) ermöglicht ein besseres Verständnis mit Quantifizierung der wichtigsten treibenden Faktoren in der Vorbereitungsphase eines bevorstehenden Felssturzes. Die zeitliche Vorhersage des endgültigen Versagens (iii) kann schließlich mit dem neuen prospektiven Vorhersagemodell durchgeführt werden, das robust und einheitlich mit verschiedenen Versagens- und Sensortypen funktioniert. Damit trägt diese Dissertation zu einer zuverlässigeren Antizipation und Frühwarnung von massiven Felsversagen bei.

Acknowledgements

I want to acknowledge all support, help and assistance that made this thesis possible. In case I have forgotten anyone, please be assured that I am very thankful. Acknowledgments belonging to the specific papers are given in the respective sections at the end of each paper.

First, I want to thank Michael Krautblatter, for initiating and feeding my interest in rock slope failures, for giving me the opportunity to work in extraordinary mountain landscapes, for offering me a PhD position in the landslide research team, and for supervising this PhD project. Thanks for giving me the support I needed and the trust and freedom to pursue my scientific and personal goals.

Thanks also to Michael Dietze for mentoring me in the most pleasant way. Thanks for your timely answers, the deep thematic discussions, the introduction to the interesting field of environmental seismology and your support with *R* and the *eseis* package.

Installing and maintaining a continuous high-alpine monitoring system is not possible alone. There were many helping hands, strong backs and expertise in various disciplines. Thanks to Benedikt Friedrich for drilling the fix points, which are still in use, and the endless effort in setting up the system in the beginning. Thanks to the skillful pilots Udo Ramm and Steffen Becher from Helixcopter for safe flights and good decisions when the weather was (again) not perfect. Thanks to the major of Hinterhornbach Martin Kärle for the friendly collaboration, the local support and the possibility to mount and power our Gateway in the village. Thanks to Francisco Llorens for setting up the first automatic system on the summit. Thanks to the lightning engineer Peter Biebl for taking the time to meet and explaining the principles of lightning protection. Thanks to Verena Stoll for the permanent good mood, local expertise and discussions during the hikes. Thanks to everyone who helped me to maintain the system on the summit: Ric, Ben, Philipp, Gunnar, Anne, Theresa, Lukas, Fe, Michl, Max, Max, Max, Felix, Verena, Verena, Doris, Michael, Niko, Mateja, and Matthias.

Then, I want to acknowledge the whole landslides team at the university. The atmosphere is always friendly, collaborative and we had a lot of fun. Thanks to everyone in the team! Thank you Riccardo for being my office buddy, my highbird mountain buddy and my friend on the way through our PhD. Thank you Ben for somehow mentoring me through the life in science and the group since my master thesis in Norway. Thank you Stephi for your daily support with all the administrative stuff. Thanks to my PhD partners from the AlpSense project Lukas, Lukas and Natalie, collaboration was always motivating. Thanks to Sämi for fruitful discussions for the publications, your shared PhD and non-PhD experiences and

the Latex-template. Thank goes also to my students writing their final thesis, doing first data analyses and trying out various things: Max Jokel, Niko Lehner, Mari Sachs, Manfred Meindl and Ilona Holneicher.

Last but not least, I would like to express my heartfelt thanks to my entire family. Many thanks to my grandparents for supporting my studies. Thanks to my parents for supporting me and letting me follow my path. Thanks to my siblings Martin, Michl, Bene, and Anna for the strong bond we share. My greatest thank goes to my wife Fe. Thank you for always being there for me, for believing in me, and for the ability to always talk about everything. Thank you Romi, for starting my day with a smile early in the morning and welcoming me home with joy after work. Thank you all.

Table of contents

Abbreviations

EWS	early warning system
LoRa	long-range radio
GNSS	Global Navigation Satellite System
InSAR	interferometric synthetic aperture radar
GB-InSAR	ground-based interferometric synthetic aperture radar
UAV	uncrewed aerial vehicle
TDR	time domain reflectometry
CSM	continuous shear monitor
OOA	onset of acceleration
VW	vibrating wire
GSM	Global System for Mobile Communications
SMS	short messaging service
IQR	inter-quartile range
UTC	coordinated universal time
STA-LTA	short term average - long term average
SNR	singal-to-noise ratio
FOS	factor of safety
PGV	peak ground velocity
PFTF	prospective failure time forecasting
w_smooth	smoothing window
w_v	velocity window

1 Introduction

1.1 Motivation and relevance

Massive rock slope failures including rockslides, rock avalanches and rockfalls are an important geomorphic process and the most destructive landslide type. They account for 75 % of all fatalities from landslide disasters (Evans et al., 2006a). A global dataset of non-seismically triggered landslides estimates several thousand deaths per year (Petley, 2012). In Italy alone, over 10,000 people were killed or went missing in the 20th century due to landslides (Guzzetti, 2000). Additionally, the material loss in the last decades sums up to billions of Euros (Lacasse and Nadim, 2009, Pfurtscheller and Thieken, 2013). Alpine communities in all parts of the world must regularly cope with those catastrophic and more frequent minor events. They constantly face the challenge of avoiding fatalities and damage to infrastructure. However, ongoing climatic changes and population growth exacerbate future landslide risk in some regions, e.g. due to more frequent and stronger heavy precipitation events, permafrost degradation and increasing vulnerability (Huggel et al., 2012a,b, Krautblatter et al., 2013, Picarelli et al., 2021).

Mitigation measures like protective structures and land management can be effective, but they are expensive. The European countries alone invest many billion Euros every year for (re-)installation and maintenance of protective structures with an increasing tendency, especially during the last years (PLANALP, 2015). However, early warning and alarm systems add a cost-efficient and widely applicable possibility to solve this problem (Pecoraro et al., 2019), especially when the failing volumes are too big to be controlled by fences or dams.

Early warning systems (EWS) successfully helped to prevent from damage in the past, e.g. recently in Brienz (Switzerland) in June 2023 or in Preonzo (Switzerland) in 2012 (Sättele et al., 2016, Loew et al., 2017). Historic events like the famous Vajont failure (Italy) in 1963 with more than 2,000 fatalities (Ghirotti, 2013) could have been forecasted, if present-day forecasting methods had been available (Kilburn and Petley, 2003). However, due to the great diversity of different landslides and the limited number of events, early warning of rock slope failures is still a complex challenge. This is for example illustrated by the 2019 Veslemannen failure (Norway), where the operating experts had to evacuate the valley 16 times before the failure happened (Kristensen et al., 2021). Other events, like the 10^6 m^3 Fluchthorn rockfall (Austria) in 2023 happened completely unforeseen. These examples highlight the demand for research progress in the field of landslide early warning. Not only

do we need more case studies to learn from, we also need a better understanding of the ongoing process dynamics to anticipate future events. The rapid progress in the development of wireless automatic sensors and remote sensing in recent years helps to gather valuable data (Chae et al., 2017), but we must learn to apply these methods reliably in extreme environments and to process the data meaningfully to benefit the society.

The Hochvogel rock slope instability (2592 m a.s.l, DE/AT) is one of the rare alpine pre-failure rockfall sites offering the possibility to fill this research gap. With its imminent failure, the site is paradigmatic of slope failure dynamics in high alpine carbonate rock. The high activity and ongoing movement of >200,000 m³ in the range of 1–2 cm/a make it a benchmark for developing effective monitoring and early warning under the effects of climate change. Since 2018, extensive multi-method monitoring enables the analysis of the unstable slope during the preparation phase of massive rock slope failure. The decipherment of anticipative signals at the Hochvogel is thus contributing to an improvement of reliable early warning of rock slope failures.

1.2 Main goals and research questions

As early warning systems (EWS) offer a promising tool for future risk mitigation, there is a great demand for improvement. This mainly concerns the reliability of reasonable monitoring methods, the understanding and anticipation of underlying process dynamics and the confidence of forecasts - all in the light of constant technical development and severe climatic changes. The United Nations states that end-to-end EWS need four key elements (Fig. 1.1a): (i) "knowledge of the risk", (ii) "monitoring, analysis and forecasting of the hazards", (iii) "communication or dissemination of alerts and warnings" and (iv) "local capabilities to respond to the warnings received" (UN/ISDR, 2009). For the Hochvogel case, the knowledge of the risk (i) already exists, while (iii) and (iv) are rather organizational challenges in cooperation with authorities and local stakeholders. The focus of this work therefore lies on (ii), rock slope failure monitoring, analysis and prediction. The structure of this thesis mainly follows this three-fold composition (Fig. 1.1b).

Rock slope monitoring and early warning (Paper ①)
The Hochvogel rockslide had to be monitored with low-medium cost and with highly available technique that could be re-installed within several days at other alpine sites. This leads to the following main research questions.

1. How can we install and operate a reliable benchmark monitoring system at a high-alpine summit (Hochvogel 2592 m a.s.l.)?
2. What design is needed to enable implementation in an operational local early warning system?
3. How can we build up a resilient network of wireless sensors to increase the reliability?

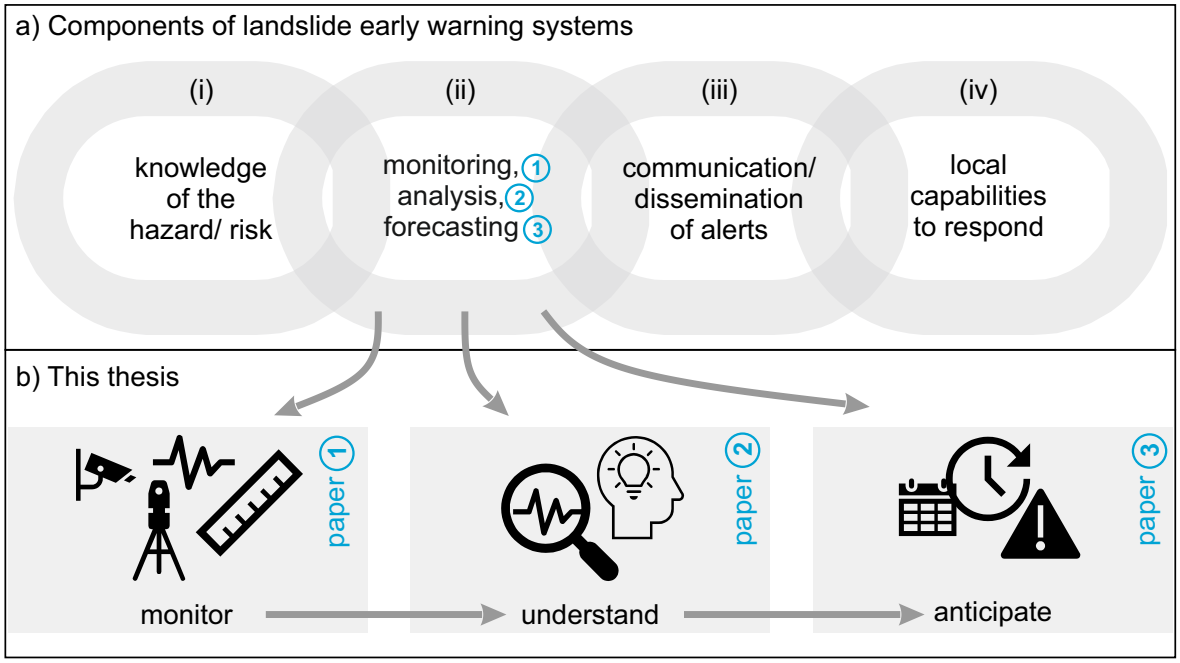

Figure 1.1: (a) Key elements of early warning systems (adapted from UN/ISDR 2009 and Intrieri et al. 2013). (b) Structure of this thesis.

Quantification of promoting and triggering processes (Paper ②)
Successful anticipation and prediction of a future rock slope failure necessitates a detailed understanding of the process dynamics including knowledge of all potential drivers and triggers. The following key questions arise from this aspect.

4. What are the relevant drivers in the preparation phase of the Hochvogel rock slope failure?
5. Can we quantify the proportional effects of these drivers based on monitoring data?
6. What can most likely promote and trigger the future failure?

Failure time forecasting (Paper ③)
Finally, timely mitigation measures require a precise failure time forecast before the event happens including measures of uncertainty, leading to the following main questions.

7. How can we modify existing retrospective failure time forecasting methods to apply them prospectively?
8. How can we minimize the subjectivity of data smoothing and add real-time uncertainty estimations to the forecasts?
9. How can we detect the onset of acceleration automatically with a uniform and objective approach?
10. How does a uniform forecasting model perform with 46 diverse datasets from available benchmark failures worldwide?

1.3 Thesis structure

This thesis consists of 7 chapters. Chapter 1 introduces the topic, main goals and key research questions of this thesis. Chapter 2 gives a detailed overview of the current state of the art in monitoring, analysis and anticipation of rock slope failures. The following 3 chapters present the main results containing the three stand-alone research papers that are incorporated in this thesis. Additionally, a short section highlights the developments and updates to each publication. Paper ① (Section 3) introduces the monitoring and EWS developed at the Hochvogel. Paper ② (Section 4) analyses the gathered data and presents a detailed characterization of all relevant factors that control the preparation phase of the future Hochvogel rock slope failure. Paper ③ (Section 5) suggests a novel concept for prospective failure time forecasting with an automatic algorithm that has been tested with multiple historical slope failures and datasets. Chapter 6 shortly synthesises the main findings by answering the research questions stated in Chapter 1 with a discussion in the broader context. Chapter 7 gives an outlook and future perspectives on the topic of rock slope failure early warning.

2 State of the art

2.1 Rock slope failure - definitions and consequences

2.1.1 Definitions

Landslides are masses of rock, earth or debris that move down a slope (Cruden, 1991) and are typically classified based on the type of material, failure mechanism and the type of movement (Varnes, 1978, Cruden and Varnes, 1996, Hungr et al., 2014). Rock slope failures are characterized by the failure of solid rock mass and are thus differentiated from failure in other weak material like soil. The most important movement types in this category are falling, toppling and sliding (Fig. 2.1). Falls are defined by the descent of a mass predominantly through "air by free fall, leaping, bounding, or rolling" (Varnes, 1978). Block toppling describes the tilting of a block by "forward rotation [...] about some pivot point" (Varnes, 1978). Post-failure, deposits of topples and falls might be difficult to distinguish due to their similar appearance. At slides, all movement results from shear displacement within a narrow zone, e.g., along a sliding surface (Varnes, 1978). In hard rock, planar sliding is the dominant process as bedding and discontinuities mostly predefine the development of a planar sliding plane.

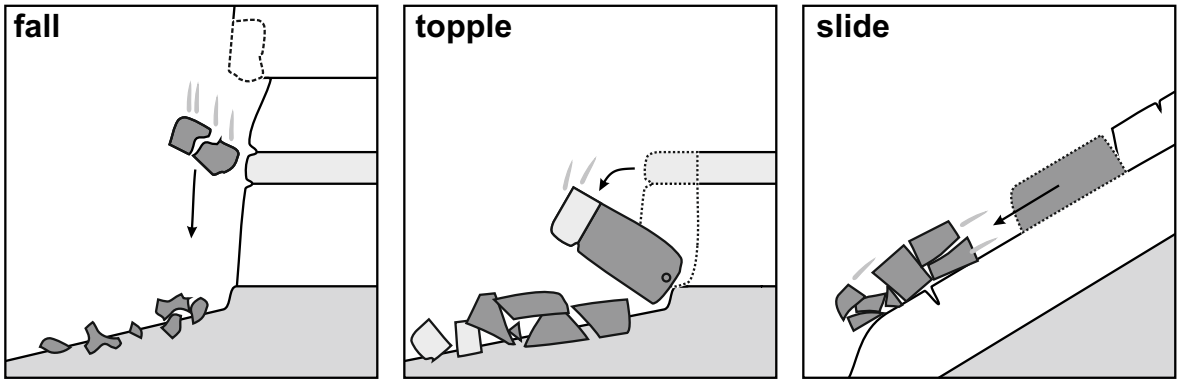

Figure 2.1: Most important movement types of rock slope failures.

In nature, slope failures are often compound in terms of material and movement type. In high-alpine and glaciated areas, rockslides can contain or entrain ice (e.g. Walter et al., 2020). High-magnitude rockfalls and rockslides are further capable of mobilizing colluvial

debris (e.g. Hungr and Evans, 2004) and can transform into highly mobile and rapid rock avalanches with flow-like behaviour due to the fragmentation and dynamic disintegration of the detached rock mass (Hungr et al., 2014). Runout distances can then reach several kilometres. Famous prehistoric examples from the European Alps are Flims in Switzerland (e.g. Poschinger et al., 2006) and Tschirgant in Austria (e.g. Dufresne et al., 2016), or recently, the 2017, 3×10^6 m³ failure on Pizzo Cengalo, where the initial rock slope failure transformed in to a rock avalanche, entraining over one million m³ of glacier ice and debris deposits, followed by several debris flows that reached the village Bondo 6 km down-valley (Walter et al., 2020).

Such event cascades appear frequently in steep and confined terrain with diverse geomorphological settings. The assessment of multi-hazards and their interactions is complex (Kappes et al., 2012), but important, as primary hazards can often trigger one or more secondary hazards or at least increase their probability (Gill and d. Malamud, 2014). Besides the initiation of secondary debris flows (e.g. Hungr and Evans, 2004, Walter et al., 2020, Barbosa et al., 2024), river damming and the accompanied threats like dam breach and lake outburst flood are among the most dangerous induced risks following rock slope failure (e.g. Costa and Schuster, 1991, Awal et al., 2007, Evans et al., 2011, Do et al., 2016, Nibigira et al., 2018).

Landslides can furthermore be classified based on velocity and volume. Rockfalls, topples and rockslides usually fall into velocity class 7 "extremely rapid" after Hungr et al. (2014) and Varnes (1978), accelerating to above 5 m/s, making an escape of persons unlikely. Rock avalanches can even reach runout velocities above 100 m/s (Wang et al., 2017). Depending on the detached volume, rockfalls are classified and named accordingly as debris fall (<10 m³), boulder fall (10-100 m³), block fall (10^2-10^4 m³), cliff fall (10^4-10^6 m³) or bergsturz (>10^6 m³) (Whalley, 1974, 1984, Heim, 1932).

Among high-impact slope failure events, the term "catastrophic rock slope failure" has been defined by Hewitt et al. (2011) as "sudden failure and downslope movement of a large mass of intact rock". Especially in high-alpine and glaciated or de-glaciated areas, those catastrophic events happen frequently and show high mobility. Another established term is "massive rock slope failure", which describes "large or unusually large rock slope failures" ($10^5 - 10^{10}$ m³) with massive "geomorphic and socio-economic impact" (Evans et al., 2006b). Primary and secondary processes of massive rock slope failures together bare a great destructive potential.

2.1.2 Consequences

Landslides frequently harm infrastructure, property or human lives all over the world (e.g. Guzzetti, 2021). Some of the most destructive events caused catastrophic disasters affecting thousands of people. Examples are the 1963, Vajont rock slope failure in Italy, where 270×10^6 m³ of rock slid into a reservoir, generating a displacement wave that killed over 2,000 people (e.g. Ghirotti, 2013) or the 1970, $50 - 100 \times 10^6$ m³ Huascarán rock avalanche in Peru causing more than 18,000 causalities (Plafker and Ericksen, 1978). Some countries like

Italy are particularly affected by frequent landslides (over 10,000 dead or missing people in the 20th century, Guzzetti, 2000), while globally, several thousand deaths result from non-seismically triggered landslides per year (Petley, 2012). In addition to the damage to human life, there is also material loss that sums up to billions of Euros over the last decades (Lacasse and Nadim, 2009, Pfurtscheller and Thieken, 2013).

Massive rock slope failures with volumes $> 20 \times 10^6$ m³ occurred on average every 2.7 years on a global scale in the last century (Evans, 2006). In the last millennium, they caused 58 % of the global disasters from all single landslide events, accounting for 75 % of total deaths, most of them due to earthquake-triggered events and indirect effects (Evans, 2006). The magnitude-frequency relation of deaths from single-event landslide disasters in the last millennium, derived from the same dataset, suggests a disaster with 1,000 fatalities to occur approximately every 25 years and a disaster with 10,000 fatalities every 250 years respectively (Fig. 2.2). Consequences of landslides are thus in the range of other natural hazards like volcanic eruptions or earthquakes (Evans, 2006).

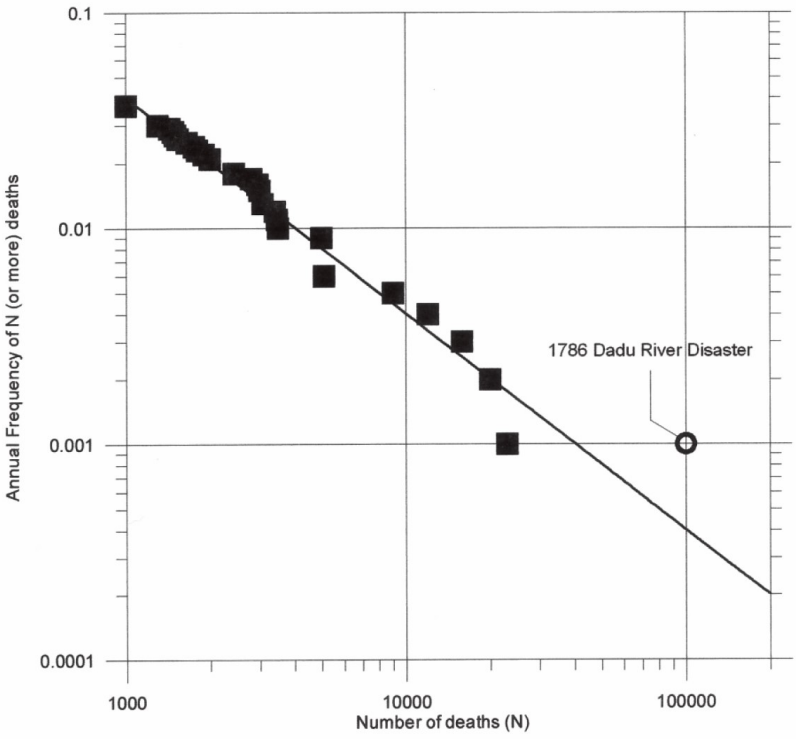

Figure 2.2: Magnitude-frequency plot of deaths in single event landslide disasters in the last millennium (power-law fit without the 1786 Dadu River event as the frequency of such an event likely exceeds 1000 years. From Evans, 2006).

Climate change and population growth will likely exacerbate the situation in many places (cp. Section 2.3.4, Lacasse and Nadim, 2009, Huggel et al., 2012b, Picarelli et al., 2021). However, there is also the possibility of reducing the risk and avoiding severe consequences by reliable anticipation strategies. In some historical cases, fatal catastrophes could have been avoided, if a better knowledge and possibilities on landslide forecasting methods had been available (eg. Kilburn and Petley, 2003). Today, modern monitoring and data processing methods create possibilities with great potential (e.g. Intrieri and Gigli, 2016, Intrieri et al., 2019) and must therefore be improved further. They provide valuable data that can be used

to anticipate slope failures (Sättele et al., 2016, Chae et al., 2017, Intrieri et al., 2019, Pecoraro et al., 2019).

2.2 Monitoring and early warning of slope instabilities

2.2.1 Monitoring methods

Overview

Landslide monitoring provides crucial information for the detection and delimitation of unstable areas and early warning purposes (Chae et al., 2017). It includes the observation of slope deformations, associated environmental factors, and geotechnical parameters (Uhlemann et al., 2016). Alarm thresholds mainly rely on slope displacement or its derivatives velocity and acceleration (e.g. Intrieri et al., 2012, Carlà et al., 2017a, Kristensen et al., 2021, Valletta et al., 2021), but without a precise understanding of the controlling factors like meteorological or material conditions, failure anticipation is hindered (Angeli et al., 2000).

Nowadays, multitudinous landslide monitoring methods exist and can be classified based on various aspects (Fig. 2.3). Monitoring devices usually either observe meteorological parameters like rainfall, surface parameters like displacement, or subsurface parameters like pore water pressure (Fig. 2.3a). This can be done in-situ, usually with ground-based sensors, or via air-borne or space-borne remote sensing techniques (Fig. 2.3b). Some techniques provide absolute values (e.g. geodetic total stations) while others measure relative to a reference point (e.g. crackmeters, Fig. 2.3c). Single fixed sensors usually deliver point information (e.g. GNSS station), but scanning devices like radars can give areal information (Fig. 2.3d). However, in the subsurface monitoring, there are also methods that provide 2D or 3D information (like seismic surveying). Lastly, some monitoring methods can be deployed continuously and in (near) real-time (e.g. seismic stations), while others can usually only provide data periodically (e.g. satellite radar, Fig. 2.3e). Great variability exists in the temporal and spatial resolution from seconds to weeks and sub-millimeter to meters. In most applications, a high temporal and spatial resolution is often beneficial or even crucial (Uhlemann et al., 2016). However, only a small percentage of all landslides worldwide are monitored adequately in terms of forecasting, as most cases lack the final failure stages or the monitoring has a too low temporal resolution (Intrieri and Gigli, 2016).

Table 2.1 gives an overview of available monitoring techniques including basic information and references. The methods that are further used in this dissertation are described in more detail in Section 2.2.1. A review of landslide monitoring for prediction and early warning can be found in Chae et al. (2017). A flow chart-based toolbox for the choice of a suitable instrumentation at local EWS is given in Intrieri et al. (2013).

Traditionally, monitoring data are saved on a data logger connected to the measuring device, from where all observations can be retrieved. Technical developments during the last years focused on automatic devices with wireless data transfer. This usually enables a higher

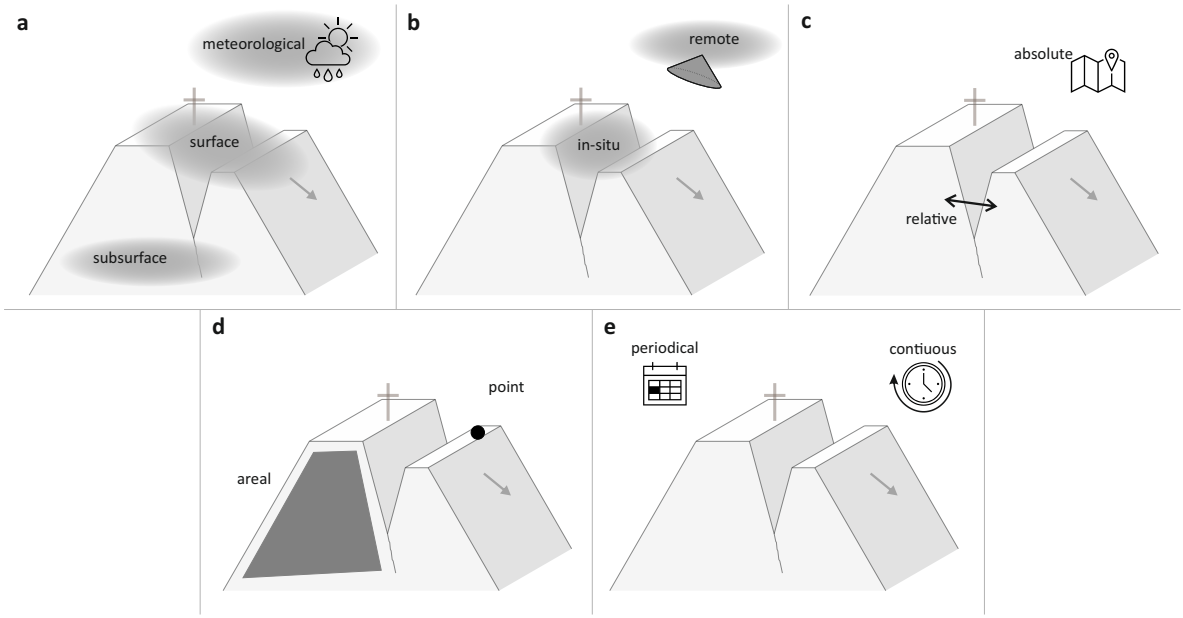

Figure 2.3: Classification of landslide monitoring techniques based on various aspects.

sampling rate and automatic observation even of remote sites. For geotechnical sensors, the LoRa technology (long-range wide area network) emerged to an increasingly important technique (e.g. Gamperl et al., 2021, Wang et al., 2022, Piciullo et al., 2022).

Multi-method approach

Early warning usually requires a multi-method monitoring system with a combined observation of deformation and controlling factors (Chae et al., 2017). In Europe, there are several examples of multi-method monitoring systems. In Italy, the LaSaxe landslide has been monitored with optical targets, GNSS, GB-InSAR, inclinometers, piezometers and geophysical surveys (Crosta et al., 2014), the Ruinon landslide with laser scans, distometers, extensometers, GNSS, and borehole inclinometers (Crosta and Agliardi, 2003) and the Torgiovannetto landslide with extensometers, rain gauge, cameras and GB-InSAR (Intrieri et al., 2012). The slope instability at Marzellkamm (Austria) is monitored with ground-based and air-borne laser scans, extensometers, UAV photogrammetry and tachymetry (Hormes et al., 2020, Rechberger et al., 2021) and the 2021 failure of Veslemannen in Norway has been monitored with GB-InSAR, extensometers, cameras and a meteorological station (Kristensen et al., 2021).

A major challenge with multi-method monitoring systems is the fusion of sensor data, especially, if different data types must be compiled. Often, information is aggregated based on expert knowledge (e.g. Carlà et al., 2019, Kristensen et al., 2021). More recently, Schild et al. (2023) proposed a low-level sensor data fusion based on a Multimodal Asynchronous Kalman Filter, which they applied to a 50,000 m^3 multi-stage failure in 2023 in Norway, that has been monitored by an on-site sensor network and remote sensing.

Table 2.1: Overview of available landslide monitoring techniques. "Expensive" is used in terms of monetary and/ or labor cost.

monitoring method	meteorological	surface	subsurface	remote	in-situ	absolute	relative	point	areal	periodical	continuous	limitations	example reference
rain gauge	+				+	+		+			+	heated gauge needed when T < 0 °C	Intrieri et al. (2012), Kristensen et al. (2021)
piezometer	+		+		+	+		+			+	access to subsurface/ soil needed	Crosta et al. (2014), Uhlemann et al. (2016), Gamperl et al. (2021), Piciullo et al. (2022)
snow height	+				+	+		+			+	snow drift can distort	Matsuura et al. (2003), Kristensen et al. (2021)
crackmeter, extensometer		+			+		+	+			+	relative displacement only in direction of instrument, limited range	Crosta and Agliardi (2003), Intrieri et al. (2012), Sättele et al. (2016), Hormes et al. (2020), Kristensen et al. (2021)
tiltmeter/ point inclinometer		+			+	+		+			+		Uhlemann et al. (2016), Gamperl et al. (2021)
borehole inclinometer			+		+		+	+		+	+	borehole needed	Crosta and Agliardi (2003), Crosta et al. (2014), Uhlemann et al. (2016)
laser distance gauge		+			+		+	+			+	relative displacement, target can move out of range, snow and weather	Leinauer et al. (2021)
total station/ tachymeter		+			+	+		+		+	+	targets point-wise and inside unstable area, weather	Intrieri et al. (2012), Crosta et al. (2014), Sättele et al. (2016), Hormes et al. (2020)
Global Navigation Satellite System (GNSS)		+			+	+		+		+	+	continuous measurements expensive, reference needed for high accuracy	Crosta and Agliardi (2003), Crosta et al. (2014), Uhlemann et al. (2016), Raffl et al. (2022)
terrestrial or air-born laser scanning		+		+			+		+	+	(+)	line of-sight, range, processing time and effort, vegetation, snow	Fey and Wichmann (2017), Hormes et al. (2020)
Satellite Interfereometric Synthetic Aperture Radar (InSAR)	+	+		+			+		+	+		limited coverage, low recurrence interval, snow	Mazzanti et al. (2011), Carlà et al. (2019), Hormes et al. (2020)
Ground-based Interfereometric Synthetic Aperture Radar (GB-InSAR)		+		+			+		+	+	+	expensive, phase wrapping at high deformations, vegetation, snow	Intrieri et al. (2012), Crosta et al. (2014), Dick et al. (2015), Mazzanti et al. (2015), Hormes et al. (2020), Kristensen et al. (2021)
air-born photogrammetry (plane or UAV)		+		+		+			+	+		low acquisition frequency, good weather conditions, vegetation, processing time	Nex and Remondino (2014), Hormes et al. (2020), Barbosa et al. (2024)
space-borne photogrammetry		+		+		+			+	+		low acquisition frequency, good weather conditions, vegetation, processing time	Delacourt et al. (2007), Hermle et al. (2021), Lacroix et al. (2023)
deformation camera		+		+			+		+	+	+	vegetation, snow, shadows, sensitive only line of sight	GEOPRAEVENT (2019)
Time Domain Reflectometry (TDR)/ Continuous Shear Monitor (CSM)			+		+		+	+			+	borehole or ditch needed	Singer and Kurosch (2006), Gamperl et al. (2021)
environmental seismology (geophones)	(+)	+	+		+	+	+	+	+		+	big data, noise	Suriñach et al. (2005), Helmstetter and Garambois (2010), Dietze et al. (2017a), Dietze (2018a), Weber et al. (2018)
other geophysical methods (ground penetrating radar, electrical resistivity tomography, refraction seismic, acoustiv emissions)			+		+	+	+	+	+	+	(+)	complex, often based on interpretation	Crosta et al. (2014), Borecka et al. (2015), Uhlemann et al. (2016), Keuschnig et al. (2017)

This thesis and the monitoring of the Hochvogel instability is strongly connected to the AlpSense project (`www.cee.ed.tum.de/landslides/alpsense`). Within the project, we designed a multi-method monitoring approach, which allows to compare the different methods and to determine the reliability of each technique. This particularly designed multi-method approach for the Hochvogel is shown in Fig. 2.4. The methods that are part of this dissertation will be described in the following section.

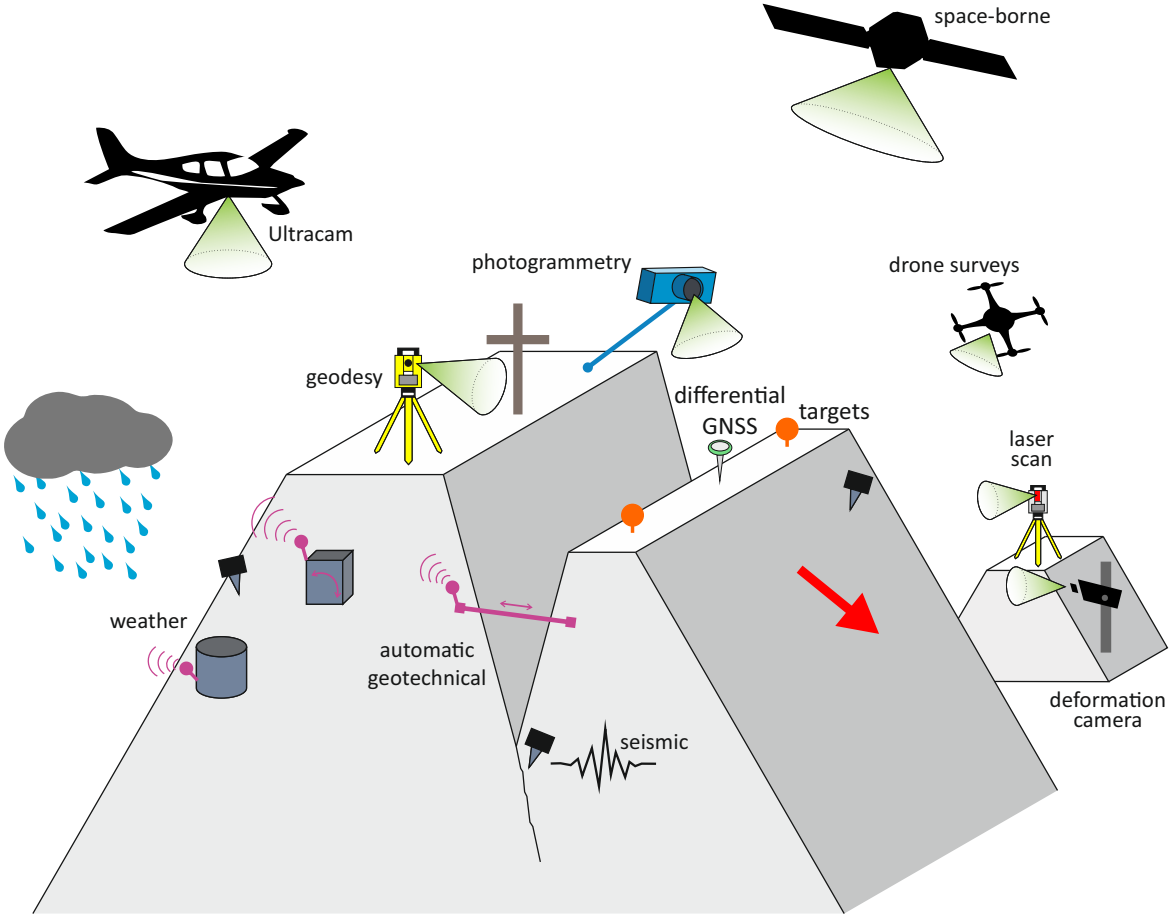

Figure 2.4: Multi-method approach of the AlpSense project for the monitoring of the Hochvogel rock slope instability. The combination of all these techniques on one alpine summit is unique.

Methods used in this dissertation

This section aims to provide a brief overview of the methods used in this dissertation. Further details are given in the respective sections where necessary. The project AlpSenseRely stipulated the use of monitoring techniques that are feasible (e.g. < 50,000 €) and highly available, meaning that the technique can be installed anywhere within a few days. We therefor mainly monitored deformation as crack opening and tilt with classical geotechnical devices: crackmeters, laser distance gauges, discontinuously with a manual tape extensometer and inclinometers (see details in Section 3). Crackmeters usually measure a relative

distance between two fixed points (e.g. two sides of a crack) with the vibrating wire technique reaching sub-millimeter accuracy. The range varies between 10 and 150 mm, but can be extended to more than a meter when using wire extensometers with drum. Longer range generally decreases the accuracy, which is typically below 1 %. Laser distance gauges measure the relative distance between sensor and target. The range reaches up to >100 m with 1-5 mm accuracy depending on distance and conditions. The manual tape extensometer is used for calibration and reference and is capable of determining the distance between two fixed anchor bolts with a sub-millimeter accuracy. We further used tiltmeters/ inclinometers to monitor tilting deformation of the instability. These devices measure the tilt in two or three axes with typical accuracy of <0.005°.

From the meteorological parameters, we only measured rainfall and temperature. The temperature is by default measured at every node. Standard simple rainfall monitoring is done with tipping bucket rain gauges. These have a fixed area to collect falling rain which is funneled into a tipping bucket with defined volume. The resolution of such a rain gauge is typically around 0.1 mm. There are heated versions which allow measuring of precipitation also at subzero temperatures, but these demand electrical power supply.

We further used geophones for seismic monitoring. The velocity of vibrating ground is monitored with geophones connected to a seismometer. Such systems can typically record frequencies of 0.5 to 250 Hz depending on their natural frequency and the sampling frequency helping to solve classical seismological problems and environmental seismology problems (seismic signal at the Earth´s surface, e.g. Larose et al., 2015, Dietze et al., 2017a).

In parts of this dissertation, data from further complementary methods are used. Uncrewed aerial vehicle (UAV, drone) photogrammetry allows the reconstruction of 3D point clouds by the photogrammetric correlation of multiple photos (usually >100) taken from different angles (structure from motion, e.g. Westoby et al., 2012). Global Navigation Satellite System (GNSS) data are absolute position data of rovers which determine their position by receiving the exact positions of more than four GNSS satellites at a given time reaching millimeter accuracy and sub-daily resolution in continuous applications (e.g. Cicoira et al., 2022). Interferometric radars emit microwave beams which can travel through cloud cover and determine surface changes by the analysis of the phase shift of the reflected waves with sub-millimeter accuracy in ground-based applications or cm-accuracy in space-borne applications (e.g. Carlà et al., 2019). Deformation cameras can detect surface displacements between two photos of the same area by a pixel tracking algorithm (see details in Section 3.2.4).

2.2.2 Early warning systems for landslides

Alarm systems and early warning systems

Early warning systems (EWS) are defined as: "The set of capacities needed to generate and disseminate timely and meaningful warning information to enable individuals, communities and organizations threatened by a hazard to prepare and to act appropriately and in sufficient time to reduce the possibility of harm or loss" (UN/ISDR, 2009). This definition

highlights the differentiation from alarm systems by the emphasis of a timely warning which enables to prepare and act in sufficient time. This is only possible, if the monitored hazard shows measurable precursors sufficiently early before the event itself. Such systems are used since several decades for landslide and other risks (e.g. hydro-meteorological, volcanic, earthquake, tsunami, human-caused, technological, biological risks), but are overall still a young field of research with continuously developing techniques (Meissen and Voisard, 2010).

The time between an issued warning and the beginning of the event itself is called lead time (Hermle et al., 2021, Pecoraro et al., 2019). Depending on the duration of this lead time, landslide EWS are sometimes further distinguished into warning systems (>1 h lead time) and forecasting systems (>1 d lead time, e.g. Pecoraro et al., 2019, Stähli et al., 2015). In cases, where the failure process is too fast to detect precursors sufficiently early (e.g. snow avalanches or small rockfalls), automatic alarm systems detecting the event itself must be applied as there is no time for expert judgment of any precursors (GEOPRAEVENT, 2019). Overall, EWS are only effective, if the time required for meaningful mitigation measures (e.g. evacuation of population) is shorter than the lead time (Hermle et al., 2021).

Early warning at territorial and at local level

EWS systems can either cover whole regions (up to national, continental or global level) or operate on a local event level (Meissen and Voisard, 2010, Piciullo et al., 2018). The first group of territorial EWS are most effective, if the prediction includes statements on *where*, *when*, *how many* and *how large* landslides are to be expected (Guzzetti, 2021). This is usually achieved by landslide inventories and susceptibility mapping (*where*) and process based modelling or rainfall thresholds (*when*). Rainfall thresholds are a wide field of research. Reasonably defined thresholds are regionally different and based on intensity-duration, total event rainfall, event duration only, or event-intensity (Guzzetti, 2021).

This thesis deals with local EWS. They can be seen as a set of components that help to reduce the risk resulting from a specific natural hazard. Local EWS are increasingly applied all other the world, because of their lower cost and environmental impact compared to engineering structures, developing monitoring methods, an increasing number of cases for warning model calibration, or because structural measures are simply not possible to be installed (Intrieri et al., 2012, Pecoraro et al., 2019). Every local EWS embeds a warning model, which defines alarm thresholds and decision-making procedures based on the relationship of triggering conditions and slope status (Pecoraro et al., 2019). These alarm thresholds are for example defined based on velocity (e.g. Intrieri et al., 2012), displacement (Valletta et al., 2023), hydrological status (Piciullo et al., 2022) or a deformation probability index (Zhang et al., 2024).

Components of local early warning systems

People-centered EWS consist of four key elements according to the UN/ISDR (2009): "knowledge of the risks; monitoring, analysis and forecasting of the hazards; communication or dissemination of alerts and warnings; and local capabilities to respond to the warnings received" (cp. Fig. 1.1). Intrieri et al. (2013) followed four main activities for the description of EWS: design, monitoring, forecasting and education (Fig. 2.5). They further constructed flow chart-based toolboxes for the choice of suitable instrumentation and organizational features for various types of slope failures.

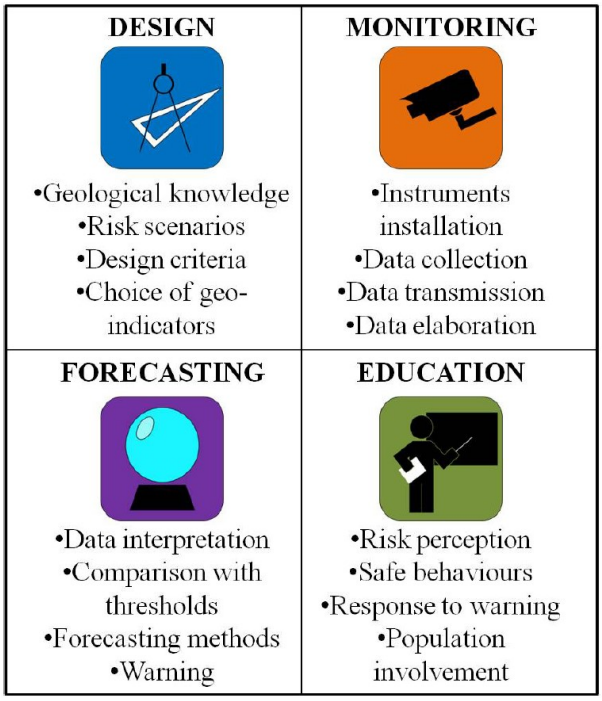

Figure 2.5: Four fundamental components of generic local landslide early warning systems from Intrieri et al. (2013).

For every EWS, it is important that all key elements are balanced, as the whole system is only as strong as the weakest element (Intrieri et al., 2012, 2013). For example, a perfect forecast of an imminent landslide event is worth nothing, if the affected people do not know how to react to a warning. Consequently, the monitoring system must be designed with suitable instruments and the system must be maintained. The data must be analysed correctly using thresholds, expert judgment or forecasting methods. Understandable warnings must be communicated (e.g. through regular bulletins, Giordan et al., 2021) and the response of the people must be prepared and trained.

2.3 Rock slope failure process dynamics

The reliable anticipation and successful early warning of rock slope failures requires a good understanding of all process dynamics controlling the preparation phase of these failures (e.g. Krautblatter and Moore, 2014, Sättele et al., 2016, Chae et al., 2017, Pecoraro et al., 2019).

Comprehensive monitoring and EWS, as described in the previous section, provide valuable data that should be exploited to to gain understanding of all relevant pre-failure process dynamics (Gischig et al., 2016).

2.3.1 Promoting factors

Promoting factors are all processes that bring a slope closer towards failure. They increase the susceptibility of a slope to be triggered, mainly by a decrease of the material strength or development of a sliding plane over months to many millions of years (Dietze et al., 2017b). This means, the the same triggering force that cannot not initiate a slope failure in an early unprepared state of the slope could indeed trigger a failure later. This concept is visualized in Fig. 2.6. Various processes can act on a slope over different time scales. Long-term material fatigue can result from crack propagation due to chemical weathering (Krautblatter and Dikau, 2007), erosion, glacial debuttressing (Eberhardt et al., 2004, Ballantyne et al., 2014), permafrost degradation (Krautblatter et al., 2013, Hilger et al., 2021), or repeated seismic loading (Gischig et al., 2016, Oswald et al., 2021). On the seasonal scale, pore pressure variations (Preisig et al., 2016) or frost bursting (Krautblatter and Dikau, 2007) can be effective.

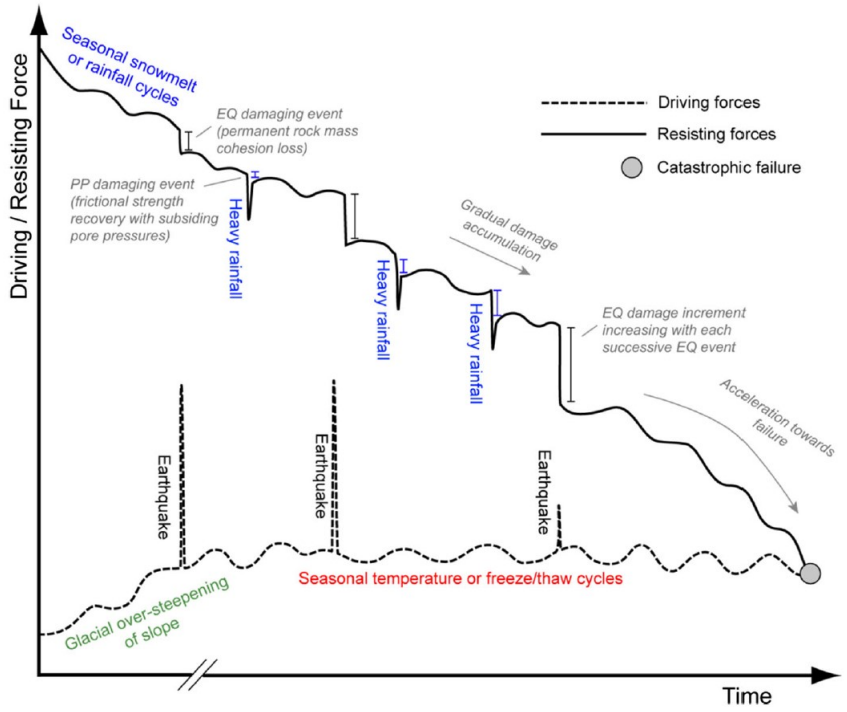

Figure 2.6: Role of driving and resisting forces in the preparation phase of a slope failure. The resisting forces are diminished continuously by promoting processes, finally leading to catastrophic failure (from: Gischig et al., 2016, originally adapted from Gunzburger et al., 2005).

2.3.2 Triggering factors

A trigger is defined as "external stimulus [...] that causes a near-immediate response in the form of a landslide by rapidly increasing the stresses or by reducing the strength of slope materials" (Wieczorek, 1996). However, while some triggers show a clear immediate response,

others require a certain response time reaching up to several years (Gischig et al., 2016, Dietze et al., 2017b). Thus, a differentiation between promoting and triggering factors is not always possible. It is rather probable that several promoting and/ or triggering factors overlap and interact. In some cases, the progressive weakening of material through chemical and physical weathering or crack propagation could lead to slope failure without an apparent external trigger (Lagarde et al., 2023). Overviews of landslide and rockfall triggering processes can be found in Wieczorek (1996), Stock et al. (2013) and Dietze et al. (2017b).

Water

Among the most important triggers is water from intense rainfall or snowmelt (e.g. Wieczorek, 1996, Helmstetter and Garambois, 2010, Stock et al., 2013, LaHusen et al., 2020). Infiltrating water can quickly destabilize rock slopes by generating significant hydrostatic pressure in fissures, lowering the joint cohesion, reducing the joint friction angle, and decreasing the effective normal stress at the sliding surface due to uplift pressure (Erismann and Abele, 2001, Wyllie and Mah, 2004, Scandroglio et al., 2021). Moreover, extended periods of hydromechanical loading have been demonstrated to play a significant role in the development of deep-seated landslides (Gischig et al., 2016). Krautblatter and Moser (2009) could connect 90 % of measured small-scale rockfall from an alpine calcareous wall to rainfall triggering. They found the rockfall response to high rainfall intensities to be highly non-linear above a certain threshold of ca. 10 mm/30 min.

Earthquakes

Another important trigger across the globe are earthquakes (e.g. Wieczorek, 1996, Jibson et al., 2006, Meunier et al., 2007, LaHusen et al., 2020, Marc et al., 2016, Massey et al., 2022). Historically, they appear to have played a significant role in both preparing and triggering large rockslides, as evidenced by the spatio-temporal coincidence of major earthquakes and rock slope failures (Knapp et al., 2018, Oswald et al., 2021). Seismic waves can have a strong destabilizing effect by introducing additional stress to slopes. During an earthquake event, a specific amount of seismic energy with characteristic frequency and direction acts on the slopes around the epicenter for a finite duration. The effect of earthquakes on slope instabilities can either be measured, or estimated using the Newmark block analysis (Newmark, 1965, Jibson, 2007). This method allows the calculation of theoretical block displacements due to seismic shaking using the Arias intensity (Arias, 1970), a measure of the total acceleration of a seismic record.

Meunier et al. (2007) and Massey et al. (2022) could show a high correlation of landslide occurrence and volume with measured peak ground acceleration. Because of topographic resonance and wave refraction in areas of steep terrain (Harp and Jibson, 2002, Sepúlveda et al., 2005, Lee et al., 2009a,b, Khan et al., 2020), this effect is not homogeneous in space, but landslides are predominantly triggered on mountain tops and ridge crests facing away from the epicenter (Meunier et al., 2008). Seismic wave amplification is frequency-dependent

and can reach factors of 2-14 in the horizontal component (Bakun-Mazor et al., 2013, Rault et al., 2020, Weber et al., 2022). Furthermore, seismic waves can experience amplification and polarization within unstable rock masses themselves, particularly perpendicular to existing open cracks (Burjánek et al., 2010, 2012). Modeling studies by Gischig et al. (2016) have shown that amplification factors become more intricate in space and frequency with higher degrees of slope damage.

Internal rock fracturing

Among internal drivers, progressive propagation of cracks within fractured rock is the most important (Petley, 2004, Lagarde et al., 2023). This process prolongs cracks and active sliding planes by both, critical and subcritical fracturing, which intensifies stress concentrations at the tips of the cracks (e.g. Amitrano and Helmstetter, 2006, Voigtländer et al., 2018). Usually, the situation progressively self-accelerates with time, as with each failing rock bridge, stress further increases at the remaining rock bridges (Kemeny, 2003). In cases, where the sliding plane is well developed and most rock bridges have been degraded, the deformation release is likely governed by macro-roughness, which creates obstacles along the sliding plane (Borri-Brunetto et al., 2004, Dietze et al., 2021). Recent developments in seismic monitoring (Senfaute et al., 2009, Helmstetter and Garambois, 2010, Hibert et al., 2011, Provost et al., 2017, Dietze et al., 2021, Lagarde et al., 2023) and machine learning procedures (Provost et al., 2017, Hibert et al., 2017, Wenner et al., 2021, Langet and Silverberg, 2023) allow the detection and analysis of numerous rock fracturing events.

Other factors

Besides rainfall, snowmelt, earthquakes and internal crack propagation, numerous other triggering factors are known, but not further discussed here: temperature gradients (Gunzburger et al., 2005, Bakun-Mazor et al., 2013, Collins and Stock, 2016), freeze-thaw-cycles (D'Amato et al., 2016), wind (Stock et al., 2013, Dietze et al., 2017b), lightning (Stock et al., 2013, Knight and Grab, 2014), snow or rock avalanches (Stock et al., 2013), volcanic activity (Wieczorek, 1996), vegetation growth and root prying (Dietze et al., 2017b), permafrost degradation (Krautblatter et al., 2013, Walter et al., 2020, Hilger et al., 2021), and human or animal activity (Dietze et al., 2017b).

2.3.3 Runout and impact

The runout and impact of fragmental rockfall is mainly controlled by the interaction of the blocks with the substrate, the degree of fragmentation, the fall height and the slope angle (e.g. Hungr et al., 2014, Chen et al., 2023). However, with increasing volume of rock slope failures, mobility tends to increase (Hungr et al., 2014). Topography plays an important role, as channeling can increase mobility significantly, while impacts on opposite slopes minimize the runout length (Nicoletti and Sorriso-Valvo, 1991). After detachment of

high-magnitude rockfalls and rockslides, they often disintegrate before transforming into hazardous flow-like avalanches (Knapp and Krautblatter, 2020) with long runout distances and high velocities (Plafker and Ericksen, 1978). The runout is likely but not necessarily prolonged with the degree of fragmentation (Davies and McSaveney, 2009), entrainment of material on the path (Frank et al., 2017, Aaron and McDougall, 2019, Pudasaini and Krautblatter, 2021), and the presence of ice or water in the runout path (Haeberli et al., 2004, Imre et al., 2010). If boundary conditions and controlling input parameters of specific events have been determined adequately, then runout length, velocity, impact and flow heights can be modelled, with one-phase (Berger et al., 2012), two-phase (Pudasaini and Krautblatter, 2014) or multi-phase models (Pudasaini and Mergili, 2019).

2.3.4 Climate forcing

Climate change is responsible for two main factors that potentially influence the stability of rock slopes: increasing temperatures and modified precipitation patterns (IPCC, 2019). The rise of minimum, mean and maximum temperatures, especially in arctic an high-alpine regions, is strongly evident and directly affects the melting of snow and ice and the degradation of permafrost (Huss et al., 2017, Picarelli et al., 2021). This can lead to an increase of the hydrostatic pressure, weaker ice and rock mechanical strength, and reduced stability of ice-filled fractures (Krautblatter et al., 2013). Where glaciers retreat, slopes are left unsupported and lots of loose sediment remains available (Huggel et al., 2012b). Therefore, for specific regions (seasonally or permanently cold regions, arctic countries, high-altitude permafrost mountains), the link between higher temperatures and increased landslide activity is quite clear (Picarelli et al., 2021, Zhu et al., 2021).

Bigger uncertainties and complexity remain for snow and wildfire implications. Higher temperatures are responsible for a shorter and thinner seasonal snow cover and a shifted melting season (Uhlmann et al., 2009, Huss et al., 2017). Overall, snowfall is projected to decrease due to more frequent rainfall favouring conditions, but, however, cold regions and high altitude mountain areas might experience slight snowfall increases (Frei et al., 2018, Le Roux et al., 2023). This is due to more frequent extreme snowfall events, a general increase in winter precipitation and the shift of very cold areas into more snowfall favouring temperatures. Higher temperatures are further expected to increase the probability of wildfires (Miller et al., 2024), which in turn could increase the probability of landslides due to the missing vegetation (e.g. Rengers et al., 2020), but here, the link is less evident.

On the other hand, there is also a shift towards more intense and more frequent rainstorms for some regions (Zhang et al., 2013, Prein et al., 2017, IPCC, 2013, 2014, Pendergrass et al., 2019). This could lead to generally wetter conditions, a higher water table for longer periods, and higher surface and subsurface flows, which in turn leads to a reduction of rainfall amounts needed as trigger, lower cohesion and shear strength, higher hydrostatic pressure and increased erosion (Gariano and Guzzetti, 2016). However, projections on the long-term mean conditions have limited value for the link to landslide activity, as landslides are rather triggered by short to medium duration rainstorms (Krautblatter and Moser, 2009, Picarelli

et al., 2021). The northern and western European Alps are projected to become generally wetter, while the southern Alps are becoming dryer, especially in winter and spring (Masson and Frei, 2016). Extreme precipitation events are increasing over large parts of the Alps on annual scale and during all seasons (Ménégoz et al., 2020), but the effect varies significantly between regions and seasons. The increase is shown to be distinct e.g. in autumns in the Southern French Alps (Blanchet et al., 2021), in winter in valleys and medium mountain areas of the Northern French Alps (Blanchet et al., 2021), or in autumn (Ménégoz et al., 2020) and winter (Frei et al., 2006) in the southern Alps, but other regions show a significant decrease of extreme precipitation events in some seasons. The link between climate change and increased landslide activity is therefore only given, where rainstorm intensity and frequency exacerbate. This is for example the case in the Northern Calcareous Alps, where an increased rainstorm activity has been linked to significantly higher debris flow rates (Dietrich and Krautblatter, 2017, Kiefer et al., 2021).

2.4 Failure time forecasting at slope scale

2.4.1 Successful and unsuccessful historic examples

The first successful prediction of a slope failure has been performed at the Motte d'Albino rock fall in Tessin (Switzerland) in 1928 (Federico et al., 2015). Two years later, geologists failed to anticipate the famous Kilchenstock instability over Linthal (CH) correctly (Heim, 1932). Another tragic example is the famous failure of Vajont 1963 with more than 2000 fatalities (Ghirotti, 2013). It has not been foreseen, but however, Kilburn and Petley (2003) showed that if the inverse velocity method had been available, the failure might have been forecasted even several weeks in advance.

To date, there are several examples of successful forecasts at natural or man-made slopes, e.g. at Monte Beni 2002 (Gigli et al., 2011), Otomura in Japan 2004 (Fujisawa et al., 2010), three open pit mine slopes in the USA 2001-2005 (Rose and Hungr, 2007) or at Preonzo 2012 (Sättele et al., 2016). However, due to the complexity and great variety of different slope instabilities, the timely forecasting at slope scale remains a highly challenging task. This is illustrated by the recent Veslemannen failure in 2019 (Norway), where the decision-making operators evacuated the people at risk 16 times before the failure happened (Kristensen et al., 2021).

2.4.2 Creep curve

Creep is an internal geomechanical process in slopes under stress causing material deformation and surface displacement (Mazzanti et al., 2015). The measured pre-failure surface displacement pattern of most landslides can be described with a classical creep curve (Intrieri et al., 2019) consisting of three phases (Fig. 2.7). Such behaviour can be observed at earth flows or reactivated landslides without active rock fracturing (Intrieri et al., 2019), but also

at rock slopes, where progressive crack propagation and non-elastic deformations prior to failure control displacements (Petley, 2004).

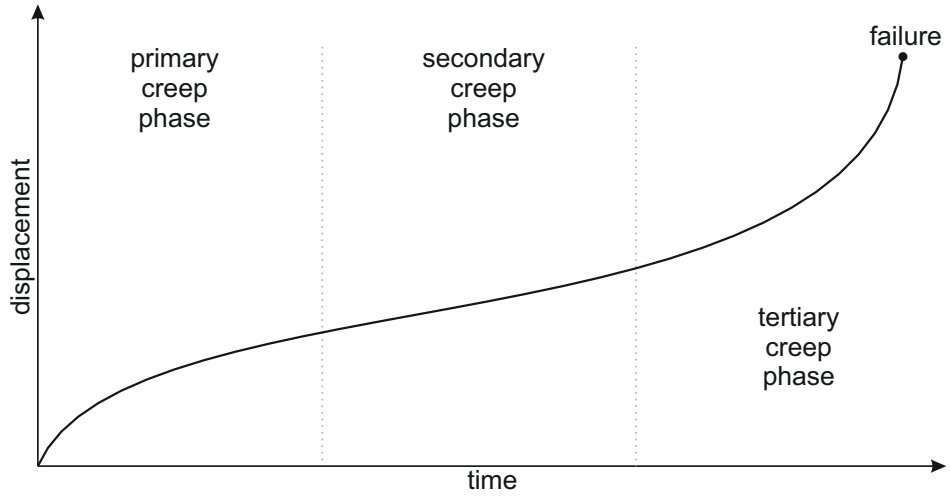

Figure 2.7: Classic theoretical creep curve consisting of primary, secondary and tertiary creep until failure.

The primary creep phase marks the start of slope movement with initially high displacement rates that then transform into a lower slope activity with constant strain rates in the secondary phase, in which driving and resisting forces balance out (Petley et al., 2008). Increasing stress, progressive failure of rock bridges and fatiguing material create a self-accelerating positive feedback effect (Amitrano and Helmstetter, 2006, Main, 2000, Corcoran and Davies, 2018, Kemeny, 2003), which leads to an accelerating regime in the tertiary creep phase until eventual final failure.

Classic landslide monitoring determines the strain or strain rate over time (cp. Section 2.2.1). For early warning applications, the detection of accelerating movement rates as precursors for imminent failure is crucial (e.g. Voight, 1989a,b, Fukuzono, 1985). To a certain extent, all slope failures are preceded by precursory ground movements (Federico et al., 2015), although they cannot always be recorded. The latter might be the case when slope failures are triggered fast by unforeseen sudden events like earthquakes or if the monitoring does not fit the amplitude, duration, or location of precursory displacements. Usually, the acceleration phase is shorter the smaller the volume and more brittle the rock is (Rose and Hungr, 2007), ranging from seconds for small blocks up to days, weeks or months for bigger slope failures.

2.4.3 Classic forecasting methods

In the final phase of a slope instability, predictions of the time of failure can be calculated with several methods (Intrieri et al., 2019). Most existing forecasting models are phenomenological models based on measurements of displacement, deformation or acoustic emission counts (Federico et al., 2015). Since the 1960s, four major approaches have been put forward and will be introduced in the following paragraphs. The most used prediction method is the

inverse velocity method after Fukuzono (1985) (Casagli et al., 2021). There is no evidence that this method is the most accurate one, but its relatively simple graphical solution might be a reason for its frequent application (Carlà et al., 2017b).

Saito

Based on the creep curve, Saito and Uezawa (1961) introduced an empirical approach to estimate the remaining time until slope failure, named creep-rupture life. Through a series of material compression tests in the lab, they found an inverse relationship between the time to failure (in min) and strain rate $\dot{\varepsilon}$ (in 10^{-4} min) during the secondary creep stage. This relationship gave a straight line in a log-log plot and led to the following equation for estimating an unstable slope's life expectancy t_{LE} in minutes:

$$log_{10}\, t_{LE} = 2.33 - 0.916\, log_{10}\, \dot{\varepsilon} \pm 0.59 \tag{2.1}$$

This relationship has been confirmed in field conditions and refined for application during tertiary creep by Saito (1965). Initially, a graphical method was proposed to solve for failure time t_f (Saito, 1969), but there is also a numerical equation that directly provides estimates for t_f:

$$t_f = \frac{t_2^2 - t_1 t_3}{2t_2 - (t_1 + t_3)} \tag{2.2}$$

where t_1, t_2, and t_3 represent points in time where the relative displacement between t_1 and t_2 is equal to the relative displacement between t_2 and t_3 (Intrieri and Gigli, 2016).

Fukuzono

Fukuzono (1985) conducted large-scale slope models which were subjected to artificial rainfall until they collapsed. Just before slope failure, towards the end of the tertiary creep phase, he observed that the logarithms of surface velocity and acceleration exhibited a proportional relationship, mathematically expressed by the following power law equation:

$$\frac{d^2x}{dt^2} = A(\frac{dx}{dt})^\alpha \tag{2.3}$$

where x is the surface displacement, t is time, and A and α (typically within the range of 1.5 to 2.2) are positive constants (Fukuzono, 1985). Integrating Eq. 2.3 over time, assuming $\alpha > 1$, results in the following equation:

$$\frac{1}{v} = [A(\alpha - 1)(t_f - t)]^{\frac{1}{\alpha - 1}} \tag{2.4}$$

where $\frac{1}{v}$ represents the inverse velocity and t_f is the failure time (Fukuzono, 1985).

The shape of a plot of inverse velocity against time depends on the value of α. For $\alpha = 2$, the plot is linear, for $1 < \alpha < 2$, the plot is convex and for $\alpha > 2$ it is concave (cp. Section 5.2). For the linear case, the time of failure (t_f) can be calculated as:

$$t_f = \frac{t_2 \frac{1}{v_1} - t_1 \frac{1}{v_2}}{\frac{1}{v_1} - \frac{1}{v_2}} = \frac{t_2 v_2 - t_1 v_1}{v_2 - v_1} \tag{2.5}$$

Fukuzono also introduced a straightforward graphical solution to this equation (see the original diagram in Fig. 2.8). In a plot of inverse velocity against time, the extrapolated straight line through the data points intersects the abscissa at the time of estimated time of failure (t_f). An inverse velocity of $\frac{1}{v} = 0$ corresponds to theoretical infinite velocity of the slope.

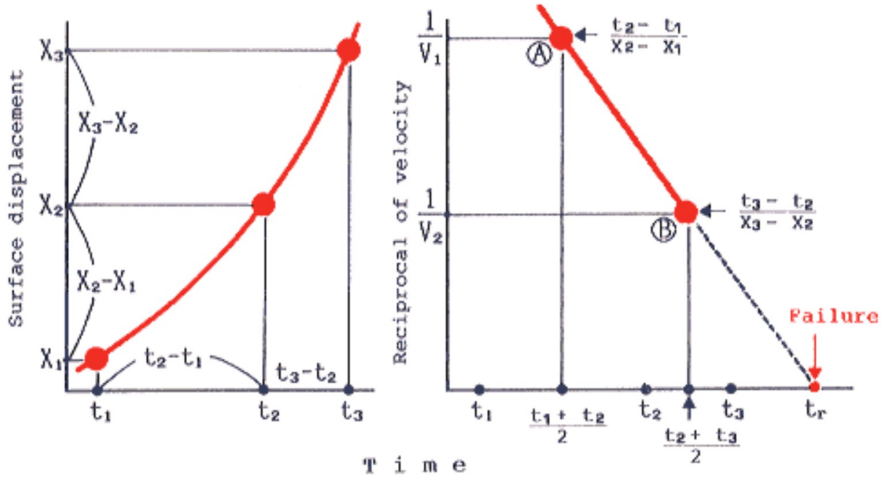

Figure 2.8: Original graphical solution for the inverse velocity method after Fukuzono (from Fukuzono, 1990).

Voight

Voight (1988, 1989a, 1989b) generalized Fukuzono's observation (cp. Eq. 2.3) to describe the behavior of various physical materials under constant stress in the final phase before failure:

$$\ddot{\Omega} = A\dot{\Omega}^{\alpha} \tag{2.6}$$

where $\dot{\Omega}$ and $\ddot{\Omega}$ are the first and second derivatives with respect to time of some measurable quantity Ω, while A and α are again positive empirical constants. Voight denotes this equation as a fundamental physical law, which is applicable in various situations, such as predicting landslides, volcanic eruptions or other material failure. Therefore, any geodetic observation that adequately captures the underlying process mechanics, such as surface displacements, may serve as Ω.

Mufundirwa

More recently, Mufundirwa et al. (2010) introduced another method based on the following equation:

$$v = \frac{B}{t_f - t} \tag{2.7}$$

where v is the displacement rate (velocity), B is a constant, t_f is the failure time and t is time. This equation can be extended on both sides with the life expectancy ($t_f - t$), giving:

$$tv = t_f v - B \tag{2.8}$$

where tv is the dependent variable, v is the independent variable, and B is the intercept in a plot. The failure time t_f then corresponds to the slope parameter and can be found by:

$$t_f = t + \frac{B}{v} \tag{2.9}$$

However, the performance of this method has been found to be limited (Mufundirwa et al., 2010, Intrieri and Gigli, 2016).

2.4.4 Prospective vs. retrospective application

On a retrospective view (post-failure), finding a linear inverse velocity fit that matches the actual time of a failure can be easy (Intrieri et al., 2021, Kristensen et al., 2021). The literature holds several examples of retrospective analyses, showing that the inverse velocity method can be a valid tool for failure time prediction at natural and man-made slopes (Kilburn and Petley, 2003, Petley and Petley, 2006, Mazzanti et al., 2015, Intrieri and Gigli, 2016, Sättele et al., 2016, Intrieri et al., 2019, Carlà et al., 2019, Kristensen et al., 2021, Grebby et al., 2021, Casagli et al., 2021, Tordesillas et al., 2021). However, for effective early warning systems, decision-makers require timely forecasts and an assessment of their accuracy before a failure occurs. This highlights the need for real-time prospective applications (pre-failure), a concept that is not straightforward and is rarely detailed in the literature.

In any case, it is recommended to initiate measurement campaigns as soon as possible, as long high-resolution datasets positively influence the precision of forecasts (Rose and Hungr, 2007, Mazzanti et al., 2015). It is further crucial to regularly update forecasts with every new data point that becomes available, ensuring that any shifts in slope movement trends are properly captured (Crosta and Agliardi, 2003, Manconi and Giordan, 2016, Intrieri and Gigli, 2016, Bozzano et al., 2018). It is also preferable to evaluate more than just the forecast with the most recent data (Intrieri and Gigli, 2016). Tracking the progression of predictions and their variability helps to identify trends that may converge towards a specific failure time.

2.4.5 Data filtering and forecast uncertainties

With the use of higher sampling frequencies, noise increases, which can have a negative effect on the quality of forecasts (Rose and Hungr, 2007, Mazzanti et al., 2015, Carlà et al., 2017b). This is, because all forecasting methods above rely on derivatives, which are typically very sensitive to minor fluctuations in the raw data depending on the specific technique used. Various smoothing techniques maintaining the quality of the data can be employed, like digital filters (Mazzanti et al., 2015), moving averages with variable window lengths (Carlà et al., 2017b), or the use of linear regressions over multiple observations for velocity determination (Rose and Hungr, 2007). Smoothing can improve the forecast results (Dick et al., 2015, Carlà et al., 2017b, Bozzano et al., 2018), but an unfavourable smoothing procedure can also distort the final forecast results.

The accuracy and uncertainty of calculated forecasts are crucial considerations for decision-makers, who typically prefer high reliability (Intrieri and Gigli, 2016). However, many inverse velocity studies fail to provide details on prediction uncertainties or how confident forecasts would have been in real-time. Traditionally, a single model with a single forecast has been the standard approach (Kilburn and Petley, 2003, Krähenbühl, 2006). Later, some studies have adopted a strategy of employing multiple targets per instability, with one inverse velocity prediction per target (e.g. Rose and Hungr, 2007, Sättele et al., 2016). More recently, a multi-method probabilistic approach has been proposed (Intrieri and Gigli, 2016), applying three different prediction models iteratively to the same data series. Instead of relying solely on the most recent forecast, which may not always be the most accurate, this approach considers all calculated predictions over time. By examining the mean and standard deviation, it becomes a probabilistic approach. The highest confidence is achieved when all forecasts converge on the same outcome. Therefore, using more than one prediction method and basing decisions on the average or the most conservative prediction is advisable (Intrieri et al., 2019). One should never rely solely on a single calculated failure time result (Carlà et al., 2017b).

Uncertainties can be expressed as standard error (Grebby et al., 2021) or as a bootstrap distribution of multiple inverse velocity regressions (Manconi and Giordan, 2016). Another useful method of representing forecast uncertainties involves calculating a failure time window during which a failure event is highly likely (Carlà et al., 2017b). Here, two (or more) forecasts with different smoothing windows are calculated simultaneously. The failure window then encompasses the time between the two forecasts, with half of that time span added on each side.

2.4.6 Identification of the starting point for reasonable forecasting

It is preferable to predict the time of an imminent failure as early as possible and at least with sufficient lead time. With the methods described above, reasonable forecasts can be calculated after the onset of acceleration (OOA) in the tertiary creep phase (Dick et al., 2015, Intrieri et al., 2019). In real-time applications and when many sensors are deployed, the

determination of this point can be quite challenging, and the result of the forecast is highly sensitive to it. For this reason, objective criteria and automatic procedures are preferable, but yet, there is no standard procedure for the OOA point identification.

The OOA point is usually marked by increasing deformation rates and decreasing less noisy inverse velocities. Traditionally, this point has been determined through visual evaluation by an expert (Mazzanti et al., 2015, Segalini et al., 2018, Valletta et al., 2021). Retrospectively, having the complete data plots available, finding an optimal OOA can be easy. Prospectively, when fast decisions are needed, this is more challenging. An advance was therefore the OOA determination based upon multiple plots (deformation/ velocity/ inverse velocity vs. time) and two filters (one short-term and one long-term, Dick et al., 2015). More recently, Carlà et al. (2017b) proposed to determine the OOA automatically based on a point where the short-term moving average of the velocity crosses over the long-term moving average. These crossover points mark the occurrence of a trend change and sometimes allow the identification of the OOA significantly earlier than through simple visual evaluation. However, depending on the chosen window lengths, this method may potentially yield numerous OOAs. Valletta et al. (2021) introduced an algorithm that assesses four criteria (positive and increasing velocity, parabolic trend, increasing concavity) for automated OOA detection. Here, an OOA is identified only if all four criteria are met across the most recent n observations. This approach is suitable for near real-time application and performs well in some cases, but sometimes also yields false positives. In some cases it is necessary, to calculate updated additional forecasts from a trend update point onwards (Dick et al., 2015, Bozzano et al., 2018).

2.5 Summary and research gaps

This section gives a short summary of the state of the art and where research gaps exist.

Monitoring
Numerous monitoring methods for landslides exist of which remote and in-situ techniques for surface displacement observations are most relevant for early warning. However, when real-time observations and low- to medium-cost solutions are required, options are limited. There is insufficient knowledge on how to install and operate a real-time monitoring system in high-alpine environment as part of an EWS. It is not clear, which sensors perform best under rough conditions, how wireless data transfer is most effective, which sensors are needed for a resilient and redundant network and how a sufficient reliability of the whole system can be guaranteed.

Analysis
Successful early warning includes and premises a detailed understanding of the unstable slope and its underlying process dynamics. Detailed and multi-method monitoring can offer a good data basis for the analysis of promoting factors in the preparation phase and triggering factors immediately before failure, but comprehensive high-resolution data are rare and not always analysed in detail. Many driving factors depend on site-specific aspects

like morphology, lithology, volume and environment, and must therefore be evaluated for as many as possible case studies, so that inferences can be drawn for similar cases. Moreover, the proportional effect of different drivers can often not be quantified due to the lack of appropriate data, although this would support the determination of most likely future triggers. Only if the most relevant drivers are known, the effect of climatic changes on the preparation of rock slope failures can be evaluated.

Forecasting

Failure time forecasting with various methods can be a successful tool in rock slope failure early warning. The linear inverse velocity method after Fukuzono (1985) is the most used state-of-the-art method, but when applied prospectively (pre-failure) and with modern high-resolution high-frequency data, its performance suffers from several drawbacks. High-frequency and multi-method monitoring adds noise to the measured signal, and thus, data must be filtered. This process underlies subjective decisions. Moreover, the starting point for the application of the inverse velocity method (onset of acceleration) must be detected automatically and robust, which is not standard yet. Then, the forecast uncertainty often remains unclear, although decision-makers need this information. Especially in cases, where the failure type is unclear and different sensors are used, there is a lack of a prospective forecasting concept, that can produce objective, automatic and robust forecasts including a measure of uncertainty.

3 Monitoring

3.1 Real-time monitoring and early warning: initial setup (Paper 1)

This section has been published as article in the Journal *Geomechanics and Tunnelling*:

Leinauer, J., Jacobs, B., Krautblatter, M. (2020): Anticipating an imminent large rock slope failure at the Hochvogel (Allgäu Alps). Geomechanics and Tunnelling 13, No. 6, pp. 597-603.
doi.org/10.1002/geot.202000027

The following changes have been made to the published version:

- The numbering of each section and figure has changed.
- The word "instable" has been replaced by "unstable".
- "Current" setup has been repplaced by "initial" setup.

3.1.1 Abstract

Costs for installation and maintenance of protective structures are increasing while alpine hazards progressively threaten alpine communities, infrastructure and economics. Thus, reliable process-based anticipation and early warning strategies offer a cost-effective and smart solution for alpine societies in the near future. However, only few comprehensive pre-failure observations of alpine rock slopes have been reported so far. In this paper, we demonstrate pre-failure observations of a rapidly deforming rock mass (potentially 260,000 m^3) at the Hochvogel (Allgäu Alps, 2,592 m a.s.l.) and our geotechnical monitoring and warning concept. This is implemented in the complementary multi-method approach of the AlpSenseBench project and the basis for an effective and reliable early warning system. Since 2014, we observe overall displacement rates in the range of 2–10 mm/month in the main decametre deep fracture. We expect that predictive acceleration patterns will appear in the final pre-failure stage. We hypothesize, that a detailed knowledge of multiple anticipative signals in correlation with accelerating rock slope deformations will contribute to an advance in accuracy and reliability of rock slide early warning.

3.1.2 Introduction

In the last decades, natural catastrophic events caused billions of Euros monetary loss and numerous fatalities in alpine valleys (Petley, 2012). Additionally, many billion Euros are annually invested in installation and maintenance of protective structures in European countries with an increasing tendency (PLANALP, 2015). Climate change and population growth exacerbate the risk caused by alpine mass movements significantly (Huggel et al., 2012b). Therefore, reliable anticipation and early warning strategies, based on a precise understanding of the underlying processes, offer a cost-effective and smart solution for alpine societies in the near future (Sättele et al., 2016, Krautblatter and Moore, 2014). Detailed monitoring of landslides and the understanding of underlying mechanisms are crucial for reasonable warning thresholds and reliable forecasting (Chae et al., 2017, Hormes et al., 2020). Worldwide, several local landslide early warning systems (EWS) are operative, including active examples in Europe (for a review see Pecoraro et al. (2019)). Besides a few case studies with well-monitored unstable rock slopes like Piz Cengalo (CH) (Walter et al., 2020) or Marzellkamm (AT) (Hormes et al., 2020) in metamorphic rock, case studies from natural carbonate rock slopes within an alpine setting are very rare. The Hochvogel is paradigmatic of natural slope failure dynamics and therefore a benchmark site for testing a multi-method risk assessment and developing an effective EWS. The geotechnical monitoring concept at the preparing Hochvogel rock slope failure is part of the AlpSenseBench project complemented with a multi-method approach including satellite, aeroplane, UAV, geodetic, photogrammetric and seismic surveys. Our part focuses on near real time monitoring of hazard hotspots and will contribute to an advance in reliable rock slide early warning.

3.1.3 Site overview

Geographical and geological context

Situated right on the Austrian-German border, the Hochvogel (2,592 m a.s.l.) is a prominent mountain of the Northern Calcareous Alps and a popular destination for hikers. The southern via ferrata "Bäumenheimer Weg" has been officially closed by the Austrian government 2014 due to high rock fall risk (Heißel and Figl, 2014), but the summit is still accessible via the stable north side. The Hochvogel massif consists of Hauptdolomit, a brittle, variably bituminous carbonate rock with a pronounced bedding (dm – m) and incidental marly inter-layers. The rock mass is tectonically stressed and highly weathered. Pronounced talus material indicates sustained rock fall activity. The main fracture is 2 to 6 m wide at the summit and boulders are trapped in the crack at ca. 10 m depth. Traceable more than 60 m down at the sides, it is dividing the summit into the stable NW part and the unstable SE (Fig. 3.1). The sliding mass has moved downward by about 3 m relative to the back-scarp edge during the last century. Lateral clefts separate different unstable blocks. All flanks of the summit pyramid are exceptionally steep resulting in high internal stress.

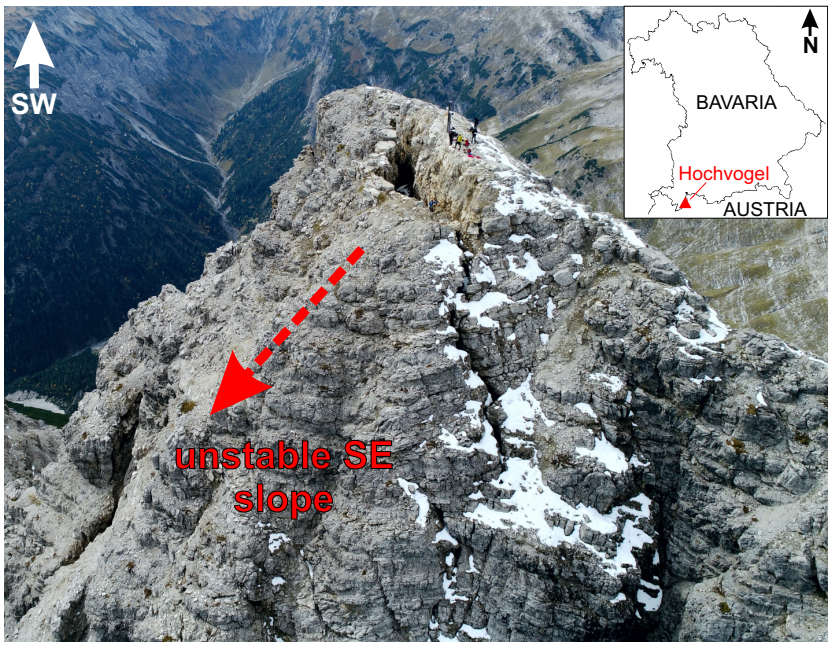

Figure 3.1: The Hochvogel summit with the main fracture (people on the summit for scale).

Rockslide volume

We traced major extended discontinuities in a 3D model to identify potential shear planes verified by field observations. Intersections of these planes generate six major potentially unstable wedges with a total volume of ca. 260,000 m³ (Fig. 3.2). We assume that subsequent failures of subunits through sliding and toppling are likely, potentially also initiating a collapse of the entire detached mass. Since the deformation of the lower flank is still below the level of detection of our structure-from-motion and terrestrial laser scan campaigns, we are working on the field verification of displacing volumes.

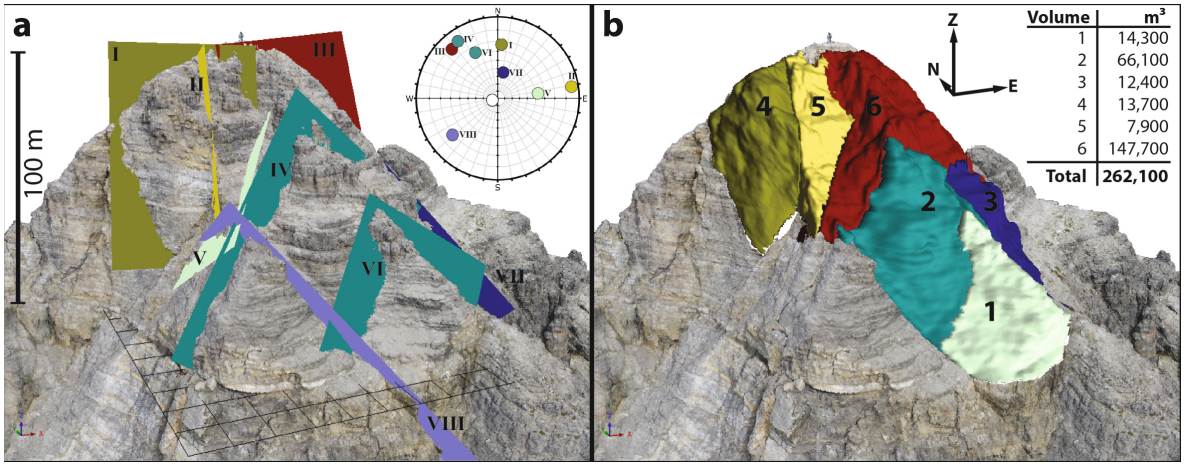

Figure 3.2: Volume estimation of potentially sliding blocks. (a) shear planes derived from 3D SfM-Model with corresponding polar plot, (b) potential volumes.

Historic process dynamics

The earliest mentioned indications of fracturing at the Hochvogel summit date to 1869 (von Barth, 1984). In the 1970–80s, people could step over the crack. Smaller cliff falls are reported in 1934/35 (SW wall) and in 2005, 2007 and 2016 (Sektion Donauwörth des DAV e. V., 2020). An analysis of selected ortho- and georeferenced aerial images shows that the main crack has lengthened more than 20 m in 72 years reaching the limits of the summit plateau in 2010 (Fig 3.3). At least since then, an obvious aperture is apparent on the flanks of the summit pyramid.

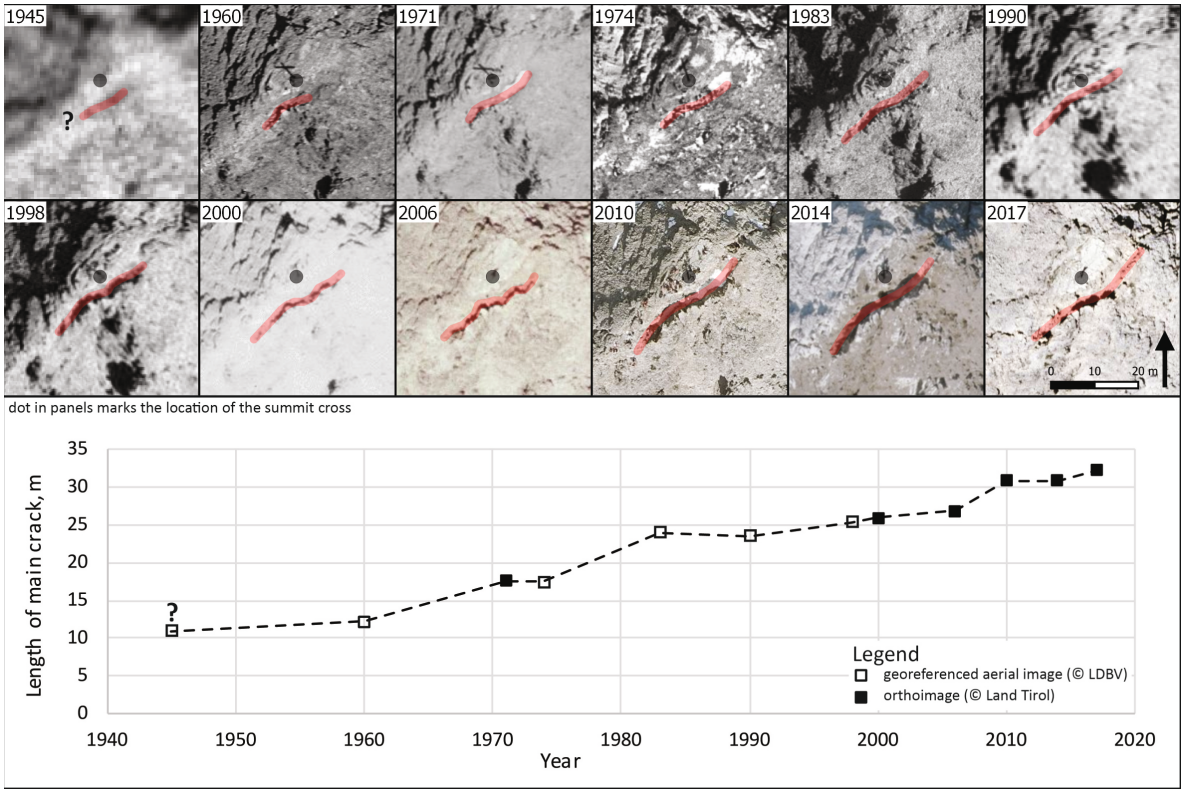

Figure 3.3: Lengthening of the main crack in the Hochvogel summit since 1945.

3.1.4 Geotechnical monitoring concept

From discontinuous to continuous real time monitoring

Initially we measured the deformation of the main cleft manually with individual tape extensometer campaigns (Fig. 3.4). Later, we expanded the discontinuous observations with more sections in the lateral cracks and annual photogrammetric UAV surveys and TLS campaigns. Over 200 mm displacement between summer 2015 and summer 2017 with mean movement rates of up to 9.6 mm/month indicated necessity to measure continuously.

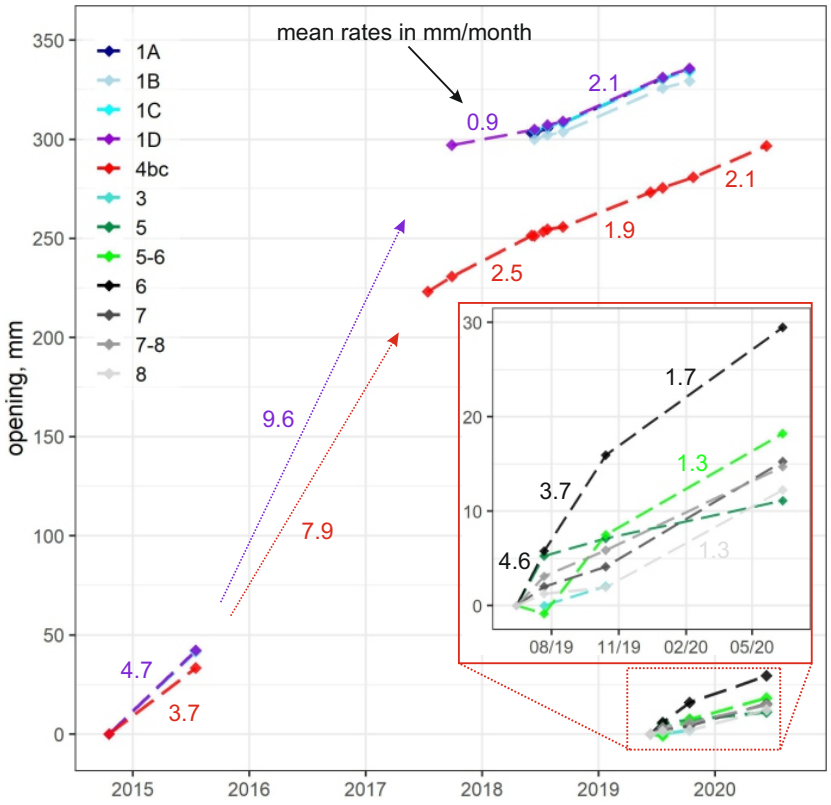

Figure 3.4: Discontinuous tape extensometer measurements (±0.1 mm) since 2014. For section locations see Fig. 3.5.

Since 2018, we are operating a continuous real time monitoring system. The exposed location of the site forced us to improve the system progressively resulting in a reliable system with independent sending nodes. For clearance, we only introduce the initially established system setup here (Fig. 3.5). Automatic vibrating wire (VW) gauges deliver high-resolution data to an online server. The currently set sampling rate of 10 min is a good balance between time resolution and amount of data. Two VW long range displacement meters with 2 m wire drum (resolution 0.5 mm, factory accuracy ±2 mm) are installed in the main crack; three VW crackmeters with a range of 150 mm (resolution 0.04 mm, accuracy ±0.15 mm) in the lateral cracks. For lightning protection, each VW gauge is connected to its own datalogger through a surge arrester module. Electrical decoupling is obtained through a piece of non-conductive glass-fibre plastic at one side of the crack. Datalogger, surge module and both rock bolts of the crackmeter are connected by a copper cable for potential equalisation. A rain gauge and a webcam complete the setup at the summit. The entire system is accessible and adjustable remotely via internet.

Exemplified at "Crack02", we measured a total widening of 25 mm in 20 months (Fig. 3.6). An overall acceleration of the unstable mass is not evident in the data. An acceleration of the sliding during snowmelt or heavy rain fall events is likely but yet difficult to detect due to data gaps. Daily fluctuations are in the order of 1 mm.

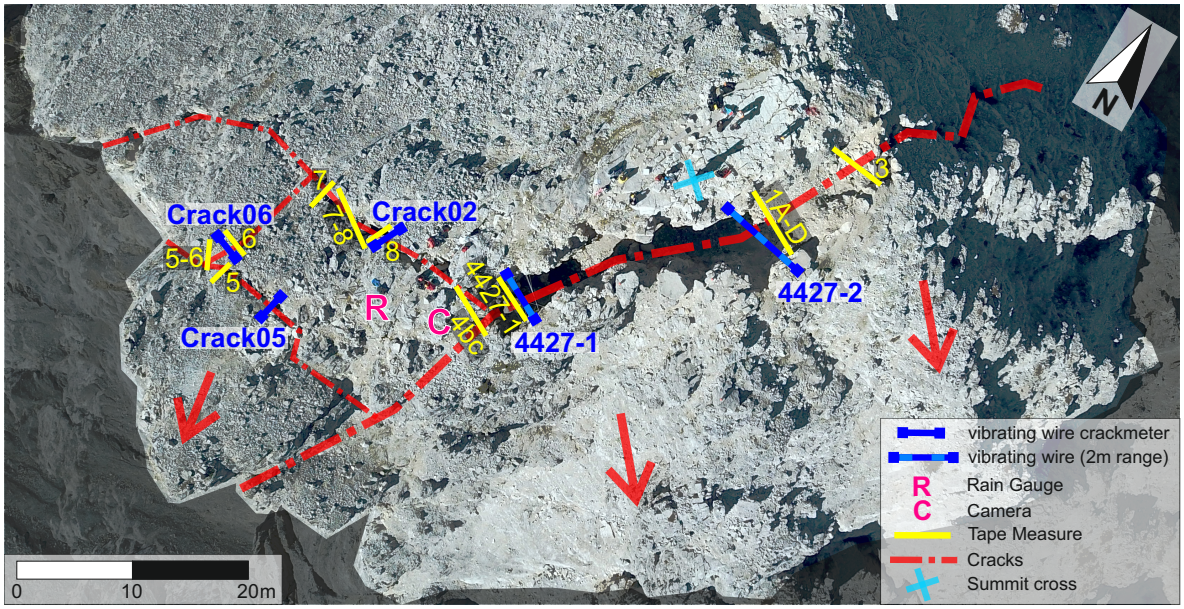

Figure 3.5: Plan of the initial monitoring system at the Hochvogel.

Automatic data analysis and warning

The concept of the Hochvogel monitoring and warning system is visualized in Fig. 3.7. A gateway in the valley collects all data from each individual node via LoRa (low power, long-range radio) and transfers compiled data automatically to a safe server via GSM. A data platform performs automatic data processing and plotting. Real time display, dashboard, reports and overviews facilitate easy online access and data control. For this early stage of investigations, we defined simple, displacement-based thresholds for every sensor. To avoid false alarming, thresholds are chosen conservatively (10 mm above current value), and alarms are only sent to the operating experts via email and SMS. After expert judgment, an alarm is forwarded to authorities and local stakeholders if applicable. Age of data and alarm task execution are monitored automatically by the system itself. Early warning implies knowledge of the timing of the event sufficiently early before the event. In the past, several methods for slope failure prediction have been put forward by different authors (Intrieri et al., 2019). Existent methods like the inverse velocity approach, are only reliable if the unstable slope is in the "tertiary creep phase" with accelerating movements resulting in an exponential velocity curve (Intrieri et al., 2019). Note, an unstable slope with constant displacement rates is considered in "secondary creep phase". So far, our measurements do not indicate tertiary acceleration of the movements and thereby impede a reasonable prediction of the time of failure. The requirements for the detection of initiating acceleration are met through our installations and data.

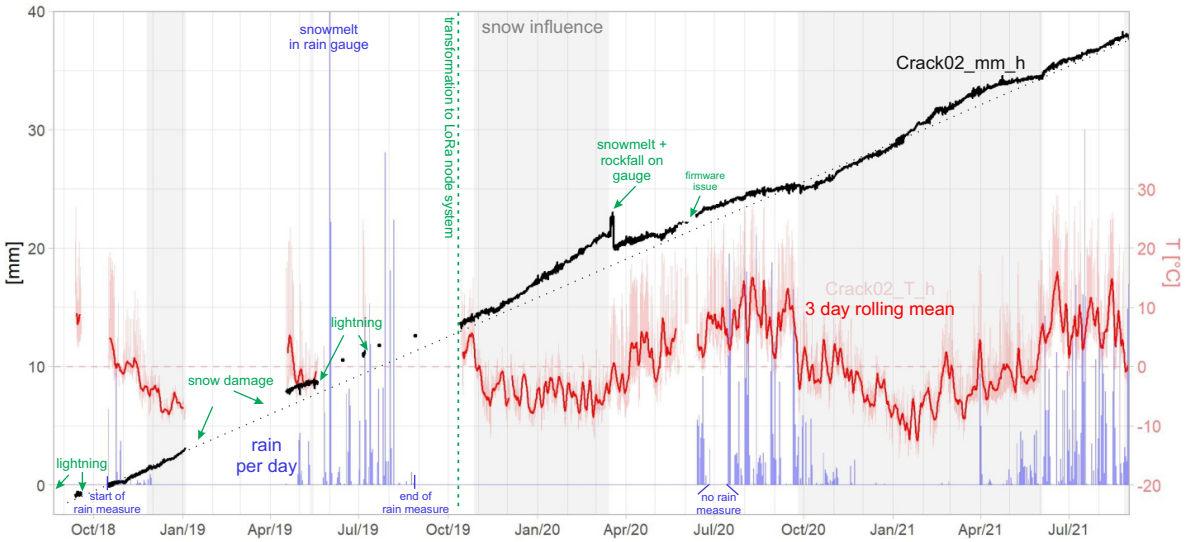

Figure 3.6: Most continuous crack opening measurements of "Crack02" relative to 22 Oct. 2018 (hourly values).

3.1.5 Discussion

We established a near real time monitoring and warning system at the Hochvogel summit that contains all typical elements of a local EWS (Huggel et al., 2010). The system performs well under the challenging conditions of the remote site since the transformation to individual LoRa nodes with lightning protection in Oct. 2019 and is transferable to other alpine sites. Reliable EWS are characterized by redundancy, a precise understanding of process dynamics, a high probability of detection of an event and a low probability of false alarming. Hence, many EWS use multiple monitoring methods (Pecoraro et al., 2019). An optimal redundant system would require multiple gauges per crack, but every operator must balance between redundancy and costs. So far, we only use VW gauges for continuous observations, validated by our discontinuous measurements. These will be the basis for detecting the response of the unstable mass to environmental influences. Other methods like optical ranging or borehole measurements are pricey and more difficult to operate at the exposed site. Continuous GB-InSAR can be a valuable extension in the future. Our discontinuous measurements are redundant to geodetic measurements, both yielding totally consistent results. Geodetic (summit) and point cloud measurements (lower flank) from the AlpSenseBench project will help to interpret 3D movements, once the deformations exceed the detection threshold. Seismic observation of rock bridge collapses will be used for process analysis and early warning in combination with our measurements. Provided the expected failure volumes are correct, we assume that except for the already closed hiking path, no other infrastructure will be directly affected according to our first models. These can be improved by surveys in the runout channel, as only investigating the release area is insufficient (Walter et al., 2020). Nevertheless, to provide additional safety, no one should be close to the en-

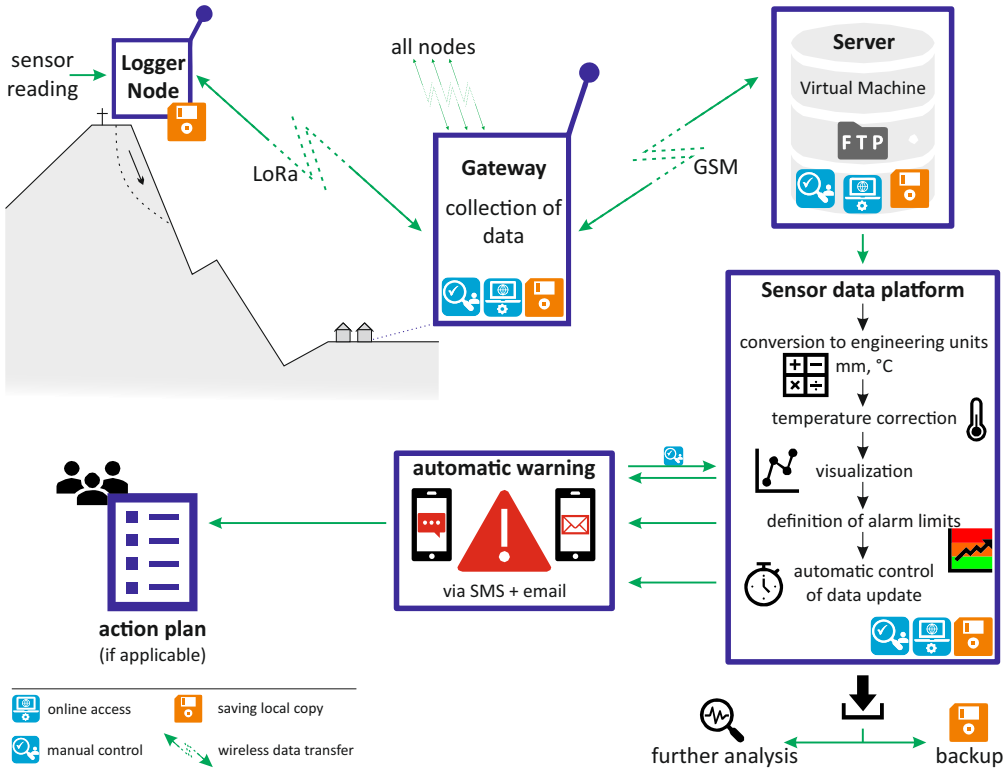

Figure 3.7: Data transfer, automatic analysis and warning of the Hochvogel system.

dangered zone or the summit when failure occurs. Therefore, a close communication with authorities, the local commune and the hut personnel is of high importance.

3.1.6 Conclusions and outlook

We investigated the imminent large rock slope failure at the Hochvogel summit (possibly ca. 260,000 m³). Analysis of historical ortho- and aerial images proves ongoing fracturing since at least 70 years. Tape extensometer measurements show 35 cm opening of the main cleft between 2014 and 2020 with mean movement rates up to 9.6 mm/month. During the last 3 years, movement rates were roughly constant with 2 mm/month. Since 2018, we are operating an automatic geotechnical monitoring system providing high-resolution crack opening and rain data. These near real time observations are the basis for an operational EWS and represent the monitoring of hazard hotspots within the AlpSense approach. As we interpret the instability still being in secondary creep phase, a prediction of the time of failure is not yet possible. We will improve our alpine monitoring system in terms of continuity, redundancy and reliability. Important tasks for effective early warning will be inclusion of stakeholders and reasonable scenario-based runout models. The correlation with corresponding (e.g. seismic or geodetic) measurements in the follow-up project AlpSenseRely will help to decipher anticipative signals even better providing insights into rock slope dynamics and thereby contributing to an advance in reliable rock slide early warning.

3.1.7 Acknowledgments

The AlpSenseBench research project was funded by the Bavarian Ministry of Economic Affairs, Regional Development and Energy. We would like to thank everyone who helped with organization, intense field work and advice.

3.2 Dynamic development towards high reliability: current system (Update 1)

This section is an update to Paper ① in Section 3.1.

3.2.1 Overview

Since the initial monitoring setup from 2019, we have continuously updated and advanced the system to increase its reliability in terms of redundancy, data availability and spatial coverage. An updated plan of the improved and currently active monitoring devices is shown in Fig. 3.8.

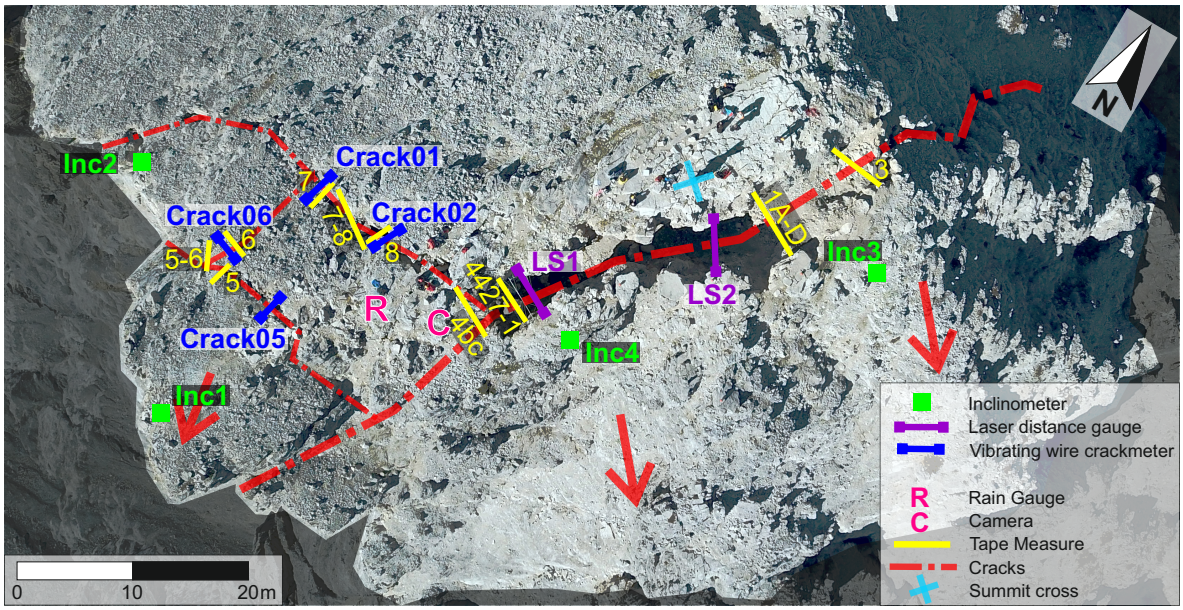

Figure 3.8: Updated plan of the improved monitoring system at the Hochvogel including new crackmeters, laser distance gauges and inclinometers.

3.2.2 Lightning protection

In 2019, after repeated electrical surge damages at the exposed summit, we implemented a lighting protection concept for all VW nodes (Leinauer et al., 2021). Each crackmeter device is connected with short as possible cables to a surge arrester module and then to its individual logger node (Fig. 3.9). To hinder electrical coupling of the two sides of the crack via the VW device, one side of the crackmeter is connected to a non-conductive glass-fiber plastic rod. High potential differences within one measuring node (crackmeter, surge module, logger) are counteracted by keeping each node compact and connecting all components to thick copper cables for equalization of electrical potential. Strong currents due to superficial potential gradients, that can be induced by close lightning strikes, are thus avoided. No

lightning protection can protect VW gauges from direct lightning hits, but however, there was no crackmeter loss at the Hochvogel since the implementation of the lightning protection concept.

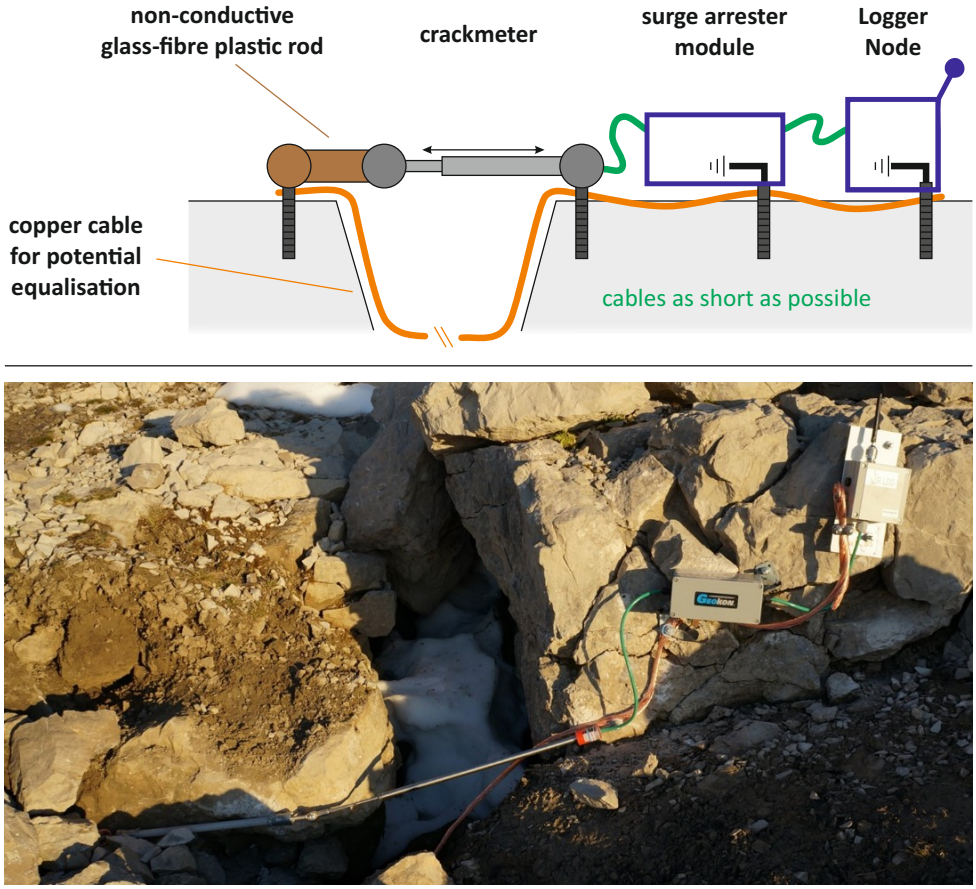

Figure 3.9: Concept of the lightning protection for crackmeters and according photo from the site (from Leinauer et al., 2021).

3.2.3 Additional LoRa-nodes and protective roofs

In 2021, we installed seven additional LoRa-nodes (one crackmeter, two laser distance gauges and four inclinometers). On the most distinct lateral crack, next to crackmeter "Crack02", we have installed an additional crackmeter "Crack01". Here, the second device increases redundancy and allows interpretation of rotational displacements, e.g., "Crack02" indicates slightly higher displacements than "Crack01". This is likely connected to an outward rotation of the SW block towards the steep SW-wall.

The main crack is now monitored with two laser distance gauges (resolution 0.1 mm, accuracy ±1-2 mm). At the summit, the crack is ca. 4 m wide open and blocked with boulders in ca. 10 m depth. This space is filled completely with massive snow deposits over each winter.

When this snow settles, it causes great drag forces that inhibit the observation of the main crack opening with VW devices. We therefore installed laser distance gauges which can measure the distance between the stable and the unstable side whenever the snow deposits are below sensor and target (6-9 months per years). In spring, when the snow has melted enough, the laser distance gauges transmit reasonable observations automatically without the need for maintenance.

To gain additional continuous information on the tilt of the unstable rock blocks, we have installed four inclinometers (two on the main SE block and one each on the outer SW blocks, see Fig. 3.8). The inclinometers measure the tilt in two axes with respect to the direction of gravity with a resolution of 0.0001° and an accuracy of ±0.0025°. The devices are fixed to the ground and can thus deliver reliable measurements even in winter under thick snow conditions, which could potentially influence the crackmeters. These inclinometers increase the redundancy of the system by adding another dimension of measured displacement and can be used for anticipation tasks. As a precursory sign for imminent failure, we expect that the failing rock blocks tilt significantly, whereas stable blocks might not be affected. Additionally, failure time forecasts can also be calculated with tilt rates (see Chapter 5 and Leinauer et al., 2023b).

In the same year, we protected all measuring devices from rockfall and strong snow pressure in snow-rich winters with roofs. These roofs are made of wood to guarantee high stability without attracting lightning potential gradients as it could be the case with solid metal. One side of each roof is fixed to the ground while the other side allows movement in terms of crack opening. Photos of "Crack06" with and without its wooden roof are shown in Fig. A.1.1 and A.1.2.

3.2.4 Deformation camera

In 2022, the assessment of repeated terrestrial laser scans showed first signs of potential deformation in the steep SW-wall below blocks 2, 5 and 6 in Fig. 3.2. Although this potential deformation is still below the level of detection of 2-3 cm, we decided to continuously monitor this flank. This steep rock wall is not accessible for the installation of in-situ crackmeters and since the lower delimitation of the unstable mass is not clear yet, we decided to install a deformation camera system by the company Geoprevent. We installed this camera with solar panel and battery on a metal mast on a stable ridge looking upward into the steep SW-wall (Fig. 3.10). The camera is a 42 Megapixel High-Dynamic-Range camera taking and transmitting 6 photos per day via mobile network. During winter, the lens is kept snow-free with a warm air system. In order to achieve the optimum balance between high resolution and a wide image section, we have chosen a 25 mm focal width lens resulting in pixel sizes of 15-35 mm/pixel.

During the snow-free season, deformation analyses are automatically calculated weekly by Geoprevent with the company´s algorithm. The algorithm finds best-matching photo pairs of a current photo (±8 d) and one reference photo from one month or one year before (±8 d)

Figure 3.10: Drone photo of the installed deformation camera looking at the steep SW-wall of the Hochvogel summit. The 4 m-pole with camera, solar panel and battery is fixed to the rock mass and is grounded with copper cables.

and accounts for different lighting conditions. Then, it tracks displacements of contrast-rich patterns in the two scenes. Shifts of the entire image due to a slight change in the camera viewing direction are corrected by stable areas, which we defined based on our geological model and laser scans. The deformation analysis is capable of resolving deformations of ca. 1 cm under optimal conditions. Fig. 3.11 shows a photo taken by the deformation camera and the deformation analysis from the same day with 1-year reference period. Left and right in the picture (yellow perimeter) are the defined stable areas. In the center (roi01 and roi02), the analysis indicates small potential deformations in the range of 0.004 px/d. Below the summit, the area with purple-blue colours indicates coherence loss due to the failure of several 100 m^3 of rock in Oct. 2022 (see Section 4.2).

With the described setup, we are able to monitor the steep SW-wall of the Hochvogel summit. Total deformations are currently still below the level of detection within the monthly and yearly reference periods. However, we expect these deformations to increase to a detectable level when a failure of the flank approaches. On the other hand, we can detect precursory failures of smaller rock towers and blocks along the sliding surface. A good performance of the system is limited to snow-free areas, good weather conditions and deformations perpendicular to the line of sight. An interferometric radar could operate in all weather conditions, but a permanent operation of such generates a multitude of costs.

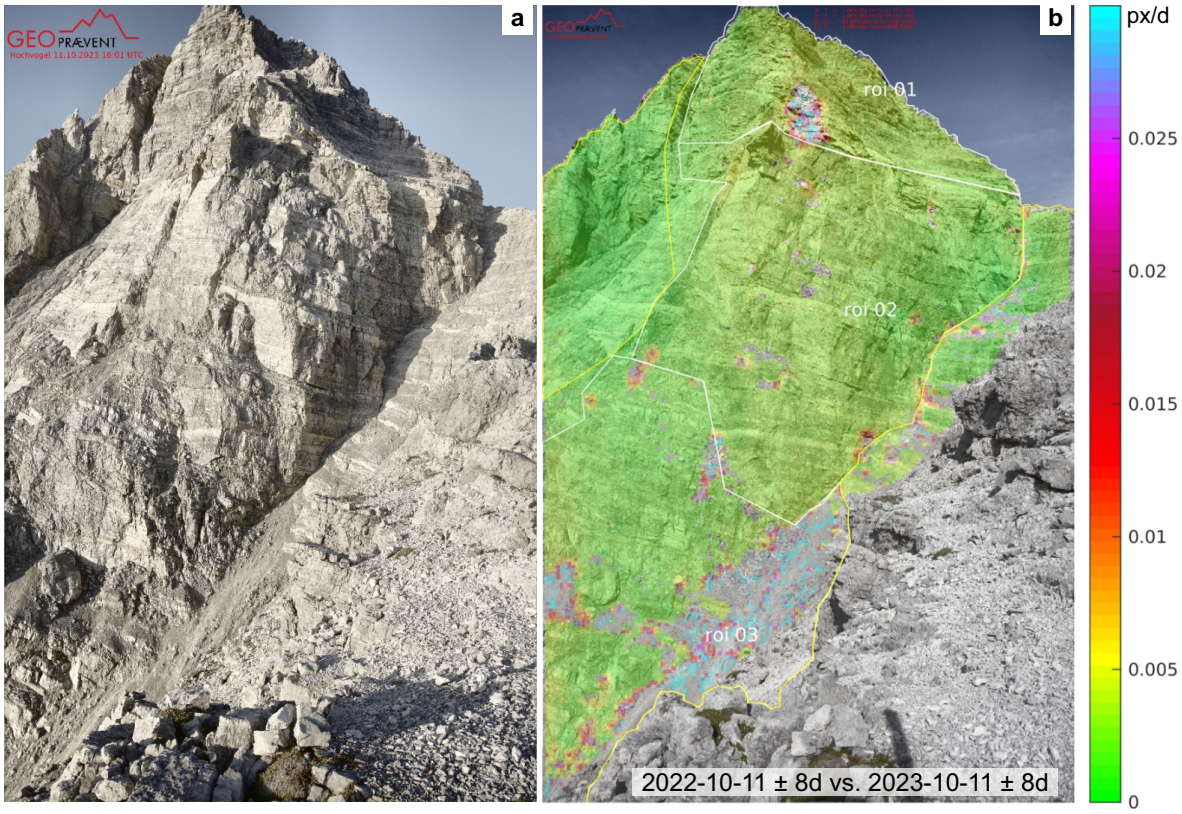

Figure 3.11: (a) Picture taken by the deformation camera on 2023-10-11 16:00 UTC. (b) Automatic deformation analysis from the same day with 1-year reference period.

3.2.5 Benchmark crack opening patterns

After the installation of a new real-time monitoring system, every operator must first gather data for a meaningful time, before setting reasonable and site-specific alarm thresholds. Only if normal behaviour and typical patterns are known, exceptional behaviour, that could indicate imminent failure, can be identified. At the Hochvogel, daily fluctuations are in the order of 1 mm. The seasonal benchmark crack opening patterns vary between different sensors and are best accessible in cumulative displacement plots per year.

In 2020-2023, "Crack02" measured a yearly opening of 11-14 mm with slightly higher deformation rates in the summer months where the temperatures are mainly positive (Fig. 3.12). The displacement rate is almost linear over each year. Total deformation was highest in 2023 and lowest in 2020, but within a narrow range. All years show normal behaviour.

"Crack06", shows a different benchmark pattern (Fig. 3.13). Here, yearly deformations are 16-18 mm between 2020 and 2022. In 2023, the total crack opening was 30 mm. In winter, between December and May when the temperatures are below 0 °C, there is no significant displacement. In May-June, there is a sharp increase in displacement when temperatures become positive, while displacement rates gradually decrease in autumn. In 2023, the deformation in the summer months was higher than in previous years and the deceleration in

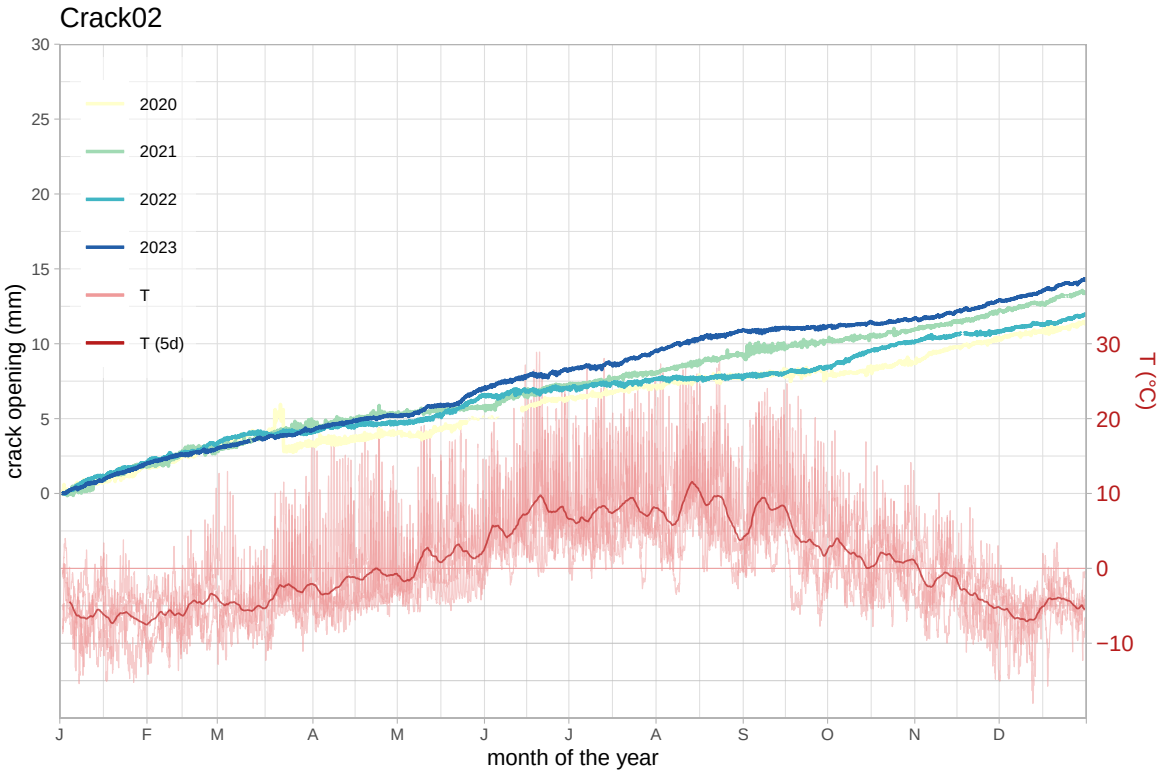

Figure 3.12: Cumulative displacement per year of "Crack02" between 2020 and 2023 showing the benchmark crack opening behaviour at the measured point. The temperature is plotted in light red. The solid red line is the 5-day rolling average of all years.

autumn was slower, resulting in a higher cumulative displacement. This pattern is exceptional compared to the benchmark behaviour of previous years and could be precursory for a failure of the measured rock block. The gap in 2023 data was due to a failed rock anchor at one side of the crackmeter. After re-installation of the crackmeter, the displacement has been corrected with the manual tape measurements.

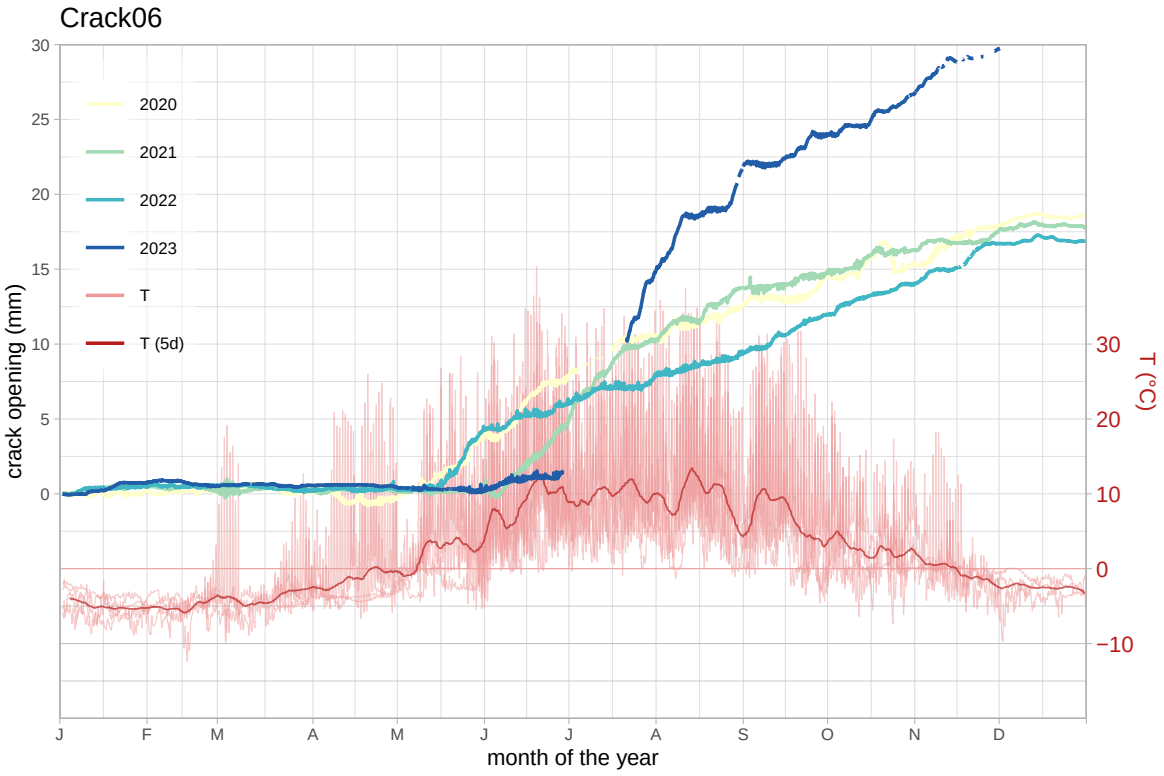

Figure 3.13: Cumulative displacement per year of "Crack06" between 2020 and 2023 showing the benchmark crack opening behaviour at the measured point. Displacements have been higher than previous years in 2023. The temperature is plotted in light red. The solid red line is the 5-day rolling average of all years.

4 Analysis

4.1 Quantified drivers of massive rock slope failure preparation (Paper 2)

This section has been submitted as article to the Journal *Earth Surface Dynamics* (IF 4.6):

Leinauer, J., Dietze, M., Knapp, S., Scandroglio, R., Jokel, M., and Krautblatter, M. (2024): How water, temperature and seismicity control the preparation of massive rock slope failure (Hochvogel, DE/AT), EGUsphere [preprint, submitted to Earth Surf. Dynam.].
https://doi.org/10.5194/egusphere-2024-231

The following changes have been made to the submitted version:

- The numbering of each section, figure and supplementary material has been changed.

4.1.1 Abstract

The increasing hazard of major rock slope failures, exacerbated by climate change, underscores the importance of anticipating pre-failure process dynamics. While standard triggers are recognized for small rockfalls, few comprehensive driver quantifications exist for massive pre-failure rock slopes. Here we exploit >4 years multi-method high-resolution monitoring data from a well-prepared high-magnitude rock slope instability. To quantify and understand the effect of possible drivers - water from rain and snowmelt, internal rock fracturing and earthquakes - we correlate slope displacements with environmental data, local seismic recordings and earthquake catalogues. During the snowmelt phase, displacements are controlled by meltwater infiltration with high correlation and a time lag of 4-9 days. During the snow-free summer, rainfall drives the system with a time lag of 1-16 h for up to several days without a minimum activation rain sum threshold. Detected rock fracturing, linked to temperature and freeze-thaw cycles, is predominantly surface-near and unrelated to displacement rates. A classic Newmark analysis of recent and historic earthquakes indicates a low potential for immediate triggering of a major failure at the case site, unless it is already very close to failure. Seismic topographic amplification of the peak ground velocity at the summit ranges from a factor of 2-11 and is spatially heterogeneous, indicating a high criticality of the slope. The presented methodological approach enables a comprehensive

rockfall driver evaluation and indicates where future climatic changes, e.g. in precipitation intensity and frequency, may alter the preparation of major rock slope failures.

4.1.2 Introduction

Massive rock slope failures are an important geomorphic hazard that causes increasing risk in the wake of climate change and population growth (Lacasse and Nadim, 2009, Picarelli et al., 2021). To prevent damage to people or property, the anticipation of such events becomes highly crucial (Sättele et al., 2016, Chae et al., 2017, Pecoraro et al., 2019, Leinauer et al., 2023b), and thus, relevant drivers and potential triggers of imminent failures must be identified and understood. Exploiting the available data of comprehensive monitoring and early warning systems to gain understanding of all relevant pre-failure process dynamics should therefore become a standard procedure (Gischig et al., 2016). However, while standard and qualitative rock fall triggering factors are known, site-specific quantifications of the relevant drivers of high-magnitude rock instabilities based on monitoring data are often missing.

Rockfall release can be caused by a reduction of resisting forces and/or an increase of driving forces. In the preparation phase, promoting drivers act on a rock slope over months to millions of years (Dietze et al., 2017b) bringing the system progressively closer towards critical slope stability (Oswald et al., 2021). This is achieved by the development of a sliding plane over different time scales, e.g. through seasonal pore pressure increase (Preisig et al., 2016), repeated seismic loading (Gischig et al., 2016), or long-term fracture propagation following weathering and erosion, glacial debuttressing (Eberhardt et al., 2004, Ballantyne et al., 2014) or permafrost degradation (Hilger et al., 2021). Imminently before failure, a trigger acts on the balance between stabilising forces and stress leading to unstable conditions initiating rockfall within short time (Wieczorek, 1996). Of course, promoting drivers in the preparation phase and triggering factors terminating this phase can overlap and interact, and the transition between the two may be gradual. In some cases the progressive weakening of material could lead to slope failure without an apparent external trigger (Lagarde et al., 2023) but in such state, the rock slope instability becomes increasingly sensitive to external drivers. However, a detailed and comprehensive knowledge of how and how much internal and external drivers control the pre-failure stage of imminent rock slope failures is missing at most sites, but crucial for anticipation tasks.

Possible rockfall drivers and triggers (Fig. 4.1) include (e.g. Stock et al., 2013, Dietze et al., 2017b) (a) rainfall, (b) snowmelt, (c) rock fracturing and crack propagation, (d) earthquakes, (e) temperature gradients, (f) freeze-thaw-cycles, (g) wind, (h) lightning, (i) rock or ice fall inducing secondary rockfall, (j) snow or rock avalanches, (k) volcanic activity, (l) vegetation growth and root prying, (m) permafrost degradation (Krautblatter et al., 2013), and (n) human or animal activity. The significance of some of these factors might change in the future due to climatic shifts, e.g. precipitation frequency and severity or temperature (IPCC, 2019).

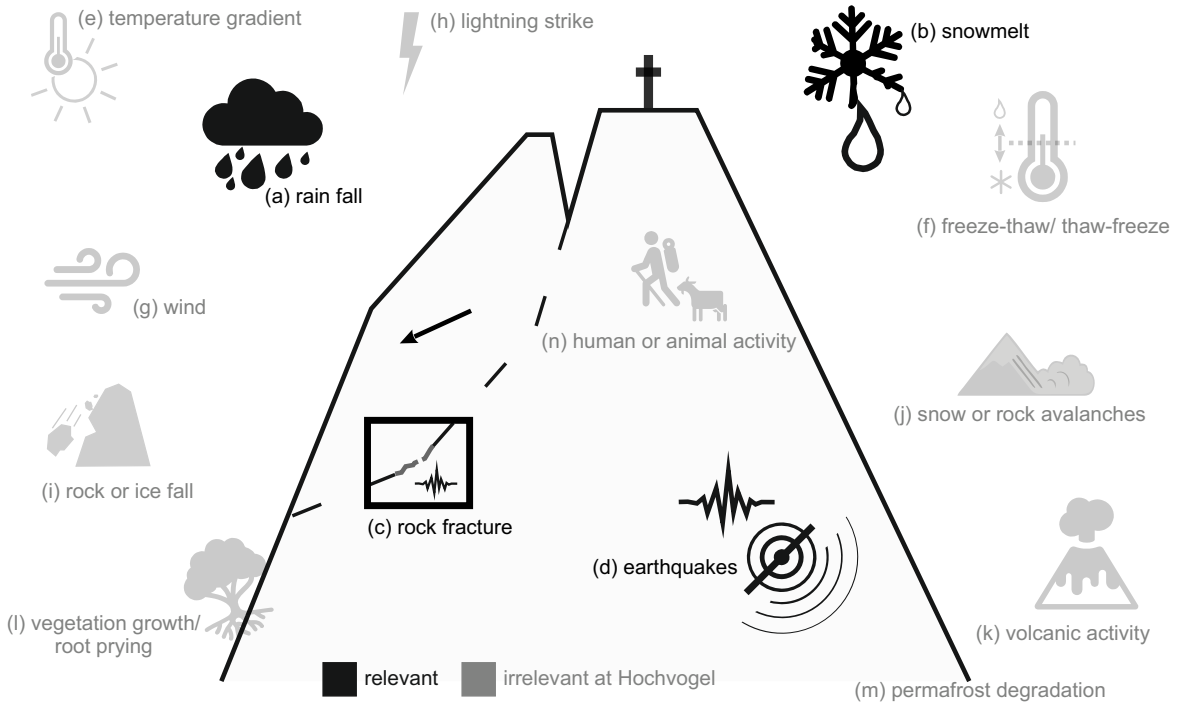

Figure 4.1: Factors that can potentially promote and/or trigger rockfalls. Black processes (a-d) are relevant for a major failure at our case site Hochvogel, grey ones (e-n) can be excluded due to the reasons in the text.

Heavy precipitation and rapid snowmelt are documented to be amongst the most important drivers for rockslides across the globe (e.g. Wieczorek, 1996, Helmstetter and Garambois, 2010, Stock et al., 2013, LaHusen et al., 2020). Infiltrating water can destabilize rock slopes repeatedly in short time scales by building significant hydrostatic pressure in clefts, elimination of the joint cohesion, lowering of the joint friction angle and reduction of the effective normal stress at the sliding surface due to uplift (Erismann and Abele, 2001, Wyllie and Mah, 2004, Scandroglio et al., 2021). Additionally, long-term hydro-mechanical loading cycles are proven to have a promoting effect in deep-seated landslides (Gischig et al., 2016). Constraining the amount of water, respectively the pore pressure inside a rock slope, is challenging without the availability of boreholes. In such cases, the direct measurement of the water supply via rain gauges or snow stations is easier to obtain.

Progressive crack propagation in fracturing rock is one of the main internal drivers of rock slope failures (Petley, 2004, Lagarde et al., 2023). Critical and subcritical crack growth along active sliding planes intensifies the stress concentration at the crack tips (e.g. Amitrano and Helmstetter, 2006, Voigtländer et al., 2018), as with every failing rock bridge, the stress increases at the remaining rock bridges (Kemeny, 2003). Once most rock bridges have been degraded, episodic deformation release might be controlled by macro-roughness creating obstacles along the sliding plane (Borri-Brunetto et al., 2004, Dietze et al., 2021). Stress release in the form of rock fracturing generates typical and distinguishable seismic signals that can

be recorded with local seismic networks (Senfaute et al., 2009, Helmstetter and Garambois, 2010, Hibert et al., 2011, Provost et al., 2017, Dietze et al., 2021, Lagarde et al., 2023). Isolating the episodically occurring short events within the large datasets is challenging with manual techniques and thus, established machine learning procedures can help to build a database of rock fracturing events (Provost et al., 2017, Hibert et al., 2017, Wenner et al., 2021, Langet and Silverberg, 2023).

Earthquakes frequently trigger numerous landslides (e.g. Wieczorek, 1996, Jibson et al., 2006, Meunier et al., 2007, LaHusen et al., 2020, Marc et al., 2016, Massey et al., 2022). Prehistorically, they seem to have played a significant role in preparing and triggering large rockslides due to the spatio-temporal coincidence of major earthquakes and rock slope failures (Knapp et al., 2018, Oswald et al., 2021). The correlation of landslide occurrence and volume with peak ground acceleration (PGA) values (Meunier et al., 2007, Massey et al., 2022) reinforces the destabilizing nature of strong seismic waves, but recurring earthquakes are further a promoting factor due to seismic fatigue (Gischig et al., 2016, Oswald et al., 2021). Earthquake waves add additional stress to a slope instability by accelerating the ground with a specific amount of energy for a limited time depending on frequency and direction. This ground motion can be measured directly at an instrumented instability with the same local seismometers that also record rock fracturing. If direct observations at the site of interest are not available, theoretical block displacements can be estimated with the well-known Newmark analysis (Newmark, 1965). This method allows to evaluate a great number of historic earthquakes from earthquake catalogues or systematic parameter sets towards their triggering potential and deformational influence. In steep topography it is furthermore important to consider frequency-dependent seismic wave amplification due to topographic site effects (Harp and Jibson, 2002, Sepúlveda et al., 2005, Lee et al., 2009a,b, Khan et al., 2020). Through topographic resonance and refraction of waves, seismic amplification can reach factors of 2-14 in the horizontal component at specific frequencies, predominantly triggering landslides at mountain tops and ridge crests facing away from the epicenter (Meunier et al., 2008, Bakun-Mazor et al., 2013, Rault et al., 2020, Weber et al., 2022). Moreover, seismic waves can be amplified and polarized within unstable rock mass itself due to existent open cracks, mainly perpendicular to them (Burjánek et al., 2010, 2012). Gischig et al. (2016) found through modelling that amplification factors increase and become more complex in space and frequency with a higher degree of slope damage, which may in turn be used for assessing the slope´s criticality. However, comprehensive site-specific analyses of how seismicity controls the preparation phase of rock slope failures based on field observations and historical earthquakes are usually not performed.

In this study, we focus on massive rock slope failures (>20,000 m^3). As a case site we use a well-prepared high-magnitude alpine rock slope instability in dolomite rock at the summit of the Hochvogel mountain (2592 m a.s.l., see details in Section 4.1.3), where we have more than four years of multi-method high-resolution monitoring data available. Due to its magnitude, location and altitude, some generic drivers or triggers can be supposed irrelevant (Fig. 4.1). Strong temperature gradients and freeze-thaw cycles can only affect surface-near rock mass (Bakun-Mazor et al., 2013, Weber et al., 2017) without reaching deeper-seated slid-

ing zones. Wind and lightning strikes can potentially induce small scale rockfall, but significant influence on several thousand cubic meters of rock is unrealistic. Excluding large-scale slope engineering, this likewise holds for human or animal activity. As the Hochvogel rock slope instability is located at the summit of the mountain, no rock or ice fall can impact on the instability. The same applies to snow or rock avalanches. Volcanic activity is absent in this region. Due to its altitude, the Hochvogel summit is above the treeline but below the permafrost limit. Thus, four relevant drivers remain and are therefore extensively analysed in this study: rain provided water, snowmelt derived water, rock fracturing and earthquakes. Here, we analyse displacements as the phenomenological result of all drivers and correlate them with meteorological data, local seismic recordings and earthquake catalogues. This approach allows to quantitatively evaluate promoting and triggering factors for massive rock failures similar to our case study.

4.1.3 Study site and instrumentation

The Hochvogel (2592 m a.s.l.) is a dominant and outstanding peak in the eastern Allgäu Alps on the border between Germany and Austria consisting of brittle, well layered dolomite rock (Hauptdolomit) with incidental marly interlayers. The summit area is characterized by a 2-6 m wide main crack that divides the massif into a stable NE-side and an unstable SW-side. The total unstable volume sums up to 260,000 m³ above a distinct 1 m thick marly layer (Fig. 4.2a-A, Leinauer et al. (2020)). Including a potentially unstable mass below, the total volume reaches 400,000-600,000 m³. The rock slope instability has been developing at least since the 1940s with higher deformation rates of about 2 cm/a during the last two decades and is currently preparing to (partially) fail. Several lateral cracks at the almost vertical SW-wall have shown higher activity in the last decade. This flank shows frequent failure of rock towers, as for example a 130,000 m³ rockfall in 2016 (Fig. 4.2a-B, Barbosa et al. (2024)). The site has been under comprehensive monitoring since 2018/19 (Leinauer et al., 2021, Dietze et al., 2021), including observation of crack opening, temperature, rain and seismic signals. A detailed description can be found in Leinauer et al. (2020).

In this study, we exploit several high-resolution data from between October 2018 and November 2022. This includes displacements measured as crack opening by a vibrating wire crackmeter (Crack06) at the most active lateral crack (see photos in Fig. A.1.1 and A.1.2). Measurements are available with 10 min frequency from our real-time monitoring system (resolution 0.04 mm, accuracy ± 0.15 mm). With the same frequency, the air temperature is measured directly at the crackmeter and rainfall is measured with a non-heated tipping bucket rain gauge (resolution 0.1 mm, see photo in Fig. A.1.3).

To monitor seismic processes, we installed a local seismic network on the summit consisting of 4 PE6B 4.5 Hz 3-component geophones and Digos DataCube3ext loggers (maximum distance 75 m). Three of the sensors (SA_{21}, SA_{22}, SA_{23}) are on the stable side, and one station (HV_1) is on the unstable side next to the main crack (Fig. 4.2a, see photos of the seismic stations in Fig. A.1.4 and A.1.5). Additionally, we have installed a wider network with spacings between 0.9 and 1.6 km on the SW flank below the summit, consisting of TC120s or PE6B

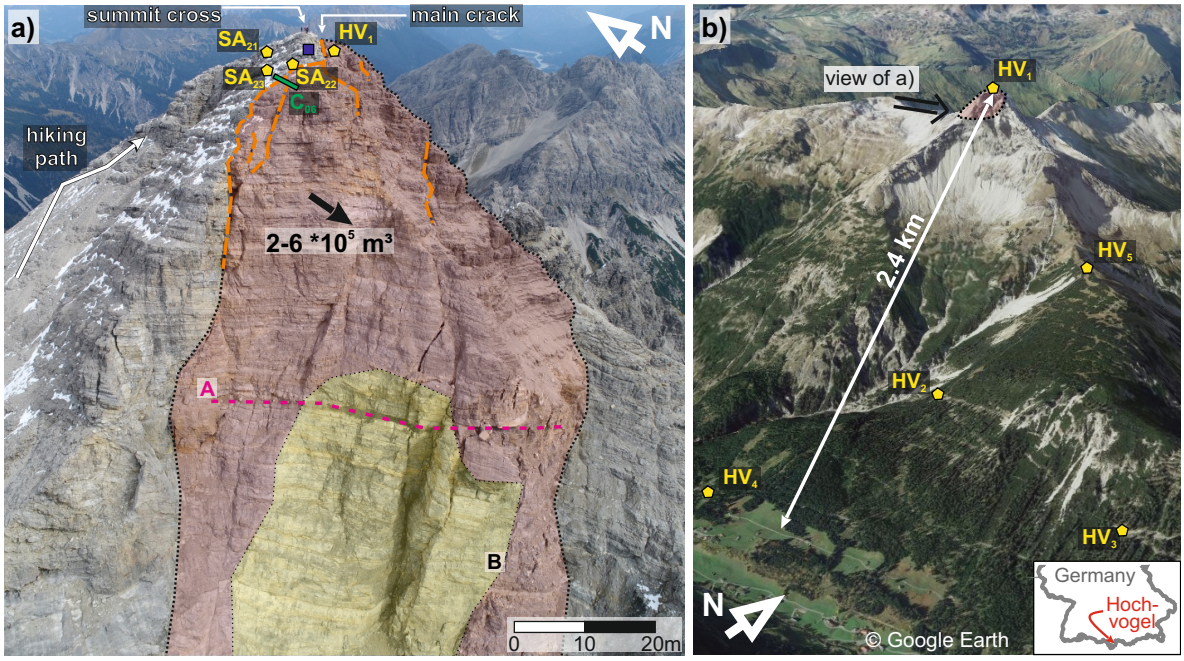

Figure 4.2: Overview of the study site. (a) Photo of the summit area and the steep SW-wall. The unstable mass is marked with the red area, obvious cracks are traced by dashed orange lines. Measurement devices in this study include the stations of the seismic summit network (yellow pentagons), rain gauge (blue square) and crackmeter "C06" (green line). A distinct 1 m thick marly layer is marked by the dashed magenta line (A). The source area of a 130,000 m³ rockfall from 2016 is marked by the yellow colour (perimeter B). (b) Hochvogel mountain with the unstable mass at the summit (red area) and the seismic stations of the flank network (yellow pentagons). The village Hinterhornbach (AT) in the valley below the Hochvogel is in the bottom left of the image. Image source: © Google Earth.

geophones and DataCube3ext or DataCube3extBOB loggers (Fig. 4.2b). All stations recorded ground velocity values at 100-400 Hz, but signals have been uniformly aggregated to 100 Hz before further analysis. The station meta data are listed in Table A.1.1.

Data for snowmelt modelling come from two stations of the Bavarian Avalanche Warning Service in the region of the Hochvogel (yellow diamonds in Fig. A.1.26) that measure all necessary parameters (wind, surface and air temperature, snow height). The Nebelhorn (2075-2220 m a.s.l.) station is 9 km away from the Hochvogel, the Zugspitze station (2420-2960 m a.s.l.) 41 km.

To analyze the effect of local or regional earthquakes, we exploit the earthquake event catalogues of Germany (BGR, 2023) and Switzerland (SED, 2023) containing all registered regional earthquakes with M_w >2 since 1692 and 250 AD, respectively. Continuous observations with sub-second resolution are available since 1975 and 2009, respectively. To study the effect of strong distant earthquakes during station operation of our local seismic network, we use the catalogue of the US Geological Service (USGS, 2023).

4.1.4 Data processing

All data were processed with the software R v. 4.3.0 (R Core Team, 2023). R scripts of all major processing and analysis steps are available in an online repository under `https://doi.org/10.5281/zenodo.10567098` (Leinauer, 2024). For the availability of the underlying data see the code and data availability statement.

Seismic crack events

All seismic analysis was performed with the R package eseis v. 0.7.3 (Dietze, 2018a,b). To get corrected ground velocity time series (m/s), the seismic data were deconvolved according to each instrument specifications (see Table A.1.1). Using the data from the summit network, we isolated discrete seismic events. We selected all times during which at least two stations operated simultaneously (860 days, 60 % coverage) to include only events that were captured by more than one station. The basic picking routine then followed the approach by Dietze et al. (2021), using a classic short-term average/ long-term average (STA-LTA) ratio picker (Allen, 1982), applied to the 20–40 Hz filtered signal envelopes (on-ratio = 6, off-ratio = 1, STA-window = 0.2 s, LTA-window = 120 s). With these settings, even low-energy events were detected, but also many false positives. The following automatic check of potential events premises an event duration of 0.2-5 s as the typical duration of discrete rock fracturing activity at the summit (e.g. Senfaute et al., 2009, Dietze et al., 2017a, 2021). Furthermore, the detection time difference between two stations needs to be less than 0.3 s according to a conservative wave travel time across the entire network. This excludes signals with longer detection time differences that result from the coincidence of unrelated signals or waves initiated by sound travelling through air. This led to a detection of 109,492 picked potential events for which we plotted seismograms and spectrograms. A meaningful localization of of the signal source was hindered due to the steep and complex topography, strong jaggedness of the rock mass and unclear wave velocity distribution (cp. Helmstetter and Garambois, 2010).

Finally, to sort the picked events into two groups of seismic rock fracturing events (= target) and other events (steps of humans, rockfalls, coincident noise, false detections), we filtered the events further and used machine learning with a Random Forest classifier (Breiman, 2001), that has been developed in multiple processing steps. First, we calculated the signal-to-noise (SNR) ratio and re-defined all start and end times of the events with a kurtosis picker (Baillard et al., 2014, Hibert et al., 2017), that can identify the picked onset more accurate than the robust STA/LTA picker used in the first step. We then rejected events without distinct ending where the picker could not identify a sharp decrease of the signal (4,813 events, usually humans walking next to the stations or signals with >5 s duration or high background noise not connected to cracking). We further rejected events where the kurtosis picker did not trigger (1,128 events), where the two picking routines identified start times differing more that 1 s (2,071 events) and events where the kurtosis-picked event ended before the start of the STA/LTA-pick (12,560 events, usually when there was not one discrete

isolated event). The Random Forest classifier requires a set of features that describe the seismic signal and allow to separate between the different classes. We followed and adapted the approach by Hibert et al. (2017) and calculated a set of 61 statistical values from the waveform, spectral and pseudo-spectrogram domains. We did this for the station with the highest SNR at each of the remaining 88,920 events, once for the event itself and once for a longer signal including 3 s buffer before and after the picked signal start and end times. Together with maximum SNR, minumum SNR, mean duration and the duration difference between the stations per event, we used a total number 124 features as Random Forest input (see details in the Table A.1.2).

In a first step, we created a training data set by manually classifying 1,353 events (205 crack events, 1,148 others) looking at the features in the plots described in Dietze et al. (2021). We used a balanced proportion of 80 % of the data for training and validating implementing a 5-fold cross-validation. We set up a Random Forest with 500 decision trees including hyperparametertuning with random search and 1000 iterations on the minimum size of terminal nodes, the maximum number of terminal nodes and the number of variables randomly sampled as candidates at each split (see the code under `https://doi.org/10.5281/zenodo.10567098` for details). In the last step we tested the performance of the classifier with the remaining 20 % unseen data. To avoid a misclassification of seismic crack events, we defined a high true-positive rate of 0.9 by setting the prediction cutoff threshold accordingly (see Fig. A.2.7). In our case, all events were classified as crack events if the probability according to the prediction model was 17.2 % or higher. This, of course, lead to a moderately higher number of false-positives (15 %). The best performance was reached using all available features. Using only selected features did not improve the classifier (see the variable importance in the Fig. A.1.8).

Finally, we predicted the class of random 10 % (8,765) of the unclassified events using the classifier trained in the first step. We then manually corrected 1,428 false positives leading to the second larger training data set with 2,072 crack events and 8,037 others. Using this larger data set, we trained a refined Random Forest model following the same steps as described above leading to a smaller false-positive rate of 7 % (see Fig. A.1.9). The accuracy of the classifier is 94 % which is comparable to previous studies and in the range of human classifiers (Provost et al., 2017, Hibert et al., 2017, Wenner et al., 2021, Langet and Silverberg, 2023). With this refined model we classified all events leading to a dataset of 21,801 seismic crack events and 67,119 others.

Snowmelt modelling

We modelled the amount and timing of snowmelt by simulating the dynamic evolution of the snow cover using the one-dimensional open-source software SNOWPACK (Lehning et al., 1999). With meteorological measurements as inputs, SNOWPACK is capable of replicating snow microstructure, layering, and its interactions with the surrounding environment. The Bavarian Avalanche Warning Service provided input data, recorded at 10-minute intervals. This includes incoming and outgoing shortwave radiation, snow depth,

relative humidity, air temperature, total precipitation, snow surface temperature, and wind speed/direction. Simulations were conducted individually for Zugspitze and Nebellhorn and for each hydrological year from October 1 to September 31, using 15-minute time steps. The measured snow depth functioned as a proxy for precipitation inputs, influencing the mass balance. To address data gaps, the internal MeteoIO pre-processing library was employed. Where necessary, we included a constant ground temperature of 0°C and an albedo estimation from shortwave radiation.

The model parameters (see Section S3) were adjusted for each simulation to best fit the melting phase, although discrepancies between modelled and measured snow heights remained possible due to model limitations. The main output for this study was the quantity of snowmelt, expressed in kg/m², which represents the amount of liquid water flowing from the snow cover into the ground. As the Hochvogel is situated between Nebelhorn and Zugsitze (in position and altitude), we used the mean snowmelt of the two sites for further analysis, except for the melting season 2021, where Nebelhorn data were not available.

Synoptical time series analysis

To correlate deformation, rainfall, snowmelt, seismic and temperature data, we aggregated all data to hourly values and created common time series plots (Fig. 4.4 and 4.3). For better comparability we used derived rates for all variables except the temperature data set (e.g., deformation rate, rainfall intensity and snowmelt in mm/h, crack rate in events/h and temperature in °C). Due to the strong instrumental and diurnal noise in combination with partly very low signal rates, we smoothed all curves to uncover the measured process dynamics. We used smoothing window lengths with centered running means between 1.5 and 7 d depending on the SNR and the observed process (see captions of plots for individual values). Columns in each sub-plot represent 12 h non-smoothed means.

Based on an apparent correlation of variable pairs, we have identified three types of proxy behaviour: deformation during rain events, displacements in the snowmelt phase and thermally driven rock cracking. Within the complete time series, we identified 15 focus time periods highlighting the relationship of the particular variables. For each focus period we performed a detailed analysis (Fig. 4.5 to 4.10 and Fig. A.1.10 to A.1.18), including a time series plot of the two selected variables to illustrate their correlation (subplot a). Mathematically, we tested the correlation via a cross-correlation analysis of the two curves (subplot b). Here, we only considered positive time lags between the driver (e.g., rain) and the result (e.g., deformation). For the time lag with the highest correlation coefficient, we then created a scatterplot with accordingly shifted data and fitted a linear regression (subplot c).

To extend the analysis over the complete available time series, we additionally performed a running cross-correlation analysis. For two selected variables, we calculated the cross-correlation function on a subset of the data with window lengths between 20 and 60 d depending on the observed process. We iterated this by moving the analysis window in 1 d

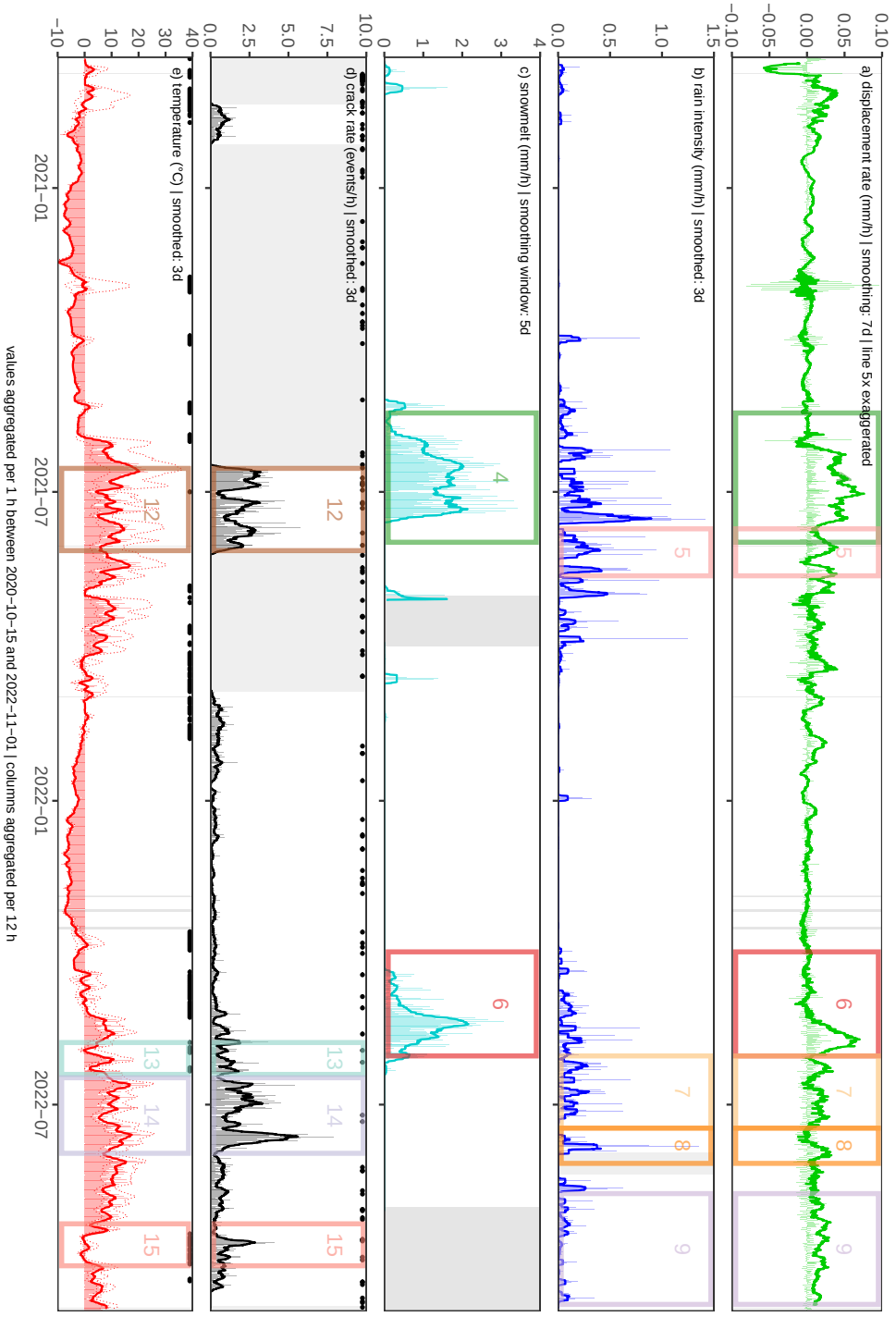

Figure 4.3: Analysed data between Oct 2020 and Nov 2022 with marked and numbered focus times (rectangles). Data are aggregated to 1 h resolution (see the degree of smoothing in the headers). Columns give 12 h means. (a) displacement rate (mm/h), (b) rain intensity (mm/h), (c) snowmelt (mm/h), (d) seismic crack rate (events/h), black dots mark the timing of earthquakes from the catalogue, (e) mean temperature (°C), dashed lines give min and max values, black dots mark days with freeze-thaw/ thaw-freeze conditions.

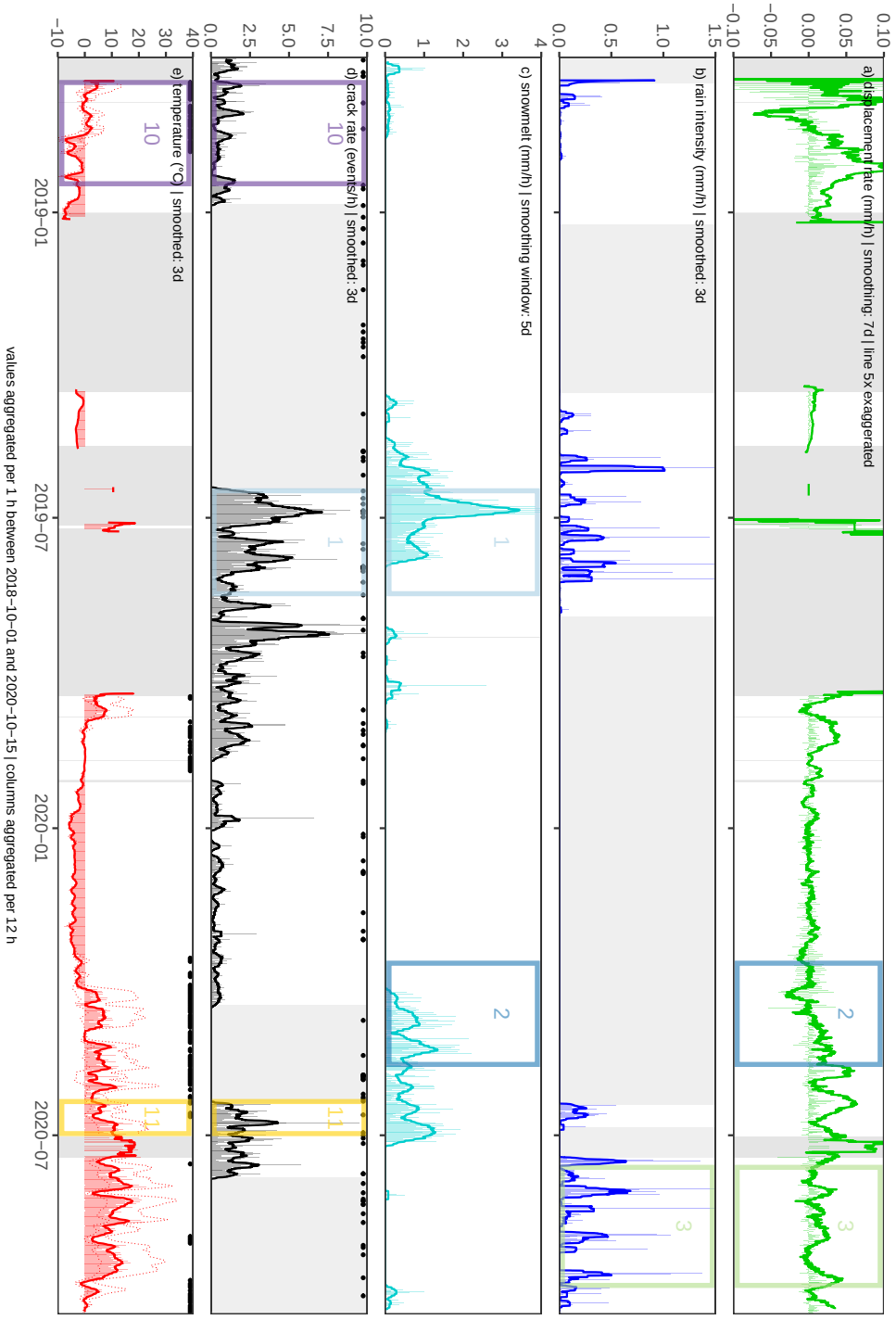

Figure 4.4: Analysed data between Oct 2018 and Oct 2020 with marked and numbered focus times (rectangles). Data are aggregated to 1 h resolution (see the degree of smoothing in the headers). Columns give 12 h means. (a) displacement rate (mm/h), (b) rain intensity (mm/h), (c) snowmelt (mm/h), (d) seismic crack rate (events/h), black dots mark the timing of earthquakes from the catalogue, (e) mean temperature (°C), dashed lines give min and max values, black dots mark days with freeze-thaw/ thaw-freeze conditions.

steps and plotted the correlation coefficient for several time lags against the time (Fig. A.1.19 to A.1.25).

Newmark displacement and topographic amplification

We calculated the theoretical Newmark displacement using a well-introduced regression model with the formula after Jibson (2007, Eq. 9):

$$log\ D_N = 2.401\ log\ I_a - 3.481\ log\ a_c - 3.230 \pm 0.656 \tag{4.1}$$

where D_N is the Newmark displacement in cm, I_a is the Arias Intensity in m/s and a_c is the critical acceleration in terms of g (the gravity constant). The critical acceleration a_c in m/s² depends on the factor of safety (FOS, ratio of resisting forces over driving forces) of the area of interest and the sliding plane's slope angle α in degrees (Newmark, 1965, Jibson, 1993):

$$a_c = (FOS - 1)\ sin\ \alpha \tag{4.2}$$

The Arias Intensity can be estimated after the formula (Wilson and Keefer, 1985, Jibson, 1993):

$$log\ I_a = M - 2\ log \sqrt[2]{D^2 + h^2} - 4.1 \tag{4.3}$$

where M is the earthquake magnitude, D is the epicenter distance in km and h is the focal depth in km.

The exact FOS at the Hochvogel instability can currently not be determined due to uncertainties in the location and condition of the sliding surface. Due to the ongoing mass movement over many decades (Leinauer et al., 2020), we assume only few remaining rock bridges in the carbonate mass and infer a FOS close to failure about 1.1 (Knapp et al., 2018, Heckmann et al., 2012). We further evaluated a variety of FOS values where a FOS of 1.05 represents conditions closer to failure, 1.2 less sensitive conditions and 1.01 a slope instability that is imminently failing. We calculated all theoretical Newmark displacements for the set of FOS between 1.01 and 1.2, slope angles between 25° and 85°, magnitudes up to M_w = 8, distances up to D = 150 km and a focal depth of h = 8 km (mean depth in the earthquake catalogue). We assume a conservative critical Newmark displacement of 2 cm above which rockslides can be triggered (Miles and Keefer, 2001, Meyenfeld, 2009). In a magnitude-distance plot, this critical displacement appears as line per FOS (for a fixed slope angle, Fig. 4.11 and Fig. A.1.26 to A.1.34). To asses the possible effect of typical earthquakes in the Hochvogel region, we filtered the BGR and SED catalogues for all events with epicenter distances of less than 150 km from the Hochvogel and plotted these into the magnitude-distance plot. More distant events are considered to have no major effect. The ten events with the biggest Newmark displacements have been assessed further including the uncertainty contained in formula (4.1) using their exact focal depth (Fig. A.1.35 to A.1.41).

To assess the effect of topographic amplification we use the peak ground velocity (PGV) measured by our seismometers after several earthquake events (see example record in Fig.

A.1.42). It is often complex to distinguish between topographic resonance effects and interacting localized site effects (Rault et al., 2020, Weber et al., 2022) but landslide appearance and rockfall volume correlate with high peak ground accelerations (Meunier et al., 2007, Massey et al., 2022). During earthquakes, the stability of slopes relies on the magnitude of ground motion and its frequency content (e.g. Jibson et al., 2000, Rault et al., 2020). We therefore look at PGV values as the phenomenologial result of seismic stimulation measured by our sensors. We compare the measured PGV during earthquakes at the summit station HV_1 with the stations HV_2, HV_3 and HV_5 at the flank lower in the valley and the station SA_{23} on the stable side of the summit. The station HV_4 had to be excluded due to the insufficient number of recorded earthquakes. We used all earthquake events from the BGR and SED catalogues that have been recorded on all three components (Z, N, E) of each particular station (Fig. A.1.27). For comparison of regional and distant earthquakes, we additionally used 18 events with a distance D > 15,000 km and magnitude M_w > 6 from the USGS catalogue. We then detected the PGV in the signal envelope in 1 Hz windows moved in 0.25 Hz steps between 0.5 and 10 Hz for all components, stations and earthquake events. The ratio of the PGV at station HV_1 against the other stations (site-to-reference ratio) is used as indicator of amplifying effects.

4.1.5 Results and discussion

Rainfall induced displacement

During the warm summer months after snowmelt (May or June to October) the rock mass shows accelerated movement in connection with strong precipitation events. During this period, 38 % of the total crack opening happens during wet days although these only account for 26 % of the total time. The average displacement rate is 1.8 times higher during wet periods compared to periods without precipitation. Looking at peak velocities, this effect reaches a factor of 4-5.

The direct comparison of rainfall intensity and displacement rates during the selected focus times reveals a high correlation with a time lag of 1-16 h (Fig. 4.5 and 4.6, and Fig. A.1.10 and A.1.12). Without superposition with other effects like snowmelt, this behaviour can be observed in more than 20 rainfall events across the four summers. The lag likely accounts for the rainfall infiltration time and until maximum hydrostatic pressure is built in the discontinuities within the rock mass. Both depend on pre-event saturation as we cannot observe a consistent change in lag time throughout each season. In addition, the saturation of the discontinuity with water might eliminate the joint cohesion in some discontinuities, lower the joint friction angle especially in the basal marl layers and reduce the effective normal stress at the sliding surface due to buoyancy (Erismann and Abele, 2001), leading to increased displacement rates.

We cannot identify an activation threshold, meaning that even small rainfalls can accelerate the mass movement (see focus time 9, Fig. A.1.12). Within dry periods, timely well-constrained intense rainfall events with several mm/h accelerate the mass up to 1 mm/d

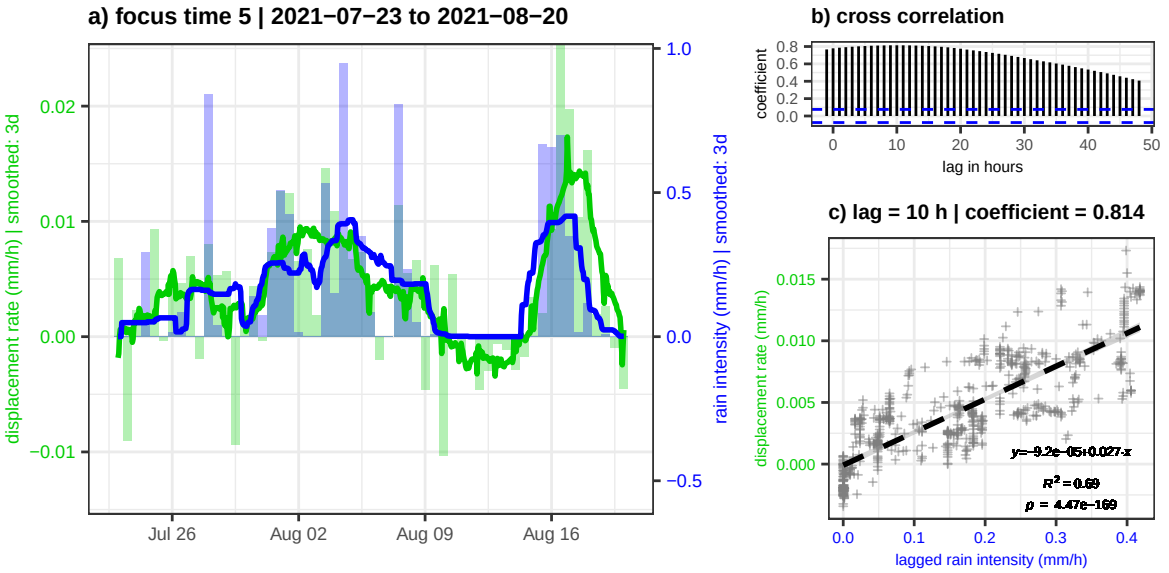

Figure 4.5: Detail plot of focus time 5. (a) displacement rate and rain intensity (lines 3 d smoothed, columns 12 h means). (b) cross-correlation coefficient of the two lines. The highest correlation appears with a lag of 10 h and a coefficient of 0.814. (c) scatter plot with linear trendline with 10 h shifted data.

(cp. August 16 in Fig. 4.5). When the water input decreases at the end of the rain event the unstable mass decelerates. There is no permanent sealing of discontinuities and perched water drains within several hours. On the other hand, rain events that happen close together within few days result in a common velocity peak due to the retention of water in the system (cp. focus time 8 in Fig. A.1.11). This proposes an immediate lowering of water saturation at least in the fractures in case of dry conditions but also that a proportion of the infiltrated water stays in the system for several days. This can precondition the system in case of further water infiltration, as partially to fully saturated conditions promote the build-up of hydrostatic pressure. Similar observations are reported by Helmstetter and Garambois (2010), who found no minimum rain threshold for rockfall triggering, time lags of up to 1 h for rockfalls and a few days for displacement rates at the Séchilienne rockslide in the French Alps. However, there, accelerated movements last for about a month which might be connected to the bigger size and deeper-seated sliding zone compared to the Hochvogel (50-100 million m³ vs. 200-400 thousand m³).

At the Hochvogel, we infer from the linear regression between rain and displacement that in general rain intensities of 0.3-0.6 mm/h trigger displacement rates of ca. 0.01 mm/h. The running cross-correlation (Fig. A.1.20) gives high correlation coefficients of >0.75 with small lag times each summer after snowmelt. This supports the interpretation of a rainfall controlled regime during the snow-free summers. However, the correlation coefficient fluctuates due to the short duration of rain events. The generally strong and immediate response of the rock slope to rain events is indicative of existing substantial damage and a high criticality of the slope (Gischig et al., 2016).

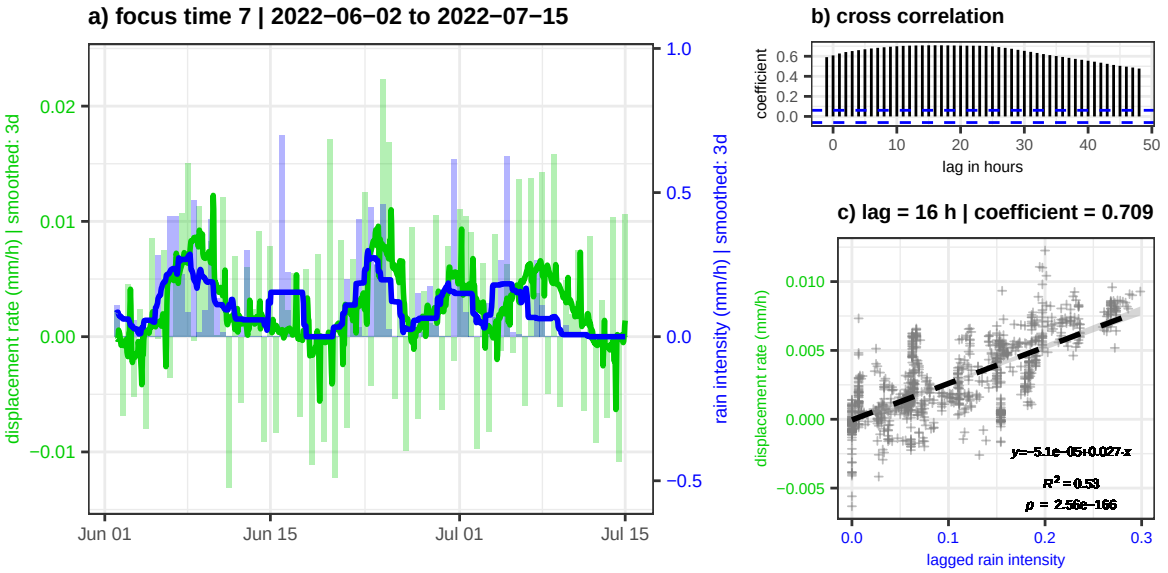

Figure 4.6: Detail plot of focus time 7. (a) displacement rate and rain intensity (lines 3 d smoothed, columns 12 h means). (b) cross-correlation coefficient of the two lines. The highest correlation appears with a lag of 16 h and a coefficient of 0.709. (c) scatter plot with linear trendline with 16 h shifted data.

Snowmelt induced displacement

Snowmelt usually occurs between April and July and contributes significant amounts of water to the system, causing accelerated slope movements (Fig. 4.7 and 4.8, and Fig. A.1.14). While melt water generally affects slope dynamics the same way as described above, our cross-correlation analysis suggests longer lag times, between 4 and 9 days. This is likely related to the slower but therefore more continuous supply of water into the rock mass. Moreover, as there is no snow station directly at Hochvogel, the snowmelt amount is modelled based on measurement data from neighbouring peaks, Nebelhorn and Zugspitze. Given that the south-oriented slopes of the outstanding Hochvogel peak become snow-free quite early, while significant amounts of snow remain in the >10 m deep main fracture much longer, we anticipate differences in the snowmelt characteristics.

The intensity of the modelled snowmelt generally surpasses the measured rain from the summit, potentially not reflecting the accurate volume of snowmelt infiltrating into the discontinuities at Hochvogel. However, our analysis indicates that, on average, modelled snowmelt of about 1.5 mm/h corresponds to displacement rates of ca. 0.01 mm/h. Secondary peaks with higher snowmelt rates inducing temporary accelerations are visible in the velocity curve too (e.g., July 2-15 in Fig. 4.7 and May 20 in Fig. 4.8). During early summer, intense rainfall from the first thunderstorm cells superimpose with the late snowmelting phase, making it challenging to distinguish the driving processes effectively during this period. However, rain falling on snow can result in higher water infiltration than from the rainfall alone (Stock et al., 2013).

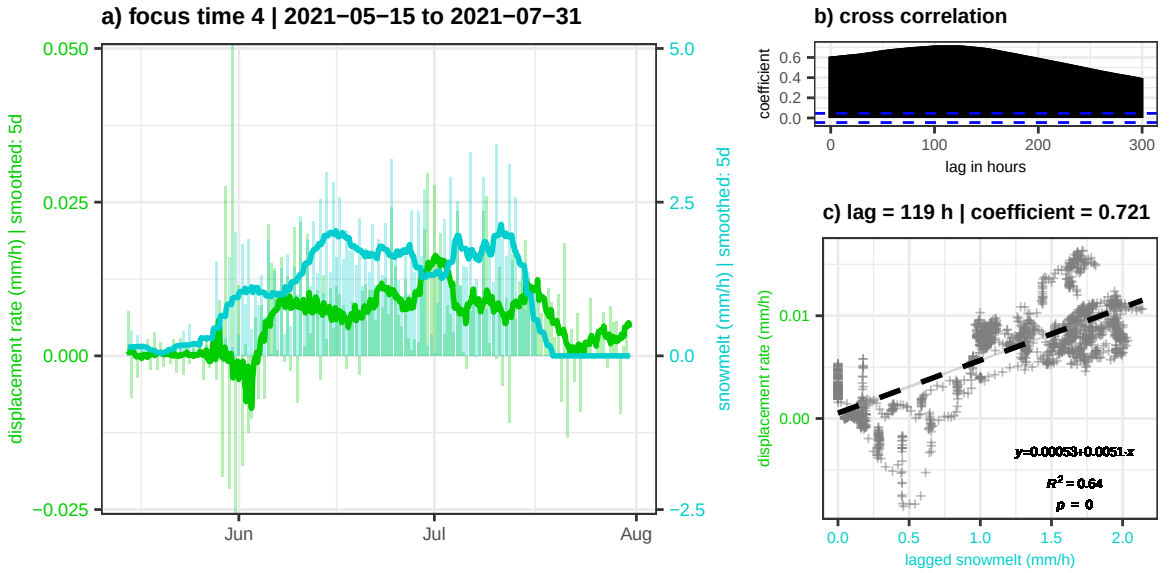

Figure 4.7: Detail plot of focus time 4. (a) displacement rate and snowmelt (lines 5 d smoothed, columns 12 h means). (b) cross-correlation coefficient of the two lines. The highest correlation appears with a lag of 5 d and a coefficient of 0.721. (c) scatter plot with linear trendline with 119 h shifted data.

The running cross-correlation (Fig. A.1.21) gives correlation coefficients above 0.75 with lag times of 4-9 d each year during snowmelt. This supports our interpretation of a meltwater-controlled regime during the snowmelt season. The snowmelt correlation coefficient fluctuates less than with the rain data, as the snowmelt appears more continuous than the distinct short rain events.

Seismic crack events

The summit network recorded 21,801 discrete events that fall into the class of rock cracking. Their duration was $1.4^{+0.5}_{-0.4}$ s (median and quartile range), preferentially occurring during daytime, matching the conclusions of Dietze et al. (2021). On annual scale, the crack rate is higher during the summer months coinciding with higher displacement rates, higher rain fall intensities and higher temperatures (Fig. A.1.6). We therefore analysed if rock cracking rates and displacement rates interact directly, or if the correlation is rather indirect meaning that environmental forcing increases both, crack rates and slope movement.

We could not find specific time periods where the smoothed crack rate correlates well with the smoothed displacement rate (Fig. 4.3 and 4.4). Likewise, the running cross-correlation analysis (Fig. A.1.19) did not reveal stable high correlation coefficients with a specific time lag. This implicates that there is no obvious correlation between crack rate and displacement rate.

The same applies for the correlation between crack rate and rain fall intensity (Fig. A.1.23). In the melting period 2019 (focus time 1, Fig. A.1.13), we found a high correlation between

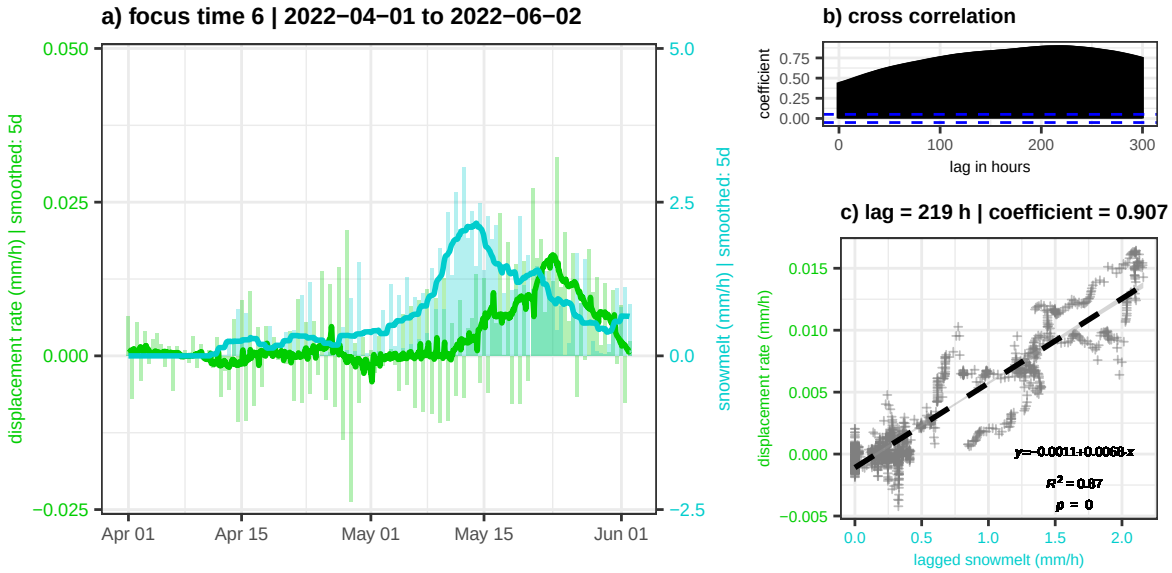

Figure 4.8: Detail plot of focus time 6. (a) displacement rate and snowmelt (lines 5 d smoothed, columns 12 h means). (b) cross-correlation coefficient of the two lines. The highest correlation appears with a lag of 9 d and a coefficient of 0.907. (c) scatter plot with linear trendline with 219 h shifted data.

7 d-smoothed snowmelt and crack rate at a time lag of 40 h. However, this relation did not emerge in other years and it remains unclear if strong snowmelt can induce enhanced rock cracking.

In contrast, we found the crack rate peaking during temperature peaks (c.p. Fig. 4.9 and Fig. A.1.15 and A.1.16), likely related to thermal forcing through volumetric expansion and contraction of the rock mass and its minerals. Even small oscillations are represented in both curves. The maximum correlation coefficient appears with a time lag of 0-15 h. Additionally, we observed peaks of rock cracking activity during days with freeze-thaw and/or thaw-freeze conditions (Fig. 4.10 and Fig. A.1.17 and A.1.18). Furthermore, the first deep frost of the season without thawing conditions seems to enhance the crack event rate for 4-5 d (e.g., November 16 and December 11 in 2018, Fig. A.1.17). Here, stress is caused by cryogenic processes in ice-filled fractures or pores, volumetric expansion/ contraction and/or ice segregation (Weber et al., 2017).

Heat conduction in rock is relatively slow in the range of 1 cm/h (Weber et al., 2017, Mulas et al., 2020). The fast reaction of rock cracking activity towards air temperature changes in turn means that most of the crack events that we detected happened close to the surface. This is in line with the results of Dietze et al. (2021). The thermally induced stress can only affect surface-near rock mass (Bakun-Mazor et al., 2013) unless advective heat transport by percolating water or air can act in fractures (Blikra and Christiansen, 2014, Weber et al., 2017). The shallowness of the detected fracturing events can explain why there is no obvious correlation between crack and displacement rates. Displacements can only result from cracking if rock bridges fail at the sliding plane which we expect to be >10 m away from

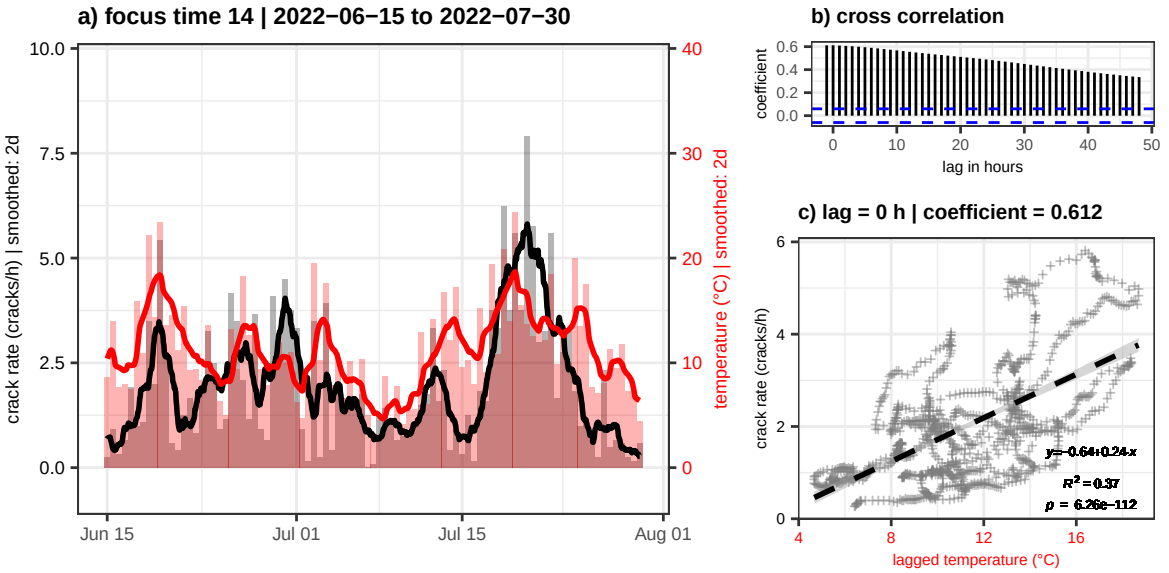

Figure 4.9: Detail plot of focus time 14. (a) crack rate and mean temperature (lines 2 d smoothed, columns 12 h means). (b) cross-correlation coefficient of the two lines. The highest correlation appears without any lag and a coefficient of 0.612. (c) scatter plot with linear trendline with data not shifted (0 h).

the rock surface. We assume, that we also detected rock fracturing originating from the sliding plane but the frequency of those events is obscured by the dominant surface-near crack events. Lagarde et al. (2023) state that crack signals might not always be intense enough to distinguish them from other ambient seismic noise. However, this likely changes when the instability develops closer to failure and the rock fracturing frequency and intensity at the active sliding surface increases. More pronounced rock deformation in the final stage of failure will concurrently intensify the shallow cracking activity. As this activity is then less dependent on temperature changes, it might still be possible to detect a precursory change in activity. On the other hand, crack rates could be altered imminently before failure, when no rock bridges are left (Lagarde et al., 2023), yet it remains unclear if this can be observed at a multi-block rockslide with the size of the Hochvogel.

The effect of earthquakes and topographic amplification

The analysis of the earthquake catalogue yielded coincidence of a major earthquake with a major rockfall at the Hochvogel in one case only, on June 30, 1935, three days after a M 5.2 earthquake in Bad Saulgau in a distance of 103 km (Hutter, 2010). Potentially, several historical rockfalls at the Hochvogel might not be documented. An event-specific analysis is therefore not productive and thus we included the whole available earthquake database into our analysis (Fig. A.1.26). It shows that a low-energy background activity is present, mainly originating in the tectonically active alpine valleys, but close high-magnitude events are rare (only 2 events > M_w 5.5 since 1900). This frequent seismic activity could contribute

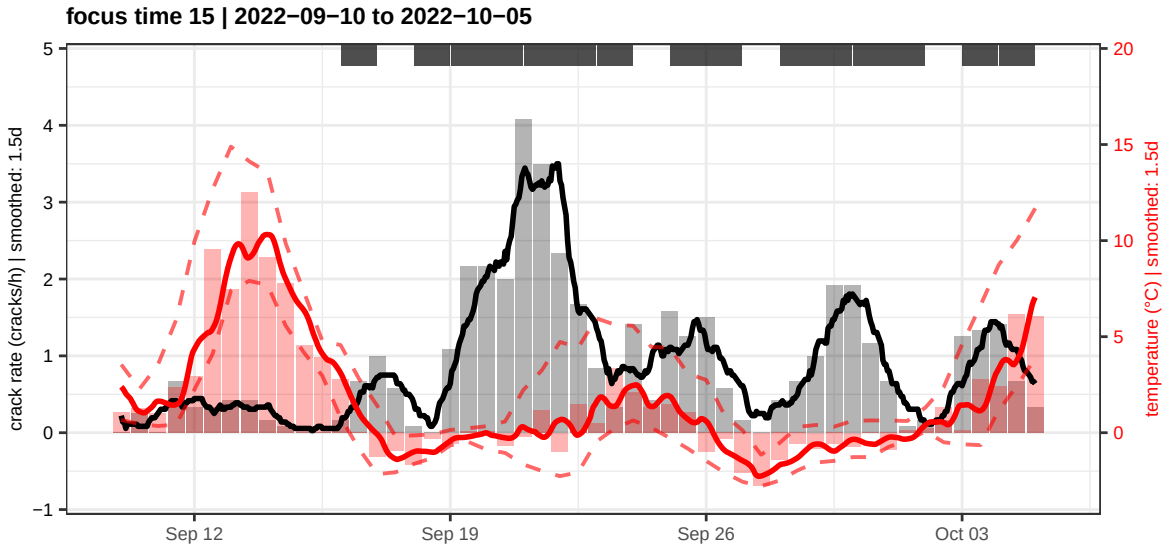

Figure 4.10: Detail plot of focus time 15. Crack rate, mean temperature (solid line), minimum and maximum temperature (dashed lines, all lines 1.5 d smoothed, columns 12 h means). Peaks in the crack rate coincide with days with freeze-thaw or thaw-freeze conditions (black bars on top). The cross-correlation is not shown due to the missing correlation of both curves.

to a low-level promotion of slope instabilities through seismic fatigue. Gischig et al. (2016) could show that earthquake-induced displacements can vary by more than two orders of magnitude depending on pre-existing damage. However, they used a model with several events with magnitudes >M_w 5.7 and shorter distance. For the Hochvogel, a direct comparison of earthquake timings (black dots in Fig. 4.4d and 4.3d) with crack or deformation rates did not show obvious significant influence.

To evaluate the potential of earthquakes in the Hochvogel region to immediately trigger a major rockfall event, we conducted the Newmark analysis. The calculation of all theoretical Newmark displacements in the magnitude-distance plot (Fig. 4.11) illustrates how strong an earthquake must be at what distance to have the potential to trigger a rockslide. From the >5,000 historical earthquakes in the database, only very few events are in the range of having triggering potential for very low FOS <1.03. A further analysis of the ten events from the catalogue with the biggest Newmark displacements including the uncertainty contained in formula (4.1) confirms this implication (Fig. A.1.35 to A.1.41). Thus, typical earthquakes around the Hochvogel (e.g. M_w 5 in 20 km distance or M_w 6 in 100 km distance) might only be able to trigger a major rockfall, if the unstable mass is anyways very close to failure (FOS around 1.01). As we interpret the current FOS to be between 1.05 and 1.1, only an exceptionally strong earthquake (e.g. M_w 6 in 15 km distance or M_w 7 in 50 km distance) could immediately trigger a major failure. Recurrence intervals for such events in this area are estimated to vary between 1,000 and 2,000 years (Oswald et al., 2022). The previously identified 1935 Bad Saulgau event was too weak to have a clear triggering potential. The biggest, but still very moderate displacement is indicated by the historic 1930 Namlos earth-

quake (M_w 5.3-5.5, 20 km distance). This event induced enhanced mass wasting processes recorded in local lakes (Oswald et al., 2022), but did not trigger any high-magnitude slope failures (Oswald et al., 2021).

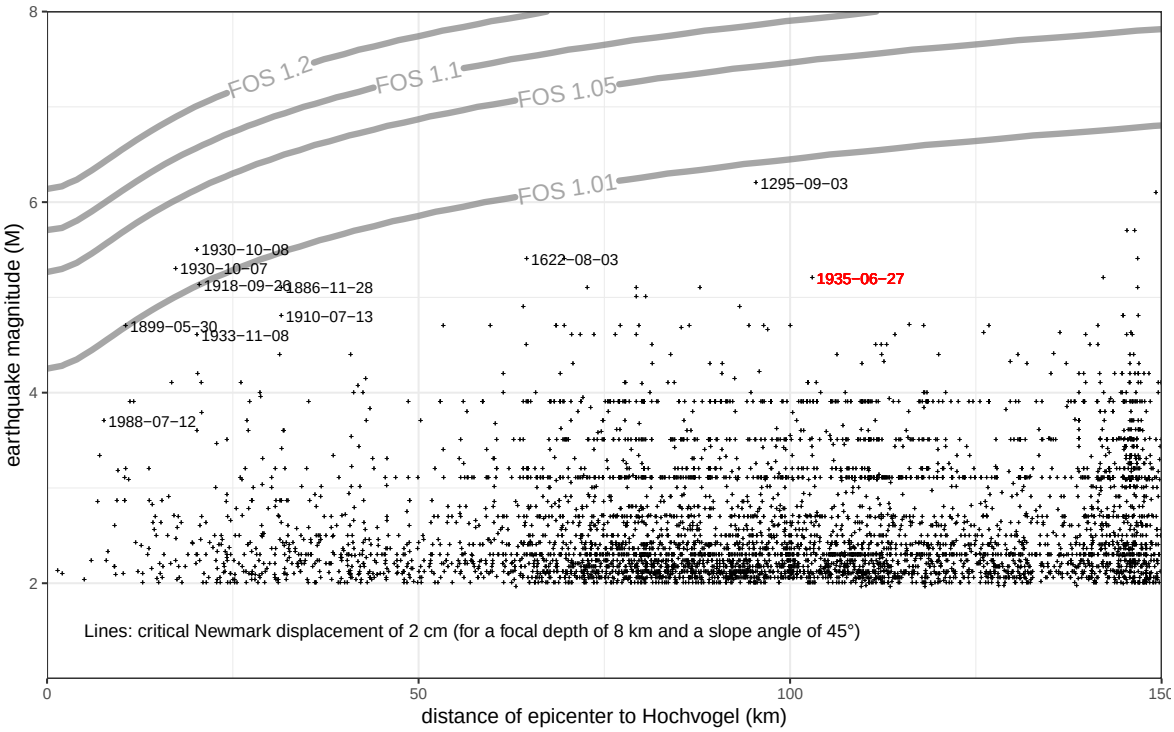

Figure 4.11: Lines indicate for different factors of safety, at which magnitude and distance of an earthquake a theoretical Newmark displacement of 2 cm is expected. This calculation is based on the mean focal depth of 8 km and the mean slope angle of the Hochvogel SW flank (45°). All earthquakes from the catalogues are plotted with black crosses. The earthquakes with the 10 biggest Newmark displacements are labelled in black with their dates. The Bad Saulgau 1935 event is labelled in red. Plots for all other slope angles are in the Supplementary Material.

The evaluation of low earthquake triggering potential holds, although we used a conservative threshold for the critical Newmark displacement of 2 cm. Other studies suggested even higher thresholds between 2-15 cm (Wilson and Keefer, 1985, Jibson et al., 2000, Miles and Keefer, 2001, Meyenfeld, 2009). Additionally, we checked the regression estimate of the Arias intensity with earthquake signals that could be recorded with our local stations. In theses cases, the formula (4.3) after Wilson and Keefer (1985) overestimates the Arias intensity about 1-2 magnitudes compared to the direct determination after Arias (1970) with the measured ground motion values from our stations. But still, the calculated Newmark displacements are below the threshold.

However, this evaluation could change under the influence of topographic amplification. The geomorphological shape of the Hochvogel massif as well as the location of the unstable mass at the ridge generally favour the effect of topographic amplification (Meunier et al., 2008, Lee et al., 2009a, Khan et al., 2020, Rault et al., 2020). A comparison of the measured

peak ground velocity (PGV) during earthquakes at the summit station HV_1 against the lower stations shows up to 11 times higher median PGVs at the summit (mean = 3.2, Fig. 4.12). The extent of this effect varies between the horizontal (E_{mean} = 4.5, N_{mean} = 3.4) and vertical components (Z_{mean} = 1.7), which is typical for topographic amplification (e.g. Bakun-Mazor et al., 2013, Burjánek et al., 2012, Weber et al., 2022), but it remains consistent across the various stations at the valley flank. The horizontal components show the first low-frequency amplification factor peak between 1.5-3 Hz, which is probably around the fundamental resonance frequency of the Hochvogel mountain. Weber et al. (2022) determined a fundamental frequency of 1.8 Hz for the Grosser Mythen, a mountain of comparable shape and similar scale. The amplification effect at the Hochvogel is least pronounced when referencing to the highest valley station HV_5 (1933 m) that is situated on a ridge (mean of E-component medians: HV_2 = 4.5, HV_3 = 4.2, HV_5 = 3.8). This is in line with the results of Weber et al. (2022) who measured a mean amplification factor of 9 at the Matterhorn summit and 5 at a ridge below. In general, there is no major difference in median PGV ratios between the local and the far earthquakes. A directional analysis of earthquake epicenters is yet not meaningful due to the limited number of recorded earthquakes.

This could indicate that the summit experiences a significant amplification of factor 2-11 due to topographic site effects and resonant amplification. Then, true displacements due to earthquakes are higher than predicted by the theoretical Newmark displacement analysis and thus the triggering potential is higher than previously assumed. Likewise, the importance of seismic fatigue as a promoting driver is increased by topographic amplification. However, PGV ratios are >1 at station SA_{23} too, which is very close to HV_1 but on the stable side of the summit. The general theory would expect a similar amplification at the two summit stations and thus a ratio close to 1. In the low frequencies <4 Hz, there is no amplification peak at station SA_{23}, other than at the other stations further down the valley flank. This could be a result of similar site effects at the two summit stations, but still, higher PGVs have been recorded at the HV_1 station. This might be due to an amplification and polarization within unstable rock mass itself due to the open main and lateral cracks (Gischig et al., 2016). Burjánek et al. (2010, 2012) measured similar amplification factors with strong variations on the slope scale on two slope instabilities. It is possible that the unstable mass of the rock slope instability close to the wide open and deep main fracture reacts stronger to ground motions than the intact bedrock on the stable side of the summit. As we set up all stations the same way, we assume that all stations have a comparable coupling to the ground. Hence, any differences are supposed to be due to different material properties below the stations, e.g. a massive rock block at the summit and a weathered layer further down the flank. However, large amplification factors and a strong spatial heterogeneity across the rock slope may indicate a high criticality of the slope (Gischig et al., 2016). If the seismic amplification and its heterogeneity increases in future monitoring, it could be used as a precursory sign for imminent failure.

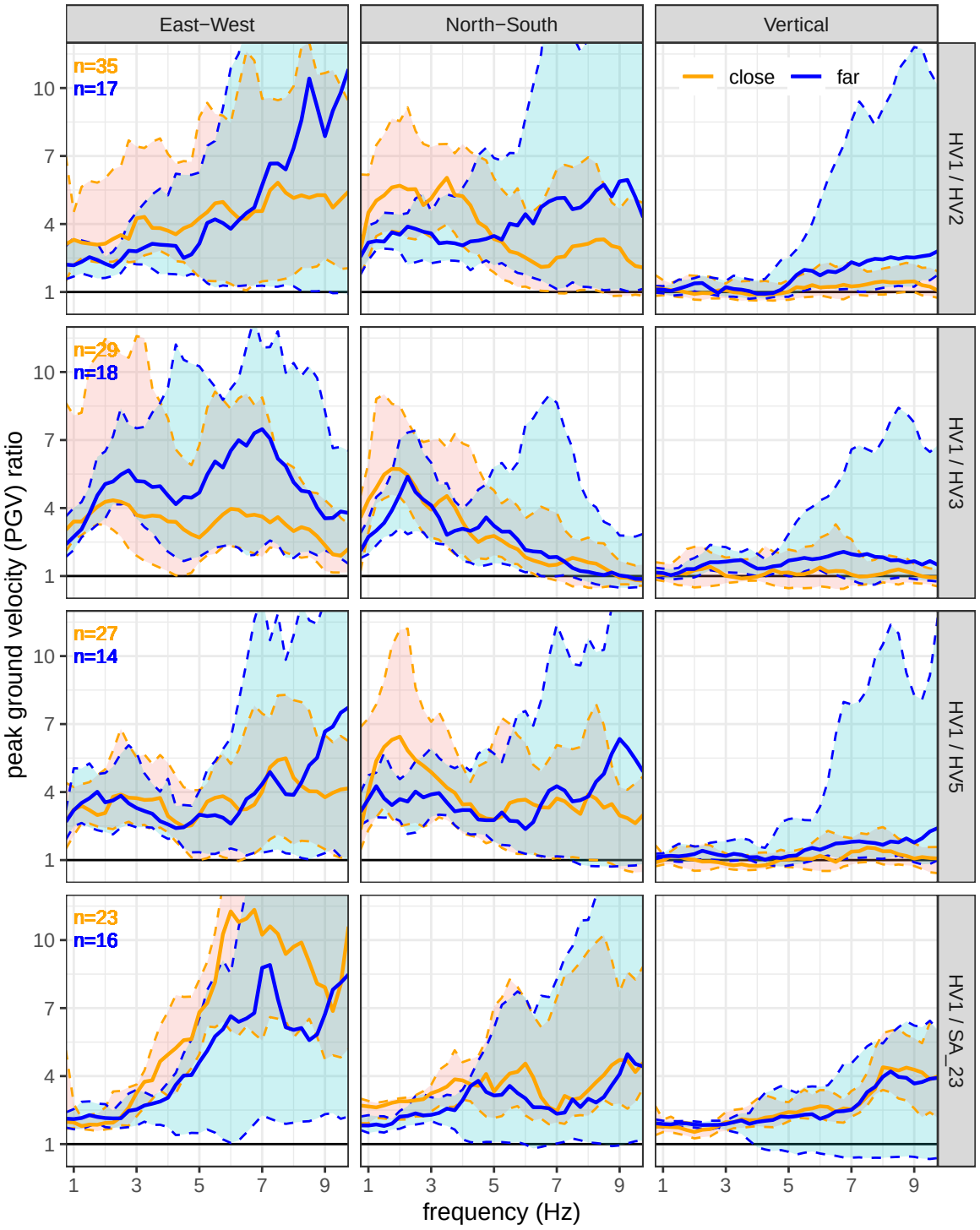

Figure 4.12: Ratio of measured peak ground velocity (PGV) of HV_1 on the unstable side at the summit against other stations for close (<150 km, orange) and far (>15,000 km and M>6, blue) earthquakes. The solid line marks the median and the dashed lines the 10th and 90th percentiles. HV_2, HV_3 and HV_5 are located further down the flank, SA_{23} is located on the stable side of the summit.

4.1.6 Conclusions

We processed more than four years of high-resolution monitoring data from a very active alpine rock slope instability including displacement, rain, snowmelt, temperature and seismsic observations to quantify the main drivers and their triggering potential. This methodological procedure can be transferred to similar cases. At the Hochvogel, the acceleration of the unstable mass even due to small environmental impacts proves a highly sensitive close-to-failure status, at least for parts of the summit.

1. During the *snowmelt phase in spring*, displacements are controlled by meltwater infiltration. The cross-correlation analysis indicates a time lag of 4-9 days between snowmelt input and landslide velocity.
2. During the *snow-free summer*, rainfall controls displacement rates with a time lag of 1-16 h, indicating the possibility of fast hydrostatic pressure increase in the system. Even small rainfalls can accelerate the mass and previous water infiltration preconditions the system in case of consecutive rain events for few days. The rock cracking frequency is mainly controlled by high temperature with a time lag of 0-15 h indicating that we mostly detected surface-near crack events.
3. During the *first frost of the season in autumn*, days with freeze-thaw cycles or clear negative temperatures show higher crack rates. The crack rate might secondarily be controlled by snowmelt or rainfall with low correlation, but it seems not to correlate with displacement directly.
4. During *frozen conditions in winter*, the landslide activity is generally low.

According to our Newmark analysis, recent and historic earthquakes are too weak to have an immediate triggering potential for a major failure at the Hochvogel, unless the FOS is already very close to 1. Seismic topographic amplification of the peak ground velocity of factor 2-11 in the low frequencies is likely and the spatial and frequency-wise heterogeneity of amplification at the summit suggests a high damage and criticality of the slope. In summary, we identified water from rain and snowmelt to be the main driving factor. Future increases of rock mass displacements following small environmental impacts as well as changes in the seismic response to earthquakes can express a development towards higher criticality. In the light of ongoing climatic changes that lead to more frequent and intense heavy precipitation events and faster snowmelt, our findings suggest that the Hochvogel and similar unstable alpine rock slopes may experience stronger environmental forcing in the future.

4.1.7 Code and data availability

All R-Codes for analysis of the data are available in an online repository together with displacement, temperature and rainfall data from the summit, modelled snowmelt and derived seismic crack event statistics under `https://doi.org/10.5281/zenodo.10567098` (Leinauer, 2024). Snow station data can be obtained from the Bavarian Avalanche Warning Service (Lawinenwarnzentrale im Bayerischen Landesamt für Umwelt). Earthquake catalogues can

be accessed via https://services.bgr.de/geophysik/gerseis and http://www.seismo.ethz.ch/en/research-and-teaching/products-software/earthquake-catalogues/ and https://earthquake.usgs.gov/earthquakes/search/. Seismic raw data sum up to 1.09 TB and are available from the authors upon request.

4.1.8 Author contribution

JL wrote the manuscript, designed the figures, supervised the real-time monitoring and performed the synoptical data analysis. MD designed and performed the seismic monitoring. JL and MD analysed the seismic data. JL and SK did the earthquake analysis. RS did the snowmelt modelling. JL and MJ performed the rainfall and snowmelt event analysis. MK and MD supervised the study. All authors improved the final version of the manuscript.

4.1.9 Competing interests

At least one of the (co-)authors is a member of the editorial board of Earth Surface Dynamics. The authors have no other competing interests to declare.

4.1.10 Acknowledgements

This study was developed within the AlpSenseRely project which is funded by the Bavarian State Ministry of the Environment and Consumer Protection (TUS01UFS-76976). We thank all numerous colleagues and friends that helped with field work and technical support during the last 5 years and the Bavarian Avalanche Warning Service for providing original snow station data.

4.2 Detailed analysis of a block failure in October 2022 (Update 2)

This section is an update to Paper ② in Section 4.1.

4.2.1 Event detection with deformation camera and seismic sensors

Six days after the latest available seismic data for the previous Section 4.1, we detected a rockfall event that detached from the steep SW-wall below the summit. The event was marked by an area with coherence loss in the automatic deformation analysis (see Fig. 3.11b). From the photos we could constrain the timing of the event to be between 2022-10-25 18:00 and 2022-10-26 08:00 local time and estimated a failure volume of few hundred m^3. Using only one camera inhibits a classical photogrammetric point cloud reconstruction and thus, volumes could not be determined with the deformation camera.

However, the seismic data from the local network (cp. Fig. 4.2) that could be retrieved from the stations later, allow an advanced analysis of the event in terms of timing and volume estimation. The local seismic record shows two distinct high-energy events in the evening of October 25, 2022 with an offset of ca. 10 min (Fig. 4.13). The first sub-event contains less energy and could not be detected at the closest earthquake observatory station in Oberstdorf ca. 11.8 km away (Fig. 4.14). The second sub-event contains more energy and is even present in the Oberstdorf record with a time lag of ca. 6 s (Fig. 4.15).

To assure that the identified seismic events originate from the rockfall event that has been detected with the deformation camera, their source location can be estimated. This is done with the *spatial_migrate* function of the *eseis*-package (Dietze, 2018a,b). This function performs a signal migration in space using a topography-corrected distance raster and the lag between the seismic signals. The most likely source location of the two sub-events is plotted in Fig. 4.16 for a mean wave velocity of 950 m/s. The source location cluster in the middle of the network on the summit can be excluded. The second cluster lies outside the network in the steep SW-wall near and below the true detachment zone (marked by the black cross) and thus fits the impact area of the analysed block fall. This localization is sensitive to the set wave velocity. However, source locations are reasonable for mean velocities of 600-1100 m/s, which is within the typical range for fractured carbonate rock (Helmstetter and Garambois, 2010, Dietze et al., 2017a, 2021). Thus, it can be assumed that the seismic energy of the two detected events originates from the analysed block fall.

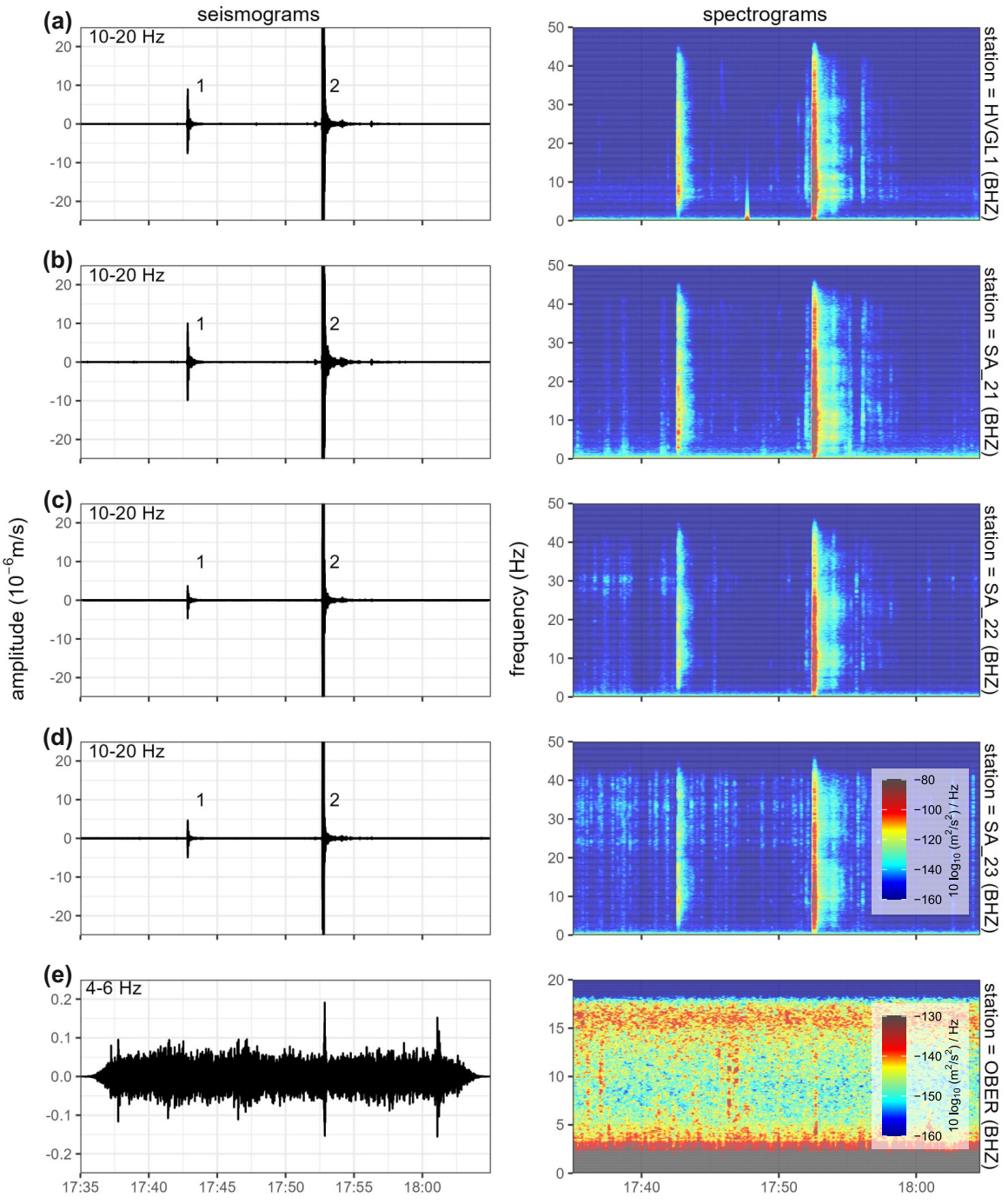

Figure 4.13: Seismograms and spectrograms of the four local summit stations (a-d) and the earthquake observatory station in Oberstdorf (OBER, e) from October 25, 2022. Time is in UTC. Note the different frequency band and spectral color scaling at station OBER.

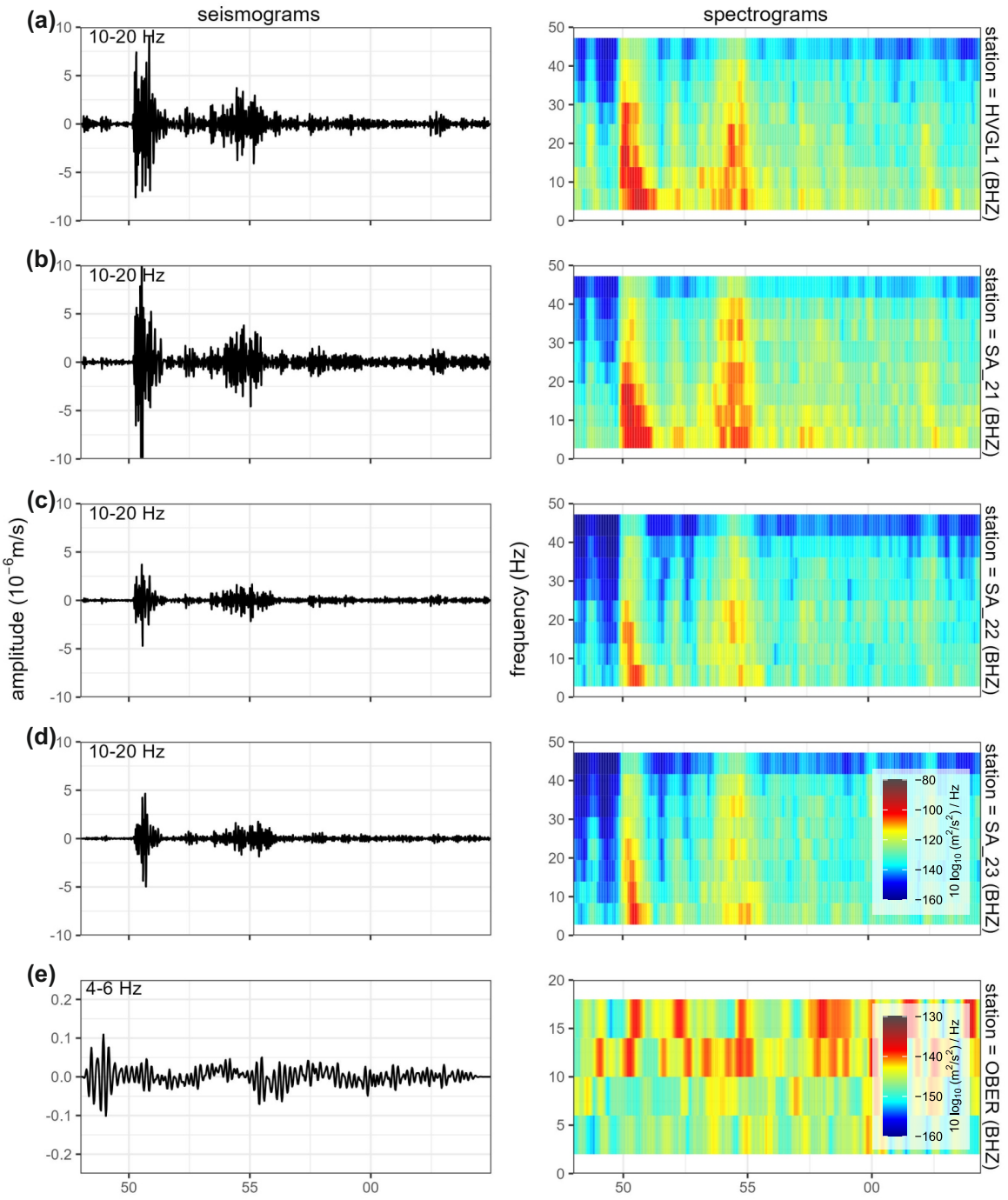

Figure 4.14: Detailed seismograms and spectrograms of the four local summit stations (a-d) and the earthquake observatory station in Oberstdorf (OBER, e) for the smaller sub-event 1 (17:42:48-17:43:05 UTC). This sub-event is not detected at station OBER. Note the different frequency band and spectral color scaling at station OBER.

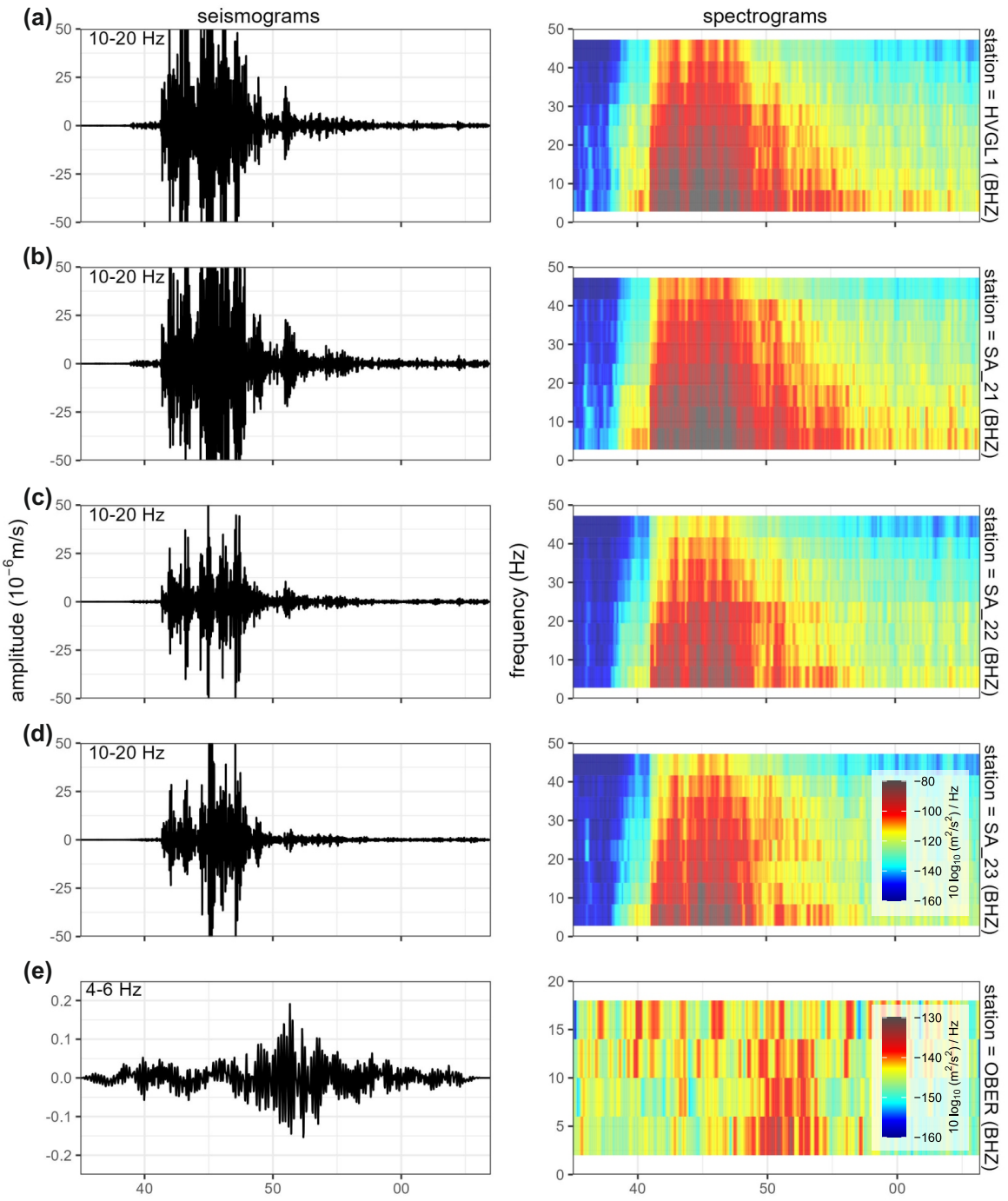

Figure 4.15: Detailed seismograms and spectrograms of the four local summit stations (a-d) and the earthquake observatory station in Oberstdorf (OBER, e) for the bigger sub-event 2 (17:52:35-17:53:07 UTC). This sub-event has been detected at station OBER. Note the different frequency band and spectral color scaling at station OBER.

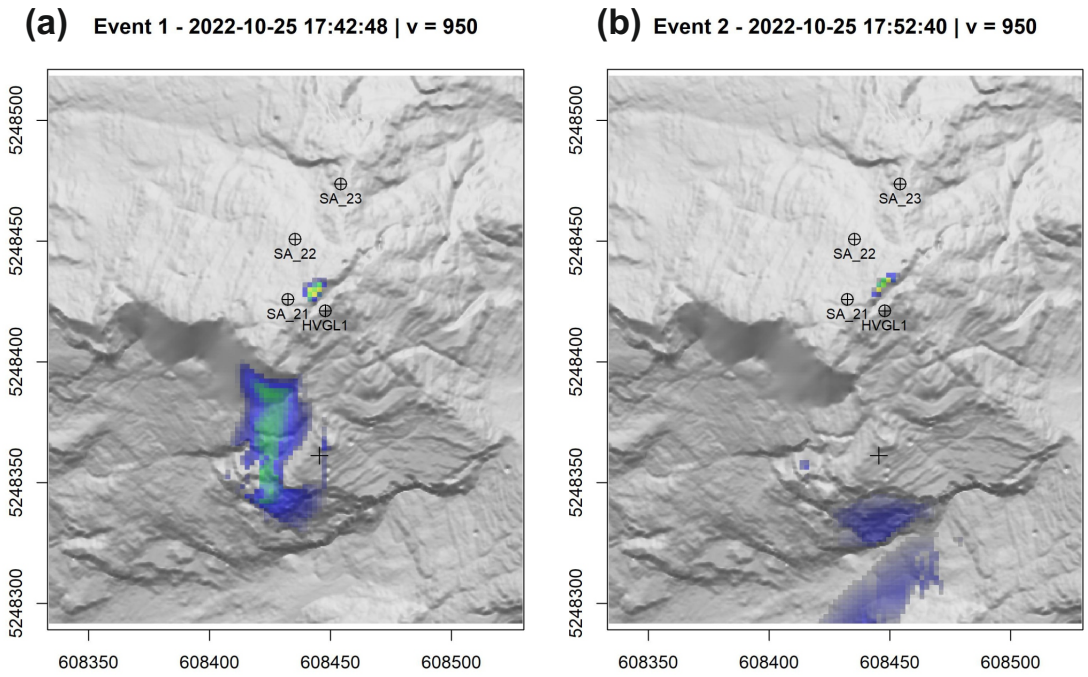

Figure 4.16: Most likely source location for the seismic signals of (a) sub-event 1 and (b) sub-event 2 determined by signal migration in space with a seismic velocity of 950 m/s. The black cross marks the location of the block detachment area determined with the deformation camera.

4.2.2 Volume estimation via seismic energy

Following the methodology described in Le Roy et al. (2019), the volume of a rockfall event can be estimated by using a relation between the seismic energy caused by the event and the initial potential energy of the failed block. The detailed procedure for the determination of the input parameters at the Hochvogel is described in Barbosa et al. (2024) (supplementary material). For the earthquake observatory station in Oberstdorf (OBER), all parameters except the fall height remain the same. For the four local stations, the parameters are set following the same procedure, except for the attenuation factor. The local attenuation factor cannot be determined if the seismic waves mainly travel outside the network, as it is the case here. Therefor, an attenuation factor of $8.8 \times 10^{-4} \pm 0.9 \times 10^{-4}\ m^{-1}$ as determined by Le Roy et al. (2019) for their network in limestone and marl is used. The potential fall trajectory of the block suggest a likely first impact on very steep terrain after 20 m, but the main impact was likely 100 m below the detachment area on flat rock surface. The fall height is therefor set to 100 m. For the estimation of the final calculated volume error, a Monte-Carlo simulation with 1000 iterations is used, where all parameters are sampled within the given range.

The median volume of all Monte-Carlo iterations and all four local seismic stations is estimated to be 2,566 m³ with a standard deviation of 665 m³ and an interquartile range (IQR)

of 919 m³ (Fig. 4.17). This is slightly higher than the previously assumed few hundred m³, but given the relatively high uncertainty, volumes are still in a realistic range. The fraction of the first sub-event is only 2 % of the total failed volume, meaning that the main failure happened during sub-event 2. This is similar to the 130,000 m³ failure of 2016, where the biggest part of the volume detached in the last of the six sub-events (Barbosa et al., 2024).

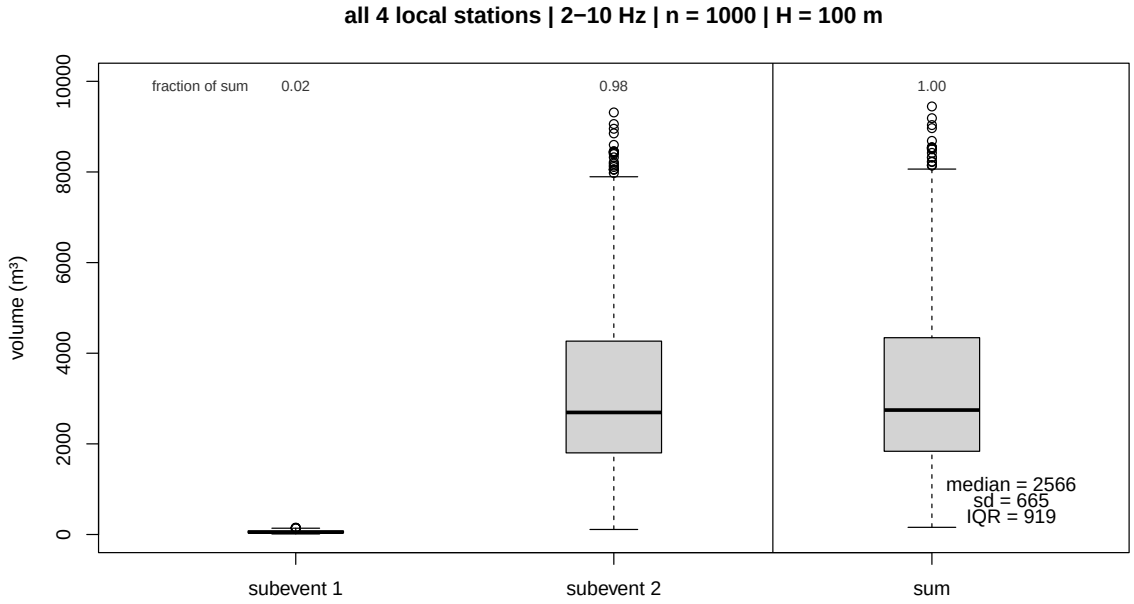

Figure 4.17: Volume estimation of the block failure from 2022-10-25 via the local seismic stations.

The analysis of the OBER signal suggest a median volume of 921 m³, which is in the range of the previous estimation. However, 37 % (ca. 400 m³) of this volume is contributed by the first sub-event, which is hidden in noise in the seismic data of the OBER station (Fig. 4.14e). This reflects the uncertainty of the volume calculation with the OBER signal and thus, the method has limited use for rockfalls with small volume, where significant parts of the seismic energy are obscured by noise.

4.2.3 Potential triggering

The knowledge of the exact timing of the block fall event allows an analysis of potential triggers. There was no earthquake preceding the failure and most of the triggers listed in Section 4.1.2 (Fig. 4.1), like wind, lightning, vegetation and human or animal activity can be excluded. The most likely triggers are rain fall, snowmelt, temperature gradient or thaw-freeze conditions.

The weather conditions before and during the block failure (Fig. 4.18) have been monitored in detail by the real-time monitoring system on the summit (Chapter 3). One day before

the failure, there was rainfall, that turned into snow fall during the day, indicated by a temperature drop below 0 °C. In the night before the failure, the thermistors on the summit measured ca. 0 to -2 °C. The day of the failure itself was dry and sunny, marked by a strong rising and falling temperature gradient of >15 °C/4 h. Finally, the failure happened when the temperatures first fell back to 0 °C. The constellation of preceding weather conditions suggests a combination of all four aforementioned triggering mechanisms. Due to the precipitation, there was enough water available to increase hydrostatic pressure in the fractures. Additionally, this available water could freeze in the cold night before the event. The warm temperatures on the next day could melt ice and snow, and the strong temperature gradient could increase surface-near stress due to thermal expansion and contraction. Finally, the freezing conditions coinciding with the rockfall event mark the next thaw-freeze-cycle, that may have increased the stress via cryostatic pressure (Krautblatter et al., 2013). This highlights the complex interplay and superposition of different triggering factors for rockfall and the difficulty to determine the exact trigger, even in well-monitored cases.

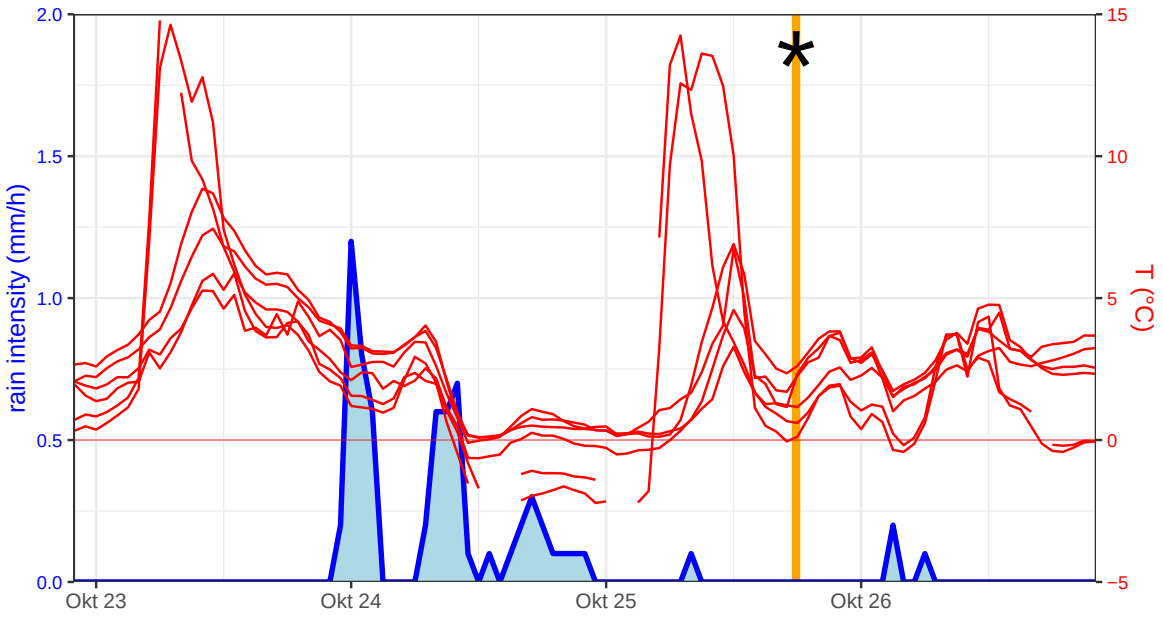

Figure 4.18: Weather conditions before and during the block failure. The blue line shows the rain measured on the summit and the red lines mark the temperatures of all VW instruments on the summit. The timing of the detachment is marked by the vertical orange line and the black asterisk. Time is in UTC.

5 Forecasting

5.1 Prospective failure time forecasting (Paper 3)

This section has been published as article in the Nature Journal *Communications Earth & Environment* (IF 7.9):

Leinauer, J., Weber, S., Cicoira, A., Beutel, J., and Krautblatter, M. (2023): An approach for prospective forecasting of rock slope failure time. Commun Earth Environ 4, 253.
doi.org/10.1038/s43247-023-00909-z

The following changes have been made to the published version:

- The numbering of each section, figure and supplementary material has been changed.
- The references to subsections have been adjusted.

Note that due to the Journal style of *Nature Communications Earth & Environment*, the detailed methods are described after the results and discussion.

5.1.1 Abstract

Rock slope failures globally account for most single-event landslide disasters. Climatic changes in mountain areas boost failure activity and the demand for reliable failure time forecasts. State-of-the-art prediction models are often confused with high-frequency slope deformation data. Prospectively, they provide ambiguous forecasts as data filtering, starting point definition and forecast uncertainty remain arbitrary. Here, we develop a prospective failure time forecast model that applies multiple filtering and inverse velocity percentiles to minimize subjective decisions. We test the concept with 14 historic slope failures of 10^2–10^8 m³ including 46 displacement datasets from different sensors. After automatic detection of the onset of acceleration, the failure time of all events is forecasted to within -1±17 h for higher-frequency data and -1±4 d for daily data with a final mean uncertainty of 1±1 d and 7±4 d that is estimated in real-time. This prospective approach overcomes previous long-standing problems by introducing a robust and uniform concept across various types of catastrophic slope failures and sensors.

5.1.2 Introduction

Slope instabilities of varying magnitude frequently threaten the life, health or property of humans in all parts of the world (Lacasse and Nadim, 2009, Petley, 2012, Guzzetti, 2000, 2021). Massive rock slope failures alone, including rock slides, rock avalanches and rock falls caused 58 % of the global disasters from single landslide events (downslope mass movements in general) in the last millennium (Evans, 2006). Under the current ongoing climatic changes, landslide risk is expected to increase critically (Picarelli et al., 2021) and therefore, cost-efficient mitigation measures with a wide applicability are needed. Such measures as alarm systems or evacuation of endangered zones require reliable forecasts of the imminent event (Kilburn and Petley, 2003, Intrieri and Gigli, 2016). Local monitoring systems provide important data that can be used to predict the time of slope failures (Intrieri et al., 2019). However, to meet social, economic and scientific requirements, existing forecasting methods need amendments in the real-time processing of modern monitoring data and a conceptual basis that is valid for diverse failure processes.

All slope failures are preceded by precursory deformations of particular amplitude and duration (Federico et al., 2015). The precursory signals, increasing deformation rates or seismic activity, originate within the unstable rock masses due to progressive crack propagation and non-elastic deformations prior to failure (Petley, 2004). The measured pre-failure surface displacement pattern can be described with a classical creep curve (Intrieri et al., 2019) (Fig. 5.1 top). In the secondary creep phase, under constant stress conditions, stabilizing and destabilizing forces balance each other and strain rates remain constant. Increasing stresses in the fatiguing material create a self-accelerating positive feedback setting of progressively failing retaining sectors (Amitrano and Helmstetter, 2006, Main, 2000, Corcoran and Davies, 2018, Kemeny, 2003). As a result, in the final accelerating phase, the strain rate is in a power-law relation to time, fitting tertiary creep. Usually, the acceleration phase is shorter the smaller the volume and more brittle the rock is (Rose and Hungr, 2007), ranging from seconds for small blocks up to days, weeks or months for bigger slope failures. In the accelerating phase, more or less accurate failure time forecasts are so far calculated with several methods (Saito and Uezawa, 1961, Saito, 1969, Fukuzono, 1985, Voight, 1989a,b, Mufundirwa et al., 2010, Intrieri et al., 2019). The most common prediction method is the inverse velocity method after Fukuzono (Fukuzono, 1985), possibly due to its relatively simple graphical solution (Cabrejo-Liévano, 2013, Carlà et al., 2017b, Casagli et al., 2021). Here, the inverse velocity of a failing mass is plotted against time during tertiary creep and the intersection of the extrapolated trend with the abscissa , i.e. at infinite velocity, indicates the predicted time of failure (Fig. 5.1 bottom).

While it can be easy, to find a linear inverse velocity fit that matches the actual time of a failure retrospectively post-failure (Kilburn and Petley, 2003, Petley and Petley, 2006, Mazzanti et al., 2015, Intrieri and Gigli, 2016, Sättele et al., 2016, Carlà et al., 2019, Intrieri et al., 2019, Grebby et al., 2021), the challenge in real-time scenarios is to obtain reliable forecasts prospectively (Intrieri et al., 2021, Kristensen et al., 2021). Modern monitoring systems are able to measure surface displacements in (near) real-time at high spatial and temporal reso-

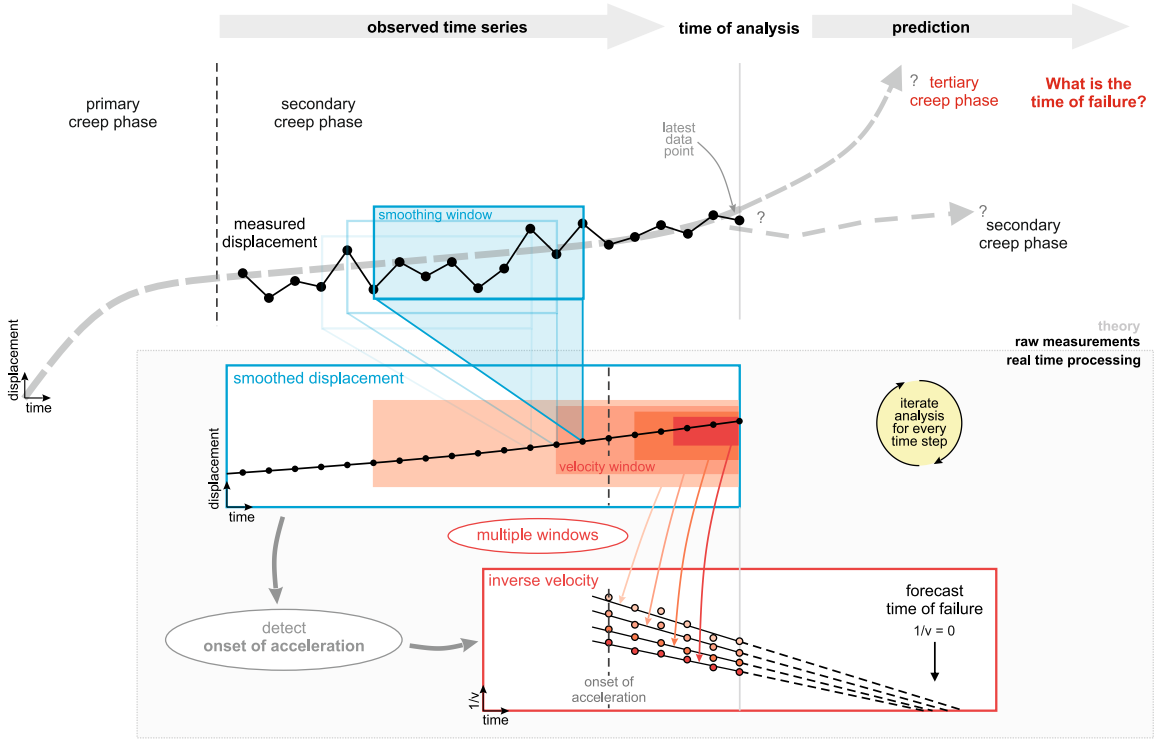

Figure 5.1: Concept of the prospective failure time forecast model (PFTF). Displacements of unstable rock slopes follow a creep curve. Usually, monitoring starts in the secondary creep phase without knowing the transition point to tertiary creep (onset of acceleration, OOA). This point is used as starting point for failure time forecasting. The real time processing of PFTF uses multiple filtering windows to identify the OOA and to derive multiple inverse velocities that are used to forecast the time of failure and estimate the forecast uncertainty (for details see Methods).

lution by in situ devices (e.g. crackmeter, tiltmeter, Global Navigation Satellite System), or by satellite or ground-based remote sensing techniques (Chae et al., 2017, Carlà et al., 2019). These data types create early warning opportunities, but present prediction models have not kept pace and are not ready to be used with high-frequency and therefore often noisy slope deformation data. Thus, they provide ambiguous forecasts.

Specifically, data filtering, starting point definition and forecast uncertainty remain unclear. Filtering the raw monitoring data can improve the forecasts, but the process is often arbitrary and involves subjective decisions (Cabrejo-Liévano, 2013, Dick et al., 2015, Carlà et al., 2017b, Bozzano et al., 2018). Although the forecasted failure time is sensitive to the degree of data smoothing, most applications of the inverse velocity method in the literature include only one or two subjectively selected time windows. Furthermore, the outcome of the prediction model is highly sensitive to the definition of the transition point from secondary to tertiary creep (from constant velocity to accelerating regime). This point is called onset of acceleration (OOA) and is used as starting point for forecasting (cp. Fig. 5.1) (Dick et al., 2015, Intrieri et al., 2021). Monitoring usually starts in the secondary creep phase and in

real-time it remains challenging to decide at what time the slope enters the tertiary creep phase (Fig. 5.1 top). An unfavourable OOA setting can result in misleading forecasts as the regression of inverse velocities may include points which do not belong to the final failure phase in case of a too early OOA or may exclude important measurements in case of a too late OOA. Modern early warning systems deliver observations of multiple sensors at high temporal frequency. A prospective real-time application of forecasting methods therefore requires a predominantly automatic method for the starting point definition. However, the few recently published approaches for this (Carlà et al., 2017b, Bozzano et al., 2018, Valletta et al., 2021) perform well in some cases but also detect non-optimal OOAs or false positives. Moreover, responsible decision-makers are dependent on a measure of reliability and uncertainty of the derived forecasts. In the past, the uncertainty has often not been evaluated (e.g. Kilburn and Petley, 2003, Krähenbühl, 2006). More recently, uncertainty estimations via the distribution of inverse velocity regressions (Manconi and Giordan, 2015, 2016), via the calculation of a standard error (Grebby et al., 2021) or via the calculation of a failure window during which a failure event is highly probable (Carlà et al., 2017b) have been put forward. However, there is no standard procedure for a statistical real-time uncertainty estimation.

Therefore, there is a lack of a forecasting concept that operates fully prospectively without post-tuning of the results, with a clear smoothing process, a non-arbitrary OOA detection and a systematic real-time uncertainty estimation. Here, we present a prospective failure time forecast model (PFTF) developed by analysing 46 datasets from 14 slope failures with daily or higher observation frequency. We acquire a uniform robust concept across sensor and failure types overcoming previous major drawbacks. The onset of acceleration is detected sufficiently early and reliable forecasts including uncertainty estimation can automatically be calculated in real-time. Overall, forecast accuracy is higher with higher-frequency data and closer towards the actual time of failure. This model can support decision-makers in various critical situations.

5.1.3 Conceptual framework

Our forecasting concept (Fig. 5.1) includes iterative real-time data processing, a two-step filtering process with multiple filtering window lengths (blue and red in Fig. 5.1), an automatic starting point definition and a statistical uncertainty estimation of every forecast. We implemented the concept into an operational prospective failure time forecast model (PFTF) complying with the requirements for real-time failure forecasting. PFTF iterates with every new available data point (Carlà et al., 2017b, Casagli et al., 2021) including only past observations without knowing the time of failure. It exclusively uses pre-accessible data in a forward model. Therefore, the open-source algorithm design (Fig. 5.2a) allows real-time prospective forecasting of imminent failures but also a prospective analysis of past events (simulated real-time). It is capable of processing multiple high-frequency observations (for details see Methods).

The first key element of PFTF is a two-step smoothing approach with multiple window lengths (Section 5.1.4), as this enables the automatic detection of the onset of acceleration

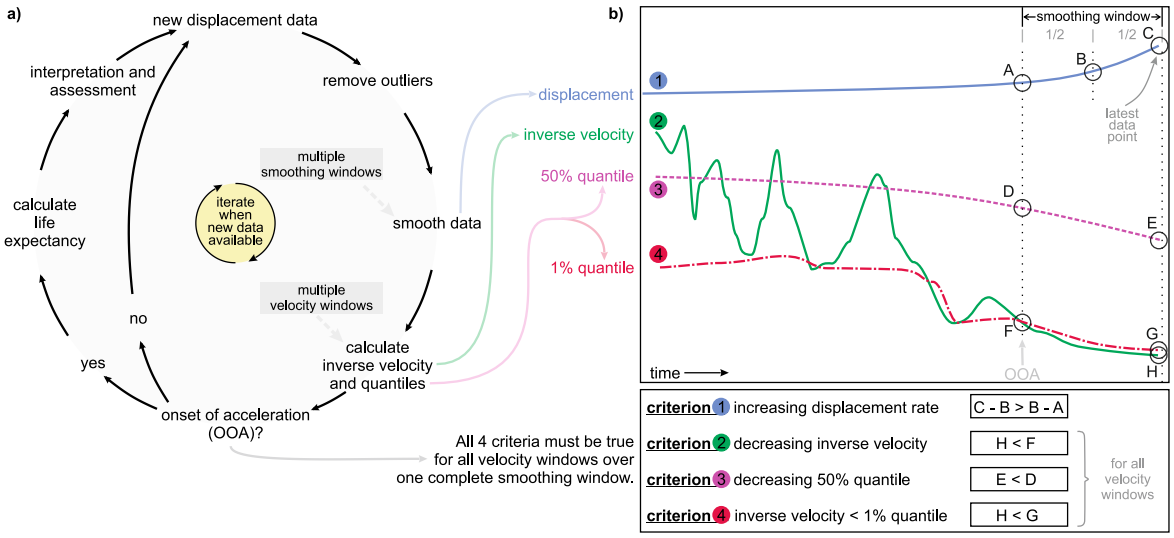

Figure 5.2: Flowchart of the PFTF model and OOA detection criteria. **a** Flowchart of the PFTF model steps (for explanation see Methods). **b** Criteria for the automatic detection of the onset of acceleration (OOA) that is used as starting point for forecasting (for details see Methods).

(OOA) (Section 5.1.4) and the statistical uncertainty estimation (Section 5.1.4). In the first filtering step, the displacement trend is clarified via a rolling mean of raw displacements over specific smoothing windows (w_smooth). In the second step, a variety of inverse velocities is calculated from each displacement data via linear regressions over multiple velocity windows (w_v, see Methods). The amount of data-points used to derive the velocity depends on the length of the velocity windows (Fig. 5.1 red boxes and arrows).

Secondly, we implement an automatic OOA detection method that is based on four simple criteria and includes all data points within the latest smoothing window (w_smooth, Fig. 5.2b, for details see Methods). Criterion 1 requires an increasing displacement rate. Criterion 2 requires decreasing inverse velocities for all velocity windows (w_v), which is different from criterion 1 as the multiple inverse velocities can differ. Criterion 3 requires an overall accelerating regime, represented by a decreasing 50 % inverse velocity quantile. Criterion 4 requires a short term accelerating trend, detected by inverse velocities smaller than the 1 % quantile, meaning that the latest velocity is greater than 99 % of all velocities before. If all criteria are true over one complete smoothing window, the OOA is detected. This method is operating automatically within the algorithm.

Once the OOA has been detected, an expected time of failure is calculated with all inverse velocities after the OOA with the linear version ($\alpha = 2$) of Fukuzono´s method (Fukuzono, 1985). We evaluate the forecast results based on consistently updated life expectancy plots where the predicted time until failure is plotted against the time when the forecast is made (Dick et al., 2015, Carlà et al., 2017b) with additional real-time statistical information (see Supplementary Fig. A.2.1a and details in Methods). To give a real-time statistical uncertainty information for all diverse test sites, we enhanced the failure window approach (Carlà et al., 2017b) by using multiple smoothing windows simultaneously and adding the mean

forecasted time to failure. The width of the failure window and the consistency of its limits are useful indicators for the reliability of the forecasts. Additionally, we show important updated statistical information in the boxplots (Supplementary Fig. A.2.1b).

Methods

Due to the Journal style of Nature Communications Earth & Environment, the detailed methods appear after the results and discussion in Section 5.1.5.

5.1.4 Results and discussion

Prospective real-time forecasting with multiple data filtering

The introduced concept allows the calculation of prospective failure time forecasts with diverse rock slope monitoring data. With the presented multiple smoothing approach, we can diminish primary instrumental noise on the raw data and include all observed displacement data into the inverse velocity determination. The stability of the forecasts is improved without losing the sensitivity to changing trends (Bozzano et al., 2018) and the effects of various window lengths can directly be analyzed in the resulting plots in real-time (see Supplementary Fig. A.2.1).

Typically, the window lengths vary between few hours and multiple days, but reasonable window lengths always depend on the following factors:

- signal-to-noise ratio/ quality of the data; controlled by
  - deformation rates (signal)
  - measurement technique (noise)
  - measurement frequency
- expected duration of precursory accelerations and the time needed for emergency actions (smoothing windows should be shorter than that)
- amplitude of other natural noise producing divergence of the measured data from a perfect linear inverse velocity trend (Carlà et al., 2017b).

Instabilities with high movement rates usually require shorter smoothing windows, while slow moving instabilities and noisy data require stronger smoothing (Carlà et al., 2017b). Also, higher measurement frequencies require filtering over a greater number of observations as more background noise is recorded. In contrast, noise has less influence when a sparse monitoring frequency (e.g. 1 d) is applied (Carlà et al., 2017b). This might also be the reason for the increasing prediction accuracy with greater measurement intervals reported by Iwata & Sasahara (2021) (Iwata and Sasahara, 2021). However, the analysis of the sites Galterengraben, La Saxe, Veslemannen and Weissmiess from this study show that if the monitoring frequency is too low, precursory accelerations can be over-seen or too few data points exist to perform reliable forecasting. This is most relevant in geomechanically

strong rock slopes consisting of brittle hard rock where the acceleration phase can be quite short (Carlà et al., 2017b). Therefore, we identified a high monitoring frequency as a key factor, especially in situations with short acceleration phases (Bozzano et al., 2018). Hence, we suggest using a sufficiently high sampling frequency, e.g. daily or faster for volumes $> 10^6$ m³ and hourly or faster for smaller volumes, in combination with adequate data filtering, depending on frequency and signal-to-noise ratio (cp. Supplementary Fig. A.2.2). Many monitoring methods allow higher sampling frequencies without additional costs or effort. Although longer smoothing windows can diminish the uncertainty of the forecasts, excessive smoothing using too long smoothing windows distorts the calculations and adds a lag to the time series (compare Section 5.1.4). As a result, forecasts are shifted towards unsafe predictions (forecast after failure) which should be avoided. Therefore, the smoothing windows should be as short as possible but as long as necessary.

Due to the specific complexity of each individual slope instability, it is impossible to define a universal rule for optimal window lengths at this stage. However, for the sake of comparability between the sites in this study, we use three sets of fixed window lengths depending on the data resolution and the expected acceleration phase duration (see Supplementary Fig. A.2.2). In real-time cases, a detailed knowledge of the unstable slope, its geological process and the site specific data quality is needed. The operating specialist has then to decide on reasonable window lengths and might even calculate with multiple windows simultaneously, although the interpretation of the results can become more complex. Also, the smoothing process is not necessarily fixed over all time. In cases where conditions change, e.g. when decelerations appear after the OOA but failure is assumed imminent, the smoothing windows might need adaption (see Supplementary Fig. A.2.2 and the sites La Saxe and Veslemannen).

Automatic onset of acceleration detection

The automatic determination of the OOA minimizes the subjectivity of critical real-time decisions under the pressure of imminent failure and could also be combined with previously published methods. Our approach is robust for all 14 tested sites in this study (see Supplementary table A.2.1 and details in Section 5.1.4). The OOA is prospectively detected sufficiently early (0.1-200 d prior the actual time of failure) while the timing of the OOA is dependent on failure volume and process (Section 5.1.4). Analogue to the smoothing windows, a restart of the OOA detection analysis is necessary in case of trend updates.

False alarms should always be kept to a minimum, but can never be ruled out due to periodic accelerations and natural variations. From the 14 tested sites, the PFTF model detects false OOAs in two cases (La Saxe and Veslemannen). A typical life expectancy plot of such a setting is shown in Supplementary Fig. A.2.3. A false detection of the OOA can be identified as such as soon as a consistent deceleration with increasing life expectancies appears. Then, a restart of the analysis only with data after the deceleration phase gives the best results. It is worth noting that a false OOA detection is not necessarily leading to a false alarm immediately. After evaluation of the forecast results by the early warning system operators,

either a manual intervention in case of a false OOA or the triggering of an alarm in case of a threshold exceedance are possible. On the other hand, if no clear OOA point can be detected sufficiently early before the actual failure, the model fails leading to a missed alarm. This is the case in 4 % of the analyses. All difficulties leading to a bad or non-representative signal-to-noise ratio (noise fluctuations in the order of the acceleration signal hiding or substantially distorting it) can contribute to such a case. Then, an improvement of the monitoring quality and smoothing window lengths, the use of different methods, and a better understanding of the instability's process dynamics can assist.

Converging forecasts

Our real-time uncertainty estimation, enabled by the usage of multiple windows, is expressed by the plotting of failure window and mean in the life expectancy plot. A converging failure window corresponds to an increasing confidence of the forecasts. In operating systems, predefined alarm limits can be graphically drawn as horizontal lines (e.g., at a life expectancy of 24 h). Different warning levels or required mitigation measures could be triggered when the failure window or the mean reaches specific alarm thresholds. The site-individual alarm time before failure is dependent on the required time for mitigation measures like evacuation and the desired level of safety.

Additionally, with the updated boxplot, the reader can easily evaluate the range of all past forecasts and the influence of the applied smoothing. With ongoing updated iterations, anomalous forecasts, mainly appearing before the forecasts converge, turn into outliers. The over-plotting of the latest forecasted time of failure per velocity window (w_v, red diamonds) is helpful when evaluating the latest calculations and trends. Unstable and inconsistent forecasts can be detected. A stable position of the marker above the box represents a trend to a later expected time of failure and vice versa. Although the boxplots must be assessed with care, they present more valuable information than just the life expectancy plots usually presented by most authors, as the most recent forecast is not necessarily the most accurate one (Intrieri and Gigli, 2016).

All tested sites show a similar pattern of converging forecasts towards failure. As an example of the achieved results, we present a time lapse video animation of the Preonzo site (Reflector 9) showing how the PFTF result appears to a responsible operator or decision-maker in real-time in the Supplementary Movie (Appendix A.2). Fig. 5.3 displays the final three weeks before failure of the same data and boxplots at two paradigmatic time steps close to the OOA and close to failure. The resulting PFTF outcome can be divided into three phases. In Phase 1 shortly after the OOA, the calculated life expectancies (Fig. 5.3d) are scattered. The mean is unstable with no clear trend 45° downward and the failure window is wide. Subfigure 5.3e shows a corresponding boxplot from April 29. The boxes and the failure window cover a wide time range and the latest forecasts (red diamonds) are spread over 10 days. In this phase, the uncertainty is rated high. In the second phase (point A in Fig. 5.3d), the forecasts converge and the failure window becomes narrower. The exact position of this point is dependent on the degree of smoothing and the position of the OOA. In

the last phase of 6-10 days prior to failure, the life expectancies of all w_v lie within a short time span, the mean plots stable 45° downward, and the failure window becomes small (ca. 2 d). Subfigure 5.3f shows a corresponding boxplot from May 12. The boxes and the failure window cover a narrow time range and the latest forecasts are consistent. In this phase the uncertainty is rated low. In fact, the mean forecasted time of failure is 1 day too early, while the failure on May 15 lies within the failure window.

The application of the PFTF model to all 46 datasets proves it to be a powerful and robust concept for prospective forecasting of slope failures. It is essential to asses the forecast results relative to the lead time which is the time between warning and the impact of an event (Hermle et al., 2021). The application as an early warning tool premises that the forecasts must be early enough (life expectancy $<$ lead time) and accurate enough (uncertainty $<$ lead time). Our single PFTF concept is successful with a variety of monitoring methods, different rock failure processes in different geological settings and over seven failure magnitudes. The mean life expectancy at the actual time of failure of all sites is -1±17 h for sub-daily and -1±4 d for daily data sets respectively, representing a good fit of the forecasts to reality. The mean failure window width is 24±23 h and 7±4 d, which is in the range of an earlier estimated general forecast uncertainty in 74 pit wall failures of up to 21 h Cabrejo-Liévano (2013). In general, our results suggest a better performance of the forecasting method with higher frequency data. Yet, forecast uncertainties of less than a day, or a few days respectively, are usually sufficient compared to the respective lead time (Fig. 5.4g; (Hermle et al., 2021)).

All forecast results are summarized in Fig. 5.4a-f, separated into two groups of daily (d-f) and higher (a-c) data frequencies. The most probable failure time is plotted as black diamond and the coloured bars represent the width of each failure window during which a failure is likely. Differences between the sites or datasets can be connected to inhomogeneous deformations of the unstable body and the positioning of the sensors. Prospectively, these variations cannot be ruled out. The operating experts must evaluate them statistically, taking into account which trends are reflected by which sensors combined with their knowledge of the process dynamics and how the site is monitored. This can be challenging (cp. Section 5.1.4). However, the results are robust considering the variability of input data. Note that stronger smoothing, i.e. the lowest group in each subplot, is usually shortening the failure window but also shifting the forecasts to later expected times of failure, possibly towards unsafe predictions (see Subfig. 5.4ab+de). Generally, the mean forecast errors are decreasing towards failure. Due to the lower data resolution and longer acceleration phase in the daily datasets, this effect is less distinct here when comparing the last five days before failure (Fig. 5.4c+f). Overall, failure windows and uncertainties are bigger in the daily datasets, and, therefore higher sampling frequencies are preferable (compare Fig. 5.4a-c with d-f).

The comparison of the acceleration time between automatically detected OOA and failure with the detached volumes is generally in line with the assumption (Rose and Hungr, 2007) that bigger volumes tend to have longer acceleration phases, although a significant correlation cannot be proven with the available data. We calculated a log-log fit of $OOA = 0.76 volume^{0.25}$ based on the 14 analysed sites (R^2 = 0.30, p = 0.07). Due to the individu-

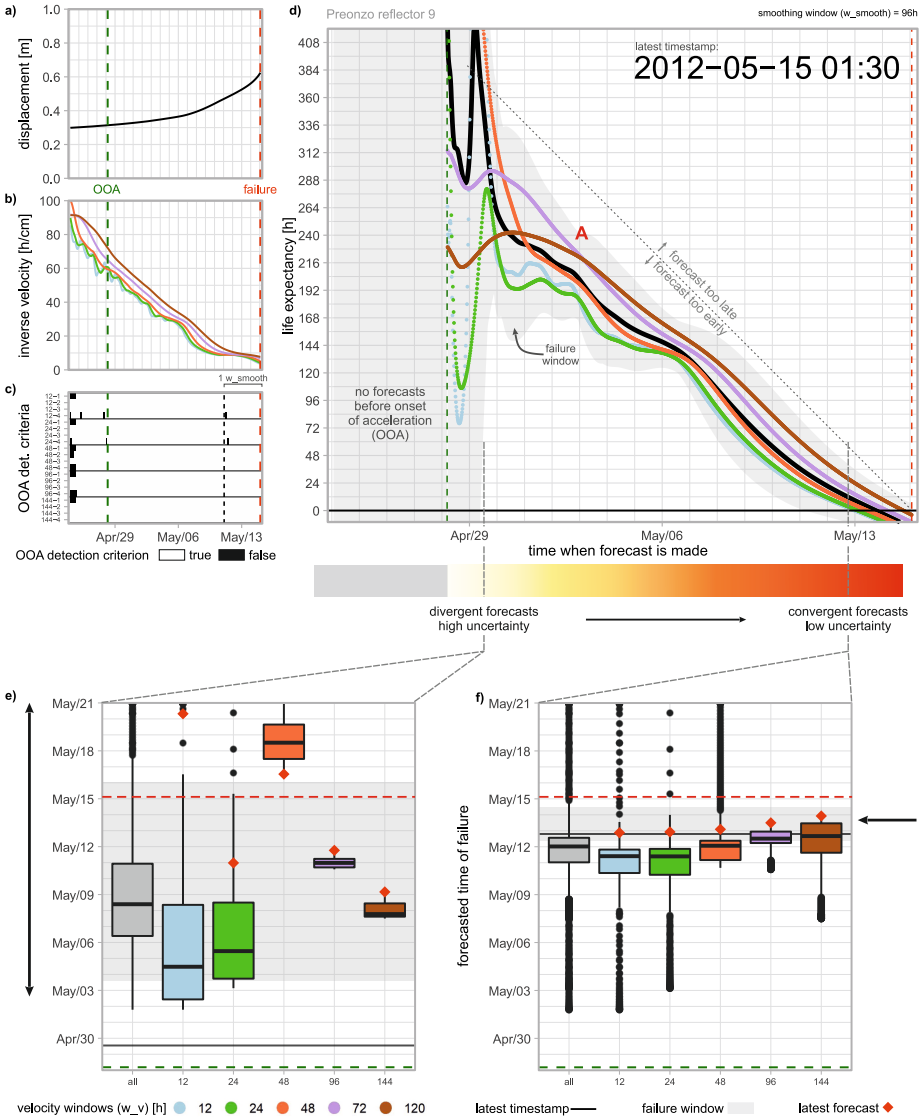

Figure 5.3: Final outcome of PFTF at Preonzo (Reflector 9) for a 96 h smoothing window. See the Supplementary Movie (Appendix A.2) for a time-lapse real-time animation of the prospective forecast and Supplementary Fig. A.2.1 for details on the visualization. Colors represent velocity windows (see legend). The dashed dark green line marks the onset of acceleration (OOA). The dashed red line marks the actual time of failure. **a** Displacement. **b** Decreasing inverse velocities. **c** Criteria for OOA detection. The OOA is detected 17 d before the failure. Labels on the vertical axis are "velocity window - criterion number". The black dashed line marks one smoothing window (w_smooth, for details see Methods). **d** Life expectancy plot showing divergent and highly uncertain forecasts during the first days after the OOA. 12 d before failure (point A), the forecasts converge and the failure window (grey area) becomes narrower indicating a low uncertainty. The black line shows the mean of all forecasts at each time step and the grey area represents the failure window during which a failure is likely. **e** Boxplot from April 29 with distributed latest forecasts (red diamonds) and a wide failure window (grey area). The horizontal black line marks the latest timestamp. **f** Boxplot from May 12 with convergent forecasts. Boxplots show the median as line, the interquartile range as box, 1.5 times the interquartile range or the minimum or maximum data point as whiskers and outliers as circles.

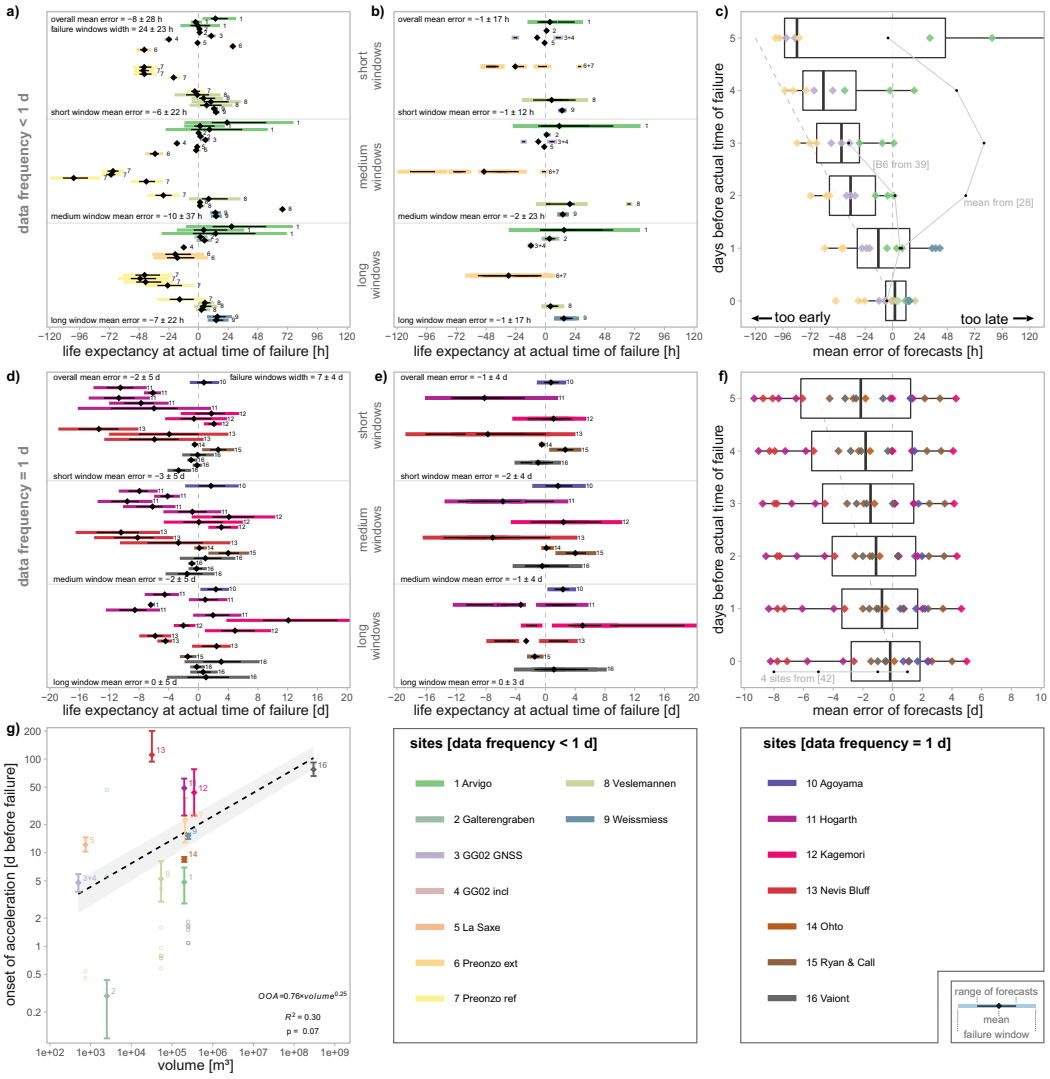

Figure 5.4: Forecast results of all tested data. Subplots a-c show high-frequency datasets; subplots d-f show daily datasets. Note the different axis scales between the two groups. Boxplots show the median as line, the interquartile range as box, 1.5 times the interquartile range or the minimum or maximum data point as whiskers and outliers as circles. **a** Life expectancy at actual time of failure for short, medium and long window sets (see Methods). A value of 0 means a perfect fit of the forecast to reality. Negative values indicate too early forecasts, positive values too late forecasts. For each sensor, the range of the forecasts (black lines), their mean (black diamonds) and the failure window (in color corresponding to the different sites, see legend) are shown. The mean failure window length is 24±23 h. **b** Forecasts merged per site. The mean merged life expectancy is -1±17 h. **c** Decreasing mean forecast errors in the last 5 d before actual time of failure. **d** Life expectancy at actual time of failure for daily datasets. The mean failure window length is 7±4 d. **e** Forecasts merged per site for daily datasets. The mean merged life expectancy is -1±4 d. **f** Decreasing mean forecast errors in the last 5 d before actual time of failure for daily datasets. **g** OOA detection time against failed volume with black dashed regression line. Larger instabilities can usually be detected earlier due to a longer accelerating phase. The grey area is delimited by the linear regressions of earliest and latest OOA per site, represented by the error bars. Open circles mark secondary OOAs (see Methods).

ality of each geological setting, strong deviations exist (Fig. 5.4g). At the biggest analysed failure of Vaiont, the OOA has been detected ca. 50 d before failure after the latest deceleration in 1963 (trend update after February 1963, see Supplementary Discussion A.2). The shortest acceleration phase of 3-10 h has been detected at Galterengraben although it is not the smallest volume. Here, the relatively small volume and the brittleness of the hanging sandstone block seem to contribute to a rapid final acceleration. At the smallest analysed event at Grabengufer, the acceleration phase of 5 d is relatively long. In fact, this was a failure of a small block that drifted on a sackung (deep-seated gravitational deformation) of ca. 400,000 m³. The complex superposition of different failure processes and volumes might contribute to the duration of final acceleration. The extraordinary long acceleration phase of up to 200 d at Nevis Bluff is possibly connected to a very consistent increase of acceleration without or with only constant external drivers.

Predictability across sensor and failure types

Our forecast model gives useful results with a variety of failure processes including rock slides, rock falls, toppling, ice fall, complex as well as different monitoring methods including Global Navigation Satellite System, total stations, displacement meters, inclinometers, InSAR and volumes from 10^2 to 10^8 m³). A quantitative comparison of the results based on failure type and monitoring method is inhibited by the diversity of the 14 test sites. Differences in the accuracy of the PFTF model might also result from other factors like the properties of the unstable mass, external drivers like precipitation, snow or pore water pressure, and the location of the sensors. The reason why the PFTF model can deal with a great variety of slope failures nonetheless, is that it uses the phenomenological effect of slope displacement which is the result of all influencing processes. Compared to previously published studies from the same sites (Kilburn and Petley, 2003, Sättele et al., 2016, Loew et al., 2017, Manconi and Giordan, 2016, Segalini et al., 2018), the PFTF results are comparable or better especially in the sense of prospective real-time application, uncertainty estimation and uniform robustness (see also black points of other studies in Fig. 5.4c+f). Our uncertainty estimation gives additional statistical information, that helps the responsible decision-maker to judge the informative value of the forecasts itself. Yet, it must be emphasised that the PFTF must be complemented with geological knowledge and that profound understanding of the unstable site is always needed. Two aspects affecting the predictability can be identified. First, some simplifications are already introduced by the linear inverse velocity method itself and secondly there are external factors that influence the outcome of the model.

Our PFTF model uses a common (Casagli et al., 2021) linear simplification of Fukuzono´s method. Although this can theoretically lead to mistakes, the linear application is mathematically least complex and therefore more likely used in practise (Rose and Hungr, 2007). Furthermore, most cases do not deviate much from the linear case (empirical value $\alpha = 2$) (Segalini et al., 2018, Intrieri et al., 2019) validating this simplification. Deviations from the linear behaviour resulting in a slightly convex or concave setting can appear (e.g. Grabengufer site, Supplementary Fig. A.2.4 or Weissmiess site) due to different internal and external rea-

sons. While in concave cases linear forecasts appear to be on the conservative and safer side (too early), convex cases can be more problematic. To handle this prospectively, the resulting plots must be interpreted carefully. For example, a slightly flatter than 45° slope of the mean life expectancy line and a position of the latest forecasts above the boxes can indicate a shift to a later expected time of failure (concave case; compare Supplementary Fig. A.2.4b). However, in doubtful cases with real danger, it is always on the safer side to expect the failure too early rather than too late, although higher interruption costs might result.

Among external parameters that influence the predictability of a slope failure are the measured or derived displacement used as input, the monitoring technique and frequency, and the failure type and volume. The displacement used as input for the PFTF is not always equal to the true movement of the unstable mass when the sampling direction (e.g. the line of sight of a radar) is not in the direction of the movement or when the derived relative displacement neglects curvy three-dimensional movements. However, we could achieve good results with all tested sensor types irrespective of their sampling direction. The PFTF also works with angle differences, which has not often been used (Petley, 2004), but is cheap and effective to measure (Cicoira et al., 2022). In fact, the forecast results from the Global Navigation Satellite System position data and the inclinometer angle data from the Grabengufer block differ by only about 1 d (see Supplementary Fig. A.2.4), which is mainly due to the application of the same fixed window lengths to the two kinds of data. Another challenge in real-time and at complex instabilities is to judge, if the used sensor data such as point measurements are representative for the later failure. If not, the forecasts can become unreliable (Manconi and Giordan, 2015). E.g. only a part of an instability could fail as in the La Saxe site (Manconi and Giordan, 2016), or the location of the measurement could be inappropriate. However, the PFTF model can only calculate reasonable forecasts, if the input data are representative.

The selection of optimal input data as well as the interpretation of the data-driven forecast results still depend on experienced users (Manconi and Giordan, 2016) and further research is needed here. One possibility to constrain better, which sensors are most representative of the controlling part of an instability is to use areal measurements like radar, laser scanning or photogrammetry to find the hotspots. Nevertheless, complex cases like the La Saxe site remain challenging, especially if decision-makers have to decide conservatively on the safe side (see the Supplementary Discussion A.2).

In any case, higher sampling frequencies potentially enable better results, irrespective of the monitoring technique. Those higher frequencies often necessitate smoothing over a greater number of observations, but from our analysis we infer that higher observation frequencies provide more accurate forecasts. Then, the use of one short-term and one long-term window already brings several advantages (Dick et al., 2015, Carlà et al., 2017b), but applying multiple windows with differing lengths minimizes the subjectivity and enables a direct analysis of the effects of various window lengths in the resulting plots (see Supplementary Fig. A.2.1).

Although the data possibly indicate a relation between the failed volume and the acceleration time between OOA and failure, it is not the goal to achieve this relation in prospective

forecasting. The goal is to detect an optimal OOA as early as possible to enable timely forecasting. Concurrently, the expected duration of the acceleration phase is relevant for the determination of the smoothing window lengths. E.g. if the acceleration phase is only several hours, smoothing windows of multiple days are useless. Two sites from this study are paradigmatic for a challenging kinematic behaviour with false OOA detection that complicates interpretations (Intrieri and Gigli, 2016, Manconi and Giordan, 2016, Mazzanti et al., 2015). The La Saxe instability shows a diverse velocity regime and a strong deceleration at April 17 shortly before the partial failure. At Veslemannen, a dominant environmental forcing controls periodic accelerations. In such cases, experience, detailed knowledge of the site specific processes and the determination of secondary OOAs (circles in Fig. 5.4g) support successful forecasting. By detecting trend update points (Dick et al., 2015, Carlà et al., 2017b) and adjusting the OOA accordingly, reliable prospective forecasts can still be calculated. The only site in this study where all failure windows lie on the unsafe side (forecast after failure) is the Weissmiess ice fall. Three factors could be a reason for this: (i) the radar line of sight is not in the direction of the movement, (ii) the radar observations started after the OOA and thus no optimal OOA can be found, and (iii) the ice fall behaves different than rock slope failures. A slightly convex behaviour could result from the high strain rates increasing from 1 to over 3.5 md^{-1} during the last two days before failure. However, this site supports that the concept of increasing accelerations is not limited to fracturing (Intrieri et al., 2019) nor to rock and earth material.

Our results show, that the prospective failure time forecast concept (PFTF) is able to overcome the major drawbacks of current retrospective failure time forecasting methods achieving reliable results with a variety of slope failure processes, volumes, materials and sensor types. It can detect the onset of acceleration automatically and provides uniform forecast information including an uncertainty estimation. In combination with the ongoing progress in wireless (near) real-time monitoring and internal fracturing observations (Weber et al., 2017), the PFTF can become a key element for future reliable and quantitative real-time natural hazard management. Its application might not be limited to rock slopes, but the underlying physical principle might also be valid at earth slopes, man-made slopes, artificial structures and glaciers, thus supporting decision-makers in a multitude of critical situations.

5.1.5 Methods

Iterative prospective forecasting

The algorithm of the PFTF model calculates prospective real-time (or simulated real-time) forecasts iteratively with every new available data point. The concept of the PFTF model is shown in Fig. 5.1. Fig. 5.2a gives an overview of the algorithm steps which include:

- reading new displacement data with every iteration
- removing outliers/ erroneous measurements
- smooth raw displacement data (see 5.1.5)

- calculate velocities and inverse velocities with multiple velocity windows (see 5.1.5)
- calculate 1 % and 50 % quantiles of inverse velocities (see 5.1.5)
- automatically detect the onset of acceleration (OOA) which is used as starting point to calculate forecasts (see 5.1.5)
- calculate and plot the time to failure (life expectancy) and time of failure (see 5.1.5)

For the technical implementation of this workflow in an open-source R-Code, (RStudio Version 2021.09.0 and R Version 4.1.3 (R Core Team, 2022) see the code availability statement (Leinauer et al., 2023a).

Data preparation

The PFTF model reads displacement data as input. Thus, position data have been converted to relative displacements and inclination data to relative angle displacement respectively. All data have been formatted as time series with equal time steps and no gaps, so that every time step contains one displacement data point or missing values (NA) in time steps without measurements. For details on the monitoring method see the Supplementary Table A.2.1.

Data smoothing

The PFTF model uses a two-stage smoothing approach with multiple windows to enable OOA detection and statistical uncertainty estimation. First, the raw displacement is smoothed by a moving mean over the last *n* values while *n* is specified by the length of the given smoothing windows (w_smooth). To minimize the effect of subjective decisions, we propose the application of multiple smoothing windows. Displacements (Fig. 5.3a) are plotted after smoothing. A second step of data smoothing is performed during the calculation of the inverse velocity via linear regression over multiple velocity windows (w_v) (see 5.1.5).

To create comparability between all sites in this study, we defined three sets of standard windows that we applied to the analysed data based on a simple decision schema (Supplementary Fig. A.2.2). Note that other data might require different smoothing window lengths.

Inverse velocity calculation

Velocities are calculated from the smoothed displacement using a linear regression model over the last *n* values while *n* is specified by the length of the given velocity windows (w_v). This method includes all displacement measurements within w_v and gives the best fitting velocity over the last w_v. For the standard window sets (Supplementary Fig. A.2.2), we used five velocity windows in each case, ranging from $\frac{1}{8}w\_smooth$ to $5w\_smooth$. Inverse velocities are calculated as $velocity^{-1}$ and plotted in Fig. 5.3b.

Starting point definition

All inverse velocity data after the defined starting point (onset of acceleration, OOA) are included in the extrapolated linear regression to forecast the time of failure. The real-time detection of the OOA is based on four criteria (Fig. 5.2b). If all criteria are true over one complete smoothing window (w_smooth), the OOA is detected at $1w\_smooth$ before current time.

- **criterion 1**: increasing displacement rate. The displacement difference over the second half of the last w_smooth must be greater than over the first half of the last w_smooth.
- **criterion 2**: decreasing inverse velocity. The inverse velocity must decrease over the last w_smooth for all velocity windows w_v. This is different from criterion 1 as the different w_v can have differing trends.
- **criterion 3**: decreasing 50 % quantile. The 50 % quantile must decrease over the last w_-smooth for all velocity windows w_v. This represents a general long-term accelerating trend.
- **criterion 4**: inverse velocity smaller than 1 % quantile. The latest inverse velocity must be smaller than the 1 % quantile of all inverse velocities. Respectively, the current velocity must be greater than 99 % of all velocities before. This represents a short-term accelerating trend.

If the displacement data show a trend update due to a deceleration phase or a changing process regime, the analysis is restarted only with data after the trend update (compare Supplementary Fig. A.2.2) and secondary OOAs are determined.

Forecast and uncertainty presentation

Forecasts are calculated with the linear version ($\alpha = 2$) of Fukuzono´s method (Fukuzono, 1985). The intersection of an extrapolated linear trend line of all inverse velocities after the OOA with the horizontal time axis corresponds to the forecasted time of failure. The results are plotted in a life expectancy plot (Dick et al., 2015, Carlà et al., 2017b), where the predicted time until failure (life expectancy) is plotted against the time when the forecast is made on the abscissa. This allows simple updating with every new data point and a good visualization of all historic forecasts. The axes are scaled 1:1 for easy identification of changing forecast trends. Completely consistent new forecasts appear 45° downward while a shift to later expected failure times appears flatter and vice versa. The PFTF creates one life expectancy plot per w_smooth and one coloured point for every w_v used (see Supplementary Fig. A.2.1).

To evaluate the statistical uncertainty of the forecasts, we calculate a failure window during which failure is highly probable after Carlà et al. (2017b). It contains the time between the earliest and the latest forecast of each time step and half of that time span added on each side. In the life expectancy plot, we show the mean life expectancy of all w_v per time step as black line and the failure window as grey area.

Additionally, updated standard boxplots of all forecasts since the OOA are produced. The plot includes one box per w_v (colour) and one for all w_v (grey). The latest forecasted times of failure per w_v are plotted as red diamonds. A horizontal grey line indicates the latest timestamp. The failure window is marked as grey area (see Supplementary Fig. A.2.1).

Statistical evaluation of results

For the statistical analysis of the results of all sites in Fig. 5.4, the life expectancies, their mean, and the failure window were extracted from the forecasts five to zero days before actual time of failure. The mean error is calculated as average of all forecast means. Uncertainties are expressed as standard deviation. For the Subfigures 5.4b+e, all forecasts per site are merged to one line. The merged mean is the average of all means per site. The time of OOA detection in Subfigure 5.4g is plotted as mean and range of all values per site. The linear regression is calculated over the $\log_{10}$ values of mean OOA detection time and volume. The uncertainty area is delimited by the regression lines of minimum and maximum OOA detection times.

Site selection

The tested historical slope failure events have been selected based on availability and documentation. All sites are rock slope failures, except Weissmiess which is an ice fall. All sites have a daily or higher sampling frequency, and include measurements starting before the onset of acceleration and until failure. The 14 sites represent a variety of monitoring methods and volumes. Details on the data sets, sources and where data have been extracted from plots are listed in Supplementary Table A.2.1.

5.1.6 Acknowledgments

This study was developed within the AlpSenseRely project which is funded by the Bavarian State Ministry of the Environment and Consumer Protection (TUS01UFS-76976). We thank the Dipartimento del territorio/ Cantone Ticino, Lorenz Meier/ Geopraevent, the Tafers Community/ Fribourg, the Aosta Valley Regional Office, Ruedi Krähenbühl, Floriano Beffa and Andrea Manconi for providing original monitoring data for this study (compare Supplementary Table A.2.1).

Competing interests

The authors declare no competing interests.

Data Availability

The source of all used monitoring data is indicated in the Supplementary Table A.2.1. Data of ten sites are taken from published studies. Original data of four sites have been provided

by third party persons or institutions (Arvigo, Galterengraben, Preonzo, and Weissmiess). A collection of all data is available under https://doi.org/10.14459/2023mp1688868 (Leinauer et al., 2023c).

Code availability

The R-Code of the PFTF model including instructions is completely open-source and available under https://doi.org/10.5281/zenodo.8010361 (Leinauer et al., 2023a).

Contributions

JL wrote the manuscript and the R-code, designed the figures, collected monitoring data and performed the data analysis. SW had the initial idea for the concept. SW, AC and JB provided monitoring data and improved the concept substantially. SW, AC and MK contributed to the interpretation of the results and improved figures and manuscript.

5.2 Non-linear failure time forecasting (Update 3)

This section is an update to Paper ③ in Section 5.1.

This section contains extensively reworked findings of the following unpublished master´s thesis that I supervised:

Jokel, M. (2023): Evaluating acceleration models and respective stochasticity towards a real-time forecasting model for landslides.
https://mediatum.ub.tum.de/1579885.

5.2.1 Theory

In the previous section, prospective failure time forecasting after Fukuzono (1985) based on the linear case with the parameter $\alpha = 2$ has been covered in detail (cp. Eq. 2.4). However, although linear forecasting is an adequate solution in most cases (Crosta and Agliardi, 2003, Rose and Hungr, 2007, Segalini et al., 2018, Intrieri et al., 2019), the forecast results can theoretically be more accurate using a non-linear model with $\alpha \neq 2$, as the measured data points can be fitted better. Typical inverse velocity curves for the linear, convex and concave case are shown in Fig. 5.5. Concave forecast models ($\alpha > 2$) predict the time of failure earlier than the linear case, while convex models ($1 < \alpha < 2$) predict a later time of failure. For historical slope failures, α varies between 1.5 and 2.2, mainly differing less than 0.1 from 2.0 (Segalini et al., 2018) and thus, the performance of the PFTF model with non-linear predictions should be evaluated.

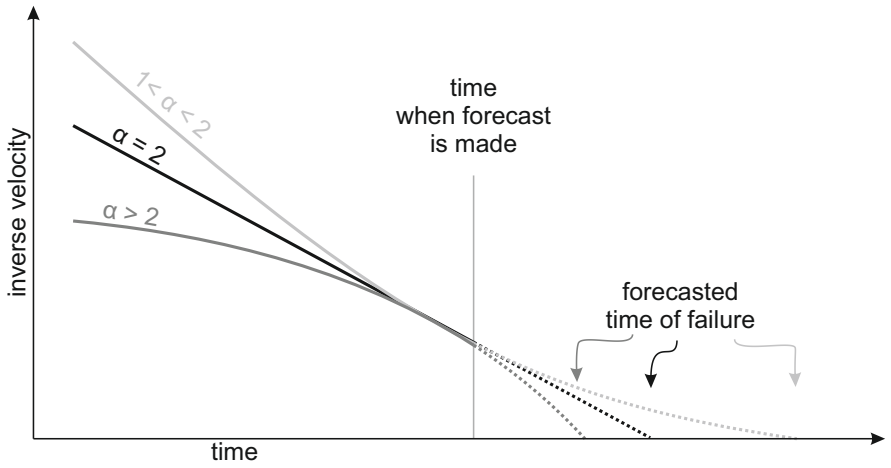

Figure 5.5: Typical inverse velocity curves (modified after Fukuzono, 1985).

5.2.2 How alpha influences the forecasts

To assess the influence of various typical α values on the outcome of the failure time forecasting model, we applied non-linear forecasting to 32 datasets from the 13 sites presented

in Section 5.1 (Jokel, 2023). For each case, we followed the same procedure for data smoothing with three window sets (short, medium, long) and the OOA detection. For the linear case ($\alpha = 2$), the time of failure is simply determined by the intercept of a linear inverse velocity regression line with the abscissa. For the non-linear cases ($\alpha \neq 2$), the parameters A and t_f (time of failure) from Eq. 2.4 are estimated by iterative curve fitting while α is fixed to a value between 1.4 and 2.4. This non-linear least-squares problem is solved with a Levenberg-Marquardt algorithm (Levenberg, 1944, Marquardt, 1963; function *nlsLM()* from the *minpack.lm* package in R). The influence of α on the accuracy and uncertainty of the forecasts is finally evaluated based on the model output at the actual time of failure (cp. Fig. 5.4).

The trend of later forecasted failure times with smaller α and earlier forecasted failure times with higher α is confirmed by all tested datasets. This is reflected by the forecast accuracy. The offset of the mean forecast (mean of all three smoothing window sets) from the actual time of failure is shifted towards positive offsets (forecast too late) with smaller α and vice versa (Fig. 5.6a). Datasets with higher temporal resolution show overall more accurate results and are less sensitive on the choice of α. The same change in α causes a smaller shift in the outcome of the forecast the better the temporal resolution of the displacement data is. For early warning applications, this reinforces the recommendation to apply high sampling rates (hourly or better, cp. Section 5.1.4). Statistically, the mean offset of all available data is minimal for $\alpha = 1.88$ (daily datasets) and $\alpha = 1.92$ (hourly datasets), but the deviation is large, especially for the daily datasets.

The mean forecast uncertainty (width of the failure window) increases clearly with smaller α values (Fig. 5.6b). This is due to the asymptotic shape of the extrapolated fitted curve for $\alpha < 2$ (cp. Fig. 5.5): the smaller α, the flatter the curve close to the abscissa. Thus, small changes in the measured data points cause significant shifts in the forecasted time of failure. Again, the hourly datasets are less sensitive to α and have smaller uncertainties. However, it is noteworthy that it is not the goal to minimize the uncertainty to 0. The failure window should rather reflect a limited time window in which the expected failure is likely to happen. For the daily datasets the mean uncertainty is longer than two weeks for $\alpha \leq 1.7$, making these forecasts less useful for decision makers, while for the hourly datasets mean uncertainties are below 2 d for $\alpha \geq 1.6$.

In any case, forecasted time of failure and failure window must be evaluated together. Ideally, the actual time of failure is close to the mean forecasted time of failure but certainly within a reasonable failure window. For the daily datasets, this is on average the case for all $\alpha > 1.7$ and for the hourly datasets for all $\alpha > 1.9$, while the best results are achieved with $1.9 < \alpha < 2.1$.

5.2.3 Post-failure estimation of alpha

In a prospective forecast application, it is impossible to know beforehand, which α is the optimal choice. To overcome this, we have two possibilities: (i) calculate multiple forecasts with various α and decide based on statistics, or (ii) fix α to a value that is statistically most

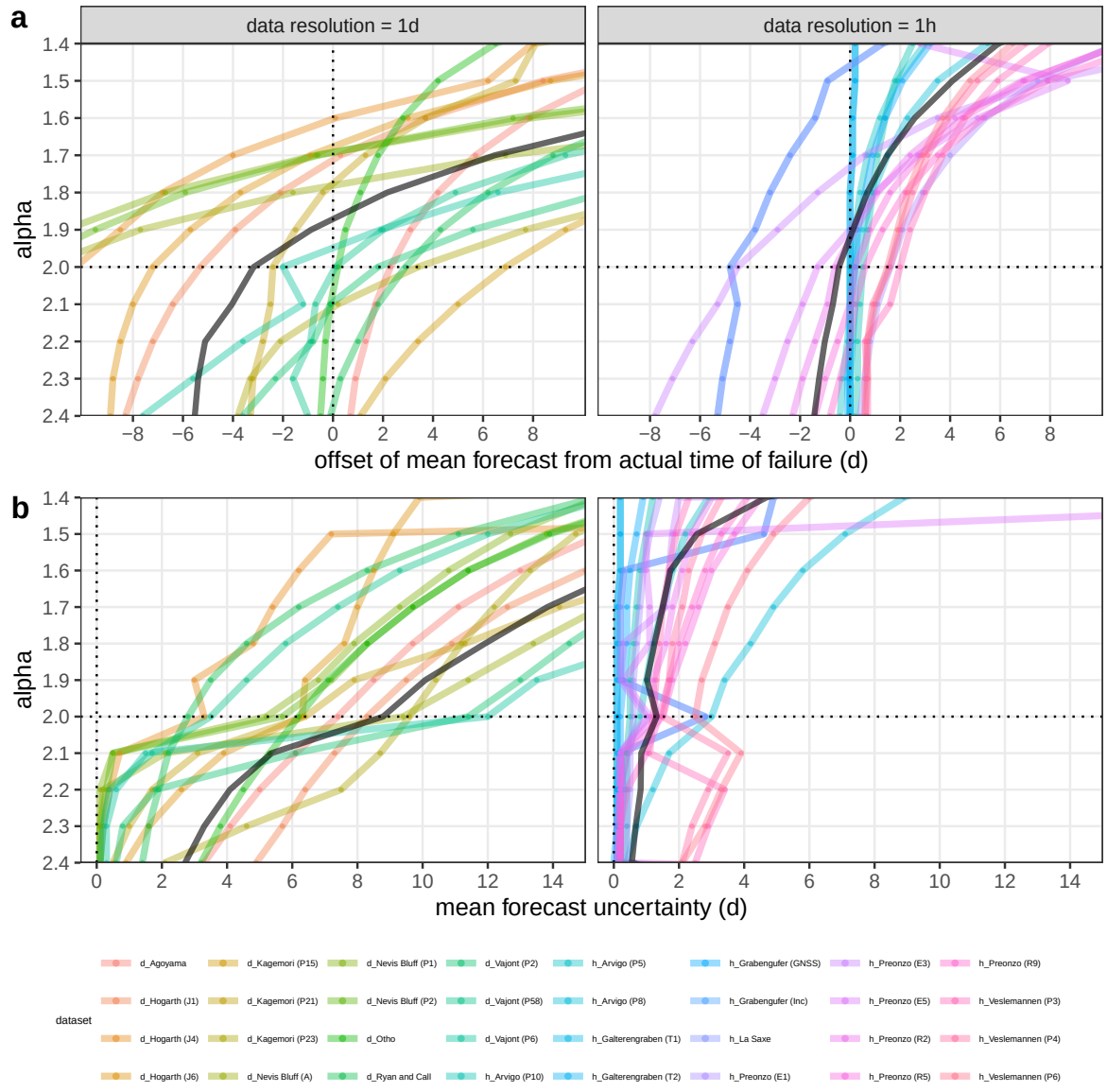

Figure 5.6: Forecast performance for 32 datasets against various α-values. The black line gives the mean per α. (a) Offset of the final mean forecast from the actual time of failure. (b) Mean width of the failure window (forecast uncertainty).

likely able to represent the data well. Given the significant variations in Fig. 5.6, the first option causes additional complexity to the decision makers. The previous section already confirmed that values close to 2 are reasonable. However, the knowledge of the actual time of failure for historical failures enables a post-failure analysis of optimal α values. Fig. 5.7 shows the clustering of determined α values around 2. In 51 % α represents a convex behaviour, and in 49 % a concave. The median α is 1.99, the mean α is 2.16. These results are in line with the studies from Segalini et al. (2018) and Intrieri et al. (2019). There is no obvious difference between the short, medium and long smoothing windows. This indicates that, if the acceleration is not obviously deviating much from the linear case, $\alpha = 2$ is a reasonable assumption for prospective forecasting. Using the linear case furthermore brings the advantage of mathematically robust uncertainty windows and less complexity, increasing the applicability in practise (Rose and Hungr, 2007, Carlà et al., 2017a, Intrieri et al., 2019).

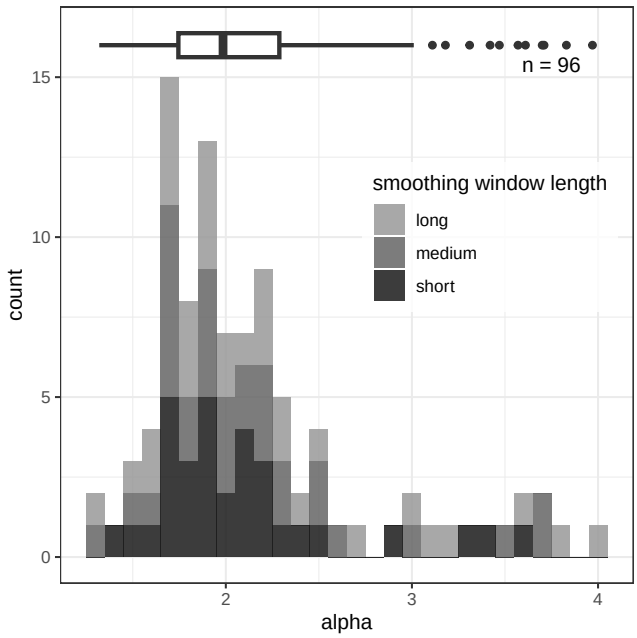

Figure 5.7: Best-fitting α-values derived by post-failure analysis of 32 datasets and three window lengths.

5.2.4 Conclusions

Our investigations of non-linear failure time forecasting yields the following findings:

1. Non-linear forecasts can improve the forecast accuracy, but are more complex and improvements are often marginal.
2. Convex forecasts tend to be less safe (less conservative) than linear forecasts and have bigger uncertainties.
3. Sensitivity towards α and forecast uncertainty decreases with higher temporal resolution of displacement data.
4. In prospective applications, $\alpha = 2$ is a reasonable choice based on the statistical post-failure analysis of historic events.

6 Main findings, synthesis and conclusions

This chapter highlights the main findings of this thesis, organized in the three-fold structure introduced in Fig. 1.1: monitoring - analysis - forecasting. All research questions stated in Chapter 1 are answered and discussed briefly. Finally, all points are synthesized.

6.1 Rock slope monitoring and early warning

6.1.1 How can we install and operate a reliable benchmark monitoring system at a high-alpine summit?

The high-alpine environment of the Hochvogel summit sets a general framework for monitoring activities (Leinauer et al., 2021): (i) limited access throughout the year especially in winter, (ii) inaccessible steep areas, (iii) no permanent power supply, (iv) high snow loads, (v) high probability of lightning strikes, (vi) highly jointed and weathered rock mass. The research project further stipulated the use of low- to medium-cost and highly available equipment. This implied the installation of ground-based geotechnical sensors in accessible areas (Chapter 3). Crackmeters can monitor the relative crack opening with high accuracy at low costs. In the main crack, where high snow pressures in winter prohibit the use of crackmeters, laser distance gauges are the better choice, although their accuracy is in the order of 1 mm (Section 4.2). Potential tilting of unstable rock blocks can be measured with simple inclinometers at high accuracy. Environmental factors are monitored with thermistors and a rain gauge, which is not in use in winter due to the lack of power supply for a heated gauge. However, at least in the case of the Hochvogel, the winter slope activity is generally very low (Section 4.1). Inaccessible areas like the steep SW-wall must be monitored with a remote technique. Here, a deformation camera provided a good balance between areal coverage, continuity of measurements, measurement frequency and cost (Section 3.2.4). However, during winter months, strong surface changes due to variable snow cover impede deformation analyses and the camera cannot operate in bad weather conditions without sight. An interferometric radar would be a more reliable option here (cp. Table 2.1), but is significantly more expensive.

For all techniques, areal pre-investigations on the potentially unstable mass and the deformation history (Section 3.1) are crucial for choosing the right instruments, with adequate resolution and range, and installing them in the right place. Particularly relative instruments

like crackmeters must be installed in the optimal direction to measure maximum displacements. Finally, due to the limited access to the site, all sensors must be installed robust to minimize the required maintenance.

Before, it was not clear, how to achieve a highly reliable of monitoring system under the challenging conditions at the Hochvogel. Such a system has been developed by following the principles of redundancy, consistency, continuity, and accuracy. Tiltmeters, multiple vibrating wire gauges and deformation camera operate redundant in the sense of redundant methods, redundant device locations and redundant data transmission. All geotechnical devices reach a high accuracy and especially tiltmeters guarantee a consistent continuity even if high snow loads hinder crack opening measurements in winter.

6.1.2 What design is needed to enable implementation in an operational local early warning system?

Local early warning systems consist of a balanced chain of the components (i) design, (ii) monitoring, (iii) forecasting and (iv) education (Fig. 2.5, Intrieri et al., 2012, 2013). The design includes a precise knowledge of the geological hazard including risk scenarios (Sections 3.1 and 4.1) while the education involves integration of stakeholders and close communication with local authorities and residents, which was an important part of the AlpSenseRely project. Forecasting includes data interpretation and alert generation and is directly based on the monitoring data. EWS can only be effective, if the lead time is longer than the time needed for mitigation measures (Hermle et al., 2021). Therefor, the time needed for data processing and interpretation must be kept short.

Accordingly, the monitoring system must be designed to operate continuously, reliably and automatically. All data must be gathered and processed automatically in a data management platform that allows the generation of alarms (Fig. 3.7). To minimize the probability of false alarms, which degrade the performance of an EWS (Sättele et al., 2016), we as the operating experts check critical situations first, before public alarms are communicated. For all alarm thresholds, stakeholders must be informed and trained beforehand, what the specific situation implicates.

At the Hochvogel, the complete early warning system chain from design and monitoring to forecasting and communication has been conducted scientifically in a real case. Especially the monitoring system could be gradually improved under the aspect of an operational early warning system.

6.1.3 How can we build up a resilient network of wireless sensors to increase the reliability?

Reliability has multiple aspects: data continuity (minimal data loss), redundancy of sensors, variety of observed parameters, and accuracy of monitoring techniques. To increase the resilience of the network towards high data coverage, we gained several learnings at

the Hochvogel. The most important modification was the transformation from a wired network with central data logger at the summit to a wireless LoRa network with individual data loggers (Section 3.1.4). The gateway, which is the main interface between the individual nodes and the internet, has been moved to the valley to a safe place. Like this, system interruptions, e.g. through lightning strikes, only affect a small part of the network instead of disabling the central data logger and with it the whole monitoring system. The use of individual monitoring nodes is also part of the effective lightning protection concept (Section 3.2.2), that minimized system damages. Furthermore, the protection of the devices with wooden roofs (Section 3.2.3) improved the resilience against rockfall or snow damage and also made the winter crackmeter data more reliable.

The second level of reliability has been increased by the use of multiple redundant sensors, e.g. two crackmeters per crack (Fig. 3.8). Furthermore, the installation of multiple tiltmeters added a second deformation parameter, which can be monitored reliably also in winter (Section 3.2.3). The whole geotechnical monitoring system at the Hochvogel is integrated into a multi-method approach (Fig. 2.4), that helps to cross-validate observations (Section 2.2.1). In the end, the level of resilience, reliability, or redundancy respectively, is always a question of available financial means. However, at the Hochvogel we could build up a resilient network of wireless sensors with limited financial means.

6.2 Quantification of preparing and triggering processes

6.2.1 What are the relevant drivers in the preparation phase of the Hochvogel rock slope failure?

Among all potential rock slope drivers and triggers are rainfall and snowmelt, earthquakes, internal crack propagation, temperature gradients, freeze-thaw-cycles, wind, lightning, snow or rock avalanches, volcanic activity, vegetation growth and root prying, permafrost degradation, and human or animal activity (cp. Sections 2.3 and 4.1.2). However, due to the high magnitude, location and altitude of the Hochvogel instability, most of those factors are irrelevant (Fig. 4.1). Four drivers could be identified relevant and were further analysed: water from rainfall, water from snowmelt, rock fracturing and earthquakes. Temperature gradients and freeze-thaw cycles might only affect smaller scale rockfalls from the flank (cp. Section 4.2). This site-specific and detailed evaluation allows further in-depth investigations concerning these relevant processes.

6.2.2 Can we quantify the proportional effects of these drivers based on monitoring data?

The high temporal resolution of the geotechnical and seismic monitoring data allowed a quantification of the relevant drivers. In the summer, 38 % of the total crack opening happens during wet days although these only account for 26 % of the total time. The average

and peak landslide velocity is 1.8 and 4-5 times higher during wet periods compared to periods without precipitation. The time lag between the rainfall signal and displacement rate is 1-16 h. Intense rainfall events with several mm/h accelerate the mass up to 1 mm/d (Section 4.1.5). Snowmelt usually occurs between April and July causing accelerated slope movements with longer lag times, between 4 and 9 days (Section 4.1.5). On average, modelled snowmelt of about 1.5 mm/h corresponds to displacement rates of ca. 0.01 mm/h.

Rock fracturing events seem not to correlate well with displacement rates. In contrast, we found the crack rate peaking during temperature peaks, likely related to thermal forcing through volumetric expansion and contraction of the rock mass and its minerals in the surface-near proportion of the rock mass. The maximum correlation coefficient appears with a time lag of 0-15 h. Additionally, freeze-thaw cycles in spring and autumn are enhancing the cracking activity (Section 4.1.5).

Earthquakes show a low-energy background activity, potentially contributing to a low-level promotion of slope instabilities through seismic fatigue. Close high-magnitude events are rare. Following a Newmark analysis, only very few events of >5,000 historical earthquakes are in the range of having triggering potential for very low FOS <1.03. Typical earthquakes around the Hochvogel (e.g. M_w 5 in 20 km distance or M_w 6 in 100 km distance) might only be able to trigger a major rockfall, if the unstable mass is anyways very close to failure (FOS around 1.01). Currently, only an exceptionally strong earthquake (e.g. M_w 6 in 15 km distance or M_w 7 in 50 km distance) could immediately trigger a major failure (Section 4.1.5). However, the geomorphological shape of the Hochvogel summit as well as the location of the unstable mass at the ridge generally favour the effect of topographic amplification. A comparison of the measured peak ground velocity (PGV) during earthquakes at the summit station against the lower stations shows up to 11 times higher median PGVs at the summit (mean = 3.2, Fig. 4.12). This could indicate that the summit experiences a significant amplification of seismic waves due to topographic site effects and resonant amplification.

This comprehensive quantification of what controls the slope deformation in the preparation phase before failure based on more than four years of high-resolution data gives rare insights into pre-failure high-magnitude rock slope dynamics and improves the understanding of rock slope failure anticipation.

6.2.3 What can most likely promote and trigger the future failure?

The process analysis revealed that meltwater infiltration controls the displacements during snowmelt in spring. Rainfall drives accelerated deformations during the snow-free summer without a minimum activation threshold. Measured internal rock cracking seems not to induce accelerations of the unstable mass directly, and also frequent typical earthquakes seem not to be strong enough to accelerate the rock mass in its current state (Section 4.1.6).

All of these factors are promoting factors at the Hochvogel, but the final failure itself will be most likely triggered in spring or summer by strong snowmelt or extreme precipitation. However, when a collapse of the slope is very imminent due to ongoing promotion, trigger-

ing through a strong local earthquake cannot be excluded. These insights help to anticipate the future failure at the Hochvogel and similar sites, and defines, where research and monitoring attention must be focused.

6.3 Failure time forecasting

6.3.1 How can we modify existing retrospective failure time forecasting methods to apply them prospectively?

Failure time forecasting using the inverse velocity method is based on observed deformations over time (Fukuzono, 1985). In contrast to retrospective applications, a prospective concept requires iteratively updated forecasts with new available data. Post-tuning of the results is impossible. Due to the ignorance of the actual failure time and missing standard procedures, data filtering, starting point definition (onset of acceleration, OOA) and forecast uncertainty remain unclear with previously existing methods. The continuous influx of monitoring data and the potentially large number of observation points in modern monitoring systems necessitate primarily automated methods for these tasks. We implemented such a prospective concept (Fig. 5.1) into an automatic algorithm with a clear smoothing process, a non-arbitrary OOA detection and a systematic real-time uncertainty estimation (Fig. 5.2). Data are processed iteratively with every new available data point using pre-accessible data only. Once the OOA has been detected automatically, an expected time of failure is calculated with all inverse velocities after the OOA, simultaneously for multiple smoothing window lengths. The forecast results are then evaluated based on consistently updated life expectancy plots where the predicted time until failure is plotted against the time when the forecast is made (Dick et al., 2015, Carlà et al., 2017b). Additional statistical information indicate the evolving reliability of the forecasts in real-time (Fig. A.2.1a and Section5.1.5).

This prospective failure time forecasting model is able to overcome the major drawbacks of previous retrospective methods achieving reliable results with a variety of slope failure processes, volumes, materials and sensor types. Furthermore, its application might not be limited to rock slopes, but the underlying physical principle might also be valid at earth slopes, man-made slopes, artificial structures and glaciers, thus supporting decision-makers in a multitude of critical situations.

6.3.2 How can we minimize the subjectivity of data smoothing and add real-time uncertainty estimations to the forecasts?

Filtering the raw monitoring data can improve forecast results, but the process involves subjective decisions and the forecasted failure time is sensitive to the degree of data smoothing. In the proposed prospective concept, this is resolved by the implementation of a two-step smoothing strategy and multiple window lengths (Section 5.1.4). In the first filtering step,

the displacement trend is clarified using a rolling mean of raw displacements across several smoothing windows. Subsequently, a range of inverse velocities is computed from each set of displacement data through linear regressions over multiple velocity windows, which define the number of data points used to derive the velocity (Section 5.1.5). The statistical information presented in the final life expectancy plot and boxplots allows a direct analysis of the chosen window lengths on the forecasts (Fig. A.2.1).

The optimal set of window lengths cannot be found prospectively, but Fig. A.2.2 gives an overview over the relative influence of various factors. Window lengths typically vary between few hours and multiple days and depend on the signal-to-noise ratio/ quality of the data, which is controlled by the deformation rate (signal), the measurement technique (noise), and the measurement frequency. Further, the expected duration of precursory accelerations and the time needed for emergency actions should be longer than the smoothing windows. A sufficiently high sampling frequency, e.g. daily or faster for volumes $> 10^6$ m^3 and hourly or faster for smaller volumes, in combination with adequate data filtering is key for good forecasting results (cp. Section 5.1.4). Longer smoothing windows can diminish the uncertainty of the forecasts, but excessive smoothing distorts the calculations and adds a lag to the time series shifting the results towards unsafe predictions (forecast after failure). Therefore, the smoothing windows should be as short as possible but as long as necessary. In case of trend updates, smoothing windows must be adjusted.

Responsible decision-makers always need a measure of reliability and uncertainty of the derived forecasts. Nonetheless, there is no standard procedure for a statistical real-time uncertainty estimation. The simultaneous use of multiple smoothing windows allows the real-time calculation of statistical uncertainty information. These are represented by a modified failure window (Carlà et al., 2017b), a forecasted period during which failure is likely. The width of the failure window and the consistency of its limits are useful indicators for the reliability of the forecasts. In most cases, failure windows converge with time, indicating an increasing confidence of the forecasts closer to the actual failure time (Section 5.1.4).

The two-step multi-window filtering concept and the generated real-time uncertainty information not only improve the performance of inverse velocity forecasting, they also add new concepts to the community that can be integrated into other forecasting approaches.

6.3.3 How can we detect the onset of acceleration automatically with a uniform and objective approach?

Our algorithm includes an automatic OOA detection method that is based on four simple criteria applied to all data points within the latest smoothing window (Section 5.1.4 and Fig. 5.2b). Criterion 1 requires an increasing displacement rate. Criterion 2 requires decreasing inverse velocities for all velocity windows. Criterion 3 requires an overall accelerating regime, represented by a decreasing 50 % inverse velocity quantile. Criterion 4 requires a short term accelerating trend, detected by inverse velocities smaller than the 1 % quantile, meaning that the latest velocity is greater than 99 % of all velocities before. If all criteria are

true over one complete smoothing window, the OOA is detected. Analogue to the smoothing windows, a restart of the OOA detection analysis is necessary in case of trend updates in the monitoring data.

This procedure minimizes the subjectivity of critical real-time decisions under the pressure of imminent failure, especially, when a multitude of monitoring data is taken into account. It can be integrated into automatic data processing and multi-sensor systems or combined with other OOA detection approaches.

6.3.4 How does a uniform forecasting model perform with 46 diverse datasets from available benchmark failures worldwide?

We tested our failure time forecasting concept with 46 datasets from 14 slope failures with daily or higher observation frequency. These failures of 10^2 to 10^8 m³ happened in diverse geological settings and the process types include rockslides, topples, rockfalls, compound failures and one ice fall (cp. Table A.2.1). The deformation data originate from various sensor types including extensometers, GNSS, inclinometers, total stations, and radars. Despite the variety of sensor and failure types, the model is able to overcome previous major drawbacks giving uniform and robust results (Section 5.1.4).

In all cases, the OOA is prospectively detected sufficiently early (0.1-200 d prior the actual time of failure). The timing of the OOA mainly depends on failure volume and process type (Section 5.1.4). The mean life expectancy at the actual time of failure of all sites is -1±17 h for sub-daily and -1±4 d for daily data sets respectively, representing a good fit of the forecasts to reality. The mean failure window width is 24±23 h and 7±4 d. All results must be assessed relative to the lead time at each specific site (Hermle et al., 2021). Overall, forecast accuracy is higher with higher-frequency data and closer towards the actual time of failure irrespective of the monitoring technique (Fig. 5.4). The reason why this concept performs well with a great variety of slope failures is that it uses the phenomenological effect of slope displacement which is the final expression of all influencing processes. Yet, it is important to complement the forecasting tool with geological knowledge and a profound understanding of each specific unstable site. At sites with challenging kinematic behaviour (e.g. Veslemannen and La Saxe), false OOA detections that complicate interpretations cannot be ruled out. Then, experience, a detailed knowledge of the site specific processes and the determination of secondary OOAs at trend update points can support reliable prospective forecasts. The Weissmiess ice fall is the only site where all failure windows lie slightly on the unsafe side (forecast after failure), but also shows that the concept of increasing accelerations is not limited to fracturing nor to rock and earth material.

The extension of the linear forecasting model ($\alpha = 2$) with non-linear models ($\alpha \neq 2$) can theoretically lead to more accurate results (Section 5.2). Concave forecast models ($\alpha > 2$) predict the time of failure earlier than the linear case, while convex models ($1 < \alpha < 2$) predict a later time of failure (Fig. 5.5). However, the results with all sites show that non-linear models can indeed improve the forecast accuracy, but they are more complex and improvements

are often marginal. The convex forecasts tend to be less safe (less conservative) than linear forecasts and have bigger uncertainties. Overall, the sensitivity towards α and the forecast uncertainty decreases with higher temporal resolution of displacement data. Based on the statistical post-failure analysis of historic events, $\alpha = 2$ is a reasonable choice in prospective applications.

Overall, we developed a forecasting model, which performs robust with all tested datasets, irrespective the great variety of slope failure processes, volumes, materials and sensor types. The onset of acceleration is detected automatically throughout at all sites and uniform forecast information including uncertainty estimation are provided.

6.4 Synthesis and conclusions

Local landslide early warning systems hold a great potential for future risk mitigation. Possibilities for improvement lie in every component of such systems. Indeed, it is important to improve every single component of landslide EWS, as, similar to a chain, the whole system is only as strong as the weakest link.

This thesis mainly focused on the three sub-topics of the second component: monitoring (Chapter 3), analysis (Chapter 4) and prediction (Chapter 5). The first two parts have been elaborated at the Hochvogel rock slope instability, a benchmark for imminent high-alpine rock slope failures. Due to the fact that the Hochvogel collapse is still a future scenario, forecasting could only be improved based on other historical slope failures. The real-time application of the developed forecasting method at the Hochvogel will generate further learnings in the final acceleration phase.

Looking at the links between the sub-topics of this thesis and the components of landslide EWS, we can redraw Fig. 1.1 from the Introduction to highlight the interconnected parts in the wider picture (Fig. 6.1). Once, knowledge of a hazard, respectively risk is present, monitoring activities are initiated. The monitoring data have to be analysed, which, on one hand improves the knowledge of the hazard and risk, and on the other hand allows to redefine the monitoring strategy (location, frequency, resolution, accuracy, etc.). The monitoring data are further the input for forecasting models. Life expectancy predictions and alarm levels must be communicated together with direct observations from the monitoring system to any eligible stakeholders. The evaluation of these data and anticipations is always strengthened by the detailed process analyses. The final component of local capabilities to respond, respectively the time needed for mitigation measures, in turn defines where to set alarm thresholds and when certain actions should be initiated. Only, if all components intertwine successfully, early warning can function reliably.

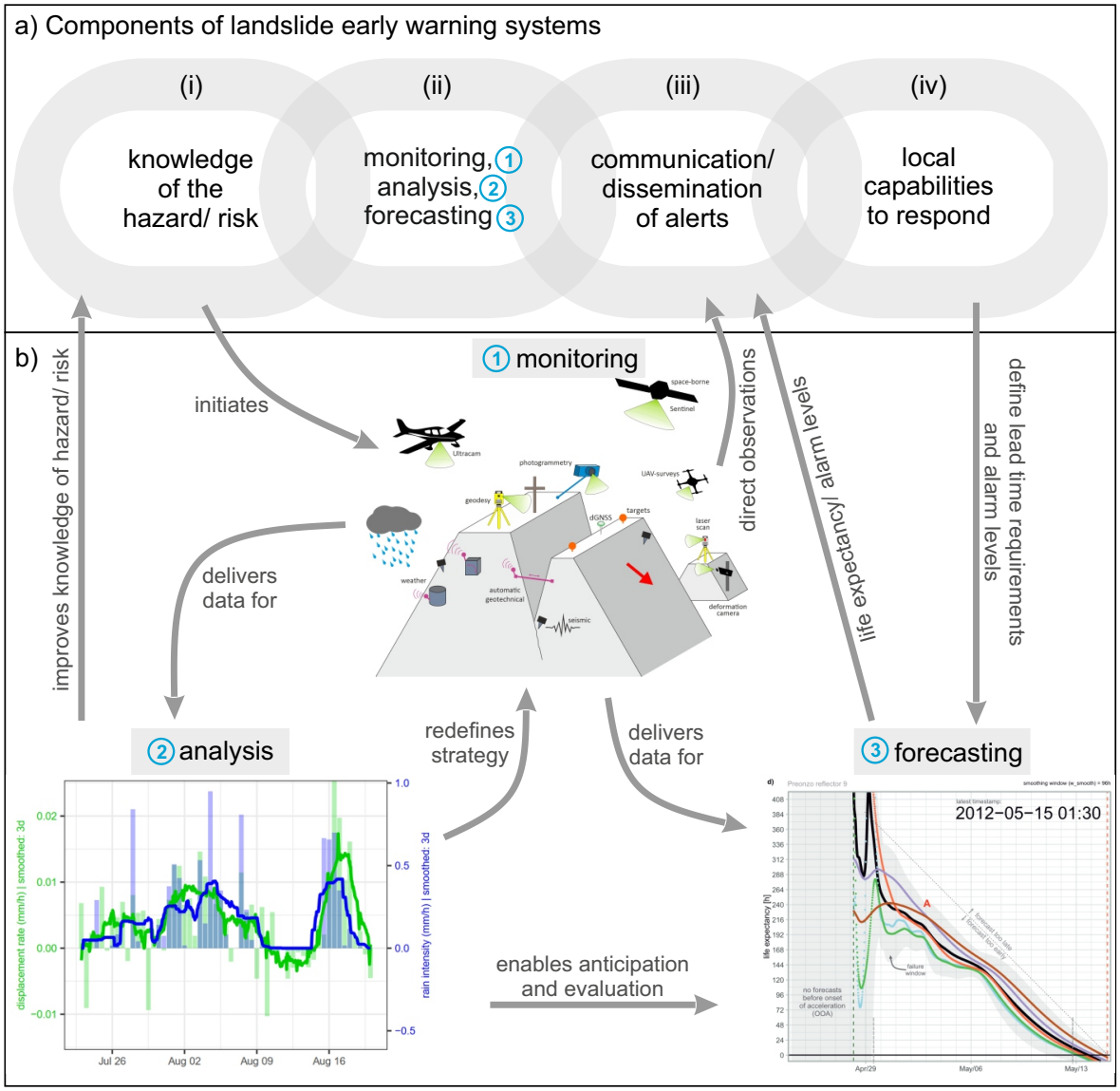

Figure 6.1: (a) Key elements of early warning systems (adapted from UN/ISDR 2009 and Intrieri et al. 2013). (b) Fields covered in this thesis and their context.

Conclusions

By enhancing the fields of real-time monitoring, process analysis and failure time forecasting in detail, this thesis advances future rock slope failure early warning capabilities. The following conclusions can be drawn:

- The developed operative real-time monitoring system at the Hochvogel consisting of twelve geotechnical wireless nodes (crackmeters, laser distance gauges and inclinometers), a rain gauge, and a deformation camera is a benchmark for reliable rock slope failure monitoring in high-alpine environment.
- The unique multi-method combination of several geotechnical, seismic, and remote sensing techniques guarantees a continuous, comprehensive, redundant and complementary observation of the unstable slope fulfilling the requirements for reliable early warning.
- More than four years of high-resolution data from the geotechnical network and the seismic stations enable the first comprehensive quantification of what controls the rock slope deformation in the preparation phase before failure.
- Accelerations of the slope instability mainly result from snowmelt in spring and strong rain events during summer with high correlation factors and time lags of few days and few hours, respectively.
- Rock fracturing events detected by the local seismic stations ($n > 21,000$) are temperature-driven, surface-near, and unrelated to measured displacement rates of the high-magnitude instability.
- Typical local earthquakes ($n > 5,000$) may contribute to a long-term seismic fatigue, but unlikely trigger a massive rockfall at the Hochvogel, unless the factor of safety is already very close to 1. Topographic amplification reaches a factor of 2-11 and is heterogeneous, indicating a high criticality of the slope in its current status.
- Once the slope passes the onset of acceleration (entering the tertiary creep phase), prospective failure time forecasts including uncertainty estimations can be calculated with the developed novel forecasting concept, which overcomes several previous major problems.
- The automatic detection of the onset of acceleration is implemented in the developed forecasting algorithm by applying four criteria and inverse velocity quantiles - a prerequisite for prospective forecasting in modern early warning systems with multiple sensors and high-frequency data.
- According to the 46 tested failure datasets, the inverse velocity method after Fukuzono (1985) can give reliable and uniform results across sensor and failure types, when the data filtering is appropriate. The subjectivity for this process is minimized by the suggested multiple window approach. Higher frequency monitoring data tend to give more accurate and more reliable forecasts.
- Based on the evaluated cases, the linear Fukuzono model with $\alpha = 2$ is the best choice in prospective forecasting applications.

7 Outlook and future perspectives

The development of landslide early warning systems is never completed. There are several factors and possibilities that influence the future development of landslide early warning systems (Fig. 7.1). Of course, an optimal system can be designed today after current state of scientific and technical knowledge, but both continue to improve with considerable potential. Every year, new ground-based sensors are introduced to the market, either offering low-cost solutions, achieving higher accuracy or sampling frequency, or simplifying wireless monitoring. In the field of remote sensing, new generations of satellites with better sensors, better coverage or shorter recurrence intervals, as well as automated drone campaigns will add even more data to the community. Following the results of this thesis, this is promising for the quality of future failure anticipation. However, the increasing amount of data, which certainly holds great potential for enhancing early warning capabilities, must be organized and made accessible so that more research can be done with them. Due to the low frequency of massive rock slope failure events and the manifold nature of geological problems, it is crucial, to evaluate more than just one well documented case study like the Hochvogel. Only then can general and robust findings be defined and exceptional cases assessed.

In recent years, artificial intelligence in data processing has been advancing at an extraordinary pace. The development of machine learning algorithms and increasing computing power enable the automatic analysis of very large and complex datasets. Even invisible connections to the human eye (or perception) can thus be highlighted, sometimes significantly faster than would be possible with traditional methods. Especially in the field of deep learning, automatic algorithms fed with continuously updated monitoring data can improve themselves significantly. Artificial intelligence is already finding increasing application in landslide mapping, detection, and regional forecasting. Therefore, the use of artificial intelligence and machine learning holds the promise of significant advancements in the local prediction of rock slope failures.

Rock slope failure process dynamics will continue to be altered by climatic changes. While some of the changes and their effects are rather clear (temperature increase), others remain less clear (precipitation patterns). Any change in the external forcing of slope instabilities has the potential to modify internal process dynamics, but the dimension and relevance of the effect might vary among different geological slopes. Ideally, these changes in the known process dynamics should be quantified and evaluations must be updated as the climatic conditions continue to change. It is already becoming apparent that the likelihood and dy-

namics of natural hazard events in the context of climate change are beyond the experiential knowledge of experts and the general population. Therefore, anticipating such events becomes more important. Science is thus one of the most crucial tools to adapt rapidly and effectively to the altered conditions in a changing climate.

Finally, many people worldwide still suffer from rock slope failures every year. The possibilities for rock slope failure anticipation developed and presented in this thesis could improve risk mitigation in many cases. However, the application of those is limited to local cases, where the knowledge of the hazard already exists, where there is enough time to set up monitoring, and where there is enough money and political structure to implement an early warning system. In many past catastrophes, knowledge of the hazard did not exist and the catastrophic event happened unforeseen. Therefore, the scientific community must work on possibilities to scale up anticipation concepts to a regional and global, spatially inclusive and comprehensive application. If it is possible to detect hazardous hotspots in whole regions or globally, then, local early warning approaches can be set up systematically to prevent from damage or loss of lives.

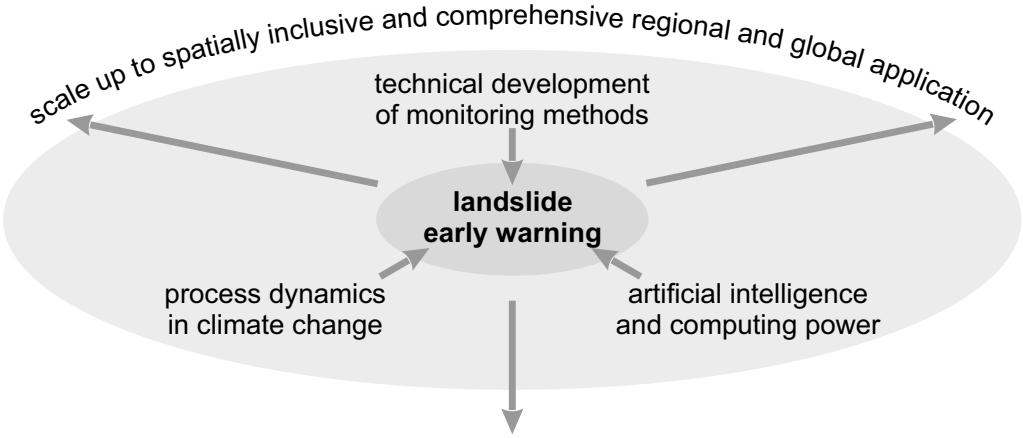

Figure 7.1: Future perspectives of landslide early warning.

List of Figures

List of Tables

References

Aaron, J. and McDougall, S.: Rock avalanche mobility: The role of path material, Engineering Geology, 257, 105–126, doi: 10.1016/j.enggeo.2019.05.003, 2019.

Allen, R.: Automatic phase pickers: Their present use and future prospects, Bulletin of the Seismological Society of America, 72, 225–242, doi: 10.1785/BSSA07206B0225, 1982.

Amitrano, D. and Helmstetter, A.: Brittle creep, damage, and time to failure in rocks, Journal of Geophysical Research, 111, doi: 10.1029/2005JB004252, 2006.

Angeli, M.-G., Pasuto, A., and Silvano, S.: A critical review of landslide monitoring experiences, Engineering Geology, 55, 133–147, doi: 10.1016/S0013-7952(99)00122-2, 2000.

Arias, A.: A Measure of Earthquake Intensity, in: Seismic Design for Nuclear Power Plants, edited by Hansen, R. J., pp. 438–483, Massachusetts Inst. of Tech. Press, Cambridge, Mass., 1970.

Awal, R., Nakagawa, H., Baba, Y., Sharma, R. H., and Ito, N.: Study on Landslide Dam Failure by Sliding, Annuals of Disas. Prev. Res. Inst., Kyoto Univ., 50B, 653–660, 2007.

Baillard, C., Crawford, W. C., Ballu, V., Hibert, C., and Mangeney, A.: An Automatic Kurtosis-Based P- and S-Phase Picker Designed for Local Seismic Networks, Bulletin of the Seismological Society of America, 104, 394–409, doi: 10.1785/0120120347, 2014.

Bakun-Mazor, D., Hatzor, Y. H., Glaser, S. D., and Carlos Santamarina, J.: Thermally vs. seismically induced block displacements in Masada rock slopes, International Journal of Rock Mechanics and Mining Sciences, 61, 196–211, doi: 10.1016/j.ijrmms.2013.03.005, 2013.

Ballantyne, C. K., Sandeman, G. F., Stone, J. O., and Wilson, P.: Rock-slope failure following Late Pleistocene deglaciation on tectonically stable mountainous terrain, Quaternary Science Reviews, 86, 144–157, doi: 10.1016/j.quascirev.2013.12.021, 2014.

Barbosa, N., Leinauer, J., Jubanski, J., Dietze, M., Münzer, U., Siegert, F., and Krautblatter, M.: Massive sediment pulses triggered by a multi-stage 130 000 m 3 alpine cliff fall (Hochvogel, DE–AT), Earth Surface Dynamics, 12, 249–269, doi: 10.5194/esurf-12-249-2024, 2024.

Berger, C., McArdell, B. W., and Lauber, G.: Murgangmodellierung im Illgraben, Schweiz, mit dem numerischen 2D-Modell RAMMS, 12th Congress INTERPRAEVENT 2012, pp. 37–45, 2012.

BGR: Deutscher Erdbebenkatalog: Bundesanstalt für Geowissenschaften und Rohstoffe, URL https://services.bgr.de/geophysik/gerseis, 2023.

Blanchet, J., Blanc, A., and Creutin, J.-D.: Explaining recent trends in extreme precipitation in the Southwestern Alps by changes in atmospheric influences, Weather and Climate Extremes, 33, 100 356, doi: 10.1016/j.wace.2021.100356, 2021.

Blikra, L. H. and Christiansen, H. H.: A field-based model of permafrost-controlled rockslide deformation in northern Norway, Geomorphology, 208, 34–49, doi: 10.1016/j.geomorph.2013.11.014, 2014.

Borecka, A., Herzig, J., and Durjasz-Rybacka, M.: Ground Penetrating Radar Investigations of Landslides: A Case Study in a Landslide in Radziszów, Studia Geotechnica et Mechanica, 37, 11–18, doi: 10.1515/sgem-2015-0028, 2015.

Borri-Brunetto, M., Carpinteri, A., and Chiaia, B.: The Effect of Scale and Criticality in Rock Slope Stability, Rock Mechanics and Rock Engineering, 37, 117–126, doi: 10.1007/s00603-003-0004-1, 2004.

Bozzano, F., Mazzanti, P., and Moretto, S.: Discussion to: 'Guidelines on the use of inverse velocity method as a tool for setting alarm thresholds and forecasting landslides and structure collapses' by T. Carlà, E. Intrieri, F. Di Traglia, T. Nolesini, G. Gigli and N. Casagli, Landslides, 15, 1437–1441, doi: 10.1007/s10346-018-0976-2, 2018.

Breiman, L.: Random Forests, Machine Learning, 45, 5–32, doi: 10.1023/A:1010933404324, 2001.

Burjánek, J., Gassner-Stamm, G., Poggi, V., Moore, J. R., and Fäh, D.: Ambient vibration analysis of an unstable mountain slope, Geophysical Journal International, 180, 820–828, doi: 10.1111/j.1365-246X.2009.04451.x, 2010.

Burjánek, J., Moore, J. R., Yugsi Molina, F. X., and Fäh, D.: Instrumental evidence of normal mode rock slope vibration, Geophysical Journal International, 188, 559–569, doi: 10.1111/j.1365-246X.2011.05272.x, 2012.

Cabrejo-Liévano, A. G.: Analysis of failures in open pit mines and consideration of the uncertainty when predicting collapses, in: Slope stability 2013, edited by Dight, P. M., pp. 483–498, ACG, Nedlands, 2013.

Carlà, T., Farina, P., Intrieri, E., Botsialas, K., and Casagli, N.: On the monitoring and early-warning of brittle slope failures in hard rock masses: Examples from an open-pit mine, Engineering Geology, 228, 71–81, doi: 10.1016/j.enggeo.2017.08.007, 2017a.

Carlà, T., Intrieri, E., Di Traglia, F., Nolesini, T., Gigli, G., and Casagli, N.: Guidelines on the use of inverse velocity method as a tool for setting alarm thresholds and forecasting landslides and structure collapses, Landslides, 14, 517–534, doi: 10.1007/s10346-016-0731-5, 2017b.

Carlà, T., Intrieri, E., Raspini, F., Bardi, F., Farina, P., Ferretti, A., Colombo, D., Novali, F., and Casagli, N.: Perspectives on the prediction of catastrophic slope failures from satellite InSAR, Scientific reports, 9, 14 137, doi: 10.1038/s41598-019-50792-y, 2019.

Casagli, N., Intrieri, E., Carlà, T., Di Traglia, F., Frodella, W., Gigli, G., Lombardi, L., Nocentini, M., Raspini, F., and Tofani, V.: Monitoring and Early Warning Systems: Applications and Perspectives, in: Understanding and Reducing Landslide Disaster Risk, edited by Casagli, N., Tofani, V., Sassa, K., Bobrowsky, P. T., and Takara, K., ICL Contribution to Landslide Disaster Risk Reduction, pp. 1–21, Springer International Publishing, Cham, doi: 10.1007/978-3-030-60311-3_1, 2021.

Chae, B.-G., Park, H.-J., Catani, F., Simoni, A., and Berti, M.: Landslide prediction, monitoring and early warning: a concise review of state-of-the-art, Geosciences Journal, 21, 1033–1070, doi: 10.1007/s12303-017-0034-4, 2017.

Chen, T., Zhang, G., and Xiang, X.: Research on rockfall impact process based on viscoelastic contact theory, International Journal of Impact Engineering, 173, 104 431, doi: 10.1016/j.ijimpeng.2022.104431, 2023.

Cicoira, A., Weber, S., Biri, A., Buchli, B., Delaloye, R., Da Forno, R., Gärtner-Roer, I., Gruber, S., Gsell, T., Hasler, A., Lim, R., Limpach, P., Mayoraz, R., Meyer, M., Noetzli, J., Phillips, M., Pointner, E., Raetzo, H., Scapozza, C., Strozzi, T., Thiele, L., Vieli, A., Vonder Mühll, D., Wirz, V., and Beutel, J.: In situ observations of the Swiss periglacial environment using GNSS instruments, Earth System Science Data, 14, 5061–5091, doi: 10.5194/essd-14-5061-2022, 2022.

Collins, B. D. and Stock, G. M.: Rockfall triggering by cyclic thermal stressing of exfoliation fractures, Nature Geoscience, 9, 395–400, doi: 10.1038/NGEO2686, 2016.

Corcoran, J. and Davies, C. M.: Monitoring power-law creep using the Failure Forecast Method, International Journal of Mechanical Sciences, 140, 179–188, doi: 10.1016/j.ijmecsci.2018.02.041, 2018.

Costa, J. E. and Schuster, R. L.: Documented historical landslide dams from around the world, U.S. geological Survey, Vancouver, USGS report no. 91-239, 91–239, 1991.

Crosta, G. B. and Agliardi, F.: Failure forecast for large rock slides by surface displacement measurements, Canadian Geotechnical Journal, 40, 176–191, doi: 10.1139/T02-085, 2003.

Crosta, G. B., Di Prisco, C., Frattini, P., Frigerio, G., Castellanza, R., and Agliardi, F.: Chasing a complete understanding of the triggering mechanisms of a large rapidly evolving rockslide, Landslides, 11, 747–764, doi: 10.1007/s10346-013-0433-1, 2014.

Cruden, D. M.: A simple definition of a landslide, Bulletin of the International Association of Engineering Geology, 43, 27–29, doi: 10.1007/BF02590167, 1991.

Cruden, D. M. and Varnes, D. J.: Landslide types and processes, in: Landslides - investigation and mitigation, edited by Turner, A. and Schuster, R., pp. 36–75, National Academy Press, 1996.

D'Amato, J., Hantz, D., Guerin, A., Jaboyedoff, M., Baillet, L., and Mariscal, A.: Influence of meteorological factors on rockfall occurrence in a middle mountain limestone cliff, Natural Hazards and Earth System Sciences, 16, 719–735, doi: 10.5194/nhess-16-719-2016, 2016.

Davies, T. R. and McSaveney, M. J.: The role of rock fragmentation in the motion of large landslides, Engineering Geology, 109, 67–79, doi: 10.1016/j.enggeo.2008.11.004, 2009.

Delacourt, C., Allemand, P., Berthier, E., Raucoules, D., Casson, B., Grandjean, P., Pambrun, C., and Varel, E.: Remote-sensing techniques for analysing landslide kinematics: a review, Bulletin de la Société Géologique de France, 178, 89–100, doi: 10.2113/gssgfbull.178.2.89, 2007.

Dick, G. J., Eberhardt, E., Cabrejo-Liévano, A. G., Stead, D., and Rose, N. D.: Development of an early-warning time-of-failure analysis methodology for open-pit mine slopes utilizing ground-based slope stability radar monitoring data, Canadian Geotechnical Journal, 52, 515–529, doi: 10.1139/cgj-2014-0028, 2015.

Dietrich, A. and Krautblatter, M.: Evidence for enhanced debris-flow activity in the Northern Calcareous Alps since the 1980s (Plansee, Austria), Geomorphology, 287, 144–158, doi: 10.1016/j.geomorph.2016.01.013, 2017.

Dietze, M.: The R package "eseis" – a software toolbox for environmental seismology, Earth Surface Dynamics, 6, 669–686, doi: 10.5194/esurf-6-669-2018, 2018a.

Dietze, M.: 'eseis' - a comprehensive R software toolbox for environmental seismology, doi: 10.5880/GFZ.5.1.2018.001, 2018b.

Dietze, M., Mohadjer, S., Turowski, J. M., Ehlers, T. A., and Hovius, N.: Seismic monitoring of small alpine rockfalls – validity, precision and limitations, Earth Surface Dynamics, 5, 653–668, doi: 10.5194/esurf-5-653-2017, 2017a.

Dietze, M., Turowski, J. M., Cook, K. L., and Hovius, N.: Spatiotemporal patterns, triggers and anatomies of seismically detected rockfalls, Earth Surface Dynamics, 5, 757–779, doi: 10.5194/esurf-5-757-2017, 2017b.

Dietze, M., Krautblatter, M., Illien, L., and Hovius, N.: Seismic constraints on rock damaging related to a failing mountain peak: the Hochvogel, Allgäu, Earth Surface Processes and Landforms, 46, 417–429, doi: 10.1002/esp.5034, 2021.

Do, X. K., Kim, M., Nguyen, H. T., and Jung, K.: Analysis of Landslide Dam Failure Caused by Overtopping, Procedia Engineering, 154, 990–994, doi: 10.1016/j.proeng.2016.07.587, 2016.

Dufresne, A., Bösmeier, A., and Prager, C.: Sedimentology of rock avalanche deposits – Case study and review, Earth-Science Reviews, 163, 234–259, doi: 10.1016/j.earscirev.2016.10.002, 2016.

Eberhardt, E., Stead, D., and Coggan, J. S.: Numerical analysis of initiation and progressive failure in natural rock slopes—the 1991 Randa rockslide, International Journal of Rock Mechanics and Mining Sciences, 41, 69–87, doi: 10.1016/S1365-1609(03)00076-5, 2004.

Erismann, T. H. and Abele, G.: Dynamics of rockslides and rockfalls, Springer, Berlin and Heidelberg, doi: 10.1007/978-3-662-04639-5, URL `https://link.springer.com/book/10.1007/978-3-662-04639-5`, 2001.

Evans, S. G.: Single-event landslides resulting from massive rock slope failure: characterising their frequency and impact on society, in: Landslides from Massive Rock Slope Failure, edited by Evans, S. G., Mugnozza, G. S., Strom, A., and Hermanns, R. L., vol. 49 of *NATO Science Series*, pp. 53–73, Springer Netherlands, Dordrecht, doi: 10.1007/978-1-4020-403

7-5_2, 2006.

Evans, S. G., Mugnozza, G. S., Strom, A., and Hermanns, R. L., eds.: Landslides from Massive Rock Slope Failure, NATO Science Series, Springer Netherlands, Dordrecht, doi: 10.1007/978-1-4020-4037-5, 2006a.

Evans, S. G., Mugnozza, G. S., Strom, A., Hermanns, R. L., Ischuk, A., and Vinnichenko, S.: Landslides from massive rock slope failure and associated phenomena, in: Landslides from Massive Rock Slope Failure, edited by Evans, S. G., Mugnozza, G. S., Strom, A., and Hermanns, R. L., vol. 49 of *NATO Science Series*, pp. 03–52, Springer Netherlands, Dordrecht, doi: 10.1007/978-1-4020-4037-5_1, 2006b.

Evans, S. G., Hermanns, R. L., Strom, A., and Scarascia-Mugnozza, G.: Natural and Artificial Rockslide Dams, vol. 133, Springer Berlin Heidelberg, Berlin, Heidelberg, doi: 10.1007/978-3-642-04764-0, 2011.

Federico, A., Popescu, M., and Murianni, A.: Temporal Prediction of landslide occurence: A possibility or a challenge?, IJEGE, 15, 41–60, 2015.

Fey, C. and Wichmann, V.: Long–range terrestrial laser scanning for geomorphological change detection in alpine terrain – handling uncertainties, Earth Surface Processes and Landforms, 42, 789–802, doi: 10.1002/esp.4022, 2017.

Frank, F., McArdell, B. W., Oggier, N., Baer, P., Christen, M., and Vieli, A.: Debris-flow modeling at Meretschibach and Bondasca catchments, Switzerland: sensitivity testing of field-data-based entrainment model, Natural Hazards and Earth System Sciences, 17, 801–815, doi: 10.5194/nhess-17-801-2017, 2017.

Frei, C., Schöll, R., Fukutome, S., Schmidli, J., and Vidale, P. L.: Future change of precipitation extremes in Europe: Intercomparison of scenarios from regional climate models, Journal of Geophysical Research, 111, doi: 10.1029/2005JD005965, 2006.

Frei, P., Kotlarski, S., Liniger, M. A., and Schär, C.: Future snowfall in the Alps: projections based on the EURO-CORDEX regional climate models, The Cryosphere, 12, 1–24, doi: 10.5194/tc-12-1-2018, 2018.

Fujisawa, K., Marcato, G., Nomura, Y., and Pasuto, A.: Management of a typhoon-induced landslide in Otomura (Japan), Geomorphology, 124, 150–156, doi: 10.1016/j.geomorph.2010.09.027, 2010.

Fukuzono, T.: A Method to Predict the Time of Slope Failure Caused by Rainfall Using the Inverse Number of Velocity of Surface Displacement, Journal of Japan Landslide Society, 22, 8–14, 1985.

Fukuzono, T.: Recent Studies in Time Prediction of Slope Failure, Landslide News, 4, 9–12, 1990.

Gamperl, M., Singer, J., and Thuro, K.: Internet of Things Geosensor Network for Cost-Effective Landslide Early Warning Systems, Sensors (Basel, Switzerland), 21, doi: 10.3390/s21082609, 2021.

Gariano, S. L. and Guzzetti, F.: Landslides in a changing climate, Earth-Science Reviews, 162, 227–252, doi: 10.1016/j.earscirev.2016.08.011, 2016.

GEOPRAEVENT: Technologie-Handbuch für die Überwachung von gravitativen Naturgefahren, Geoprevent AG, Zürich, 1 edn., 2019.

Ghirotti, M.: The 1963 Vaiont landslide, Italy, in: Landslides, edited by Clague, J. J. and Stead, D., pp. 359–372, Cambridge University Press, doi: 10.1017/CBO9780511740367.030, 2013.

Gigli, G., Fanti, R., Canuti, P., and Casagli, N.: Integration of advanced monitoring and numerical modeling techniques for the complete risk scenario analysis of rockslides: The case of Mt. Beni (Florence, Italy), Engineering Geology, 120, 48–59, doi: 10.1016/j.enggeo.2011.03.017, 2011.

Gill, J. C. and d. Malamud, B.: Reviewing and visualizing the interactions of natural hazards, Reviews of Geophysics, 52, 680–722, doi: 10.1002/2013RG000445, 2014.

Giordan, D., Wrzesniak, A., Allasia, P., and Bertolo, D.: Automatized Dissemination of Landslide Monitoring Bulletins for Early Warning Applications, in: Understanding and Reducing Landslide Disaster Risk, edited by Arbanas, Ž., Bobrowsky, P. T., Konagai, K., Sassa, K., and Takara, K., ICL Contribution to Landslide Disaster Risk Reduction, pp. 231–235, Springer International Publishing, Cham, doi: 10.1007/978-3-030-60713-5_25, 2021.

Gischig, V., Preisig, G., and Eberhardt, E.: Numerical Investigation of Seismically Induced Rock Mass Fatigue as a Mechanism Contributing to the Progressive Failure of Deep-Seated Landslides, Rock Mechanics and Rock Engineering, 49, 2457–2478, doi: 10.1007/s00603-015-0821-z, 2016.

Grebby, S., Sowter, A., Gluyas, J., Toll, D., Gee, D., Athab, A., and Girindran, R.: Advanced analysis of satellite data reveals ground deformation precursors to the Brumadinho Tailings Dam collapse, Communications Earth & Environment, 2, doi: 10.1038/s43247-020-00079-2, 2021.

Gunzburger, Y., Merrien-Soukatchoff, V., and Guglielmi, Y.: Influence of daily surface temperature fluctuations on rock slope stability: case study of the Rochers de Valabres slope (France), International Journal of Rock Mechanics and Mining Sciences, 42, 331–349, doi: 10.1016/j.ijrmms.2004.11.003, 2005.

Guzzetti, F.: Landslide fatalities and the evaluation of landslide risk in Italy, Engineering Geology, 58, 89–107, doi: 10.1016/S0013-7952(00)00047-8, 2000.

Guzzetti, F.: On the Prediction of Landslides and Their Consequences, in: Understanding and Reducing Landslide Disaster Risk, edited by Sassa, K., Mikoš, M., Sassa, S., Bobrowsky, P. T., Takara, K., and Dang, K., ICL Contribution to Landslide Disaster Risk Reduction, pp. 3–32, Springer International Publishing, Cham, doi: 10.1007/978-3-030-60196-6_1, 2021.

Haeberli, W., Huggel, C., Kääb, A., Zgraggen-Oswald, S., Polkvoj, A., Galushkin, I., Zotikov, I., and Osokin, N.: The Kolka-Karmadon rock/ice slide of 20 September 2002: an extraordinary event of historical dimensions in North Ossetia, Russian Caucasus, Journal of Glaciology, 50, 533–546, doi: 10.3189/172756504781829710, 2004.

Harp, E. L. and Jibson, R. W.: Anomalous Concentrations of Seismically Triggered Rock Falls in Pacoima Canyon: Are They Caused by Highly Susceptible Slopes or Local Amplification of Seismic Shaking?, Bulletin of the Seismological Society of America, 92, 3180–3189, doi: 10.1785/0120010171, 2002.

Heckmann, T., Bimböse, M., Krautblatter, M., Haas, F., Becht, M., and Morche, D.: From geotechnical analysis to quantification and modelling using LiDAR data: a study on rockfall in the Reintal catchment, Bavarian Alps, Germany, Earth Surface Processes and Landforms, 37, 119–133, doi: 10.1002/esp.2250, 2012.

Heim, A.: Bergsturz und Menschenleben, Fretz & Wasmuth, Zürich, 1932.

Heißel, G. and Figl, T.: Gemeinde Hinterhornbach – Hochvogel; Abklärung der aktuellen Steinschlag-, Blocksturz- und Felssturzsituation; Stellungnahme der Landesgeologie, Amt der Tiroler Landesregierung, Innsbruck, 2014.

Helmstetter, A. and Garambois, S.: Seismic monitoring of Séchilienne rockslide (French Alps): Analysis of seismic signals and their correlation with rainfalls, Journal of Geophysical Research, 115, doi: 10.1029/2009JF001532, 2010.

Hermle, D., Keuschnig, M., Hartmeyer, I., Delleske, R., and Krautblatter, M.: Timely prediction potential of landslide early warning systems with multispectral remote sensing: a conceptual approach tested in the Sattelkar, Austria, Natural Hazards and Earth System Sciences, 21, 2753–2772, doi: 10.5194/nhess-21-2753-2021, 2021.

Hewitt, K., Clague, J. J., and Deline, P.: Catastrophic Rock Slope Failures and Mountain Glaciers, in: Encyclopedia of Snow, Ice and Glaciers, edited by Singh, V. P., Singh, P., and Haritashya, U. K., Encyclopedia of Earth Sciences Series, pp. 113–126, Springer Netherlands, Dordrecht, doi: 10.1007/978-90-481-2642-2_615, 2011.

Hibert, C., Mangeney, A., Grandjean, G., and Shapiro, N. M.: Slope instabilities in Dolomieu crater, Réunion Island: From seismic signals to rockfall characteristics, Journal of Geophysical Research, 116, doi: 10.1029/2011JF002038, 2011.

Hibert, C., Provost, F., Malet, J.-P., Maggi, A., Stumpf, A., and Ferrazzini, V.: Automatic identification of rockfalls and volcano-tectonic earthquakes at the Piton de la Fournaise volcano using a Random Forest algorithm, Journal of Volcanology and Geothermal Research, 340, 130–142, doi: 10.1016/j.jvolgeores.2017.04.015, 2017.

Hilger, P., Hermanns, R. L., Czekirda, J., Myhra, K. S., Gosse, J. C., and Etzelmüller, B.: Permafrost as a first order control on long-term rock-slope deformation in (Sub-)Arctic Norway, Quaternary Science Reviews, 251, 106 718, doi: 10.1016/j.quascirev.2020.106718, 2021.

Hormes, A., Adams, M., Amabile, A. S., Blauensteiner, F., Demmler, C., Fey, C., Ostermann, M., Rechberger, C., Sausgruber, T., Vecchiotti, F., Vick, L. M., and Zangerl, C.: Innovative methods to monitor rock and mountain slope deformation, Geomechanics and Tunnelling, 13, 88–102, doi: 10.1002/geot.201900074, 2020.

Huggel, C., Khabarov, N., Obersteiner, M., and Ramírez, J. M.: Implementation and integrated numerical modeling of a landslide early warning system: a pilot study in Colom-

bia, Natural Hazards, 52, 501–518, doi: 10.1007/s11069-009-9393-0, 2010.

Huggel, C., Allen, S., Deline, P., Fischer, L., Noetzli, J., and Ravanel, L.: Ice thawing, mountains falling-are alpine rock slope failures increasing?, Geology Today, 28, 98–104, doi: 10.1111/j.1365-2451.2012.00836.x, 2012a.

Huggel, C., Clague, J. J., and Korup, O.: Is climate change responsible for changing landslide activity in high mountains?, Earth Surface Processes and Landforms, 37, 77–91, doi: 10.1002/esp.2223, 2012b.

Hungr, O. and Evans, S. G.: Entrainment of debris in rock avalanches: An analysis of a long run-out mechanism, Geological Society of America Bulletin, 116, 1240, doi: 10.1130/B25362.1, 2004.

Hungr, O., Leroueil, S., and Picarelli, L.: The Varnes classification of landslide types, an update, Landslides, 11, 167–194, doi: 10.1007/s10346-013-0436-y, 2014.

Huss, M., Bookhagen, B., Huggel, C., Jacobsen, D., Bradley, R. S., Clague, J. J., Vuille, M., Buytaert, W., Cayan, D. R., Greenwood, G., Mark, B. G., Milner, A. M., Weingartner, R., and Winder, M.: Toward mountains without permanent snow and ice, Earth's Future, 5, 418–435, doi: 10.1002/2016EF000514, 2017.

Hutter, P.: Damals im Oberallgäu: Geschichte(n) aus der südlichsten Region Deutschlands, Ed. Limosa, Clenze, 1. aufl. edn., 2010.

Imre, B., Laue, J., and Springman, S. M.: Fractal fragmentation of rocks within sturzstroms: insight derived from physical experiments within the ETH geotechnical drum centrifuge, Granular Matter, 12, 267–285, doi: 10.1007/s10035-009-0163-1, 2010.

Intrieri, E. and Gigli, G.: Landslide forecasting and factors influencing predictability, Natural Hazards and Earth System Sciences, 16, 2501–2510, doi: 10.5194/nhess-16-2501-2016, 2016.

Intrieri, E., Gigli, G., Mugnai, F., Fanti, R., and Casagli, N.: Design and implementation of a landslide early warning system, Engineering Geology, 147-148, 124–136, doi: 10.1016/j.enggeo.2012.07.017, 2012.

Intrieri, E., Gigli, G., Casagli, N., and Nadim, F.: Brief communication "Landslide Early Warning System: toolbox and general concepts", Natural Hazards and Earth System Sciences, 13, 85–90, doi: 10.5194/nhess-13-85-2013, 2013.

Intrieri, E., Carlà, T., and Gigli, G.: Forecasting the time of failure of landslides at slope-scale: A literature review, Earth-Science Reviews, 193, 333–349, doi: 10.1016/j.earscirev.2019.03.019, 2019.

Intrieri, E., Dotta, G., Raspini, F., Rosi, A., Segoni, S., and Casagli, N.: Early Warning Systems in Italy: State-of-the-Art and Future Trends, in: Understanding and Reducing Landslide Disaster Risk, edited by Sassa, K., Mikoš, M., Sassa, S., Bobrowsky, P. T., Takara, K., and Dang, K., ICL Contribution to Landslide Disaster Risk Reduction, pp. 537–543, Springer International Publishing, Cham, doi: 10.1007/978-3-030-60196-6_45, 2021.

IPCC, ed.: Climate change 2013: The physical science basis ; Working Group I contribution to the fifth assessment report of the Intergovernmental Panel on Climate Change, Cambridge

University Press, Cambridge, United Kingdom and New York, NY, USA, doi: 10.1017/CBO9781107415324, 2013.

IPCC, ed.: Climate Change 2014: Impacts, Adaptation, and Vulnerability. Part B: Regional Aspects. Contribution of Working Group II to the Fifth Assessment Report of the Intergovernmental Panel on Climate Change, Cambridge University Press, Cambridge, United Kingdom and New York, NY, USA, 2014.

IPCC, ed.: Climate Change and Land: an IPCC special report on climate change, desertification, land degradation, sustainable land management, food security, and greenhouse gas fluxes in terrestrial ecosystems: Shukla, P.R. et al. (eds.), in press, 2019.

Iwata, N. and Sasahara, K.: Influence of Intervals Measuring Surface Displacement on Time Prediction of Slope Failure Using Fukuzono Method, in: Understanding and Reducing Landslide Disaster Risk, edited by Casagli, N., Tofani, V., Sassa, K., Bobrowsky, P. T., and Takara, K., ICL Contribution to Landslide Disaster Risk Reduction, pp. 307–313, Springer International Publishing, Cham, doi: 10.1007/978-3-030-60311-3_36, 2021.

Jibson, R. W.: Predicting earthquake-induced landslide displacements using Newmark's sliding block analysis, Transportation Research Record, pp. 9–17, 1993.

Jibson, R. W.: Regression models for estimating coseismic landslide displacement, Engineering Geology, 91, 209–218, doi: 10.1016/j.enggeo.2007.01.013, 2007.

Jibson, R. W., Harp, E. L., and Michael, J. A.: A method for producing digital probabilistic seismic landslide hazard maps, Engineering Geology, 58, 271–289, doi: 10.1016/S0013-7952(00)00039-9, 2000.

Jibson, R. W., Harp, E. L., Schulz, W., and Keefer, D. K.: Large rock avalanches triggered by the M 7.9 Denali Fault, Alaska, earthquake of 3 November 2002, Engineering Geology, 83, 144–160, doi: 10.1016/j.enggeo.2005.06.029, 2006.

Jokel, M.: Evaluating acceleration models and respective stochasticity towards a real-time forecasting model for landslides: master thesis, URL https://mediatum.ub.tum.de/1579885, 2023.

Kappes, M. S., Keiler, M., von Elverfeldt, K., and Glade, T.: Challenges of analyzing multi-hazard risk: a review, Natural Hazards, 64, 1925–1958, doi: 10.1007/s11069-012-0294-2, 2012.

Kemeny, J.: The Time-Dependent Reduction of Sliding Cohesion due to Rock Bridges Along Discontinuities: A Fracture Mechanics Approach, Rock Mechanics and Rock Engineering, 36, 27–38, doi: 10.1007/s00603-002-0032-2, 2003.

Keuschnig, M., Krautblatter, M., Hartmeyer, I., Fuss, C., and Schrott, L.: Automated Electrical Resistivity Tomography Testing for Early Warning in Unstable Permafrost Rock Walls Around Alpine Infrastructure, Permafrost and Periglacial Processes, 28, 158–171, doi: 10.1002/ppp.1916, 2017.

Khan, S., van der Meijde, M., van der Werff, H., and Shafique, M.: The impact of topography on seismic amplification during the 2005 Kashmir earthquake, Natural Hazards and Earth System Sciences, 20, 399–411, doi: 10.5194/nhess-20-399-2020, 2020.

Kiefer, C., Oswald, P., Moernaut, J., Fabbri, S. C., Mayr, C., Strasser, M., and Krautblatter, M.: A 4000-year debris flow record based on amphibious investigations of fan delta activity in Plansee (Austria, Eastern Alps), Earth Surface Dynamics, 9, 1481–1503, doi: 10.5194/esurf-9-1481-2021, 2021.

Kilburn, C. R. and Petley, D. N.: Forecasting giant, catastrophic slope collapse: lessons from Vajont, Northern Italy, Geomorphology, 54, 21–32, doi: 10.1016/S0169-555X(03)00052-7, 2003.

Knapp, S. and Krautblatter, M.: Conceptual Framework of Energy Dissipation During Disintegration in Rock Avalanches, Frontiers in Earth Science, 8, doi: 10.3389/feart.2020.00263, 2020.

Knapp, S., Gilli, A., Anselmetti, F. S., Krautblatter, M., and Hajdas, I.: Multistage Rock–Slope Failures Revealed in Lake Sediments in a Seismically Active Alpine Region (Lake Oeschinen, Switzerland), Journal of Geophysical Research: Earth Surface, 123, 658–677, doi: 10.1029/2017JF004455, 2018.

Knight, J. and Grab, S. W.: Lightning as a geomorphic agent on mountain summits: Evidence from southern Africa, Geomorphology, 204, 61–70, doi: 10.1016/j.geomorph.2013.07.029, 2014.

Krähenbühl, R.: Der Felssturz, der sich auf die Stunde genau ankündigte, Bull. angew. Geol., 11, 49–63, 2006.

Krautblatter, M. and Dikau, R.: Towards a Uniform Concept for the Comparison and Extrapolation of Rockwall Retreat and Rockfall Supply, Geografiska Annaler. Series A, Physical Geography, 89, 21–40, 2007.

Krautblatter, M. and Moore, J. R.: Rock slope instability and erosion: toward improved process understanding, Earth Surface Processes and Landforms, 39, 1273–1278, doi: 10.1002/esp.3578, 2014.

Krautblatter, M. and Moser, M.: A nonlinear model coupling rockfall and rainfall intensity based on a four year measurement in a high Alpine rock wall (Reintal, German Alps), Natural Hazards and Earth System Sciences, 9, 1425–1432, doi: 10.5194/nhess-9-1425-2009, 2009.

Krautblatter, M., Funk, D., and Günzel, F. K.: Why permafrost rocks become unstable: a rock–ice–mechanical model in time and space, Earth Surface Processes and Landforms, 38, 876–887, doi: 10.1002/esp.3374, 2013.

Kristensen, L., Czekirda, J., Penna, I., Etzelmüller, B., Nicolet, P., Pullarello, J. S., Blikra, L. H., Skrede, I., Oldani, S., and Abellan, A.: Movements, failure and climatic control of the Veslemannen rockslide, Western Norway, Landslides, doi: 10.1007/s10346-020-01609-x, 2021.

Lacasse, S. and Nadim, F.: Landslide Risk Assessment and Mitigation Strategy, in: Landslides – Disaster Risk Reduction, edited by Sassa, K. and Canuti, P., pp. 31–61, Springer Berlin Heidelberg, Berlin, Heidelberg, doi: 10.1007/978-3-540-69970-5_3, 2009.

Lacroix, P., Huanca, J., Albinez, L., and Taipe, E.: Precursory Motion and Time–Of–Failure Prediction of the Achoma Landslide, Peru, From High Frequency PlanetScope Satellites, Geophysical Research Letters, 50, doi: 10.1029/2023GL105413, 2023.

Lagarde, S., Dietze, M., Hammer, C., Zeckra, M., Voigtländer, A., Illien, L., Schöpa, A., Hirschberg, J., Burtin, A., Hovius, N., and Turowski, J. M.: Rock slope failure preparation paced by total crack boundary length, Communications Earth & Environment, 4, doi: 10.1038/s43247-023-00851-0, 2023.

LaHusen, S. R., Duvall, A. R., Booth, A. M., Grant, A., Mishkin, B. A., Montgomery, D. R., Struble, W., Roering, J. J., and Wartman, J.: Rainfall triggers more deep-seated landslides than Cascadia earthquakes in the Oregon Coast Range, USA, Science advances, 6, doi: 10.1126/sciadv.aba6790, 2020.

Langet, N. and Silverberg, F. M. J.: Automated classification of seismic signals recorded on the Åknes rock slope, Western Norway, using a convolutional neural network, Earth Surface Dynamics, 11, 89–115, doi: 10.5194/esurf-11-89-2023, 2023.

Larose, E., Carrière, S., Voisin, C., Bottelin, P., Baillet, L., Guéguen, P., Walter, F., Jongmans, D., Guillier, B., Garambois, S., Gimbert, F., and Massey, C.: Environmental seismology: What can we learn on earth surface processes with ambient noise?, Journal of Applied Geophysics, 116, 62–74, doi: 10.1016/j.jappgeo.2015.02.001, 2015.

Le Roux, E., Evin, G., Samacoïts, R., Eckert, N., Blanchet, J., and Morin, S.: Projection of snowfall extremes in the French Alps as a function of elevation and global warming level, The Cryosphere, 17, 4691–4704, doi: 10.5194/tc-17-4691-2023, 2023.

Le Roy, G., Helmstetter, A., Amitrano, D., Guyoton, F., and Le Roux–Mallouf, R.: Seismic Analysis of the Detachment and Impact Phases of a Rockfall and Application for Estimating Rockfall Volume and Free–Fall Height, Journal of Geophysical Research: Earth Surface, 124, 2602–2622, doi: 10.1029/2019JF004999, 2019.

Lee, S.-J., Chan, Y.-C., Komatitsch, D., Huang, B.-S., and Tromp, J.: Effects of Realistic Surface Topography on Seismic Ground Motion in the Yangminshan Region of Taiwan Based Upon the Spectral-Element Method and LiDAR DTM, Bulletin of the Seismological Society of America, 99, 681–693, doi: 10.1785/0120080264, 2009a.

Lee, S.-J., Komatitsch, D., Huang, B.-S., and Tromp, J.: Effects of Topography on Seismic-Wave Propagation: An Example from Northern Taiwan, Bulletin of the Seismological Society of America, 99, 314–325, doi: 10.1785/0120080020, 2009b.

Lehning, M., Bartelt, P., Brown, B., Russi, T., Stöckli, U., and Zimmerli, M.: Snowpack model calculations for avalanche warning based upon a new network of weather and snow stations, Cold Regions Science and Technology, 30, 145–157, doi: 10.1016/S0165-232X(99)00022-1, 1999.

Leinauer, J.: Collection of R-codes and data for analysis of drivers at the Hochvogel rock slope instability, doi: 10.5281/zenodo.10567098, 2024.

Leinauer, J., Jacobs, B., and Krautblatter, M.: Anticipating an imminent large rock slope failure at the Hochvogel (Allgäu Alps), Geomechanics and Tunnelling, 13, 597–603, doi:

10.1002/geot.202000027, 2020.

Leinauer, J., Jacobs, B., and Krautblatter, M.: High alpine geotechnical real time monitoring and early warning at a large imminent rock slope failure (Hochvogel, GER/AUT), IOP Conference Series: Earth and Environmental Science, 833, 012 146, doi: 10.1088/1755-1315/833/1/012146, 2021.

Leinauer, J., Weber, S., and Cicoira, A.: R-Tool for prospective failure time forecasting of slope failures using inverse velocity, doi: 10.5281/zenodo.8010361, 2023a.

Leinauer, J., Weber, S., Cicoira, A., Beutel, J., and Krautblatter, M.: An approach for prospective forecasting of rock slope failure time, Communications Earth & Environment, 4, doi: 10.1038/s43247-023-00909-z, 2023b.

Leinauer, J., Weber, S., Cicoira, A., Beutel, J., and Krautblatter, M.: Collection of slope deformation data until failure with a timely resolution of daily or better supplying the papaer: "An approach for prospective forecasting of rock slope failure time" by Leinauer et al, 2023c.

Levenberg, K.: A method for the solution of certain non-linear problems in least squares, Quarterly of Applied Mathematics, 2, 164–168, 1944.

Loew, S., Gschwind, S., Gischig, V., Keller-Signer, A., and Valenti, G.: Monitoring and early warning of the 2012 Preonzo catastrophic rockslope failure, Landslides, 14, 141–154, doi: 10.1007/s10346-016-0701-y, 2017.

Main, I. G.: A damage mechanics model for power-law creep and earthquake aftershock and foreshock sequences, Geophysical Journal International, 142, 151–161, doi: 10.1046/j.1365-246x.2000.00136.x, 2000.

Manconi, A. and Giordan, D.: Landslide early warning based on failure forecast models: the example of the Mt. de La Saxe rockslide, northern Italy, Natural Hazards and Earth System Sciences, 15, 1639–1644, doi: 10.5194/nhess-15-1639-2015, 2015.

Manconi, A. and Giordan, D.: Landslide failure forecast in near-real-time, Geomatics, Natural Hazards and Risk, 7, 639–648, doi: 10.1080/19475705.2014.942388, 2016.

Marc, O., Hovius, N., Meunier, P., Gorum, T., and Uchida, T.: A seismologically consistent expression for the total area and volume of earthquake-triggered landsliding, Journal of Geophysical Research: Earth Surface, 121, 640–663, doi: 10.1002/2015JF003732, 2016.

Marquardt, D. W.: An Algorithm for Least-Squares Estimation of Nonlinear Parameters, Journal of the Society for Industrial and Applied Mathematics, 11, 431–441, 1963.

Massey, C. I., Olsen, M. J., Wartman, J., Senogles, A., Lukovic, B., Leshchinsky, B. A., Archibald, G., Litchfield, N., van Dissen, R., de Vilder, S., and Holden, C.: Rockfall Activity Rates Before, During and After the 2010/2011 Canterbury Earthquake Sequence, Journal of Geophysical Research: Earth Surface, 127, doi: 10.1029/2021JF006400, 2022.

Masson, D. and Frei, C.: Long-term variations and trends of mesoscale precipitation in the Alps: recalculation and update for 1901-2008, International Journal of Climatology, 36, 492–500, doi: 10.1002/joc.4343, 2016.

Matsuura, S., Asano, S., Okamoto, T., and Takeuchi, Y.: Characteristics of the displacement of a landslide with shallow sliding surface in a heavy snow district of Japan, Engineering Geology, 69, 15–35, doi: 10.1016/S0013-7952(02)00245-4, 2003.

Mazzanti, P., Rocca, A., Bozzano, F., Cossu, R., and Floris, M.: Landslides forecasting analysis by displacement time series derived from satelite INSAR data: preliminary results, Proc. Fringe 2011 Workshop, Frascati, Italy, 2011.

Mazzanti, P., Bozzano, F., Cipriani, I., and Prestininzi, A.: New insights into the temporal prediction of landslides by a terrestrial SAR interferometry monitoring case study, Landslides, 12, 55–68, doi: 10.1007/s10346-014-0469-x, 2015.

Meissen, U. and Voisard, A.: Current State and Solutions for Future Challenges in Early Warning Systems and Alerting Technologies, in: Advanced ICTs for disaster management and threat detection, edited by Asimakopoulou, E. and Bessis, N., pp. 108–130, IGI Global, Hershey, doi: 10.4018/978-1-61520-987-3.ch008, 2010.

Ménégoz, M., Valla, E., Jourdain, N. C., Blanchet, J., Beaumet, J., Wilhelm, B., Gallée, H., Fettweis, X., Morin, S., and Anquetin, S.: Contrasting seasonal changes in total and intense precipitation in the European Alps from 1903 to 2010, Hydrology and Earth System Sciences, 24, 5355–5377, doi: 10.5194/hess-24-5355-2020, 2020.

Meunier, P., Hovius, N., and Haines, A. J.: Regional patterns of earthquake-triggered landslides and their relation to ground motion, Geophysical Research Letters, 34, doi: 10.1029/2007GL031337, 2007.

Meunier, P., Hovius, N., and Haines, J. A.: Topographic site effects and the location of earthquake induced landslides, Earth and Planetary Science Letters, 275, 221–232, doi: 10.1016/j.epsl.2008.07.020, 2008.

Meyenfeld, H.: Modellierungen seismisch ausgelöster gravitativer Massenbewegungen für die Schwäbische Alb und den Raum Bonn und Erstellen von Gefahrenhinweiskarten: Dissertation, ULB Bonn, Bonn, 2009.

Miles, S. B. and Keefer, D. K.: Seismic Landslide Hazard for the City of Berkeley, California, U.S. Geological Survey, doi: 10.3133/mf2378, 2001.

Miller, J., Böhnisch, A., Ludwig, R., and Brunner, M. I.: Climate change impacts on regional fire weather in heterogeneous landscapes of central Europe, Natural Hazards and Earth System Sciences, 24, 411–428, doi: 10.5194/nhess-24-411-2024, 2024.

Mufundirwa, A., Fujii, Y., and Kodama, J.: A new practical method for prediction of geomechanical failure-time, Int J Rock Mech Min, 47, 1079–1090, doi: 10.1016/j.ijrmms.2010.07.001, 2010.

Mulas, M., Marnas, M., Ciccarese, G., and Corsini, A.: Sinusoidal wave fit indexing of irreversible displacements for crackmeters monitoring of rockfall areas: test at Pietra di Bismantova (Northern Apennines, Italy), Landslides, 17, 231–240, doi: 10.1007/s10346-019-01248-x, 2020.

Newmark, N. M.: Effects of earthquakes on dams and embankments, Geotechnique, 15, 139–160, 1965.

Nex, F. and Remondino, F.: UAV for 3D mapping applications: a review, Applied Geomatics, 6, 1–15, doi: 10.1007/s12518-013-0120-x, 2014.

Nibigira, L., Havenith, H.-B., Archambeau, P., and Dewals, B.: Formation, breaching and flood consequences of a landslide dam near Bujumbura, Burundi, Natural Hazards and Earth System Sciences, 18, 1867–1890, doi: 10.5194/nhess-18-1867-2018, 2018.

Nicoletti, P. G. and Sorriso-Valvo, M.: Geomorphic controls of the shape and mobility of rock avalanches, Geological Society of America Bulletin, 103, 1365–1373, doi: 10.1130/0016-7606(1991)103{\textless}1365:GCOTSA{\textgreater}2.3.CO;2, 1991.

Oswald, P., Strasser, M., Hammerl, C., and Moernaut, J.: Seismic control of large prehistoric rockslides in the Eastern Alps, Nature communications, 12, 1059, doi: 10.1038/s41467-021-21327-9, 2021.

Oswald, P., Strasser, M., Skapski, J., and Moernaut, J.: Magnitude and source area estimations of severe prehistoric earthquakes in the western Austrian Alps, Natural Hazards and Earth System Sciences, 22, 2057–2079, doi: 10.5194/nhess-22-2057-2022, 2022.

Pecoraro, G., Calvello, M., and Piciullo, L.: Monitoring strategies for local landslide early warning systems, Landslides, 16, 213–231, doi: 10.1007/s10346-018-1068-z, 2019.

Pendergrass, A. G., Coleman, D. B., Deser, C., Lehner, F., Rosenbloom, N., and Simpson, I. R.: Nonlinear Response of Extreme Precipitation to Warming in CESM1, Geophysical Research Letters, 46, 10 551–10 560, doi: 10.1029/2019GL084826, 2019.

Petley, D.: Global patterns of loss of life from landslides, Geology, 40, 927–930, doi: 10.1130/G33217.1, 2012.

Petley, D. N.: The evolution of slope failures: mechanisms of rupture propagation, Natural Hazards and Earth System Sciences, 4, 147–152, doi: 10.5194/nhess-4-147-2004, 2004.

Petley, D. N. and Petley, D. J.: On the initiation of large rockslides: Perspectives from a new analysis of the vaiont movement record, in: Landslides from Massive Rock Slope Failure, edited by Evans, S. G., Mugnozza, G. S., Strom, A., and Hermanns, R. L., vol. 49 of *NATO Science Series*, pp. 77–84, Springer Netherlands, Dordrecht, doi: 10.1007/978-1-4020-4037-5_3, 2006.

Petley, D. N., Petley, D. J., and Allison, R.: Temporal prediction in landslides–understanding the saito effect., in: Landslides and engineered slopes, edited by Chen, Z., CRC Press, Boca Raton, 2008.

Pfurtscheller, C. and Thieken, A. H.: The price of safety: costs for mitigating and coping with Alpine hazards, Natural Hazards and Earth System Sciences, 13, 2619–2637, doi: 10.5194/nhess-13-2619-2013, 2013.

Picarelli, L., Lacasse, S., and Ho, K. K. S.: The Impact of Climate Change on Landslide Hazard and Risk, in: Understanding and Reducing Landslide Disaster Risk, edited by Sassa, K., Mikoš, M., Sassa, S., Bobrowsky, P. T., Takara, K., and Dang, K., ICL Contribution to Landslide Disaster Risk Reduction, pp. 131–141, Springer International Publishing, Cham, doi: 10.1007/978-3-030-60196-6_6, 2021.

Piciullo, L., Calvello, M., and Cepeda, J. M.: Territorial early warning systems for rainfall-induced landslides, Earth-Science Reviews, 179, 228–247, doi: 10.1016/j.earscirev.2018.02.013, 2018.

Piciullo, L., Capobianco, V., and Heyerdahl, H.: A first step towards a IoT-based local early warning system for an unsaturated slope in Norway, Natural Hazards, 114, 3377–3407, doi: 10.1007/s11069-022-05524-3, 2022.

Plafker, G. and Ericksen, G. E.: Nevados Huascarán Avalanches, Peru, in: Rockslides and Avalanches, 1 - Natural Phenomena, edited by Voight, B., vol. 14 of *Developments in Geotechnical Engineering*, pp. 277–314, Elsevier, doi: 10.1016/B978-0-444-41507-3.50016-7, 1978.

PLANALP: Beständigkeit von Schutzsystemen gegen alpine Naturgefahren, Plattform Naturgefahren der Alpenkonvention, Wien, 2015.

Poschinger, A. v., Wassmer, P., and Maisch, M.: The Flims rockslide: history of interpretation and new insights, in: Landslides from Massive Rock Slope Failure, edited by Evans, S. G., Mugnozza, G. S., Strom, A., and Hermanns, R. L., vol. 49 of *NATO Science Series*, pp. 329–356, Springer Netherlands, Dordrecht, doi: 10.1007/978-1-4020-4037-5_18, 2006.

Prein, A. F., Liu, C., Ikeda, K., Trier, S. B., Rasmussen, R. M., Holland, G. J., and Clark, M. P.: Increased rainfall volume from future convective storms in the US, Nature Climate Change, 7, 880–884, doi: 10.1038/s41558-017-0007-7, 2017.

Preisig, G., Eberhardt, E., Smithyman, M., Preh, A., and Bonzanigo, L.: Hydromechanical Rock Mass Fatigue in Deep-Seated Landslides Accompanying Seasonal Variations in Pore Pressures, Rock Mechanics and Rock Engineering, 49, 2333–2351, doi: 10.1007/s00603-016-0912-5, 2016.

Provost, F., Hibert, C., and Malet, J.-P.: Automatic classification of endogenous landslide seismicity using the Random Forest supervised classifier, Geophysical Research Letters, 44, 113–120, doi: 10.1002/2016GL070709, 2017.

Pudasaini, S. P. and Krautblatter, M.: A two–phase mechanical model for rock–ice avalanches, Journal of Geophysical Research: Earth Surface, 119, 2272–2290, doi: 10.1002/2014JF003183, 2014.

Pudasaini, S. P. and Krautblatter, M.: The mechanics of landslide mobility with erosion, Nature communications, 12, 6793, doi: 10.1038/s41467-021-26959-5, 2021.

Pudasaini, S. P. and Mergili, M.: A Multi–Phase Mass Flow Model, Journal of Geophysical Research: Earth Surface, 124, 2920–2942, doi: 10.1029/2019JF005204, 2019.

R Core Team: R: A Language and Environment for Statistical Computing, URL `https://www.R-project.org/`, 2022.

R Core Team: R: A Language and Environment for Statistical Computing, URL `https://www.R-project.org/`, 2023.

Raffl, L., Schnider, R., and Holst, C.: Accuracy investigation of a novel GNSS monitoring system for geo-monitoring on Mt. Hochvogel., allgemeine vermessungs-nachrichten (avn),

129, 115–124, 2022.

Rault, C., Chao, W.-A., Gelis, C., Burtin, A., Chang, J.-M., Marc, O., Lai, T.-S., Wu, Y.-M., Hovius, N., and Meunier, P.: Seismic Response of a Mountain Ridge Prone to Landsliding, Bulletin of the Seismological Society of America, 110, 3004–3020, doi: 10.1785/0120190127, 2020.

Rechberger, C., Fey, C., and Zangerl, C.: Structural characterisation, internal deformation, and kinematics of an active deep-seated rock slide in a valley glacier retreat area, Engineering Geology, 286, 106 048, doi: 10.1016/j.enggeo.2021.106048, 2021.

Rengers, F. K., McGuire, L. A., Oakley, N. S., Kean, J. W., Staley, D. M., and Tang, H.: Landslides after wildfire: initiation, magnitude, and mobility, Landslides, 17, 2631–2641, doi: 10.1007/s10346-020-01506-3, 2020.

Rose, N. D. and Hungr, O.: Forecasting potential rock slope failure in open pit mines using the inverse-velocity method, International Journal of Rock Mechanics and Mining Sciences, 44, 308–320, doi: 10.1016/j.ijrmms.2006.07.014, 2007.

Saito, M.: Forecasting the time of occurrence of a slope failure, Proc. 6th Int. Conf. on Soil Mechanics and Foundation Engineering, Montreal, 1, 537–541, 1965.

Saito, M.: Forecasting time of slope failure by tertiary creep, Proc. 7th Int. Conf. on Soil Mechanics and Foundation Engineering, Mexico, 2, 677–683, 1969.

Saito, M. and Uezawa, H.: Failure of soil due to creep, Proc. 5th Int. Conf. on Soil Mechanics and Foundation Engineering, Paris, 1, 315–318, 1961.

Sättele, M., Krautblatter, M., Bründl, M., and Straub, D.: Forecasting rock slope failure: how reliable and effective are warning systems?, Landslides, 13, 737–750, doi: 10.1007/s10346-015-0605-2, 2016.

Scandroglio, R., Stoll, V., and Krautblatter, M.: The driving force of all nature. Modelling water pressure and its stability consequences on alpine bedrock slopes, IOP Conference Series: Earth and Environmental Science, 833, 012 109, doi: 10.1088/1755-1315/833/1/012109, 2021.

Schild, L., Scheiber, T., Snook, P., Arghandeh, R., Samnøy, S. F., Maschler, A., and Kristensen, L.: Multimodal Asynchronous Kalman Filter for monitoring unstable rock slopes, Geomatics, Natural Hazards and Risk, 14, doi: 10.1080/19475705.2023.2272575, 2023.

SED: Earthquake Catalogue: Swiss Seismological Service, URL http://www.seismo.ethz.ch/en/research-and-teaching/products-software/earthquake-catalogues/, 2023.

Segalini, A., Valletta, A., and Carri, A.: Landslide time-of-failure forecast and alert threshold assessment: A generalized criterion, Engineering Geology, 245, 72–80, doi: 10.1016/j.enggeo.2018.08.003, 2018.

Sektion Donauwörth des DAV e. V.: Dokumentierte Felsstürze im Bereich des Bäumenheimer Weges [online], URL http://www.dav-donauwoerth.de/index.php/geschichte-baeumenheimer-weg-1904-2014, 2020.

Senfaute, G., Duperret, A., and Lawrence, J. A.: Micro-seismic precursory cracks prior to rock-fall on coastal chalk cliffs: a case study at Mesnil-Val, Normandie, NW France, Natural Hazards and Earth System Sciences, 9, 1625–1641, doi: 10.5194/nhess-9-1625-2009, 2009.

Sepúlveda, S. A., Murphy, W., Jibson, R. W., and Petley, D. N.: Seismically induced rock slope failures resulting from topographic amplification of strong ground motions: The case of Pacoima Canyon, California, Engineering Geology, 80, 336–348, doi: 10.1016/j.enggeo.2005.07.004, 2005.

Singer, J. and Kurosch, T.: Development of a continuous 3D-monitoring system for unstable slopes using Time Domain Reflectometry, IAEG2006, 2006.

Stähli, M., Sättele, M., Huggel, C., McArdell, B. W., Lehmann, P., van Herwijnen, A., Berne, A., Schleiss, M., Ferrari, A., Kos, A., Or, D., and Springman, S. M.: Monitoring and prediction in early warning systems for rapid mass movements, Natural Hazards and Earth System Sciences, 15, 905–917, doi: 10.5194/nhess-15-905-2015, 2015.

Stock, G., Collins, B., Santaniello, D., Zimmer, V., Wieczorek, G., and Synder, J.: Historical rock falls in Yosemite National Park, California (1857–2011), Data Series 746, 2013.

Suriñach, E., Vilajosana, I., Khazaradze, G., Biescas, B., Furdada, G., and Vilaplana, J. M.: Seismic detection and characterization of landslides and other mass movements, Natural Hazards and Earth System Sciences, 5, 791–798, 2005.

Tordesillas, A., Zhou, S., Di Traglia, F., and Intrieri, E.: New Insights into the Spatiotemporal Precursory Failure Dynamics of the 2017 Xinmo Landslide and Its Surrounds, in: Understanding and Reducing Landslide Disaster Risk, edited by Casagli, N., Tofani, V., Sassa, K., Bobrowsky, P. T., and Takara, K., ICL Contribution to Landslide Disaster Risk Reduction, pp. 331–338, Springer International Publishing, Cham, doi: 10.1007/978-3-030-60311-3_39, 2021.

Uhlemann, S., Smith, A., Chambers, J., Dixon, N., Dijkstra, T., Haslam, E., Meldrum, P., Merritt, A., Gunn, D., and Mackay, J.: Assessment of ground-based monitoring techniques applied to landslide investigations, Geomorphology, 253, 438–451, doi: 10.1016/j.geomorph.2015.10.027, 2016.

Uhlmann, B., Goyette, S., and Beniston, M.: Sensitivity analysis of snow patterns in Swiss ski resorts to shifts in temperature, precipitation and humidity under conditions of climate change, International Journal of Climatology, 29, 1048–1055, doi: 10.1002/joc.1786, 2009.

UN/ISDR: Terminology on Disaster Risk Reduction, United Nations International Strategy for Disaster Reduction, Geneva, Switzerland, 2009.

USGS: Earthquake Catalogue: US Geological Service, URL `https://earthquake.usgs.gov/earthquakes/search/`, 2023.

Valletta, A., Carri, A., and Segalini, A.: Definition and application of a multi-criteria algorithm to identify landslide acceleration phases, Georisk: Assessment and Management of Risk for Engineered Systems and Geohazards, pp. 1–15, doi: 10.1080/17499518.2021.1952610, 2021.

Valletta, A., Carri, A., and Segalini, A.: Alert threshold assessment based on equivalent displacements for the identification of potentially critical landslide events, Natural Hazards, 115, 1549–1570, doi: 10.1007/s11069-022-05606-2, 2023.

Varnes, D. J.: Slope movement types and processes, in: Landslides, analysis and control: special report 176, edited by Schuster, R. L. and Krizek, R. J., vol. Special report 176, pp. 11–33, National Academy of Sciences, Washington DC., 1978.

Voight, B.: A method for prediction of volcanic eruptions, Nature, 332, 125–130, 1988.

Voight, B.: A relation to describe rate-dependent material failure, Science (New York, N.Y.), 243, 200–203, doi: 10.1126/science.243.4888.200, 1989a.

Voight, B.: Materials science law applies to time forecasts of slope failure, Landslide News, 3, 8–11, 1989b.

Voigtländer, A., Leith, K., and Krautblatter, M.: Subcritical Crack Growth and Progressive Failure in Carrara Marble Under Wet and Dry Conditions, Journal of Geophysical Research: Solid Earth, 123, 3780–3798, doi: 10.1029/2017JB014956, 2018.

von Barth, H.: Aus den nördlichen Kalkalpen: Repr. d. Erstausg. Gera 1874, Bavarica-Reprint, Süddeutscher Verl., München, 1984.

Walter, F., Amann, F., Kos, A., Kenner, R., Phillips, M., de Preux, A., Huss, M., Tognacca, C., Clinton, J., Diehl, T., and Bonanomi, Y.: Direct observations of a three million cubic meter rock-slope collapse with almost immediate initiation of ensuing debris flows, Geomorphology, 351, 106 933, doi: 10.1016/j.geomorph.2019.106933, 2020.

Wang, C., Guo, W., Yang, K., Wang, X., and Meng, Q.: Real-Time Monitoring System of Landslide Based on LoRa Architecture, Frontiers in Earth Science, 10, doi: 10.3389/feart.2022.899509, 2022.

Wang, Y. F., Dong, J. J., and Cheng, Q. G.: Velocity–dependent frictional weakening of large rock avalanche basal facies: Implications for rock avalanche hypermobility?, Journal of Geophysical Research: Solid Earth, 122, 1648–1676, doi: 10.1002/2016JB013624, 2017.

Weber, S., Beutel, J., Faillettaz, J., Hasler, A., Krautblatter, M., and Vieli, A.: Quantifying irreversible movement in steep, fractured bedrock permafrost on Matterhorn (CH), The Cryosphere, 11, 567–583, doi: 10.5194/tc-11-567-2017, 2017.

Weber, S., Faillettaz, J., Meyer, M., Beutel, J., and Vieli, A.: Acoustic and Microseismic Characterization in Steep Bedrock Permafrost on Matterhorn (CH), Journal of Geophysical Research: Earth Surface, 123, 1363–1385, doi: 10.1029/2018JF004615, 2018.

Weber, S., Beutel, J., Häusler, M., Geimer, P. R., Fäh, D., and Moore, J. R.: Spectral amplification of ground motion linked to resonance of large-scale mountain landforms, Earth and Planetary Science Letters, 578, 117 295, doi: 10.1016/j.epsl.2021.117295, 2022.

Wenner, M., Hibert, C., van Herwijnen, A., Meier, L., and Walter, F.: Near-real-time automated classification of seismic signals of slope failures with continuous random forests, Natural Hazards and Earth System Sciences, 21, 339–361, doi: 10.5194/nhess-21-339-2021, 2021.

Westoby, M. J., Brasington, J., Glasser, N. F., Hambrey, M. J., and Reynolds, J. M.: 'Structure-from-Motion' photogrammetry: A low-cost, effective tool for geoscience applications, Geomorphology, 179, 300–314, doi: 10.1016/j.geomorph.2012.08.021, 2012.

Whalley, W. B.: The mechanics of high-magnitude, low-frequency rock failure and its importance in a mountainous area, vol. 27 of *Geographical papers / University of Reading. Department of Geography*, University of Reading, Department of Geography, Reading, 1974.

Whalley, W. B.: Rockfalls, in: Slope instability, edited by Brunsden, D. and Prior, D. B., pp. 2017–2256, Wiley, New York, NY, 1984.

Wieczorek, G.: Landslide triggering mechanisms, in: Landslides - investigation and mitigation, edited by Turner, A. and Schuster, R., pp. 76–90, National Academy Press, 1996.

Wilson, R. C. and Keefer, D. K.: Predicting Areal Limits of Earthquake-Induced Landsliding, in: Evaluating Earthquake Hazards in the Los Angeles Region - An Earth-Science Perspective, edited by U.S. Geological Survey, pp. 316–345, USGS, 1985.

Wyllie, D. C. and Mah, C. W.: Rock slope engineering: Civil and mining, Spon Press, New York, NY, repr., 4. ed. edn., 2004.

Zhang, J., Tang, H., Tan, Q., Mao, M., Zhou, B., and Zhang, Y.: A generalized early warning criterion for the landslide risk assessment: deformation probability index (DPI), Acta Geotechnica, doi: 10.1007/s11440-023-02199-3, 2024.

Zhang, X., Wan, H., Zwiers, F. W., Hegerl, G. C., and Min, S.-K.: Attributing intensification of precipitation extremes to human influence, Geophysical Research Letters, 40, 5252–5257, doi: 10.1002/grl.51010, 2013.

Zhu, Y., Ishikawa, T., Yamada, T. J., and Siva Subramanian, S.: Probability assessment of slope instability in seasonally cold regions under climate change, Journal of Infrastructure Preservation and Resilience, 2, doi: 10.1186/s43065-021-00034-1, 2021.

Appendix

A.1 Supplementary material to Paper 2

Additional and online available material supplementing the article ②

Leinauer, J., Dietze, M., Knapp, S., Scandroglio, R., Jokel, M., and Krautblatter, M. (2024): How water, temperature and seismicity control the preparation of massive rock slope failure (Hochvogel, DE/AT), EGUsphere [preprint].
https://doi.org/10.5194/egusphere-2024-231

A.1.1 Measuring devices on summit

Supplementary Fig. A.1.1: Photo of vibrating wire crackmeter "Crack06" without its protective wood roof.

Supplementary Fig. A.1.2: Photo of vibrating wire crackmeter "Crack06" with wood roof.

Supplementary Fig. A.1.3: Photo of tipping bucket rain gauge on the summit of Hochvogel.

Supplementary Fig. A.1.4: Photo of the main crack with position of seismic station HV1 (red ellipse).

Supplementary Fig. A.1.5: Photo of seismic station SA22 during maintenance. During operation, the station is completely covered with rocks to protect the geophone from wind and rain.

Supplementary Tab. A.1.1: Station info data for all used seismic stations.

ID	x	y	z	Installation depth	Sensor type	Logger type	gain
HVGL1	608448.5	5248421.2	2586	0	PE6B	Cube3ext	32
HVGL2	609674.9	5247154.4	1588	0.5	TC120s	Cube3extBOB	4
HVGL3	610726.5	5247060.3	1489	0.4	TC120s	Cube3extBOB	4
HVGL4	609216.5	5246298.4	1252	0.3	TC120s	Cube3extBOB	4
HVGL5	609620	5248034	1933	0.3	PE6B	Cube3ext	16
SA__21	608433	5248426	NA	0.4	PE6B	Cube3ext	16
SA__22	608436	5248451	NA	0	PE6B	Cube3ext	32
SA__23	608455	5248474	NA	0.4	PE6B	Cube3ext	32

A.1.2 Snowmelt modelling configuration

```
[GENERAL]
BUFFER_SIZE = 370
BUFF_BEFORE = 1.5
DATA_QA_LOGS = FALSE

[INPUT]
COORDSYS = CH1903
TIME_ZONE = 1
METEO = SMET
METEOPATH = .\input
METEOPATH_RECURSIVE = FALSE
STATION1 = ZUGS1_2021.smet
SNOWPACK_SLOPES = FALSE
MERGE_STRATEGY = EXPAND_MERGE
TSG::CREATE = CST
TSG::CST::VALUE = 273
SNOW = SMET
SNOWPATH = ./input
SNOWFILE1 = ZUGS1

[OUTPUT]
COORDSYS = CH1903
TIME_ZONE = 1
METEO = SMET
METEOPATH = ./output
WRITE_PROCESSED_METEO = FALSE
EXPERIMENT = 2021
USEREFERENCELAYER = FALSE
SNOW_WRITE = FALSE
PROF_WRITE = TRUE
PROF_FORMAT = PRO
AGGREGATE_PRO = FALSE
AGGREGATE_PRF = FALSE
PROF_START = 0
PROF_DAYS_BETWEEN = 0.041666
HARDNESS_IN_NEWTON = FALSE
CLASSIFY_PROFILE = FALSE
TS_WRITE = TRUE
TS_FORMAT = SMET
TS_START = 0
TS_DAYS_BETWEEN = 0.041666
AVGSUM_TIME_SERIES = TRUE
CUMSUM_MASS = FALSE
PRECIP_RATES = TRUE
OUT_CANOPY = FALSE
OUT_HAZ = FALSE
OUT_SOILEB = FALSE
OUT_HEAT = TRUE
OUT_T = TRUE
OUT_LW = TRUE
OUT_SW = TRUE
OUT_MASS = TRUE
OUT_METEO = TRUE
OUT_STAB = TRUE

[SNOWPACK]
CALCULATION_STEP_LENGTH = 15
ROUGHNESS_LENGTH = 0.002
HEIGHT_OF_METEO_VALUES = 5
HEIGHT_OF_WIND_VALUE = 5
ENFORCE_MEASURED_SNOW_HEIGHTS = TRUE
SW_MODE = BOTH
ATMOSPHERIC_STABILITY = MO_MICHLMAYR
CANOPY = FALSE
```

```
MEAS_TSS = TRUE
CHANGE_BC = TRUE
THRESH_CHANGE_BC = -1
SNP_SOIL = FALSE

[SNOWPACKADVANCED]
VARIANT = DEFAULT
RESEARCH = TRUE
ADJUST_HEIGHT_OF_METEO_VALUES = TRUE
ADJUST_HEIGHT_OF_WIND_VALUE = TRUE
SNOW_EROSION = TRUE
WIND_SCALING_FACTOR = 1
NUMBER_SLOPES = 1
PERP_TO_SLOPE = FALSE
ALLOW_ADAPTIVE_TIMESTEPPING = TRUE
THRESH_RAIN = 1.2
FORCE_RH_WATER = TRUE
THRESH_RH = 0.5
THRESH_DTEMP_AIR_SNOW = 3
HOAR_THRESH_TA = 1.2
HOAR_THRESH_RH = 0.97
HOAR_THRESH_VW = 10
HOAR_DENSITY_BURIED = 125
HOAR_MIN_SIZE_BURIED = 2
HOAR_DENSITY_SURF = 100
MIN_DEPTH_SUBSURF = 0.07
T_CRAZY_MIN = 210
T_CRAZY_MAX = 340
METAMORPHISM_MODEL = DEFAULT
NEW_SNOW_GRAIN_SIZE = 0.3
STRENGTH_MODEL = DEFAULT
VISCOSITY_MODEL = DEFAULT
SALTATION_MODEL = SORENSEN
ENABLE_VAPOUR_TRANSPORT = FALSE
WATERTRANSPORTMODEL_SNOW = BUCKET
WATERTRANSPORTMODEL_SOIL = BUCKET
SOIL_EVAP_MODEL = EVAP_RESISTANCE
SOIL_THERMAL_CONDUCTIVITY = FITTED
ALBEDO_AGING = TRUE
SW_ABSORPTION_SCHEME = MULTI_BAND
HARDNESS_PARAMETERIZATION = MONTI
DETECT_GRASS = FALSE
PLASTIC = FALSE
JAM = FALSE
WATER_LAYER = FALSE
HEIGHT_NEW_ELEM = 0.02
MINIMUM_L_ELEMENT = 0.0025
COMBINE_ELEMENTS = TRUE
TWO_LAYER_CANOPY = TRUE
CANOPY_HEAT_MASS = TRUE
CANOPY_TRANSMISSION = TRUE
FORESTFLOOR_ALB = TRUE
ADVECTIVE_HEAT = FALSE

[INTERPOLATIONS1D]
ENABLE_RESAMPLING = TRUE
WINDOW_SIZE = 2419200

[FILTERS]
TA::FILTER1 = MIN_MAX
TA::ARG1::MIN = 240
TA::ARG1::MAX = 320
HS::FILTER1 = MIN
HS::ARG1::SOFT = true
HS::ARG1::MIN = 0.0
RH::FILTER1 = MIN_MAX
RH::ARG1::SOFT = TRUE
RH::ARG1::MIN = 0
RH::ARG1::MAX = 1
RH::ARG1::MIN_RESET = 0
RH::ARG1::MAX_RESET = 1

[TechSnow]
SNOW_GROOMING = FALSE
```

A.1.3 Seasonal data analysis

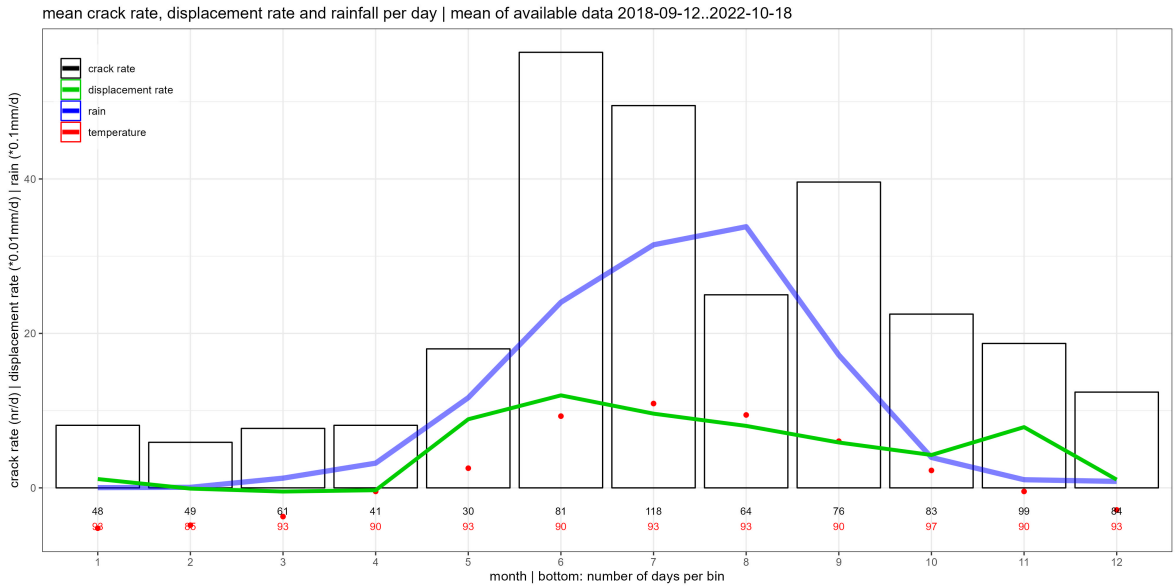

Supplementary Fig. A.1.6: All available data averaged per month of the year. Note the generally higher values of all variables in the summer months (black bars: crack rate (events/d), green line: displacement rate (0.01 mm/d), blue line: rain intensity (0.1 mm/d), red dots: temperature (°C). The numbers in the bottom give the number of available data points per bin (black for cracks, red for other variables).

A.1.4 Random Forest classifier

Supplementary Tab. A.1.2: Features that have been used as input for the Random Forest classifier. Features 6-66 have been calculated for the station with the highest signal-to-noise ratio (SNR), once for the picked signal itself (prefix "pick_") and once for a longer signal including 3 s buffer before and after the picked signal (prefix "long_"), using the function "signal_stats" from eseis.

feature nr	name	details
1	snr_min	SNR of the station with the minimum SNR
2	snr_max	SNR of the station with the maximum SNR
3	dur_mean	mean signal duration of all stations that picked the signal
4	dur_diff	duration difference between the minimum and the maximum signal duration of all stations that picked the signal
5	t_risefall	ratio of rise to fall time
6	a_skewness	Skewness of the signal amplitude
7	a_kurtosis	Kurtosis of the signal amplitude
8	a1_kurtosis	Kurtosis of the filtered (0.1-1 Hz) signal amplitude
9	a2_kurtosis	Kurtosis of the filtered (1-3 Hz) signal amplitude

feature nr	name	details
10	a3_kurtosis	Kurtosis of the filtered (3-10 Hz) signal amplitude
11	a4_kurtosis	Kurtosis of the filtered (10-20 Hz) signal amplitude
12	e_maxmean	Ratio of maximum and mean envelope value, see Hibert et al. (2017)
13	e_maxmedian	Ratio of maximum and median envelope value, see Hibert et al. (2017)
14	e_skewness	Skewness of the signal envelope
15	e_kurtosis	Kurtosis of the signal envelope
16	e1_logsum	Logarithm of the filtered (0.1-1 Hz) envelope sum, see Hibert et al. (2017)
17	e2_logsum	Logarithm of the filtered (1-3 Hz) envelope sum, see Hibert et al. (2017)
18	e3_logsum	Logarithm of the filtered (3-10 Hz) envelope sum, see Hibert et al. (2017)
19	e4_logsum	Logarithm of the filtered (10-20 Hz) envelope sum, see Hibert et al. (2017)
20	c_peaks	Number of peaks (excursions above 75)
21	c_energy1	Sum of the first third of the signal cross correlation function, see Hibert et al. (2017)
22	c_energy2	Sum of the last two thirds of the signal cross correlation function, see Hibert et al. (2017)
23	c_energy3	Ratio of c_energy1 and c_energy2, see Hibert et al. (2017)
24	s_peaks	Number of peaks (excursions above 75)
25	s_peakpower	Mean power of spectral peaks, see Hibert et al. (2017)
26	s_mean	Mean spectral power, see Hibert et al. (2017)
27	s_median	Median spectral power, see Hibert et al. (2017)
28	s_max	Maximum spectral power, see Hibert et al. (2017)
29	s_var	Variance of the spectral power, see Hibert et al. (2017)
30	s_flatness	Spectral flatness
31	s_entropy	Spectral entropy
32	s_precision	Spectral precision
33	s_sd	Standard deviation of the spectral power
34	s_sem	Standard error of the mean of the spectral power
35	s1_energy	Energy of the filtered (0.1-1 Hz) spectrum, see Hibert et al. (2017)
36	s2_energy	Energy of the filtered (1-3 Hz) spectrum, see Hibert et al. (2017)

feature nr	name	details
37	s3_energy	Energy of the filtered (3-10 Hz) spectrum, see Hibert et al. (2017)
38	s4_energy	Energy of the filtered (10-20 Hz) spectrum, see Hibert et al. (2017)
39	s5_energy	Energy of the filtered (20-30 Hz) spectrum, see Hibert et al. (2017)
40	s_gamma1	Gamma 1, spectral centroid, see Hibert et al. (2017)
41	s_gamma2	Gamma 2, spectral gyration radius, see Hibert et al. (2017)
42	f_modal	Modal frequency
43	f_mean	Mean frequency (aka central frequency)
44	f_median	Median frequency
45	f_q05	Quantile 0.05 of the spectrum
46	f_q25	Quantile 0.25 of the spectrum
47	f_q75	Quantile 0.75 of the spectrum
48	f_q95	Quantile 0.95 of the spectrum
49	f_iqr	Inter quartile range of the spectrum
50	f_centroid	Spectral centroid
51	p_kurtosismax	Kurtosis of the maximum spectral power over time, see Hibert et al. (2017)
52	p_kurtosismedian	Kurtosis of the median spectral power over time, see Hibert et al. (2017)
53	p_maxmean	Mean of the ratio of max to mean spectral power over time, see Hibert et al. (2017)
54	p_maxmedian	Mean of the ratio of max to median spectral power over time, see Hibert et al. (2017)
55	p_peaksmean	Number of peaks in normalised mean spectral power over time, see Hibert et al. (2017)
56	p_peaksmedian	Number of peaks in normalised median spectral power over time, see Hibert et al. (2017)
57	p_peaksmax	Number of peaks in normalised max spectral power over time, see Hibert et al. (2017)
58	p_peaksmaxmean	Ratio of number of peaks in normalised max and mean spectral power over time, see Hibert et al. (2017)
59	p_peaksmaxmedian	Ratio of number of peaks in normalised max and median spectral power over time, see Hibert et al. (2017)
60	p_peaksfcentral	Number of peaks in spectral power at central frequency over time, see Hibert et al. (2017)

feature nr	name	details
61	p_diffmaxmean	Mean difference between max and mean power, see Hibert et al. (2017)
62	p_diffquantile21	Mean difference between power quantiles 2 and 1, see Hibert et al. (2017)
63	p_diffquantile32	Mean difference between power quantiles 3 and 2, see Hibert et al. (2017)
64	p_diffquantile31	Mean difference between power quantiles 3 and 1, see Hibert et al. (2017)

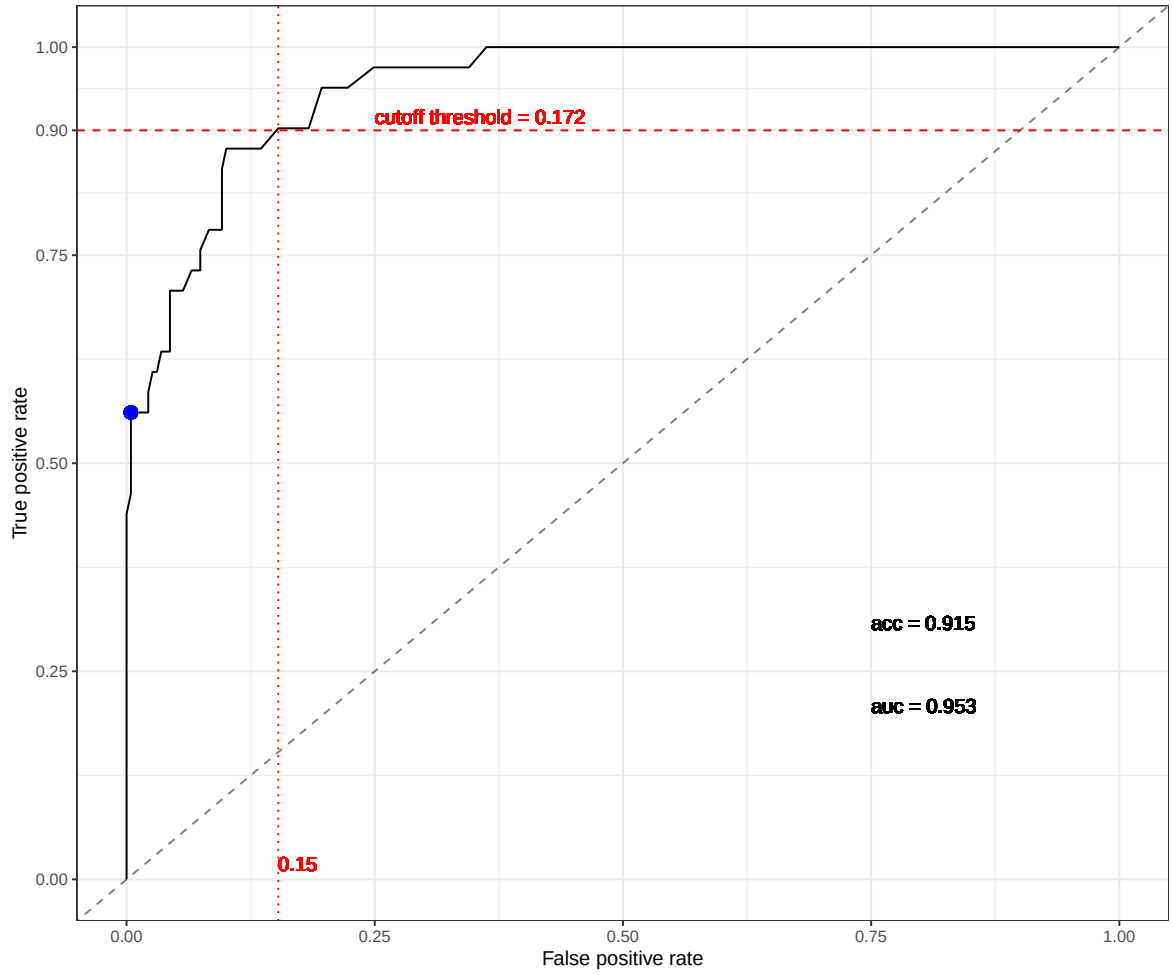

Supplementary Fig. A.1.7: ROC (receiver operating characteristic curve) for the first step Random Forest Model showing the cutoff threshold of 0.172 for a true positive rate of 0.9 leading to a false positive rate of 0.15. The blue dot marks the point with the minimum mean misclassification error.

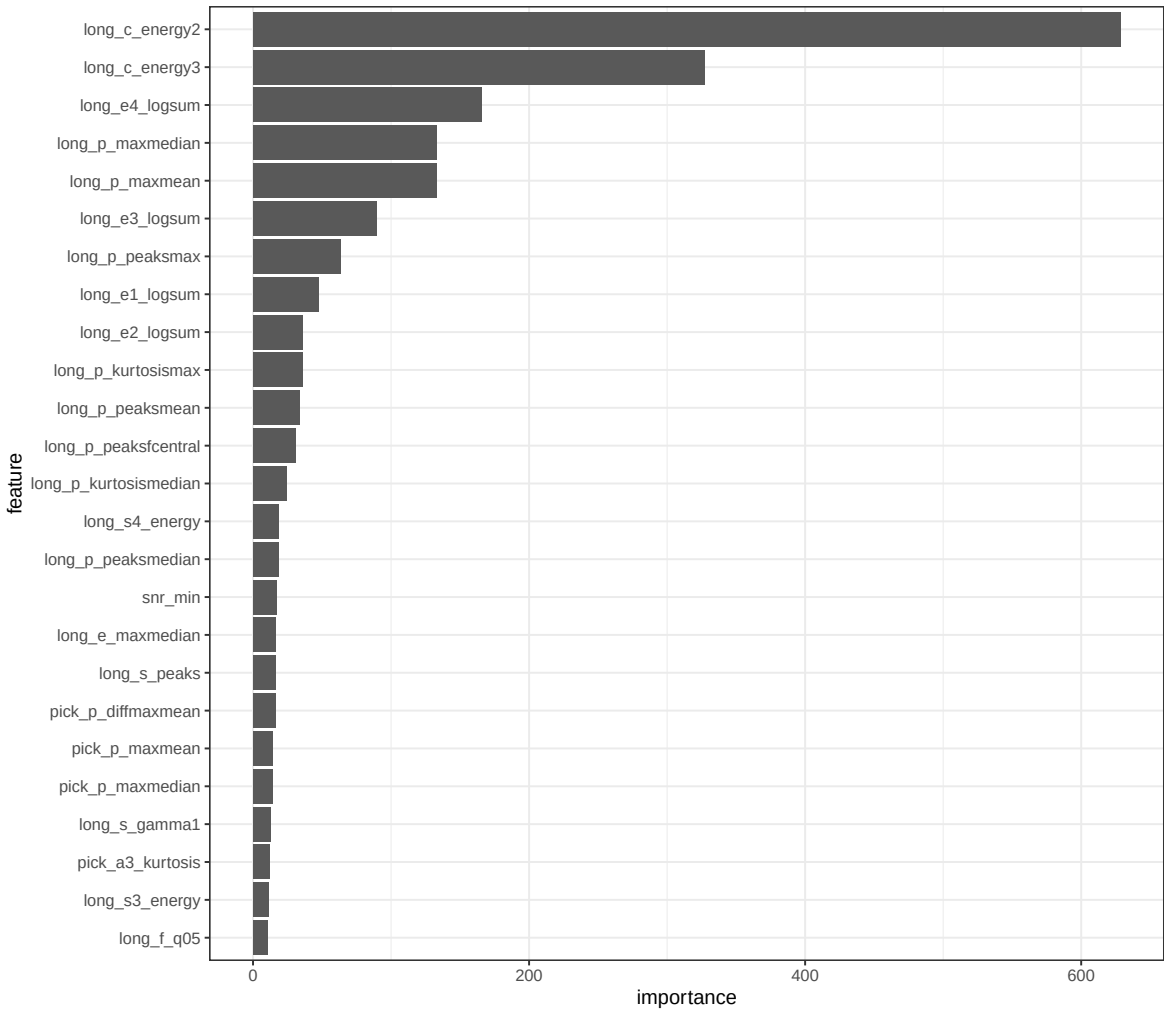

Supplementary Fig. A.1.8: Variable importance of the 25 most important features in the final Random Forest model.

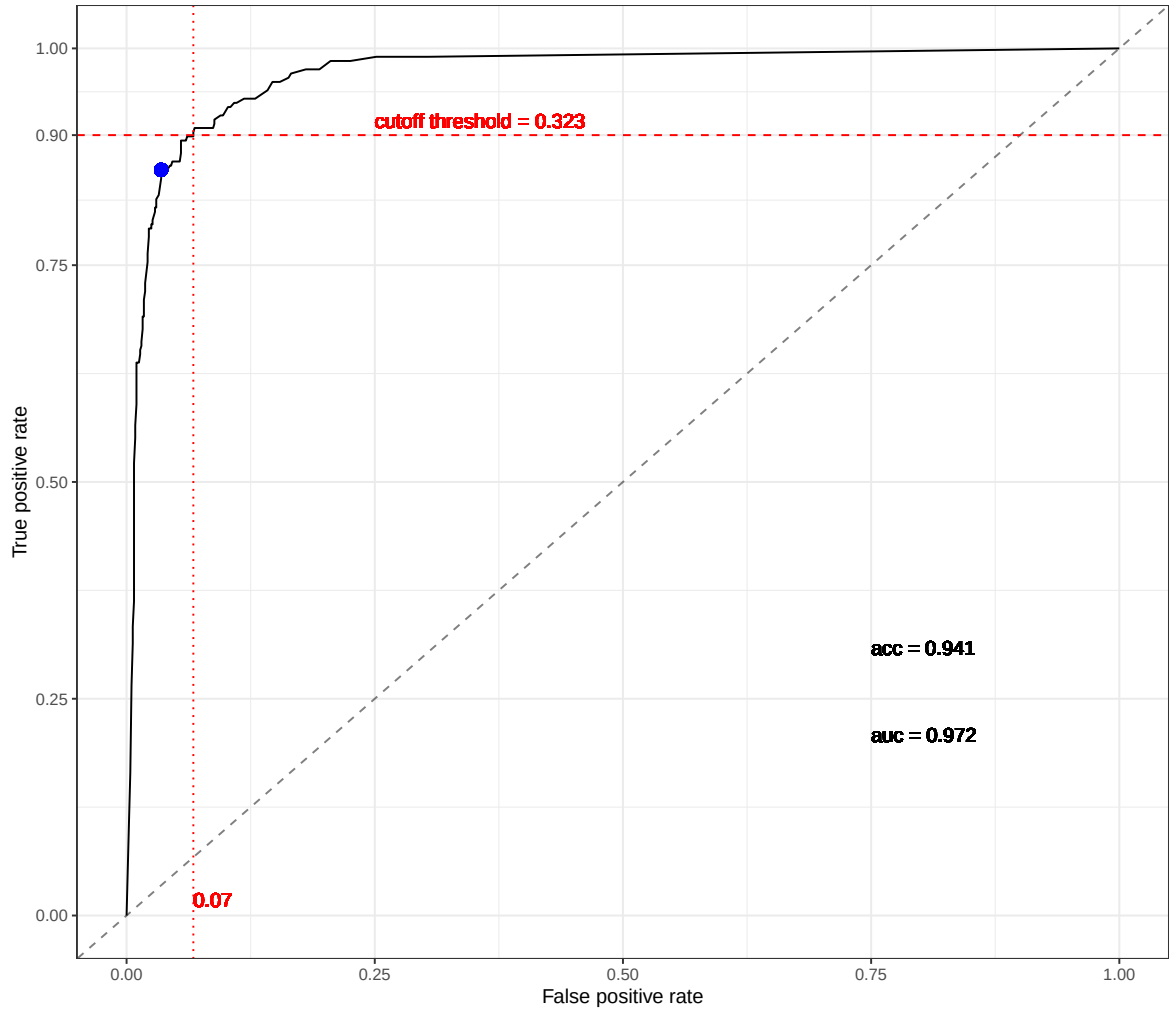

Supplementary Fig. A.1.9: ROC (receiver operating characteristic curve) for the refined Random Forest Model showing the cut-off threshold of 0.323 for a true positive rate of 0.9 leading to a false positive rate of 0.07. The blue dot marks the point with the minimum mean misclassification error.

A.1.5 Focus times

Rain

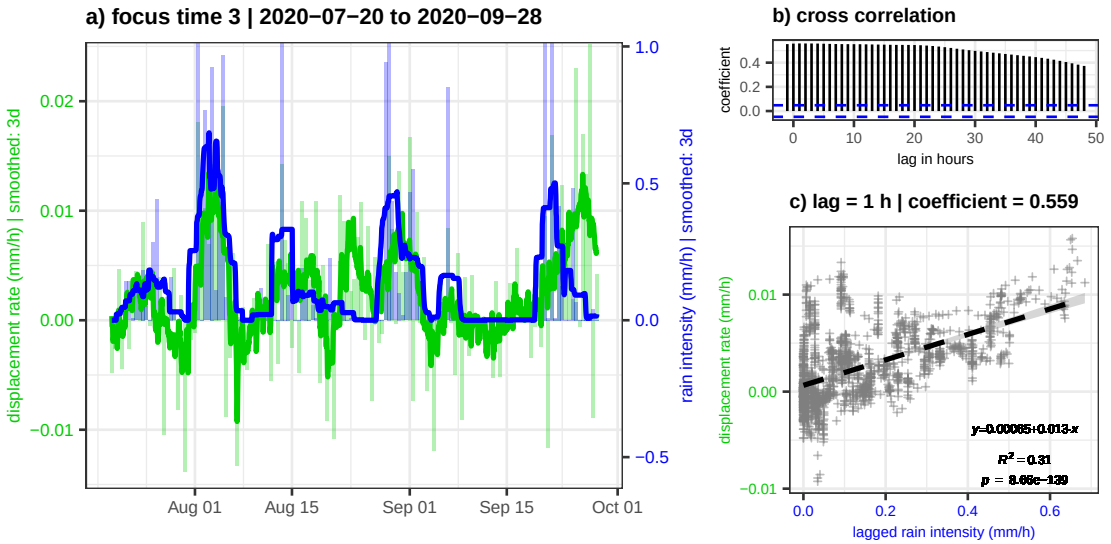

Supplementary Fig. A.1.10: Detail plot of focus time 3. (a) displacement rate and rain intensity (lines 3 d smoothed, columns 12 h means). (b) cross-correlation coefficient of the two lines. The highest correlation appears with a lag of 1 h and a coefficient of 0.559. (c) scatter plot with linear trendline with 1 h shifted data.

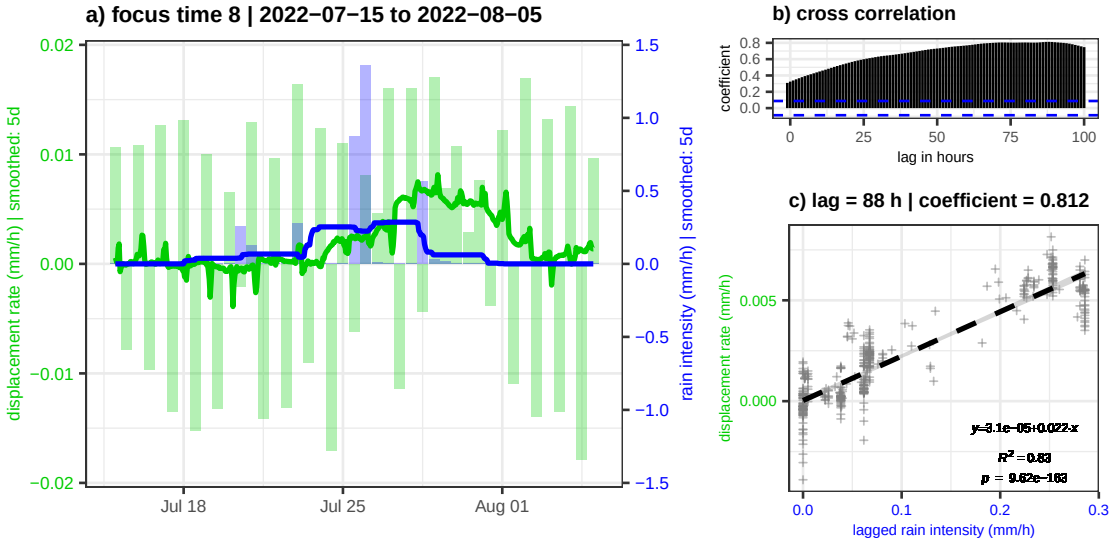

Supplementary Fig. A.1.11: Detail plot of focus time 8. See how multiple consecutive rain events accumulate in one acceleration. (a) displacement rate and rain intensity (lines 5 d smoothed, columns 12 h means). (b) cross-correlation coefficient of the two lines. The highest correlation appears with a lag of 88 h and a coefficient of 0.812. (c) scatter plot with linear trendline with 88 h shifted data.

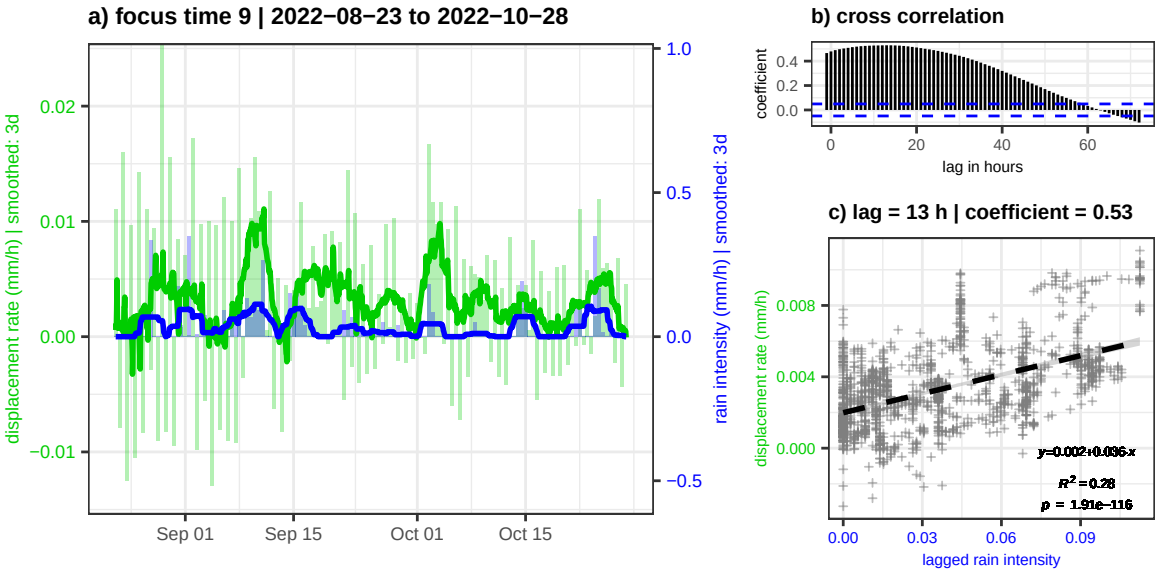

Supplementary Fig. A.1.12: Detail plot of focus time 9. (a) displacement rate and rain intensity (lines 5 d smoothed, columns 12 h means). (b) cross-correlation coefficient of the two lines. The highest correlation appears with a lag of 13 h and a coefficient of 0.530. (c) scatter plot with linear trendline with 13 h shifted data.

Snow

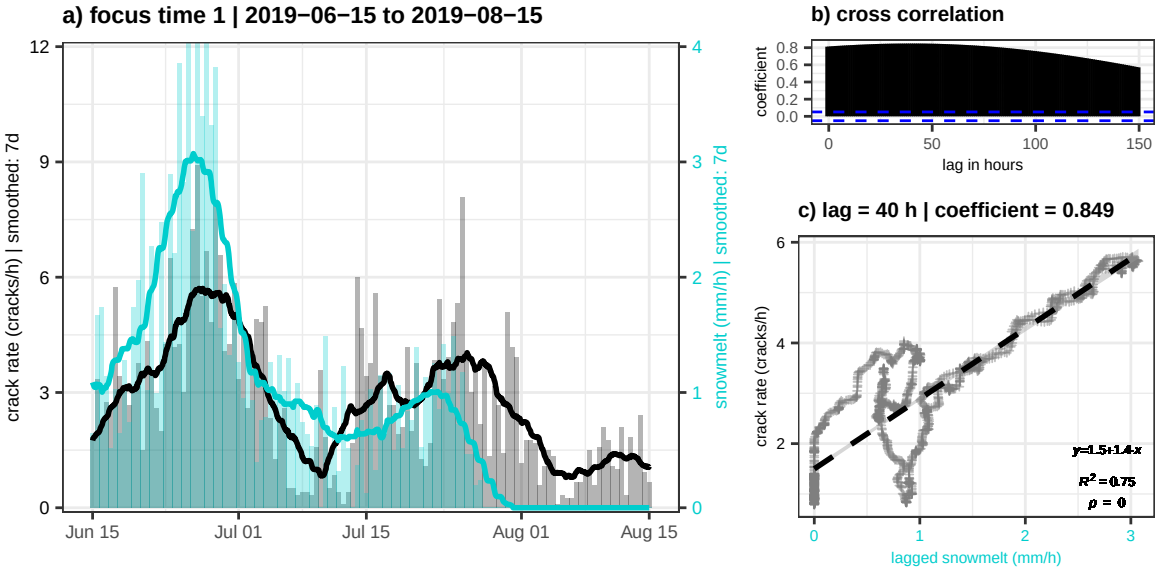

Supplementary Fig. A.1.13: Detail plot of focus time 1. (a) crack rate and snowmelt (lines 7 d smoothed, columns 12 h means). (b) cross-correlation coefficient of the two lines. The highest correlation appears with a lag of 2 d and a coefficient of 0.849. (c) scatter plot with linear trendline with 40 h shifted data.

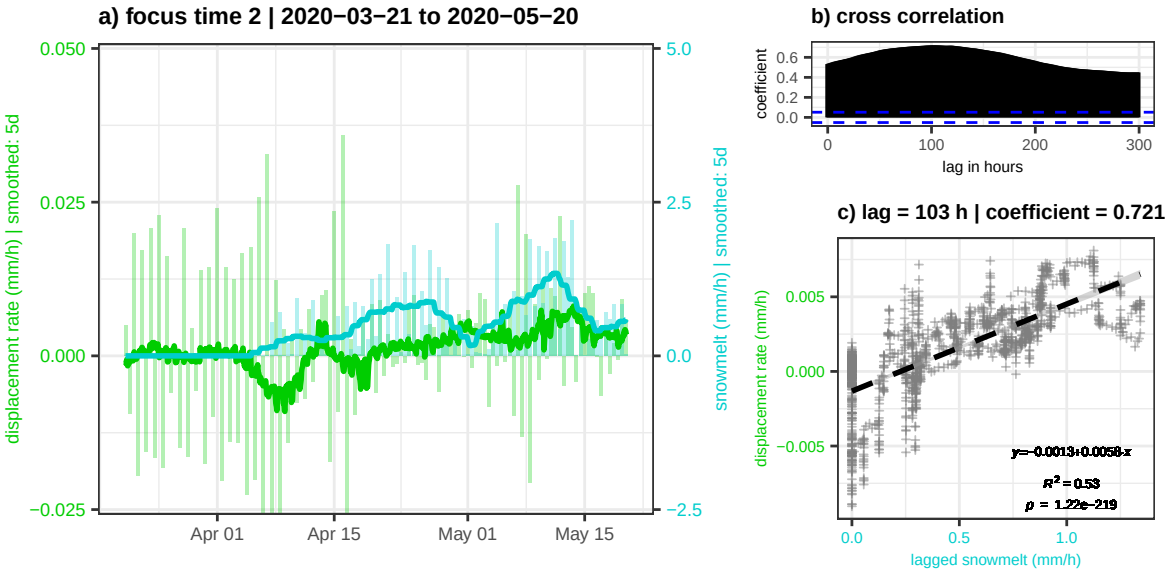

Supplementary Fig. A.1.14: Detail plot of focus time 2. (a) displacement rate and snowmelt (lines 5 d smoothed, columns 12 h means). (b) cross-correlation coefficient of the two lines. The highest correlation appears with a lag of 4.3 d and a coefficient of 0.721. (c) scatter plot with linear trendline with 103 h shifted data.

Seismic crack events

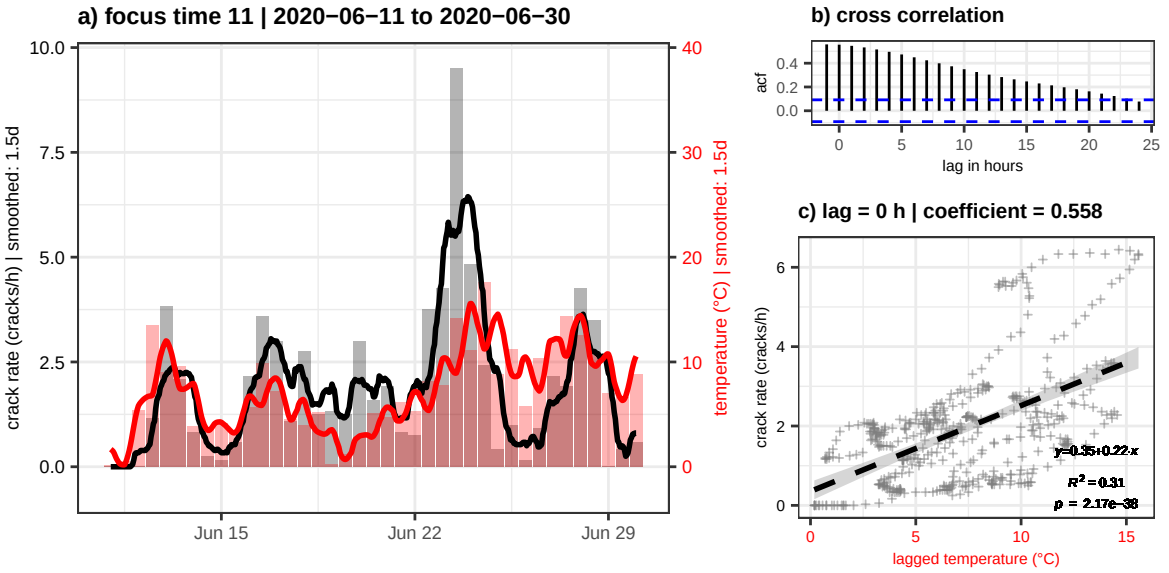

Supplementary Fig. A.1.15: Detail plot of focus time 11. (a) crack rate and mean temperature (lines 1.5 d smoothed, columns 12 h means). (b) cross-correlation coefficient of the two lines. The highest correlation appears without any lag and a coefficient of 0.558. (c) scatter plot with linear trendline with data not shifted (0 h).

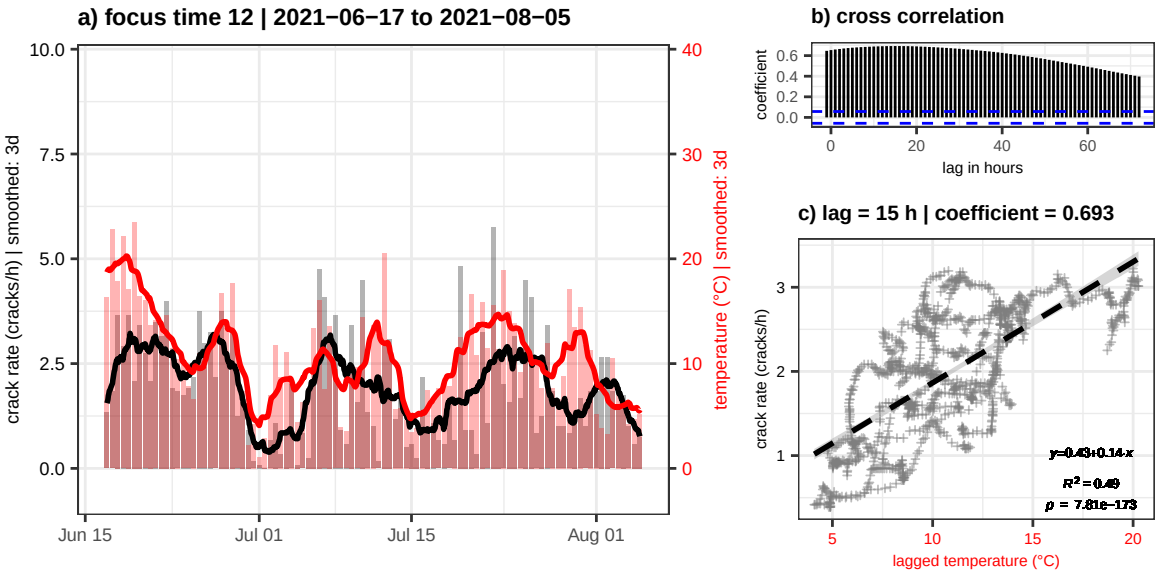

Supplementary Fig. A.1.16: Detail plot of focus time 12. (a) crack rate and mean temperature (lines 3 d smoothed, columns 12 h means). (b) cross-correlation coefficient of the two lines. The highest correlation appears with a lag of 15 h and a coefficient of 0.693. (c) scatter plot with linear trendline with 15 h shifted data.

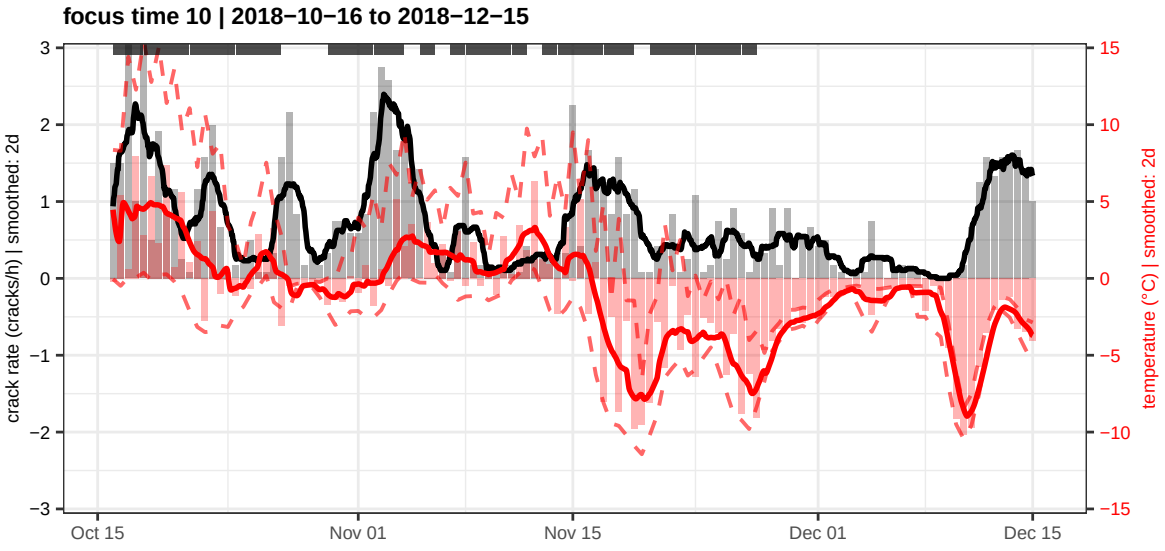

Supplementary Fig. A.1.17: Detail plot of focus time 10. Crack rate, mean temperature (solid line), minimum and maximum temperature (dashed lines, all lines 2 d smoothed, columns 12 h means). Peaks in the crack rate coincide with days with freeze-thaw or thaw-freeze conditions (black bars on top). From mid-November onwards, crack rate increases during days with severe temperature drops.

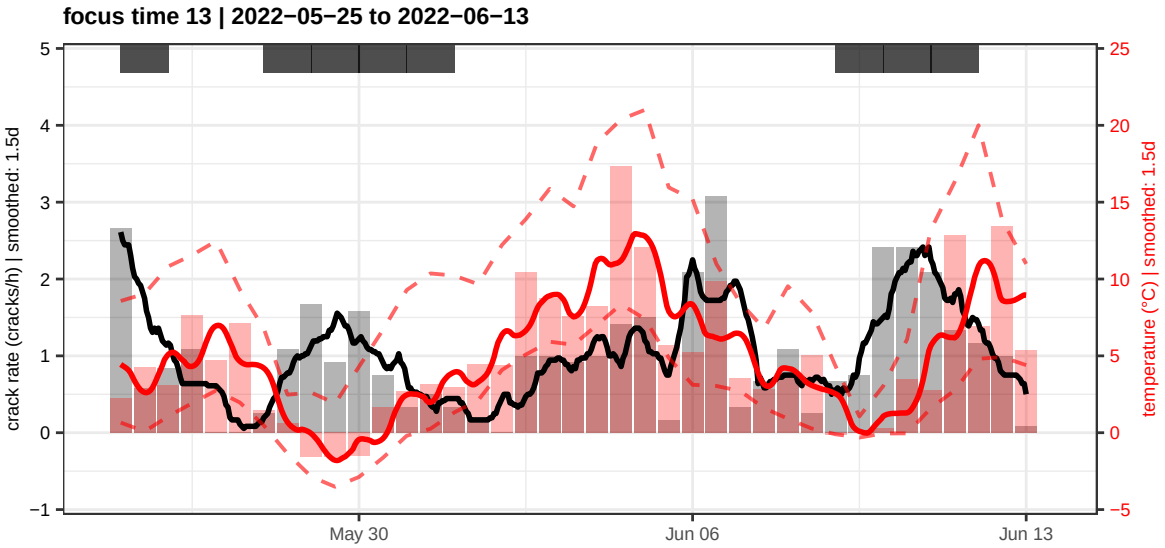

Supplementary Fig. A.1.18: Detail plot of focus time 13. Crack rate, mean temperature (solid line), minimum and maximum temperature (dashed lines, all lines 1.5 d smoothed, columns 12 h means). Peaks in the crack rate coincide with days with freeze-thaw or thaw-freeze conditions (black bars on top). Beginning of June, crack rate increases with increasing temperatures.

A.1.6 Running cross-correlations

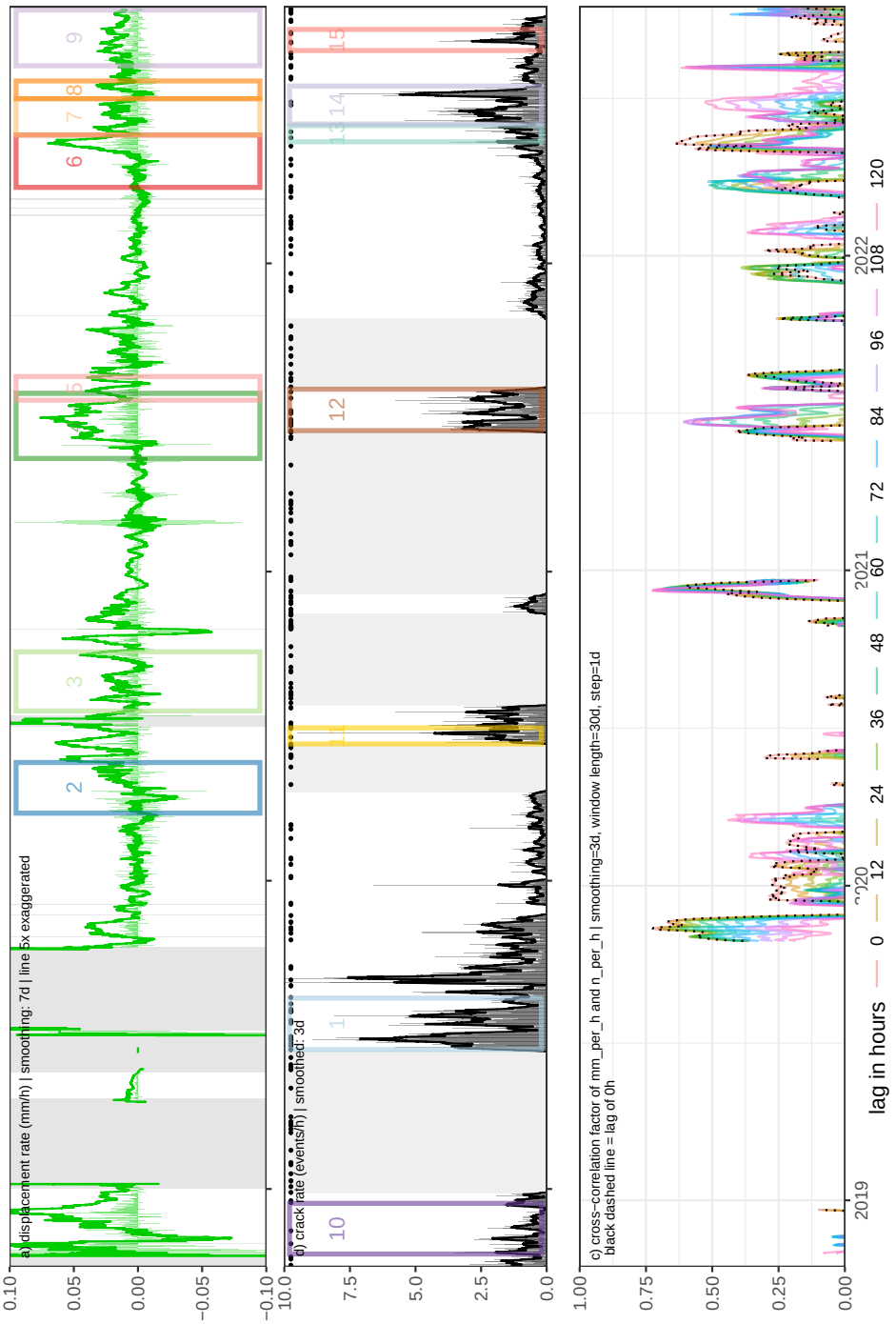

Supplementary Fig. A.1.19: Analysed data between Oct 2018 and Nov 2022 with marked and numbered focus times (rectangles). Data are aggregated to 1 h resolution (see the degree of smoothing in the headers). Columns give 12 h means. (a) displacement rate (mm/h), (b) seismic crack rate (events/h), black dots mark the timing of earthquakes from the catalogue. (c) cross-correlation factor for running cross-correlation between the two curves for a 30 d window shifted in 1 d steps. Colours represent different time lags (see legend). The black dashed line marks a lag of 0 h.

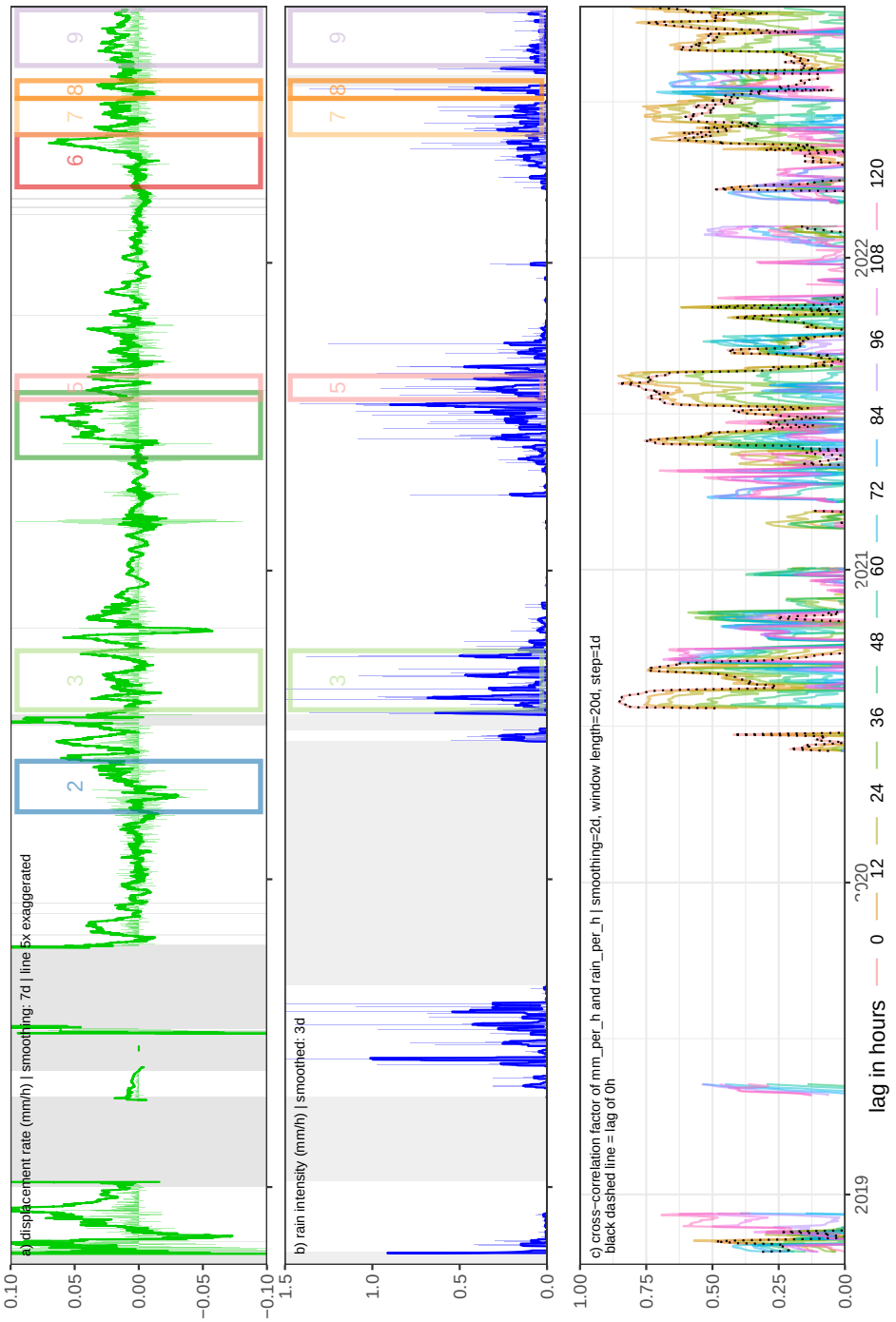

Supplementary Fig. A.1.20: Analysed data between Oct 2018 and Nov 2022 with marked and numbered focus times (rectangles). Data are aggregated to 1 h resolution (see the degree of smoothing in the headers). Columns give 12 h means. (a) displacement rate (mm/h), (b) rain intensity (mm/h). (c) cross-correlation factor for running cross-correlation between the two curves for a 20 d window shifted in 1 d steps. Colours represent different time lags (see legend). The black dashed line marks a lag of 0 h.

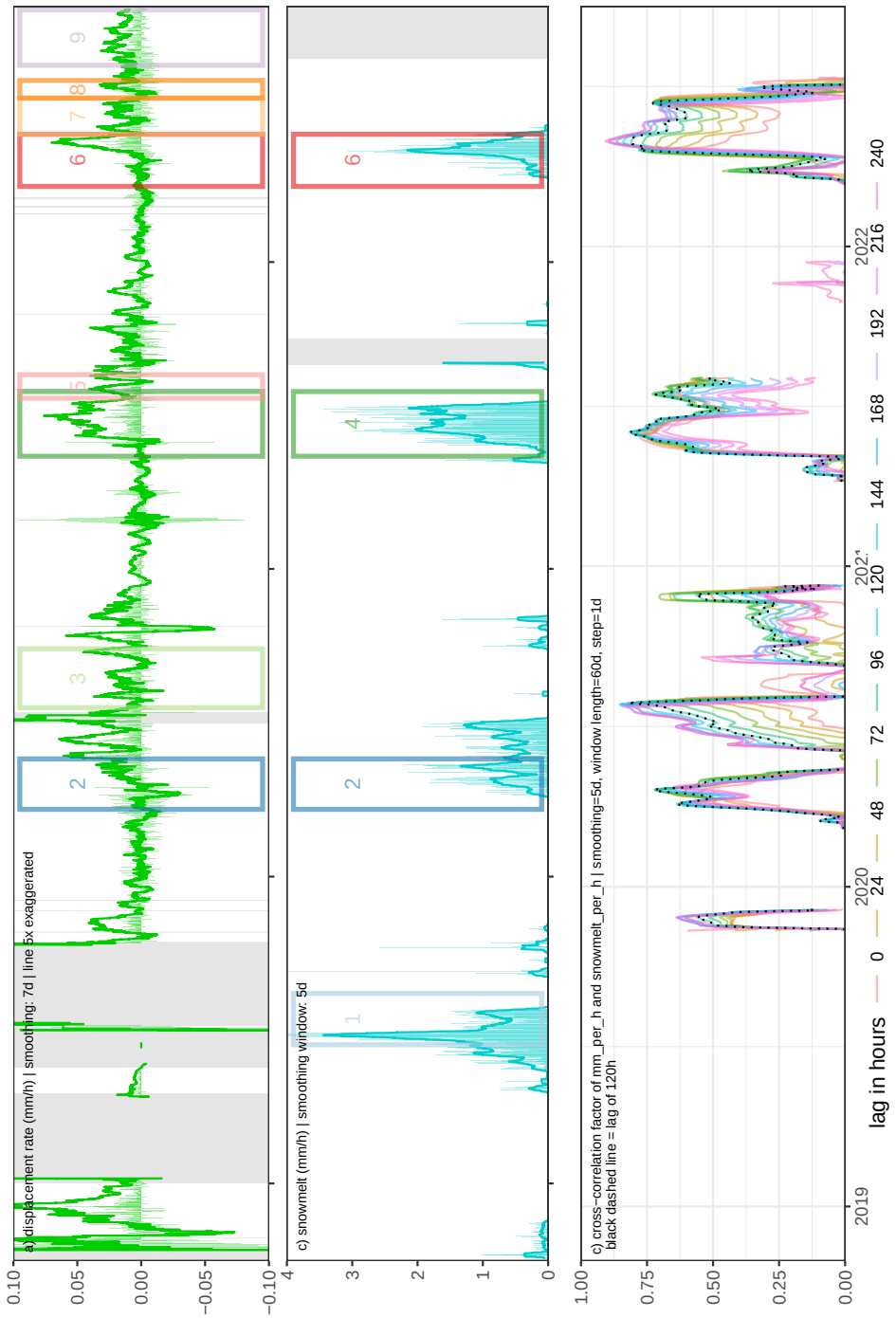

Supplementary Fig. A.1.21: Analysed data between Oct 2018 and Nov 2022 with marked and numbered focus times (rectangles). Data are aggregated to 1 h resolution (see the degree of smoothing in the headers). Columns give 12 h means. (a) displacement rate (mm/h), (b) snowmelt (mm/h). (c) cross-correlation factor for running cross-correlation between the two curves for a 60 d window shifted in 1 d steps. Colours represent different time lags (see legend). The black dashed line marks a lag of 120 h.

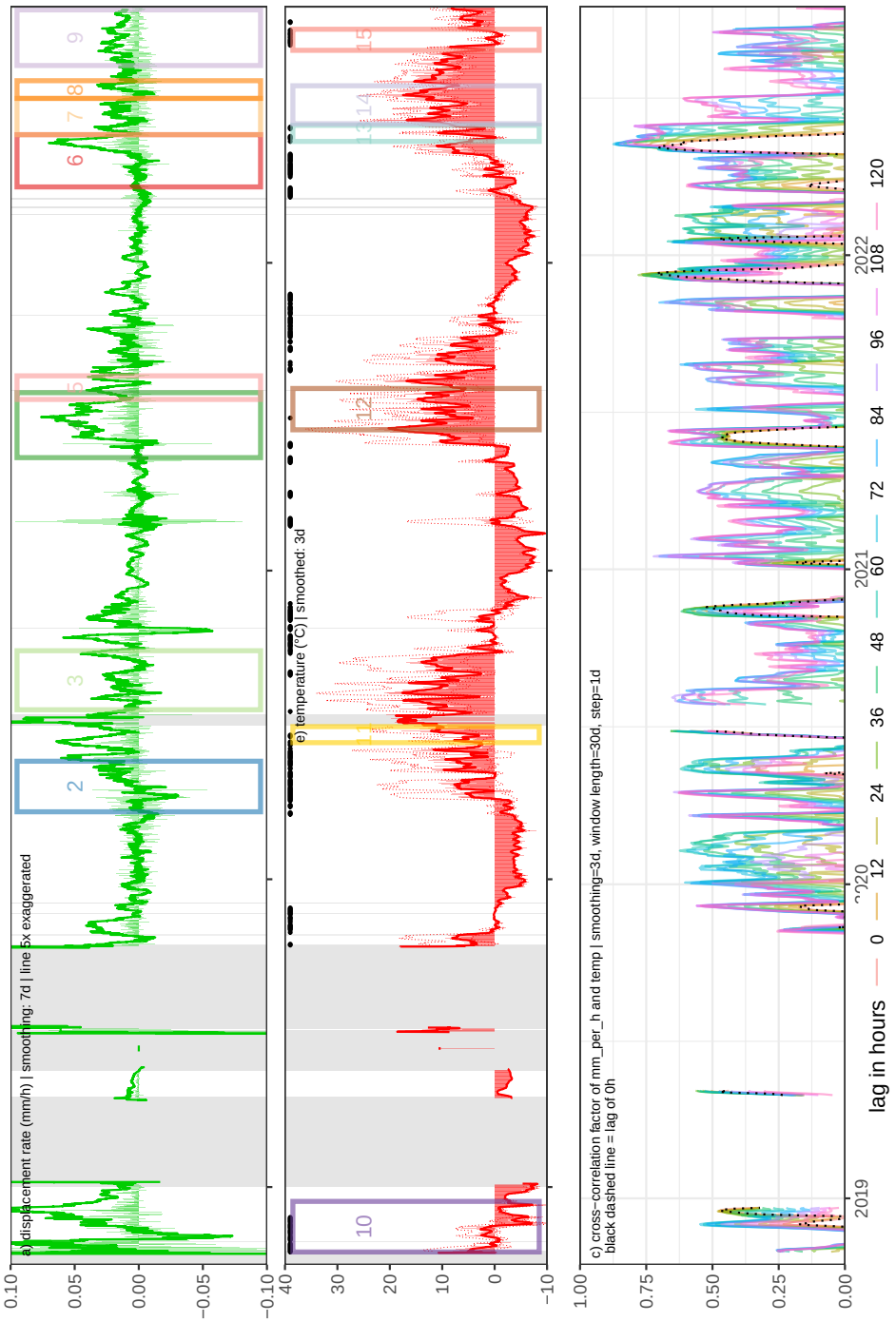

Supplementary Fig. A.1.22: Analysed data between Oct 2018 and Nov 2022 with marked and numbered focus times (rectangles). Data are aggregated to 1 h resolution (see the degree of smoothing in the headers). Columns give 12 h means. (a) displacement rate (mm/h), (b) temperature (°C, solid: mean, dashed min/max). Black dots mark days with freeze-thaw/ thaw-freeze conditions. (c) cross-correlation factor for running cross-correlation between the two curves for a 30 d window shifted in 1 d steps. Colours represent different time lags (see legend). The black dashed line marks a lag of 0 h.

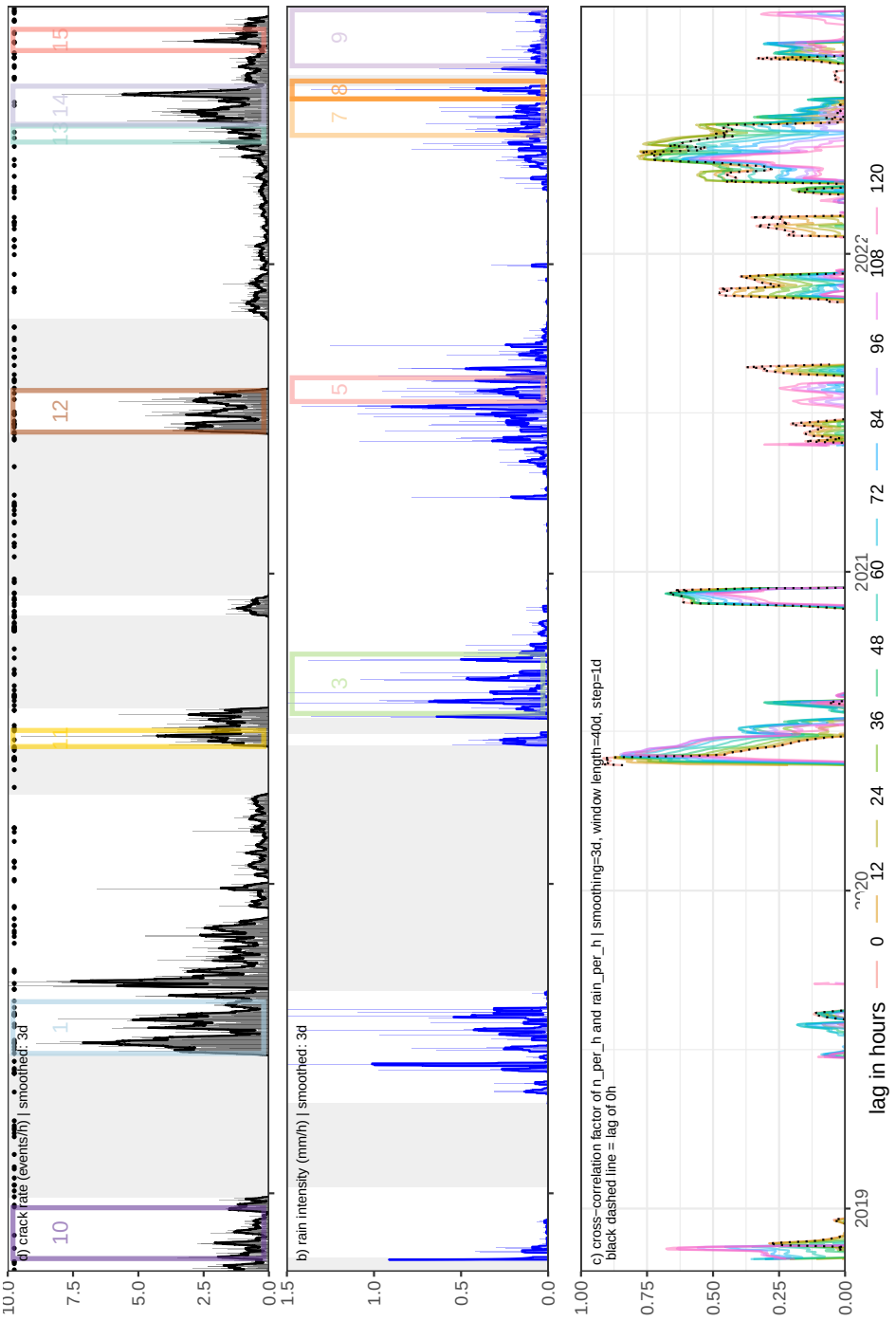

Supplementary Fig. A.1.23: Analysed data between Oct 2018 and Nov 2022 with marked and numbered focus times (rectangles). Data are aggregated to 1 h resolution (see the degree of smoothing in the headers). Columns give 12 h means. (a) seismic crack rate (events/h), black dots mark the timing of earthquakes from the catalogue. (b) rain intensity (mm/h). (c) cross-correlation factor for running cross-correlation between the two curves for a 40 d window shifted in 1 d steps. Colours represent different time lags (see legend). The black dashed line marks a lag of 0 h.

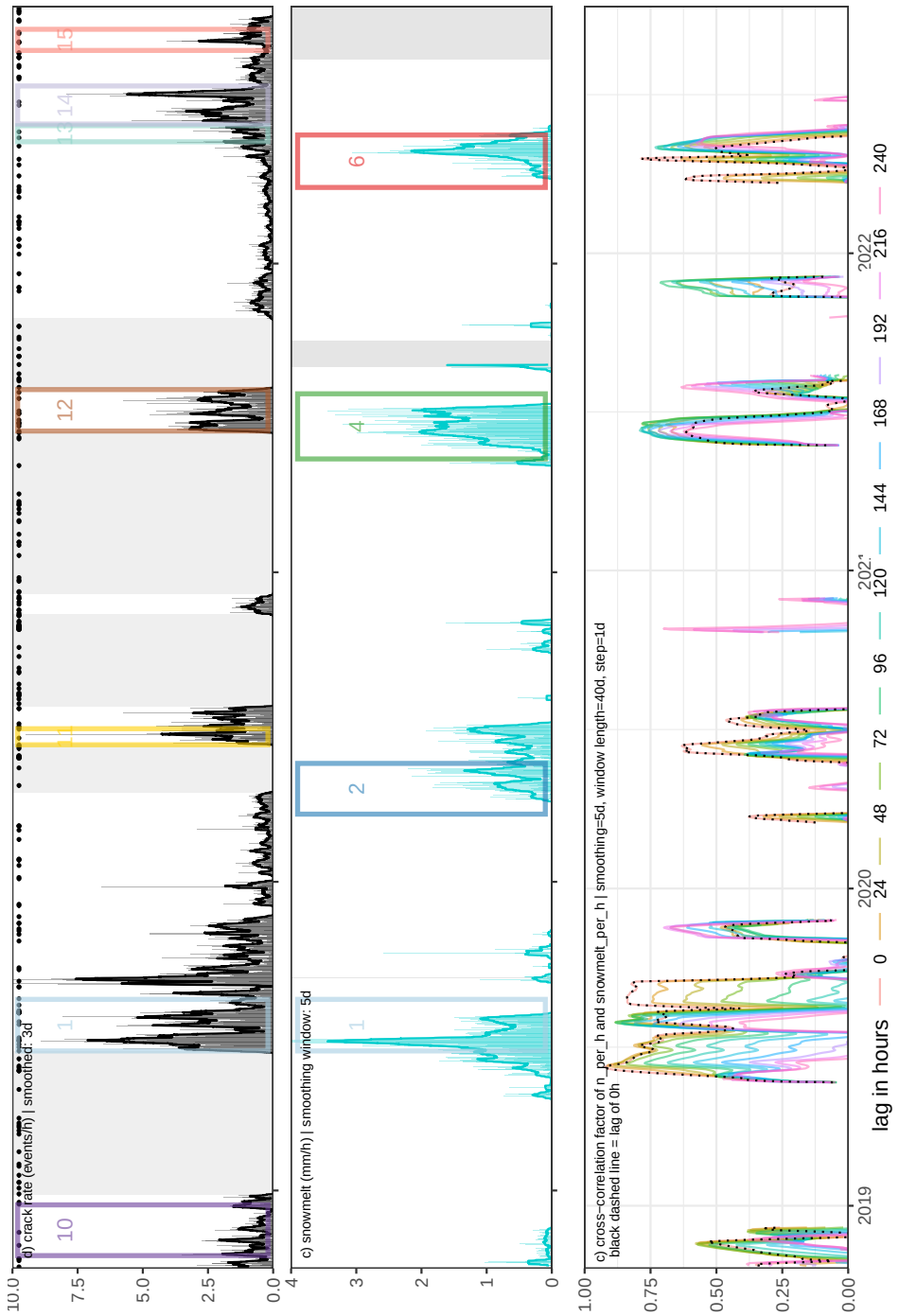

Supplementary Fig. A.1.24: Analysed data between Oct 2018 and Nov 2022 with marked and numbered focus times (rectangles). Data are aggregated to 1 h resolution (see the degree of smoothing in the headers). Columns give 12 h means. (a) seismic crack rate (events/h), black dots mark the timing of earthquakes from the catalogue. (b) snowmelt (mm/h). (c) cross-correlation factor for running cross-correlation between the two curves for a 40 d window shifted in 1 d steps. Colours represent different time lags (see legend). The black dashed line marks a lag of 0 h.

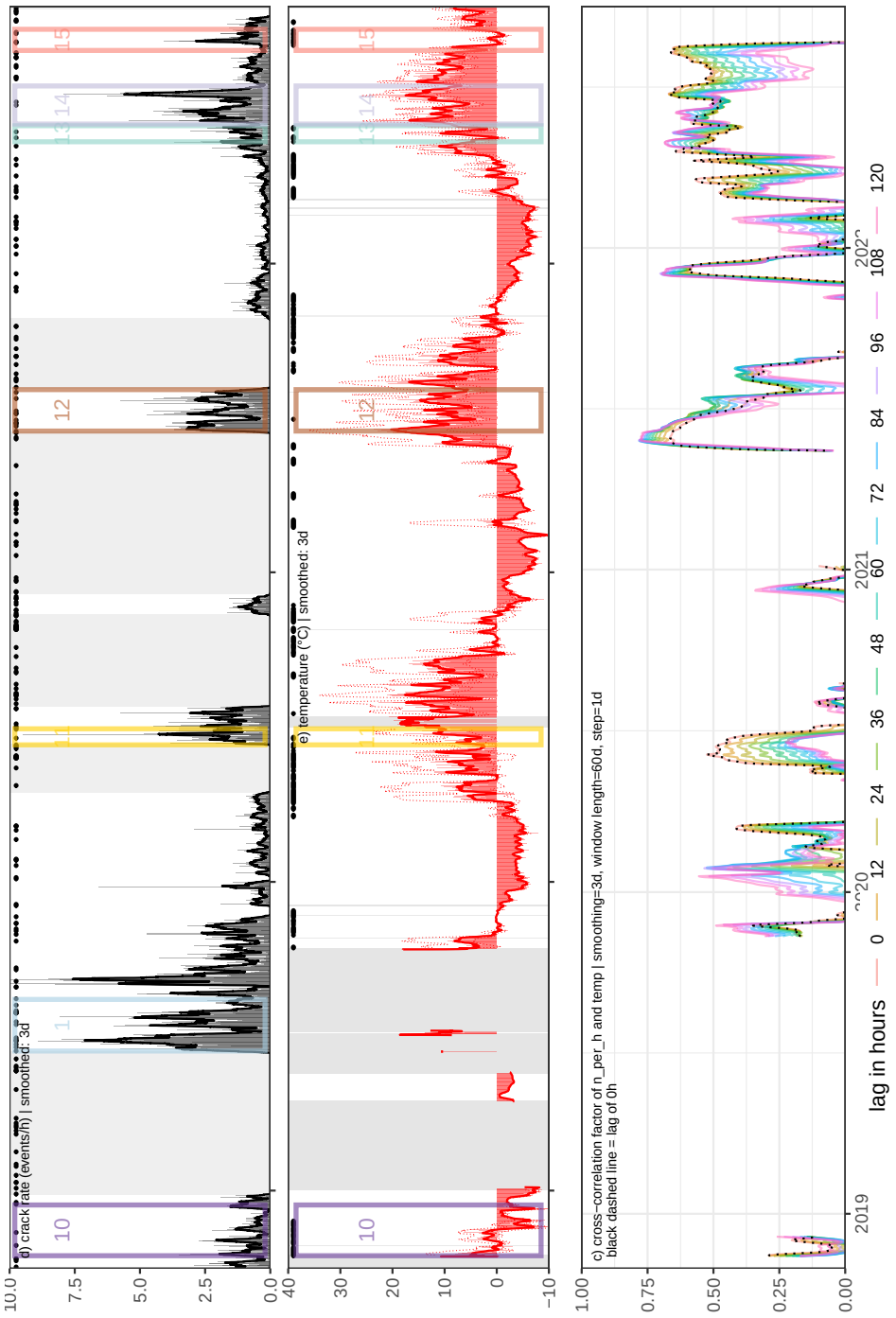

Supplementary Fig. A.1.25: Analysed data between Oct 2018 and Nov 2022 with marked and numbered focus times (rectangles). Data are aggregated to 1 h resolution (see the degree of smoothing in the headers). Columns give 12 h means. (a) seismic crack rate (events/h), black dots mark the timing of earthquakes from the catalogue. (b) temperature (°C, solid: mean, dashed min/max). Black dots mark days with freeze-thaw/ thaw-freeze conditions. (c) cross-correlation factor for running cross-correlation be-tween the two curves for a 60 d window shifted in 1 d steps. Colours represent different time lags (see legend). The black dashed line marks a lag of 0 h.

A.1.7 Earthquake analysis

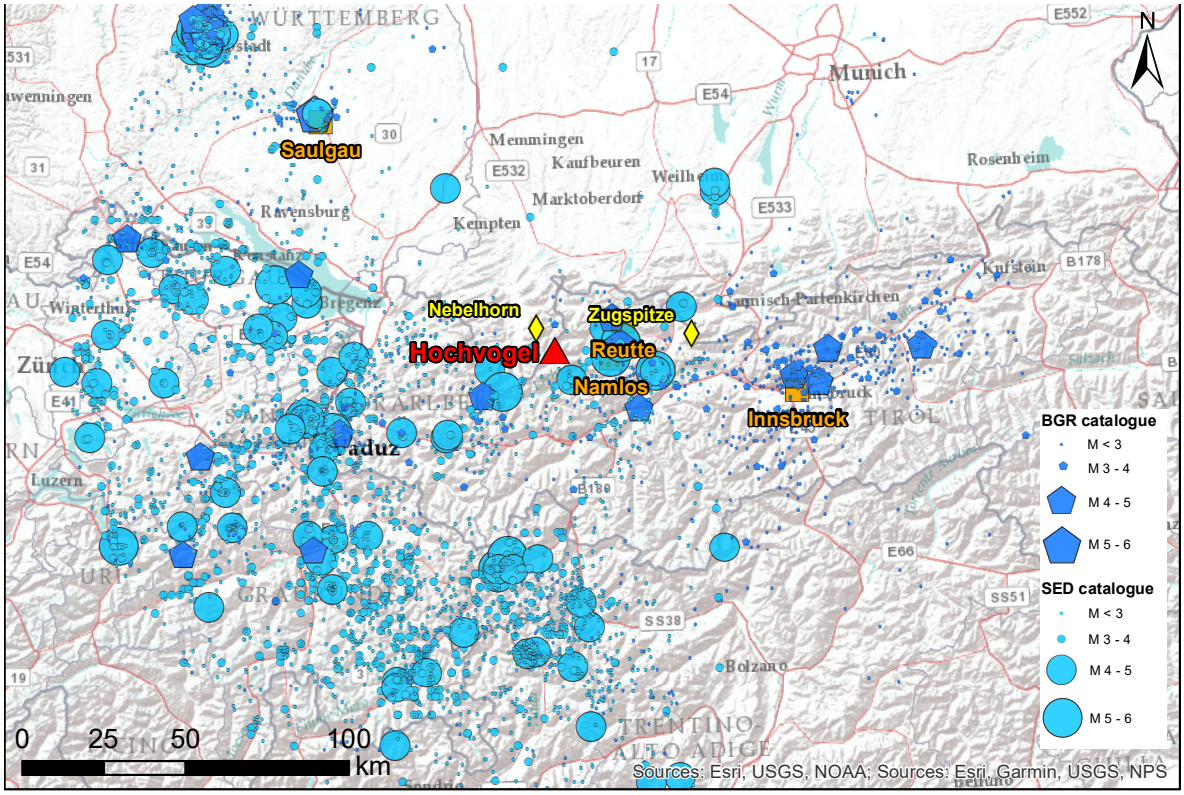

Supplementary Fig. A.1.26: Map showing all earthquakes of the catalogue with M>2 and less than 150 km away from the Hochvogel. Note the clustering of events along the valleys next to the Hochvogel region: Inn, Lech, Alfenz and Rhein. Yellow diamonds mark the two snow stations at Nebelhorn (2075 m a.s.l.) and Zugspitze (2420 m a.s.l.). Basemap and labelling source: Esri, USGS, NOAA, Garmin, NPS.

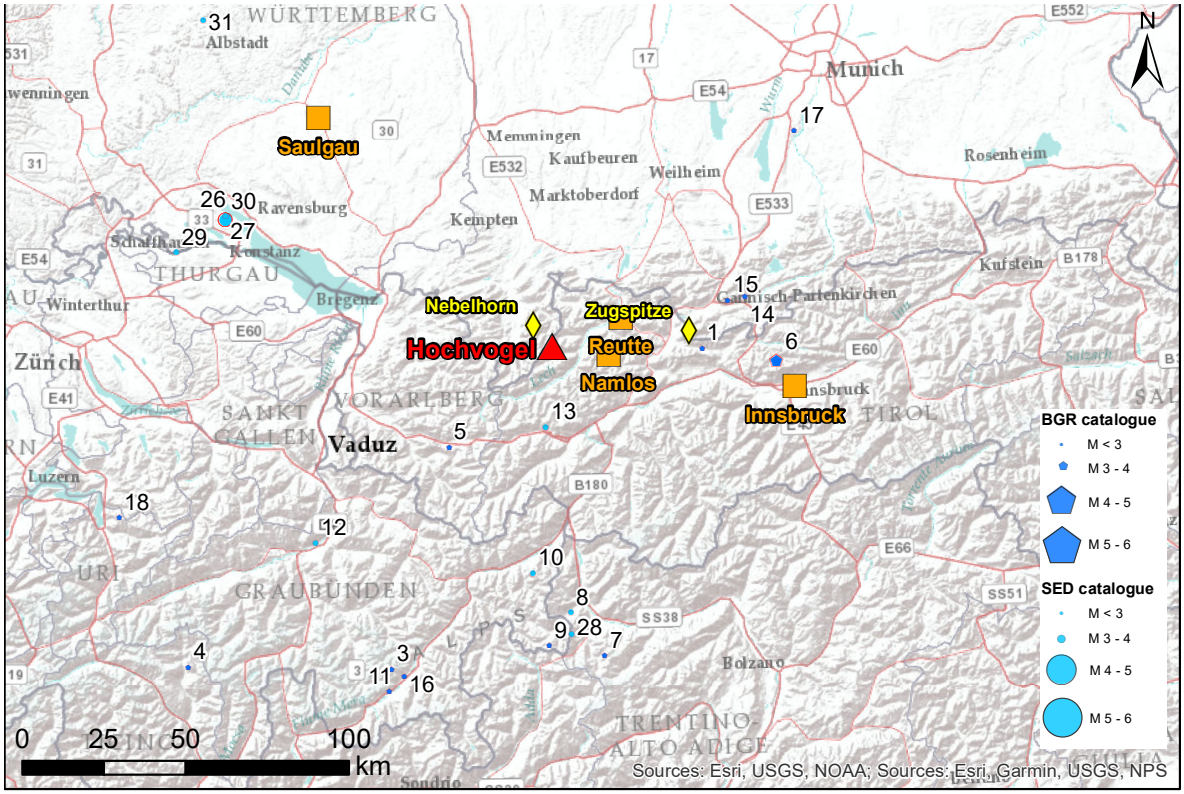

Supplementary Fig. A.1.27: Map showing all earthquakes of the catalogue with M>2 and less than 150 km away from the Hochvogel that happened during station operation of HVGL1 at the summit an at least one more station further down. Events are labelled with a ID-number between 1–31. Yellow diamonds mark the two snow stations at Nebelhorn (2075 m a.s.l.) and Zugspitze (2420 m a.s.l.). Basemap and labelling source: Esri, USGS, NOAA, Garmin, NPS.

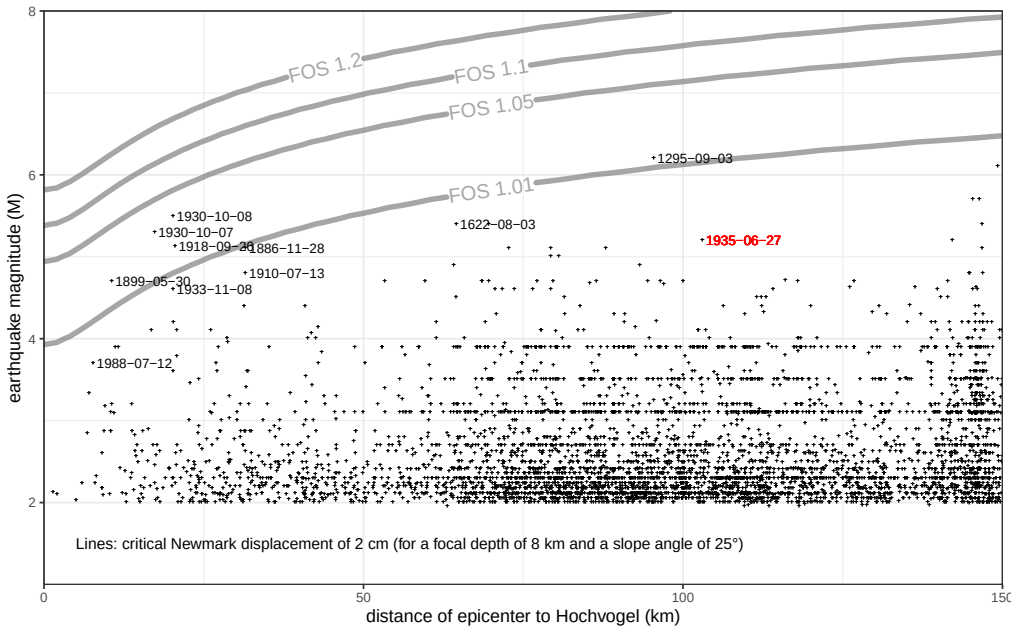

Supplementary Fig. A.1.28: Lines indicate for different factors of safety, at which magnitude and distance of an earthquake a theoretical Newmark displacement of 2 cm is expected. This calculation is based on the mean focal depth of 8 km and a slope angle of 25°. All earthquakes from the catalogues are plotted with black crosses. The earthquakes with the 10 biggest Newmark displacements are labelled in black with their dates. The Saulgau 1935 event is labelled in red.

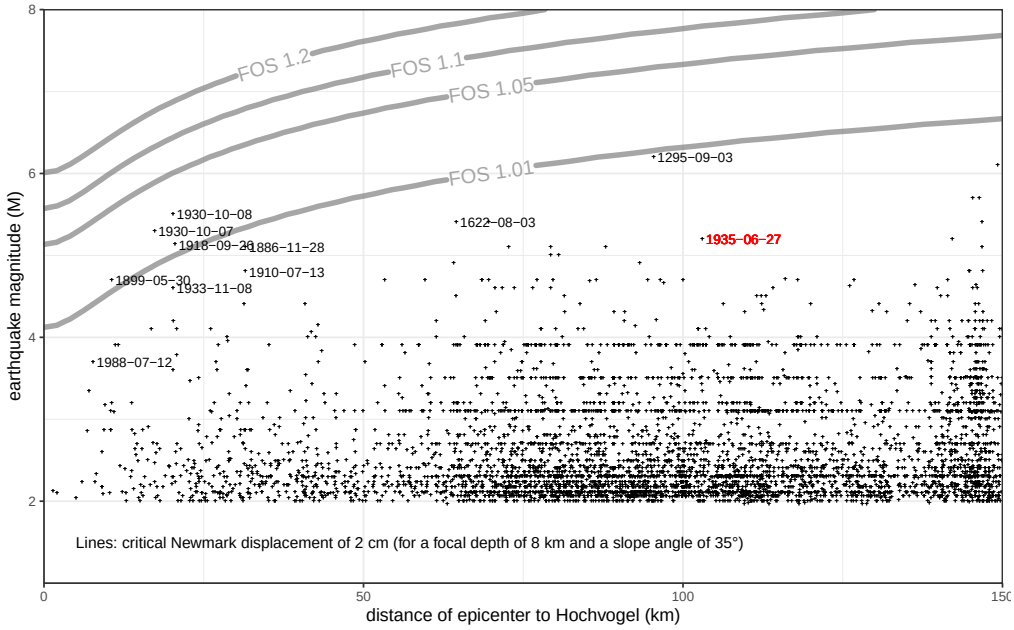

Supplementary Fig. A.1.29: Lines indicate for different factors of safety, at which magnitude and distance of an earthquake a theoretical Newmark displacement of 2 cm is expected. This calculation is based on the mean focal depth of 8 km and a slope angle of 35°. All earthquakes from the catalogues are plotted with black crosses. The earthquakes with the 10 biggest Newmark displacements are labelled in black with their dates. The Saulgau 1935 event is labelled in red.

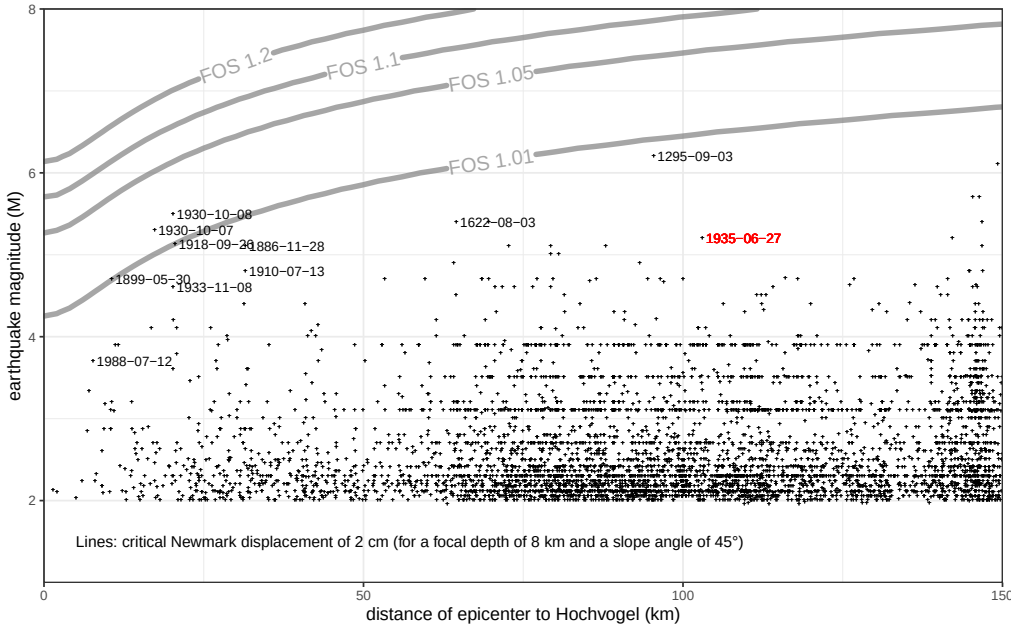

Supplementary Fig. A.1.30: Lines indicate for different factors of safety, at which magnitude and distance of an earthquake a theoretical Newmark displacement of 2 cm is expected. This calculation is based on the mean focal depth of 8 km and a slope angle of 45°. All earthquakes from the catalogues are plotted with black crosses. The earthquakes with the 10 biggest Newmark displacements are labelled in black with their dates. The Saulgau 1935 event is labelled in red.

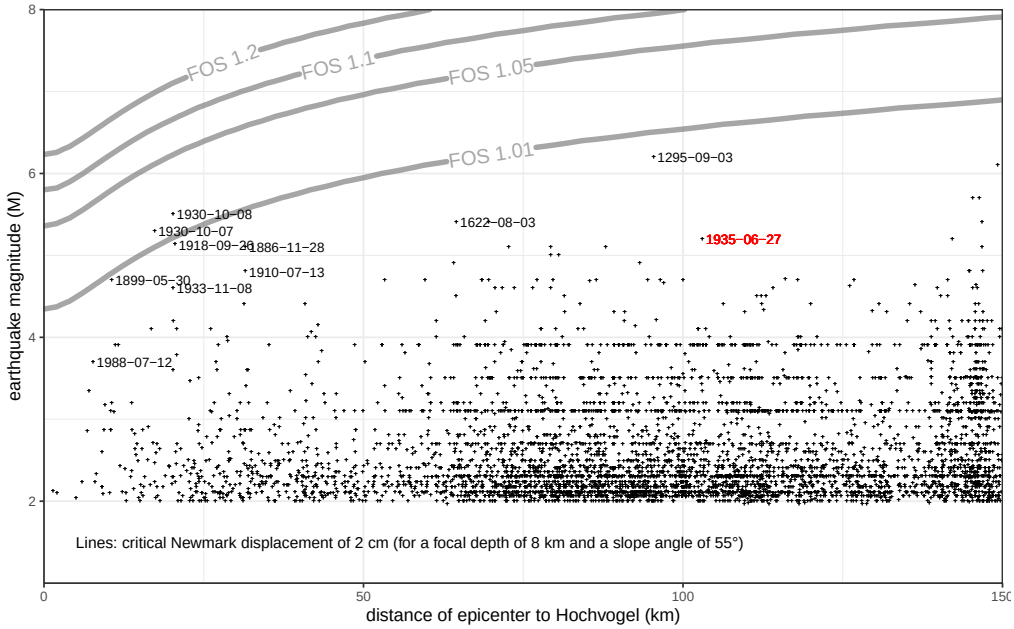

Supplementary Fig. A.1.31: Lines indicate for different factors of safety, at which magnitude and distance of an earthquake a theoretical Newmark displacement of 2 cm is expected. This calculation is based on the mean focal depth of 8 km and a slope angle of 55°. All earthquakes from the catalogues are plotted with black crosses. The earthquakes with the 10 biggest Newmark displacements are labelled in black with their dates. The Saulgau 1935 event is labelled in red.

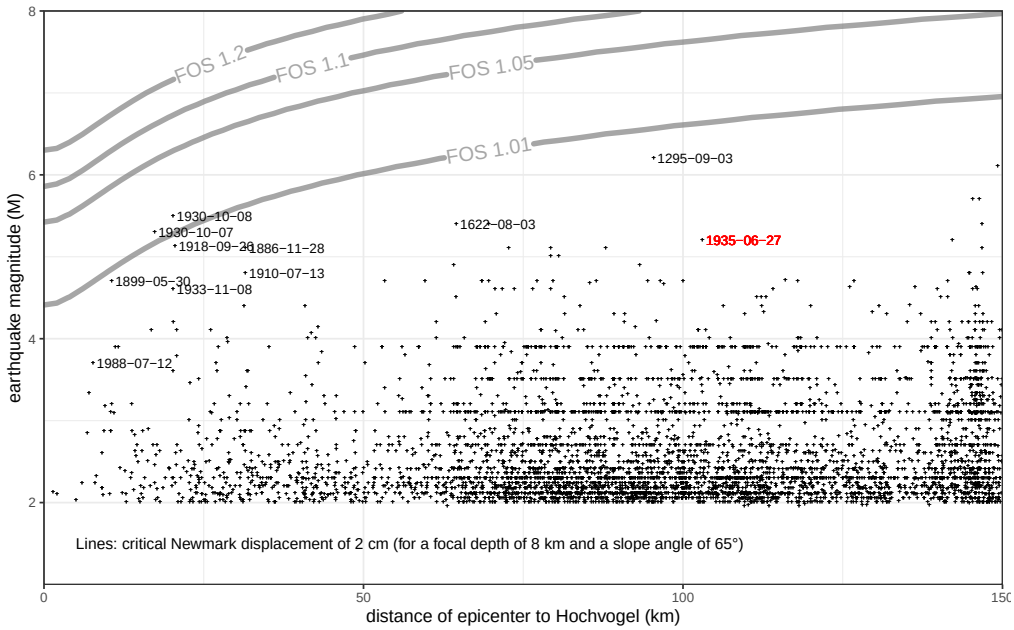

Supplementary Fig. A.1.32: Lines indicate for different factors of safety, at which magnitude and distance of an earthquake a theoretical Newmark displacement of 2 cm is expected. This calculation is based on the mean focal depth of 8 km and a slope angle of 65°. All earthquakes from the catalogues are plotted with black crosses. The earthquakes with the 10 biggest Newmark displacements are labelled in black with their dates. The Saulgau 1935 event is labelled in red.

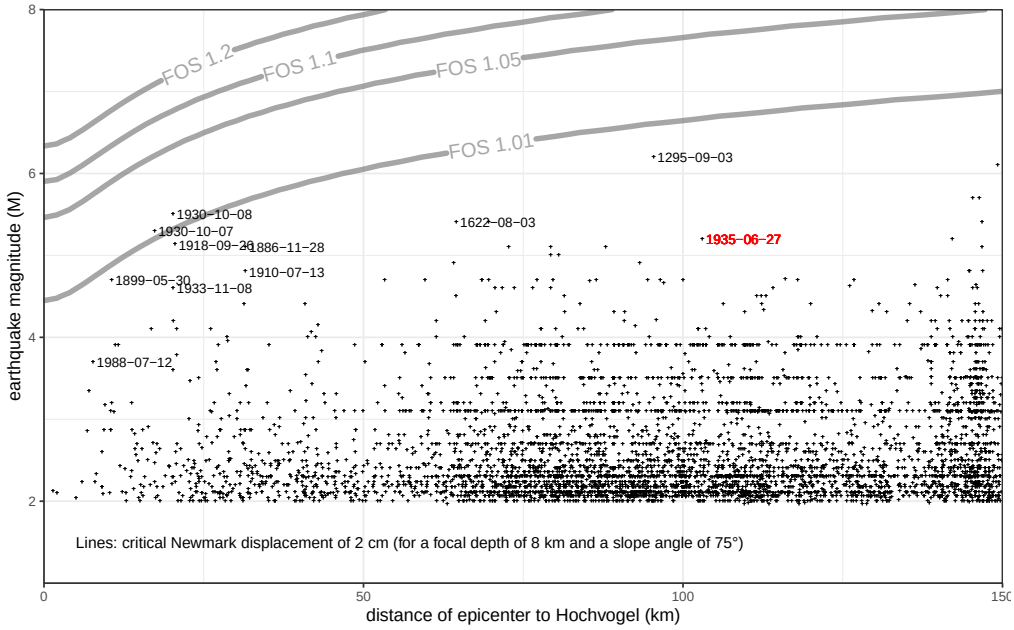

Supplementary Fig. A.1.33: Lines indicate for different factors of safety, at which magnitude and distance of an earthquake a theoretical Newmark displacement of 2 cm is expected. This calculation is based on the mean focal depth of 8 km and a slope angle of 75°. All earthquakes from the catalogues are plotted with black crosses. The earthquakes with the 10 biggest Newmark displacements are labelled in black with their dates. The Saulgau 1935 event is labelled in red.

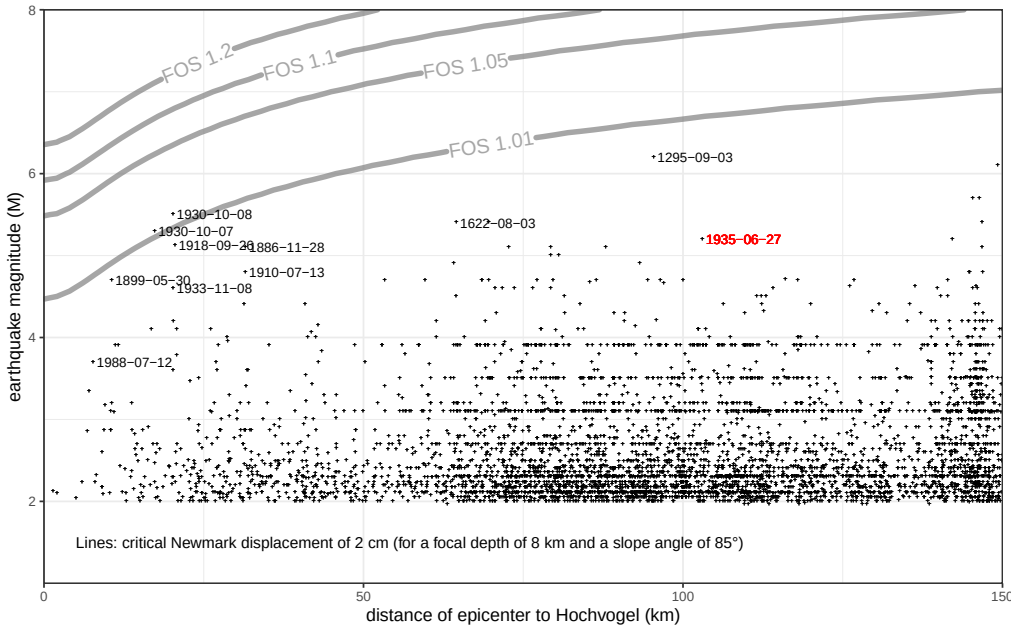

Supplementary Fig. A.1.34: Lines indicate for different factors of safety, at which magnitude and distance of an earthquake a theoretical Newmark displacement of 2 cm is expected. This calculation is based on the mean focal depth of 8 km and a slope angle of 85°. All earthquakes from the catalogues are plotted with black crosses. The earthquakes with the 10 biggest Newmark displacements are labelled in black with their dates. The Saulgau 1935 event is labelled in red.

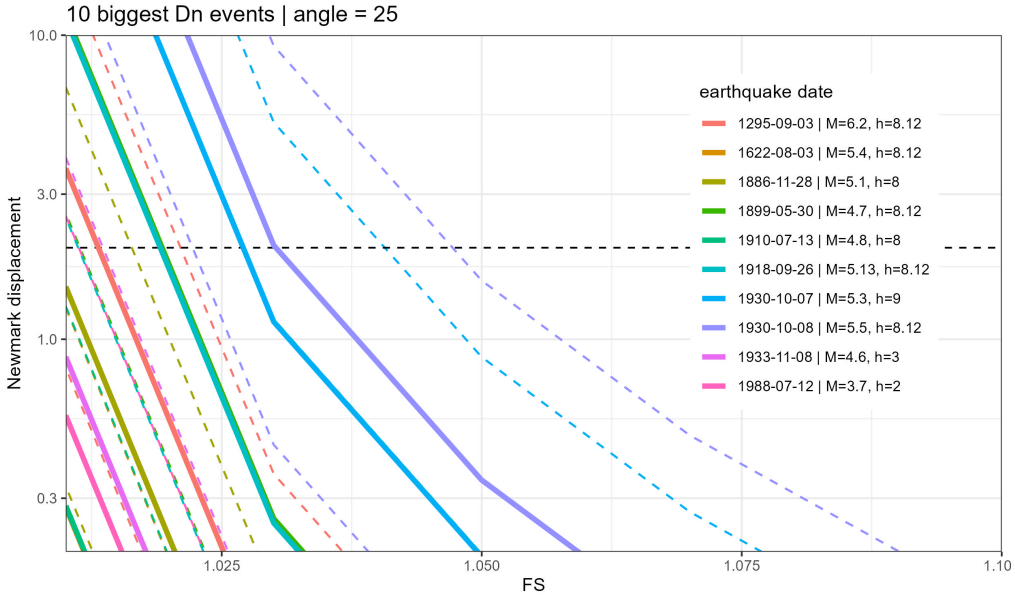

Supplementary Fig. A.1.35: Theoretical Newmark displacement against Factor of Safety (FOS) of the 10 events with the biggest Newmark displacement for a slope angle of 25°. Dashed lines mark uncertainty according to the formula. Displacements are only noteworthy for very low FOS.

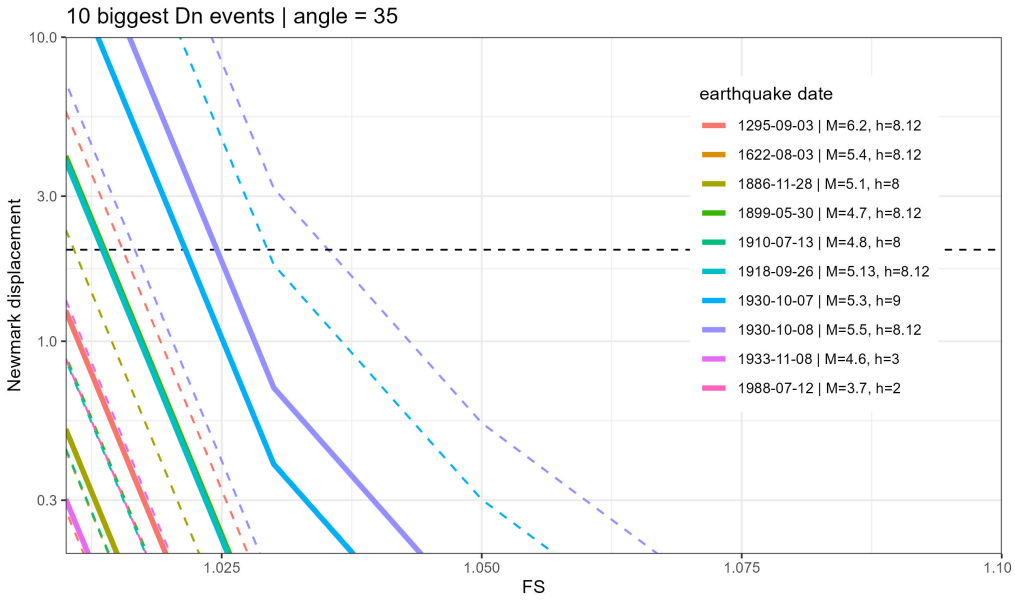

Supplementary Fig. A.1.36: Theoretical Newmark displacement against Factor of Safety (FOS) of the 10 events with the biggest Newmark displacement for a slope angle of 35°. Dashed lines mark uncertainty according to the formula. Displacements are only noteworthy for very low FOS.

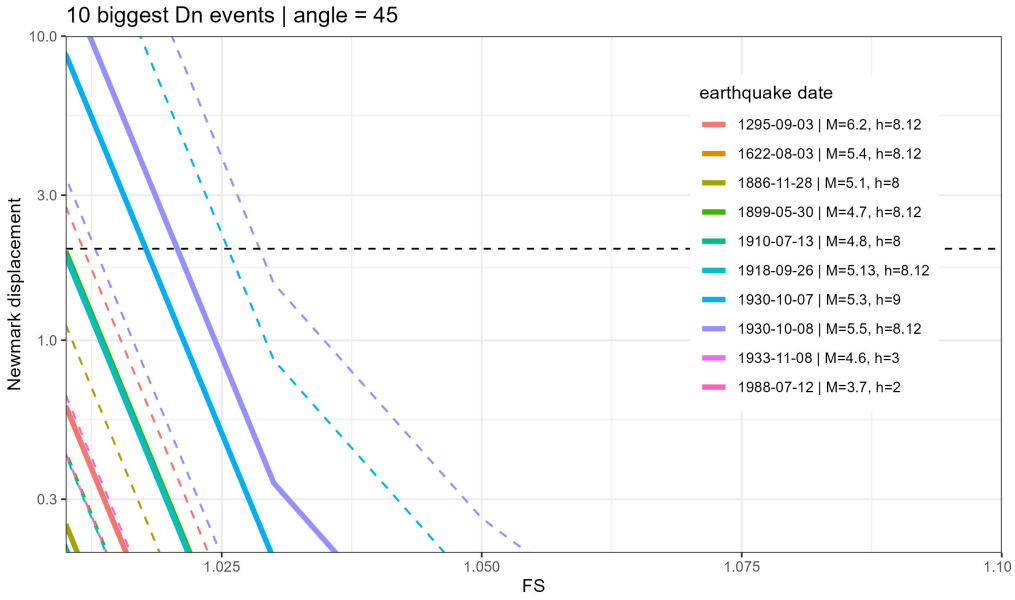

Supplementary Fig. A.1.37: Theoretical Newmark displacement against Factor of Safety (FOS) of the 10 events with the biggest Newmark displacement for a slope angle of 45°. Dashed lines mark uncertainty according to the formula. Displacements are only noteworthy for very low FOS.

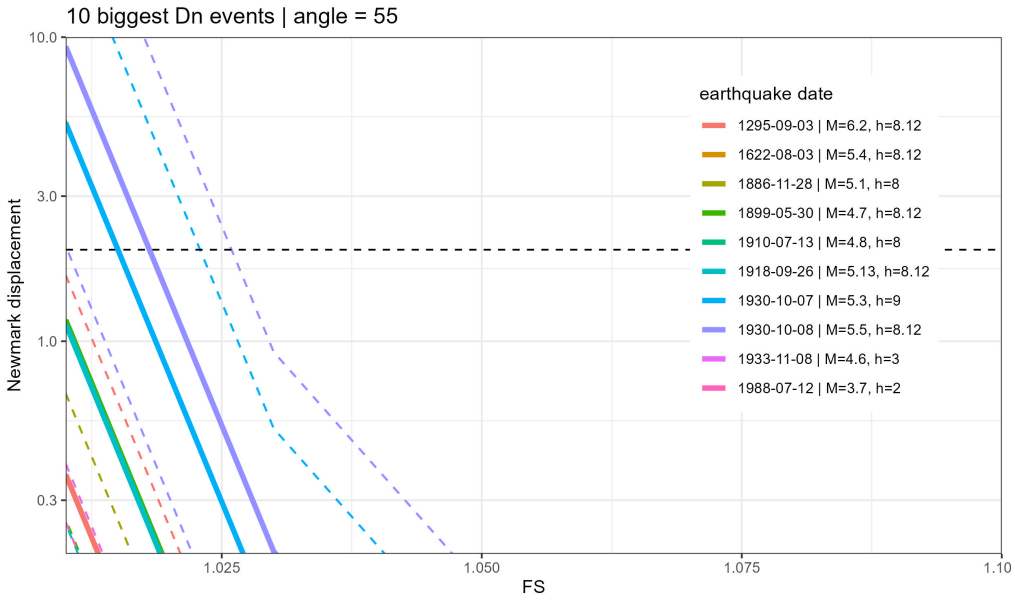

Supplementary Fig. A.1.38: Theoretical Newmark displacement against Factor of Safety (FOS) of the 10 events with the biggest Newmark displacement for a slope angle of 55°. Dashed lines mark uncertainty according to the formula. Displacements are only noteworthy for very low FOS.

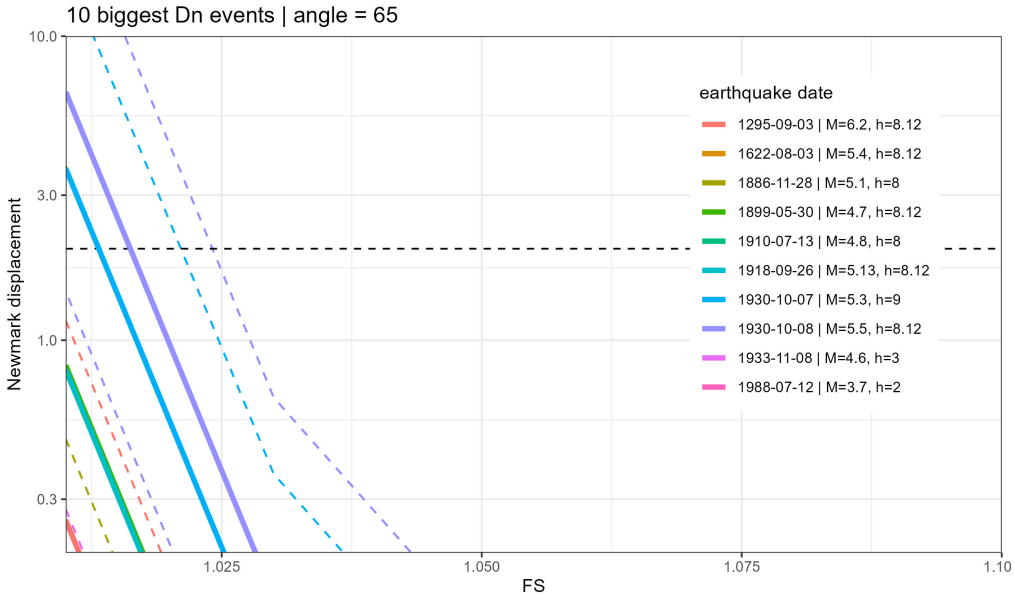

Supplementary Fig. A.1.39: Theoretical Newmark displacement against Factor of Safety (FOS) of the 10 events with the biggest Newmark displacement for a slope angle of 65°. Dashed lines mark uncertainty according to the formula. Displacements are only noteworthy for very low FOS.

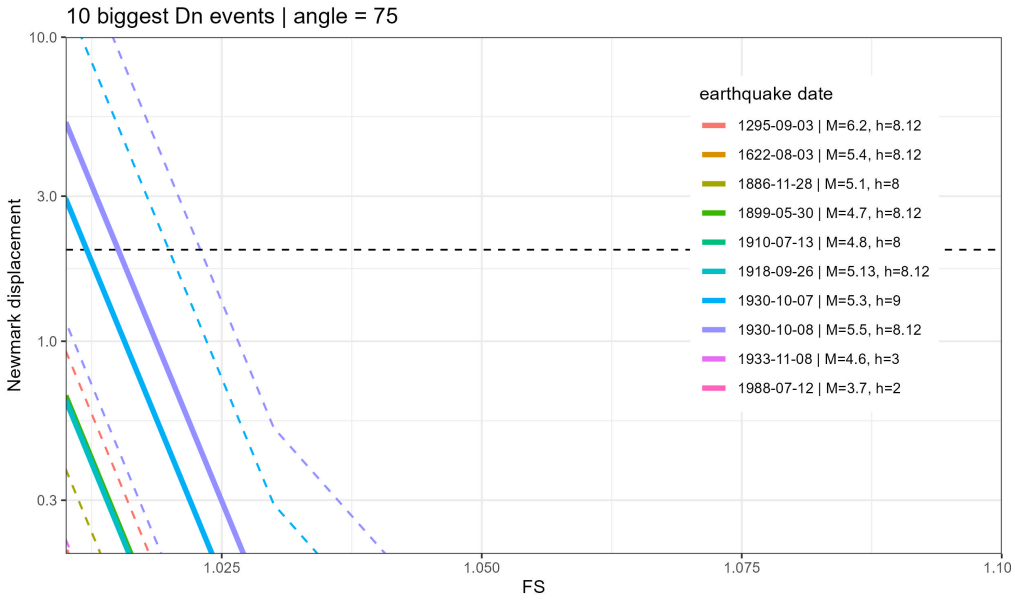

Supplementary Fig. A.1.40: Theoretical Newmark displacement against Factor of Safety (FOS) of the 10 events with the biggest Newmark displacement for a slope angle of 75°. Dashed lines mark uncertainty according to the formula. Displacements are only noteworthy for very low FOS.

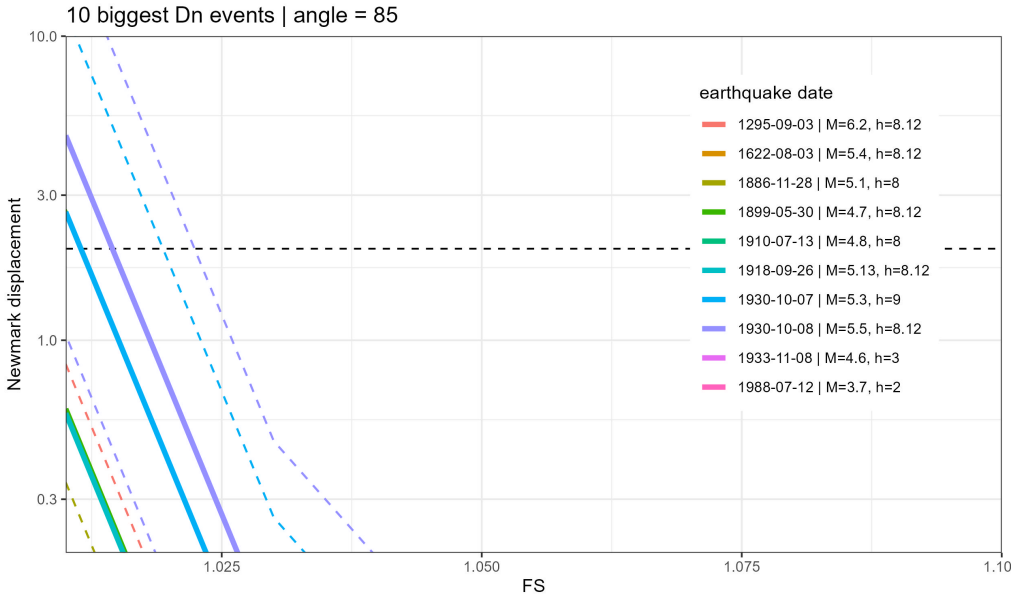

Supplementary Fig. A.1.41: Theoretical Newmark displacement against Factor of Safety (FOS) of the 10 events with the biggest Newmark displacement for a slope angle of 85°. Dashed lines mark uncertainty according to the formula. Displacements are only noteworthy for very low FOS.

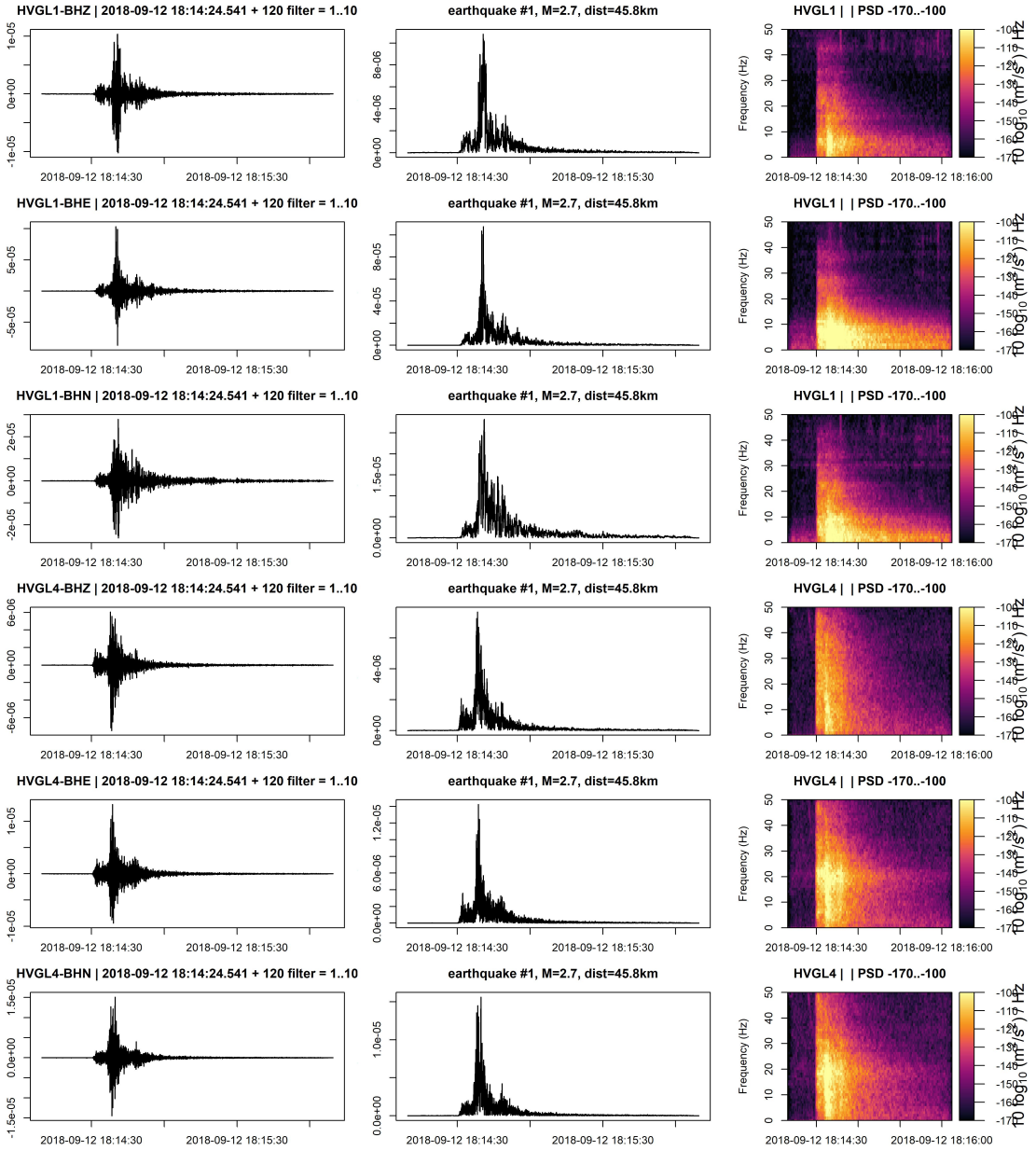

Supplementary Fig. A.1.42: Example of measured seismic signal of HV1 at summit (top three rows) and HV4 in valley (bottom three rows) for all three components (top: Z, middle: E, bottom: N) for earthquake events 1 (left: seismogram, middle: envelope, right: spectrogram).

A.2 Supplementary material to Paper 3

Additional and online available material supplementing the article ③:

Leinauer, J., Weber, S., Cicoira, A., Beutel, J., and Krautblatter, M. (2023): An approach for prospective forecasting of rock slope failure time. Commun Earth Environ 4, 253, doi.org/10.1038/s43247-023-00909-z.

Link to the Supplementary Movie:
https://static-content.springer.com/esm/art%3A10.1038%2Fs43247-023-00909-z/MediaObjects/43247_2023_909_MOESM3_ESM.mp4

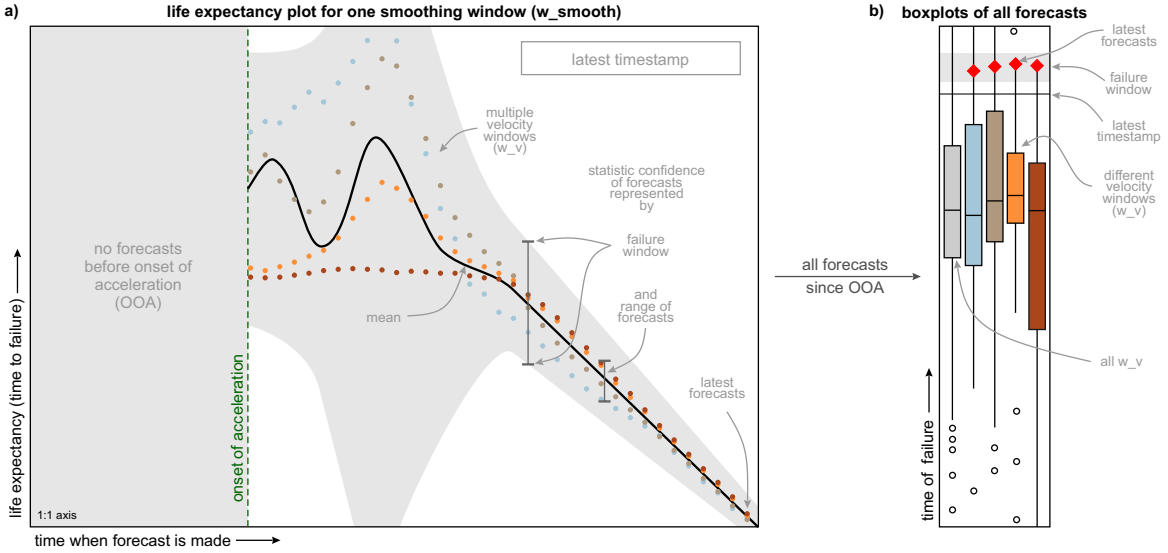

Supplementary Fig. A.2.1: Visualization of forecast results. **a** Life expectancy plot showing the history of all expected times to failure plotted against the time when the forecast is made. The black line shows the mean of all forecasts at each time step and the grey area represents the failure window during which a failure is likely. A narrow failure window corresponds to a low forecast uncertainty (for details see Methods). **b** Boxplots of all forecasts since the OOA per velocity window. The black horizontal line marks the latest timestamp, the grey area represents the failure window and the red diamonds show the latest forecasts per velocity window. Boxplots show the median as line, the interquartile range as box, 1.5 times the interquartile range or the minimum or maximum data point as whiskers and outliers as open circles.

Supplementary Tab. A.2.1: Information on all used data sets and sites

Supplementary table: Information on all used data sets and sites.

site	country	volume [m³]	process	details	data source	analysed dataset[1]	moitoring technique	analysis with data from	data resolution	time of failure	comment
Agoyama	JP	?	rockslide	unknown	Hayashi & Yamamori 1991 *[47]*	P1	?	1972-10-15	1 d**	1972-12-02	
Arvigo	CH	200 k	topple/ rockslide	jointed gneiss with layers of mica shist triggered by quarry and rain	R. Krähenbühl/ F. Beffa	POT 5 POT 8 POT 10	telejointmeter	2007-05-11	1 h*	2007-05-28 20:00	
Galterengraben	CH	2.5 k	rock fall	hanging sandstone wall with valley parallel fractures	Geopraevent AG/ Täfers municipality	TJM 1 TJM 2	telejointmeter	2015-07-06	15 min	2016-04-24 22:15	
Grabengufer	CH	500	fall from rockslide/ sagging edge	block drifting on rock-ice landslide/ sagging in permafrost creeping slope below ridge	Cicoira et al. 2022 *[44]*	GG02 GNSS GG02 incl	GNSS inclinometer	2020-01-01	1 h 2 min 1 h	2020-05-17 01:16	Same location as inclinometer. Gives same results as hourly data. Downsampled with only first measurement every hour.
Hogarth	CA	200 k	topple	iron ore mine with diorite highwall with fractures behind the crest; acceleration after period of rain	Brawner & Stacey 1979 *[48]*	J1 J2 J3 J4 J6	extensometer	1975-01-01	1 d**	1975-06-23	
Kagemori	JP	300-400 k	rockslide	open limestone quarry underlain by shale	Yamaguchi & Shimotani 1986 *[49]*	P15 P21 P23	measuring tape	1972-07-05	1 d**	1973-09-20	
La Saxe	IT	500-1000	rockslide	sector failure of large complex slide with $8*10^6$ m³	Manconi & Giordan 2016 *[39]*	B6	total station with reflectors	2013-03-01	1 h	2013-04-21 23:00	OOA detected at 04/07. Restart with data after 04/16 12:00. See Supplementary Discussion.
Nevis Bluff	NZ	32 k	flexural topple/ rockslide	strongly foliated cholrite shist wall with tension cracks	Brown et al. 1980 *[50]*	P1 P2 A	survey markers	1974-09-11	1 d**	1975-06-14	
Ohto	JP	200 k	rockslide	undercut convex stepp slope of alternating sandstone and mudstone/shale	Suwa et al. 2010 *[51]*	ext	extensometer	2004-05-13	1 d**	2004-08-10	
Preonzo	CH	210 k	rockslide	retrogressive rockslide in foliated high-metamorphic crystalline rocks with joints and faults	Dipartimento del Territorio/ Sezione Forestale Ticino	ext 1 ext 2 ext 3 ext 4 ext 5 ref 1 ref 2 ref 3 ref 4 ref 5 ref 6 ref 7 ref 8 ref 9	extensometer total station with reflectors	2012-01-01	1 h 20 min*	2012-05-15 02:45	Only data until 2012-05-09 available. Deceleration after detected OOA (outlier). Only data until 2012-04-30 available. No OOA detected.
Ryan and Call slope 2	MX	?	wedge rockslide	tetrahedral wedge failure in 80 m high slope in iron ore mine with tension crack	Ryan & Call 1992 *[52]*	P65	prisms	1990-05-17	1 d**	1990-07-26	
Vaiont	IT	270-300 M	rockslide	limestone and marly limestone with clay interbeds triggered by filling water reservoir	Nonveiller 1987 *[53]*	P2 P4 P6 P58	geodetic bench marks	1963-02-01	1 d**	1963-10-09	Analysis with data after latest deceleration in 1963 (trend update point). See details in supplementary discussion 1.

site	country	volume [m³]	process	details	data source	analysed dataset	moitoring technique	analysis with data from	data resolution	time of failure	comment
Veslemannen	NO	54 k	rockslide	instability in folded metamorphic rocks deformed by gravitational fracture opening controlled by snowmelt and rainfall	Kristensen et al. 2021 *[32]*	P3	GB InSAR	2019-01-01	1 h	2019-09-05 19:00	First OOA detected at 06/30-07/02. Restart with data after 07/10 after deceleration. Second OOA detected at 08/31-09/01. Restart with data after 09/01.
						P4					
						P6					
						P7					
Weissmiess	CH	200-300 k	ice fall	hanging glacier that lost toe support	Geopraevent AG	mean	deformation camera/ interferometric radar	2017-07-01	1 d*/ 1 h*	2017-09-10 06:00	First OOA detection with camera, final forecasts with radar.
						max					

* Interpolated many missing values.

** Extracted daily values from plot.

[1] From the available datasets of each site, these are the ones we included in the study based on their documentation, location displacement form and relevance in representing the controlling displacement.

Abbreviations follow the denotation in source:

P = point
POT = potentiometer
TJM = telejointmeter
GG02 = Grabengufer 02
GNSS = Global Navigation Satellite System
incl = inclinometer
J = jointmeter
B / A = measurement points
ext = extensometer
ref = reflector
mean = mean value of displacement in area of interest
max = maximum value of displacement in area of interest
GB InSAR = Graound Based Interferometric Synthetic Aperture Radar

a) Decision schema of standard smoothing (*w_smooth*) and velocity windows (*w_v*) used in this study.

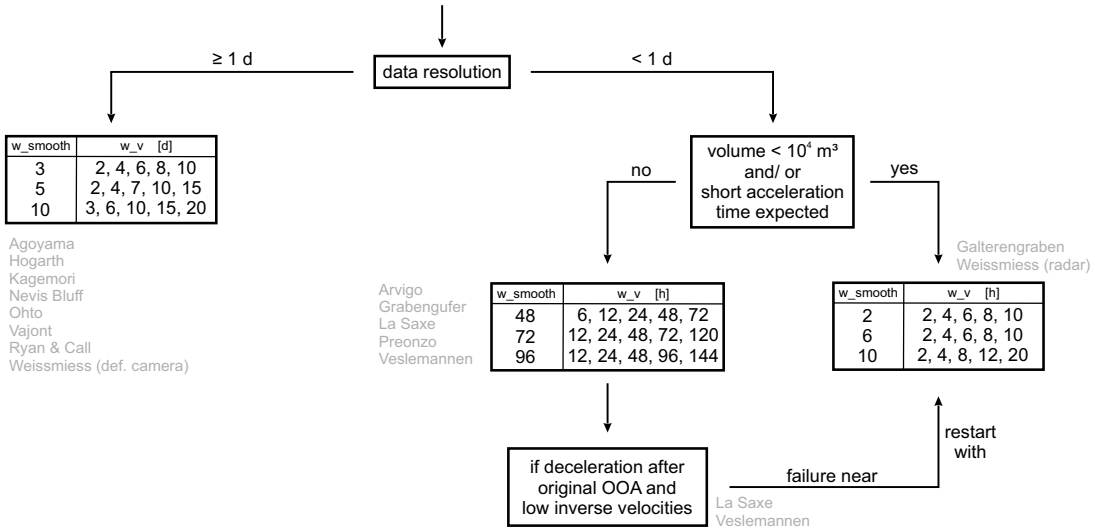

b) Factors influencing the relative window lengths.

relative window lengths	**shorter** ⟷	**longer**
sampling frequency	low ⟷	high
sampling quality	high ⟷	low/ noisy
deformation rate	high/ fast ⟷	low/ slow
displacement before failure	little ⟷	much
duration of acceleration phase	short ⟷	long
volume	small ⟷	big
geological character	brittle ⟷	ductile
lead time needed for mitigation	long ⟷	short

Supplementary Fig. A.2.2: Schema for fixed smoothing and velocity window lengths. a To create comparability between all sites in this study, we defined three sets of standard windows that we applied to the analysed data based on this decision schema. Note that other data might require different smoothing window lengths. **b** Factors and their relative influence on the window lengths.

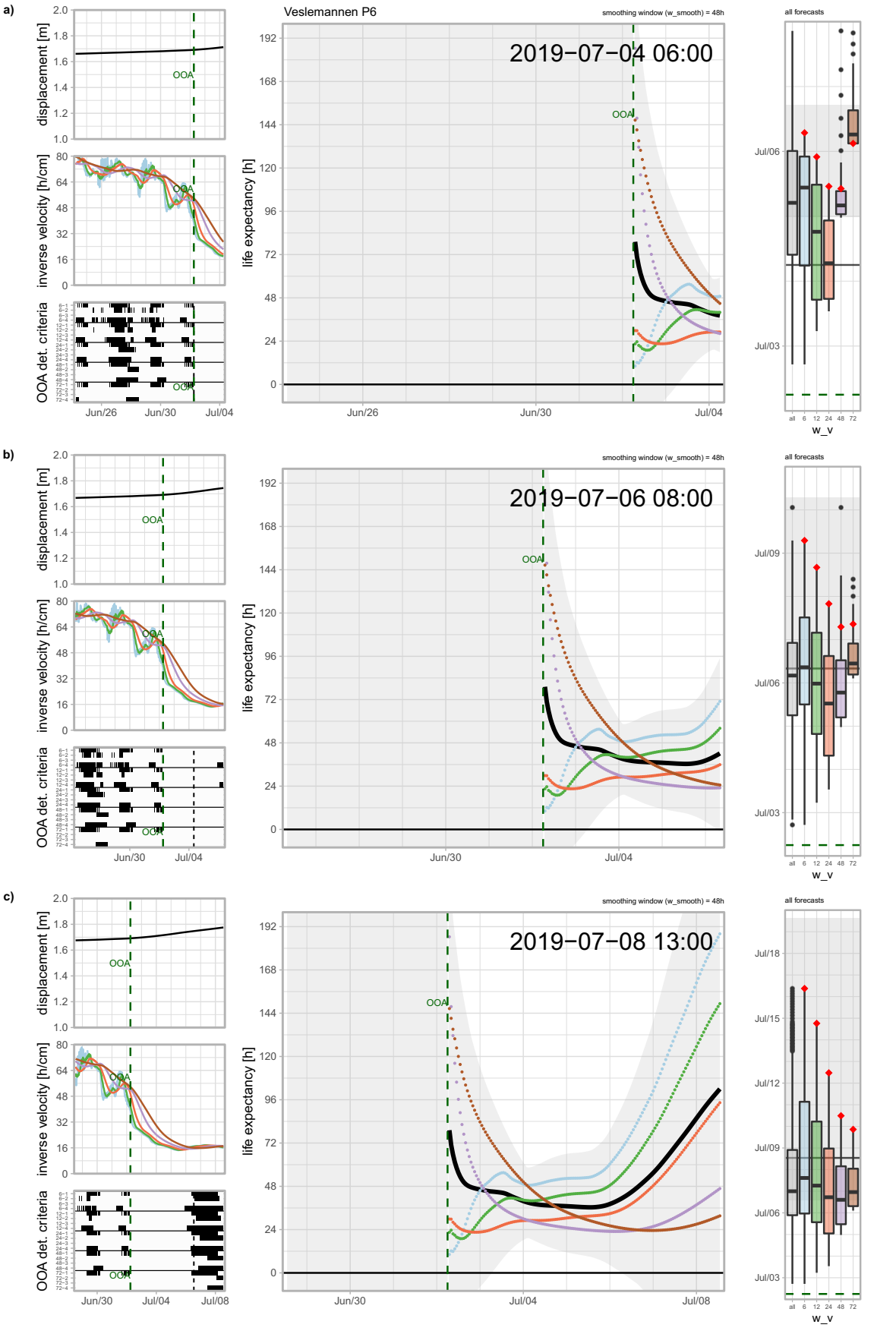
a)
b)
c)
Veslemannen P6
smoothing window (w_smooth) = 48h
2019−07−04 06:00
2019−07−06 08:00
2019−07−08 13:00
displacement [m]
inverse velocity [h/cm]
OOA det. criteria
life expectancy [h]
OOA
Jun/26
Jun/30
Jul/04
Jul/08
all forecasts
Jul/06
Jul/03
Jul/09
Jul/18
Jul/15
Jul/12
W_V
velocity window (w_v) 6 12 24 48 72

Supplementary Fig. A.2.3: Example of a false OOA detection. **a** PFTF model result at the time of OOA detection. Inverse velocities are decreasing with less noise and life expectancies are converging. **b** Result at the time when a false OOA detection is likely. The mean life expectancy is still above 30 h. **c** Result at a later time when the false OOA detection is evident due to increasing inverse velocities and increasing life expectancies. The black line in the life expectancy plot shows the mean of all forecasts at each time step and the grey area represents the failure window during which a failure is likely. Boxplots include all forecasts since the OOA per velocity window. The black horizontal line marks the latest timestamp, the grey area represents the failure window and the red diamonds show the latest forecasts per velocity window. Boxplots show the median as line, the interquartile range as box, 1.5 times the interquartile range or the minimum or maximum data point as whiskers and outliers as open circles. See Supplementary Fig. A.2.1 for details on the visualization.

Supplementary Discussion A.2.1: Using the final accelerating phase in the Vaiont case.

The 1963 Vaiont failure has been preceded by accelerating (and decelerating) creep that has been measured for almost three years (e.g. Ghirotti, 2013). During this time, the mechanical behaviour has changed several times expressed by different velocity regimes. This change in behaviour is the reason, why we only focus on the final accelerating regime (tertiary creep phase) to forecast the final failure. As stated by Rose and Hungr (2007), the first accelerating phase in late October 1962 had a linear inverse velocity regime that pointed towards a failure a few days ahead. The displacement data suggest that the change in external forcing (reservoir lowering and less precipitation) was strong enough to revert the inverse velocity trend. Consequently, most forecasting models would probably have issued a warning for that first acceleration, although this would have been a false alarm. But once the trend change towards lower velocities would have been confirmed, the warning must have been cancelled. Technically, this is not changeable and changing the behaviour of the forecasting model in such a case is not wanted, as the model cannot foresee a strong reversal of the external drivers at the time of the forecast. It can only calculate with previous observations that point towards an imminent failure. We excluded this first accelerating regime at Vaiont from our analysis, as we could not evaluate the quality of the forecasts in this phase because there was no failure.

In such a case of a clear trend change, the inverse velocity fit must be modified and adjusted to the new conditions (Rose and Hungr, 2007). Also, Dick et al. (2015), Carlà et al. (2017a) and Bozzano et al. (2018) advise to calculate additional or new forecasts in case of a trend update point. This is also in line with our concept where we restart the analysis with data after a trend update and determine secondary OOAs (Section 5.1.5). By starting the analysis with data after the latest deceleration in 1963, we focus on the phase after the last trend update point where we can evaluate the quality of the forecast based on the actual failure time.

Finally, the inverse velocity method is not suitable to calculate forecasts over very long periods of time (eg. multiple months or years) but rather for evaluating the significance of short-term acceleration trends (Rose and Hungr, 2007, Ghirotti, 2013). However, it is a valuable method for calculating quantified forecasts within the timeframe that is necessary to mitigate and evacuate (usually hours to days). It therefore appears reasonable to analyse the Vaiont failure based on the last months of data rather than including the whole record.

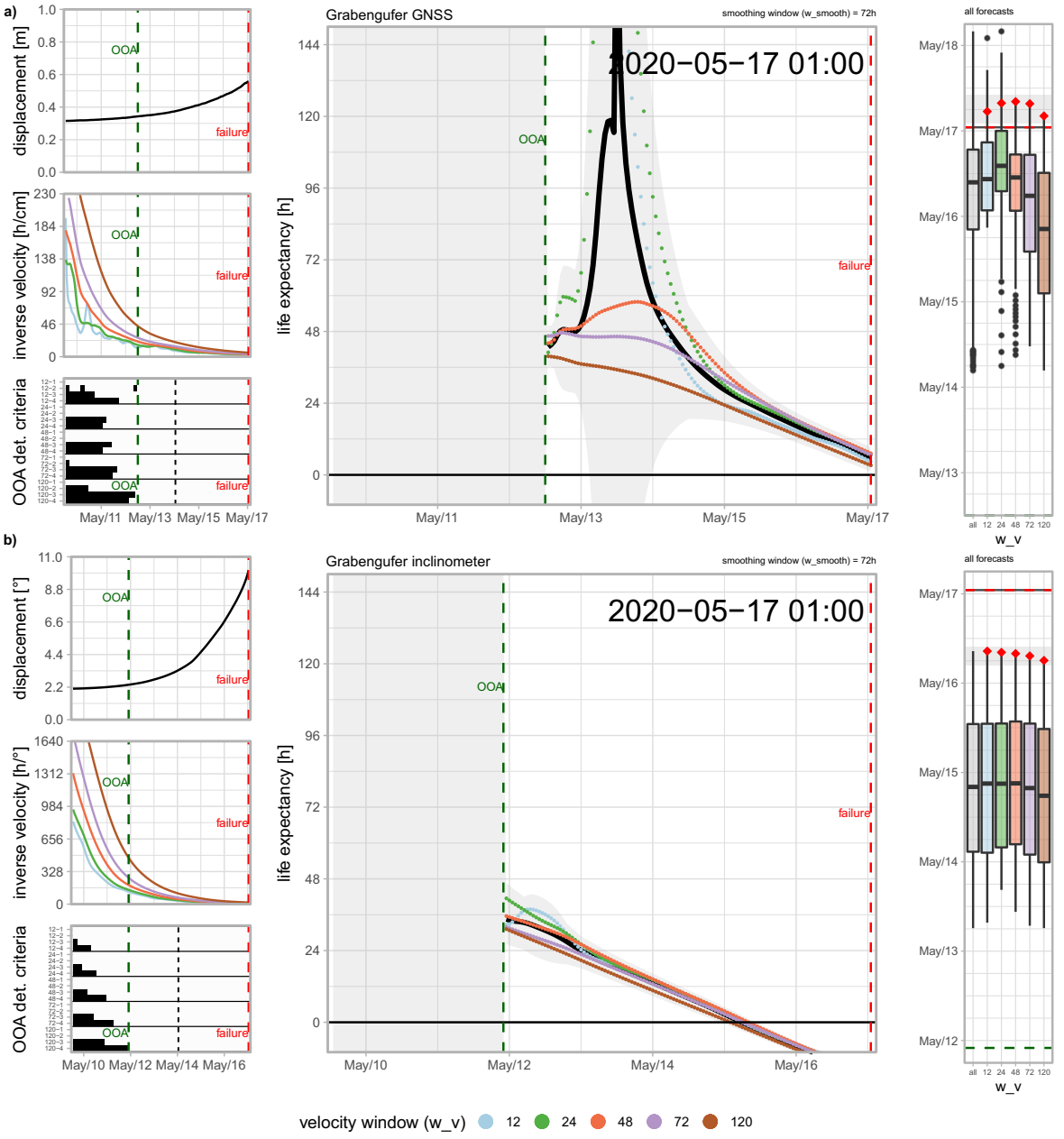

Supplementary Fig. A.2.4: Forecast results of GNSS and inclinometer data from Grabengufer. **a** PFTF model result from GNSS data at Grabengufer (data frequency = 1 h). Note the concave form of the inverse velocities. **b** PFTF model result from inclinometer data at Grabengufer (data frequency has been downsampled to 1 h by keeping only the first reading every hour). Note the concave form of the inverse (angle) velocities. The black line in the life expectancy plot shows the mean of all forecasts at each time step and the grey area represents the failure window during which a failure is likely. Boxplots include all forecasts since the OOA per velocity window. The black horizontal line marks the latest timestamp, the grey area represents the failure window and the red diamonds show the latest forecasts per velocity window. Boxplots show the median as line, the interquartile range as box, 1.5 times the interquartile range or the minimum or maximum data point as whiskers and outliers as open circles. See Supplementary Fig. A.2.1 for details on the visualization.

Supplementary Discussion A.2.2: Prospective forecasting of the La Saxe case.

The La Saxe instability showed a complex displacement pattern that hindered prospective forecasting. Especially the decision on which sensors are most representative for the final failure is challenging on a prospective approach. We therefore present and discuss the case in more detail here based on all three to us available datasets (points B4, B6 and T8).

A primary OOA has been detected by the PFTF model in spring 2012, but it is not followed by an increasing acceleration (Supplementary Fig. A.2.5). Later, the mass even decelerated making this first OOA in 2012 a clear false OOA that is easy to identify. The next acceleration appeared in April 2013. The OOA is detected with all 3 sensors and standard long window lengths between 2013-04-07 06:00 and 2013-04-13 14:00 and consecutively, forecasts are calculated.

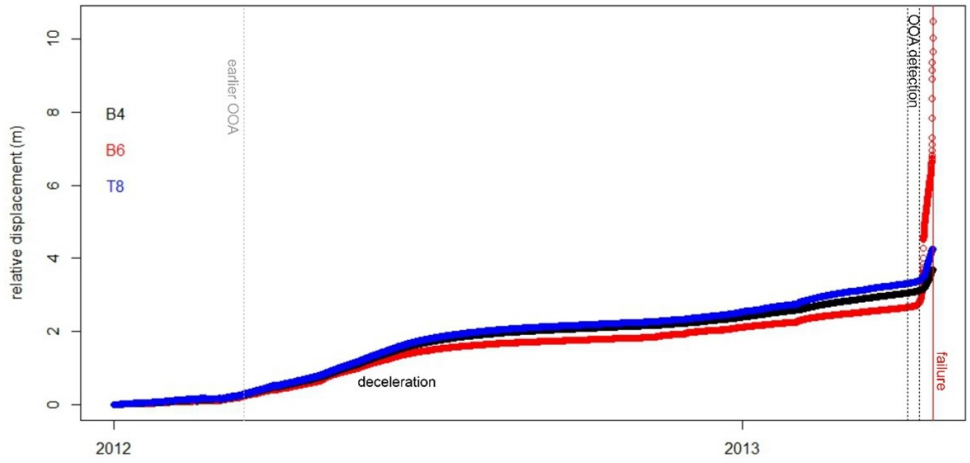

Supplementary Fig. A.2.5: Displacement of three measurement points B4 (black), B6 (red) and T8 (blue) at La Saxe after 2012-01-01 until failure of B6.

B6 points towards an imminent failure with consistent forecasts (Supplementary Fig. A.2.6). B4 and T8 show consistent forecasts with life expectancies of 2-3 days (Supplementary Fig. A.2.7-A.2.8). The displacement trend supports this, as B6 is accelerating more than B4 and T8. At this time (before April 16, 12:00), from the point of view of any decision maker, an alarm with evacuation must be triggered. It must be expected that the section of B6 is about to fail and the rest of the unstable mass with sensors B4 and T8 would follow soon or concurrently if the bigger mass failure might be triggered by the failure of the section B6.

Only in the detail displacement plot after April 16 noon (Supplementary Fig. A.2.9), it becomes obvious that the sensors behave different and B4 and T8 do not accelerate more. The sharp change in the behaviour of B6 on April 16 marks a trend update point (see methods 4.5), necessitating an updated analysis with data after the trend update point and with short window lengths, as the OOA has been detected earlier and failure is expected near (cp. Supplementary Figure A.2.2). Then, correct forecasts are calculated with point B6 (Supplementary Fig. A.2.10).

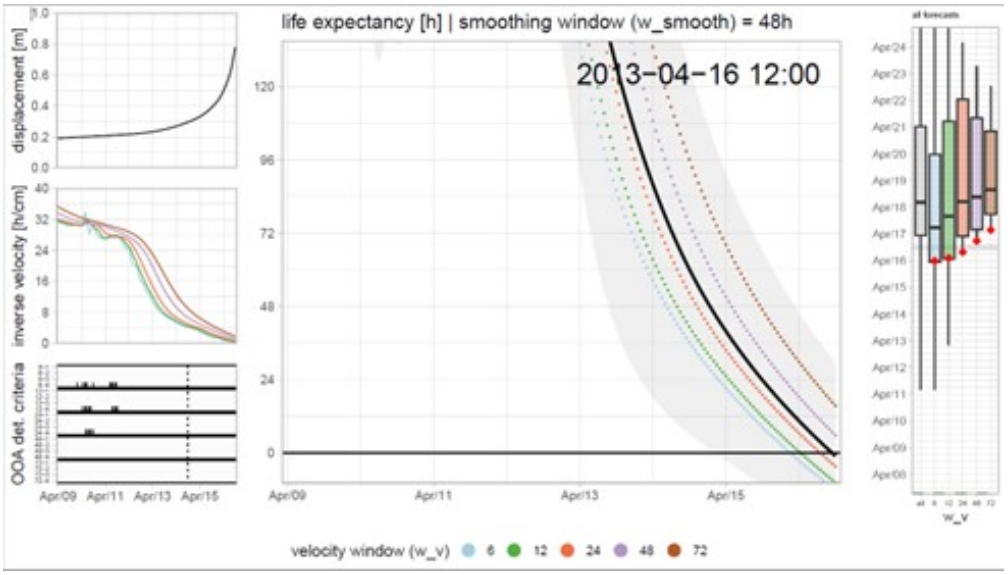

Supplementary Fig. A.2.6: PFTF forecast from 2023-04-16 12:00 at point B6. The black line in the life expectancy plot shows the mean of all forecasts at each time step and the grey area represents the failure window during which a failure is likely. Boxplots include all forecasts since the OOA per velocity window. The black horizontal line marks the latest timestamp, the grey area represents the failure window and the red diamonds show the latest forecasts per velocity window. Boxplots show the median as line, the interquartile range as box, 1.5 times the interquartile range or the minimum or maximum data point as whiskers and outliers as open circles. See Supplementary Fig. A.2.1 for details on the visualization.

Considering the risk of fatalities and based on these available data, responsible decision-makers would always have to initiate mitigation measures expecting a bigger section failure marked by all accelerating sensors before April 16. However, the focus of this study is to present a robust and uniform model for predicting divers slope failures rather than selecting the right monitoring data. Further research on the selection of the most relevant sensors for failure forecasting is needed but beyond the scope of this study.

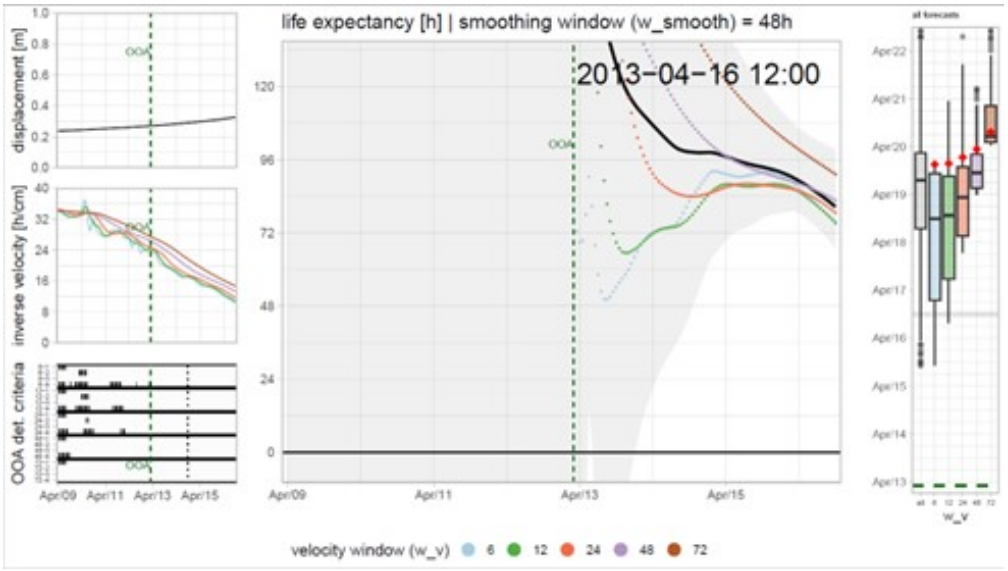

Supplementary Fig. A.2.7: PFTF forecast from 2023-04-16 12:00 at point B4. The black line in the life expectancy plot shows the mean of all forecasts at each time step and the grey area represents the failure window during which a failure is likely. Boxplots include all forecasts since the OOA per velocity window. The black horizontal line marks the latest timestamp, the grey area represents the failure window and the red diamonds show the latest forecasts per velocity window. Boxplots show the median as line, the interquartile range as box, 1.5 times the interquartile range or the minimum or maximum data point as whiskers and outliers as open circles. See Supplementary Fig. A.2.1 for details on the visualization.

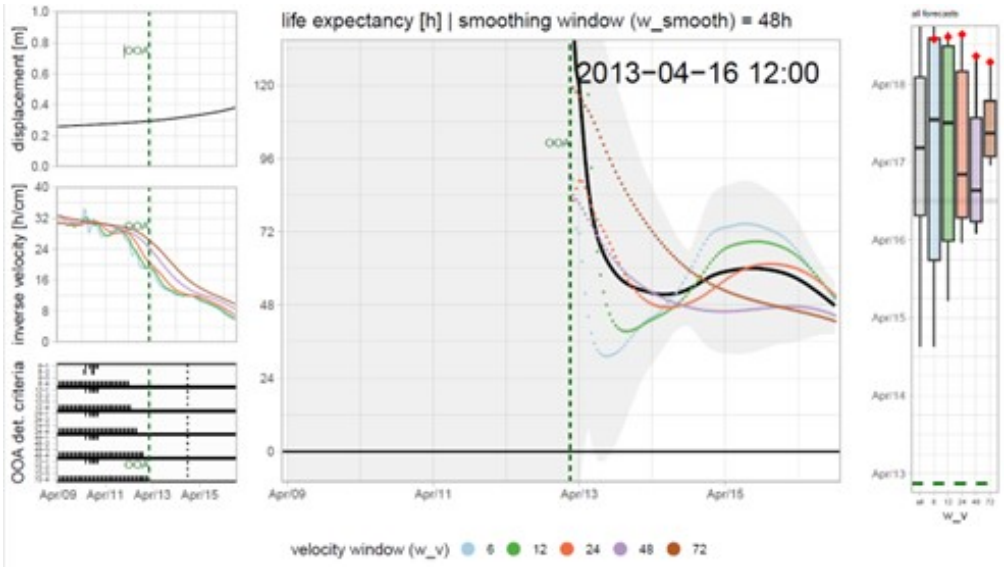

Supplementary Fig. A.2.8: PFTF forecast from 2023-04-16 12:00 at point T8. The black line in the life expectancy plot shows the mean of all forecasts at each time step and the grey area represents the failure window during which a failure is likely. Boxplots include all forecasts since the OOA per velocity window. The black horizontal line marks the latest timestamp, the grey area represents the failure window and the red diamonds show the latest forecasts per velocity window. Boxplots show the median as line, the interquartile range as box, 1.5 times the interquartile range or the minimum or maximum data point as whiskers and outliers as open circles.See Supplementary Fig. A.2.1 for details on the visualization.

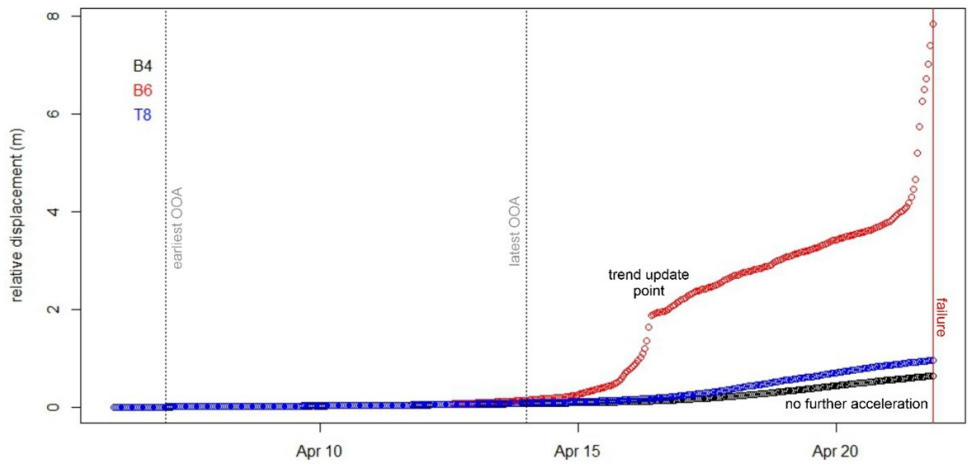

Supplementary Fig. A.2.9: Displacement of three measurement points B4 (black), B6 (red) and T8 (blue) at La Saxe after in April 2013 until failure of B6.

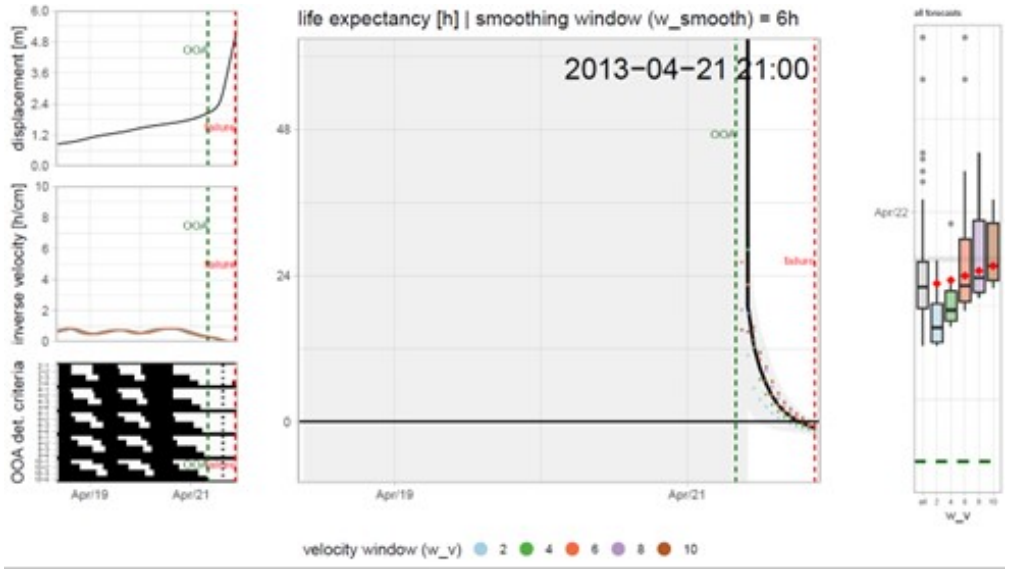

Supplementary Fig. A.2.10: PFTF forecast after the trend update point on 2023-04-16 12:00 at point B6 with short window lengths. The black line in the life expectancy plot shows the mean of all forecasts at each time step and the grey area represents the failure window during which a failure is likely. Boxplots include all forecasts since the OOA per velocity window. The black horizontal line marks the latest timestamp, the grey area represents the failure window and the red diamonds show the latest forecasts per velocity window. Boxplots show the median as line, the interquartile range as box, 1.5 times the interquartile range or the minimum or maximum data point as whiskers and outliers as open circles. See Supplementary Fig. A.2.1 for details on the visualization.